| Editorial Board |

| Editorial Board |

| Editorial Board |

| English Language Editors |

Lecturer **Gizem AÇELYA AYKAN**	Gazi University School of Foreign Languages
Lecturer **Tuğçe BÜYÜKBAYRAM**	Gazi University School of Foreign Languages

| Technical Editors |

Research Assistant Dr. **Fatih UÇAR**	Akdeniz University
Research Assistant **Özge ÖZER ATAKOĞLU**	Akdeniz University

| INDEXING |

| ACCESSIBILITY |

| CONTENTS |

| CONTENTS |

x

HR-XRD and AFM Analysis of AlN/SiC Structures for Optoelectronic Device Applications

Ozlem BAYAL[1*] (iD) Durmus DEMIR[1] (iD) Ahmet Kursat BILGILI[1] (iD) Naki KAYA[2] (iD) Mustafa Kemal OZTURK[1] (iD)
Sukru KALAYCI[3] (iD)

[1] Gazi University, Photonics Research and Application Center, Ankara, Türkiye
[2] Kafkas University, Kağızman Vocational School, Optician Program, Türkiye
[3] Gazi University, Technical Sciences Vocational School, Ankara, Türkiye

Keywords	Abstract
AIN SiC MOCVD HR-XRD UDM	In this paper, we examined the successful growth of AlN on SiC substrate using molecular beam epitaxy technique (MBE). The AlN buffer layers are grown with (100, 130, 140 and 150 nm) thickness. XRD technique was used to analyze the four samples of Wurtsite structure including strain cases, dislocation densities and other micro-structural properties. XRD peak broadening data are used to determine crystallite size and strain values by using Williamson-Hall (WH) method. High resolution X-Ray Diffraction (HR-XRD) peak analysis method is used with Scherrer, WH, modified WH, uniform deformation model (U-DM), uniform stress deformation model (US-DM), uniform deformation energy density model (UDE-DM). Crystallite size, strain, stress, energy density values are determined by using young module. According to the results obtained from our data, it is observed that the energy value sharply decreases and then increases. This behavior of energy density is consistent with the strain and stress behaviors. It has been noticed that AlN buffer layers grown without tension and relaxation are more suitable for optoelectronic devices. Therefore, it is understood that the thickness values of AlN buffer layers are important.

Author ID (ORCID Number)		Article Process	
0000-0003-0718-9734	Ozlem BAYAL	**Submission Date**	12.02.2024
0000-0002-6470-6534	Durmus DEMIR	**Revision Date**	18.03.2024
0000-0003-3420-4936	Ahmet Kursad BILGILI	**Accepted Date**	03.04.2024
0000-0003-2287-676X	Naki KAYA	**Published Date**	27.05.2024
0000-0002-8508-5714	Mustafa Kemal OZTURK		
0000-0002-8643-6731	Sukru KALAYCI		

1. INTRODUCTION

Semiconductor group elements are used to form computer chips, cell phones, solar cells, light emitting diodes and similar modern devices. Recent technological improvements gave hand to investigate and develop new materials. At the same time many technological obstacles are met during these investigations and they need to be come over. Improvements in semiconductor industry are limited with applications of materials used during device production (Bilgili et al., 2021). Diamond, Silicon carbitte (SiC), Alliminium nitrite (AlN) and Gallium nitrite (GaN) are materials which have efficiency while operating at high temperature, power and frequency. Many of research on epitaxial film growth are made with II-VI and III-V group compounds such as GaAs and GaP until GaN is discovered by Shuji Nakamura (Nakamura, 1995; Akbas & Ozturk, 2023).

III group nitrites played an important role in development of blue laser technology. GaN based blue lasers are constructed by the help of GaN alloys. Although this is a big step in the field, there are many problems about production of high quality GaN alloys. Because of difficulties on production of mono-crystals with nitrite materials, growth of nitrite thin films on different substrates is needed (Akpinar et al., 2020). One of the

problems is about %13 lattice mismatch between GaN and sapphire. This situation effects device performance in a bad way. SiC together with nitrites is used as an alternative to GaN because it has less lattice mismatch (Nakamura et al., 1994).

It is reported that LEDs grown on sapphire by using GaN alloy with MOCVD technique, has high light emitting efficiency (Nakamura, 1995). Performance of these devices is extremely high if dislocation density about 10^{10} cm^{-2} is taken into account (Lester et al, 1995). Defect density is high, because of great lattice mismatch between GaN and substrates. First LED with high luminesance is produced by (Nakamura et al., 1995). This success increased interest on GaN that can be used as blue light source.

Including lattice match and thermal expansion many similar properties of GaN and SiC give hand to produce devices with developed structural and optical properties (Sasaki & Matsuoka, 1988; Lin et al., 1993). Sasaki and Matsuoka (1988), grow GaN on SiC substrate by using MOCVD technique. They used high purity amonia as Nitrogen source. AlN is used as buffer layer between GaN and SiC because AlN resembles SiC in structural terms (Sasaki & Matsuoka, 1988). AlN is an important material that is used for improvement of optoelectronic devices and it has 6.2 eV band gap. Because of its high drift velocity, it is used for high power and high frequency applications. AlN is preferred for substrates without cracks among III nitrite semiconductors. So far there have been great development in the growth of bulk and layer AlN. In addition to this, device performance is limited on sapphire, Si and SiC substrates because of twist inducted by strain or cracks (Uehara et al., 2003; Yang, 2011) In this respect, stable strain analysis and to understand mechanical properties of AlN films is important. There are many ways to find out these properties. XRD is one of the sensitive and unharming method for these analysis (Rong et al., 2016).

In this study, structural properties of AlN alloy grown on SiC substrate by using MOCVD, are investigated. AlN/SiC structure, includes (100, 130, 140 and 150 nm) thick AlN buffer layers in four different samples. Generally, AlN buffer layer is used for maintaining lattice match in devices such as high electron mobility transistors (HEMTs) and LEDs. Decreasing of lattice mismatch gives hand to decreasing dislocations and producing high quality devices. XRD results showed that samples are in Wurtsite structure (Mote et al., 2012).

2. MATERIAL AND METHOD

All samples are grown with low pressure MOCVD technique on 4H-SiC substrate. Trimethylaliminium (TMAl) and NH3 are used as source for Al and N respectively. Hydrogen (H$_2$) is needed by using carrier gas. Before growth of AlN, SiC substrates are annealed at 1080°C to remove dirts on its surface. In all samples, 10 nm thick AlN is grown under low reactor pressure and at 845°C growth temperature. Later, reactor temperature is adjusted as (1105, 1025, 975 and 1055°C) for all samples 1, 2, 3 and 4 respectively. AlN main layer is grown under low reactor pressure for all samples respectively. During this growth NH3 flow rate is adjusted as 50, 1000, 1000 and 50 sccm. respectively. As the result of this growth operation, 100, 130, 140 and 150 nm thick AlN buffer layers are formed for samples 1, 2, 3 and 4. Growth conditions for samples are given in Table 1.

Table 1. *Growth conditions of samples 1, 2, 3 and 4*

Sample	Thickness (nm)	Growth ratio (um/h)	P (mbar)	T1 °C	T2 °C	TMAl flux (sccm)	NH3	AFM (roughness) (nm)
1	100	0.45	30	1105	1130	25	50	4.04
2	130	0.33	50	1025	1070	15	1000	3.71
3	140	0.33	50	975	1000	15	1000	3.63
4	150	0.45	30	1055	1080	25	50	3.22

3. RESULTS AND DISCUSSION

Crystallite size is calculated with equation (1). This equation comes from Scherer method.

$$\beta = \frac{k\lambda}{Lcos\theta}$$

(1)

Parameters in this method are gained from HR-XRD pattern using Scherrer method (Pandey et al., 2021). In equation (1) k is approximately equal to 1. Lambda is the wavelength of X-Ray used, L is the crystallite size. Rocking measurements gained from different symmetric and asymmetric planes are used to draw cosΘ versus 1/FWHM plot. Slope of this plot gives us crystallite size. In Figure 1 Plots of cosθ vs 1/β gained from Scherrer method can be seen.
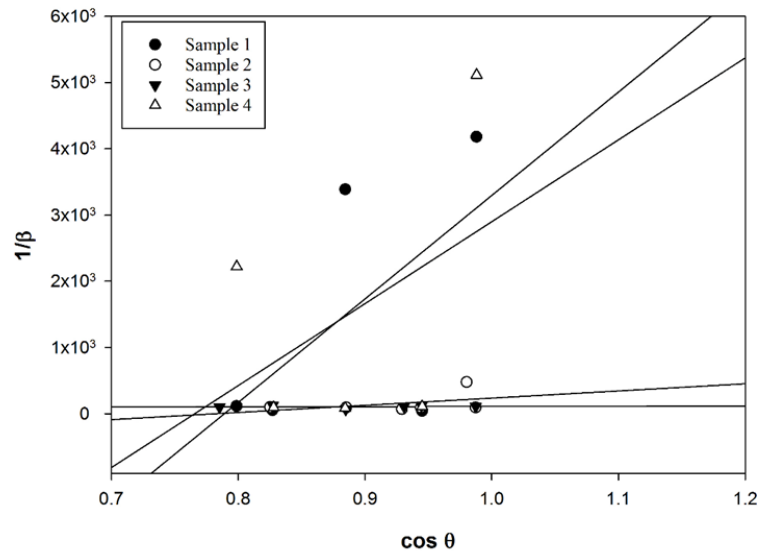
Figure 1. *Plots of cosθ vs 1/β gained from Scherrer method*

In Scherrer and modified Scherrer methods related with HR-XRD data and WH method are used in UDM, USDM and UDEDM models to calculate crystallite size, micro-structure strain and stress. During these calculations rocking curves and 2Θ measurements are used. It is noticed that these two measurement results are in agreement. Results are discussed in conclusion section.

HR-XRD graphic of aluminum nitrate buffer layers grown on silicon-on carbide substrate are shown in Figure 2. Top points of AlN buffer layers for (00.2), (00.4) and (00.6) diffraction planes can be seen in Figure 2. Peak points for all samples exhibit variations in peak widths. This situation is interested in mosaic crystally. Results are discussed in Table 2.
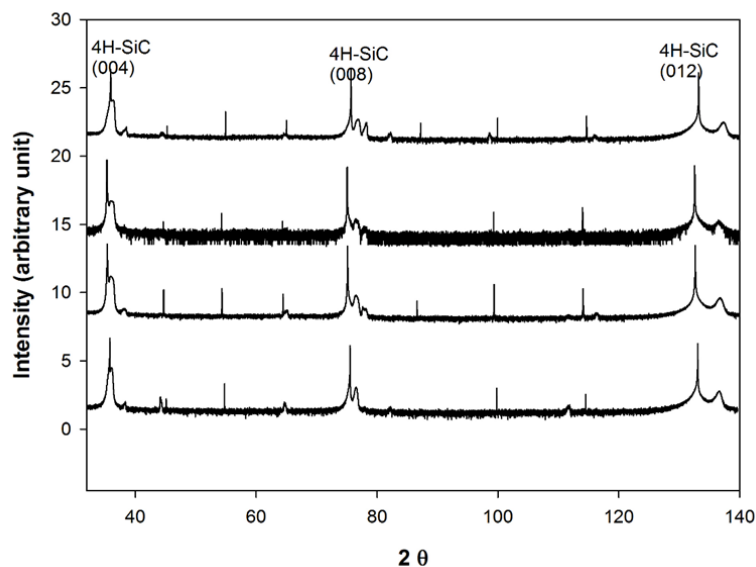
Figure 2. *High resolution Bragg reflection curves of samples 1, 2, 3 and 4 for (002), (004) and (006) planes*

Peak positions can be seen in Table 2 for different planes.

Table 2. Peak positions of AlN buffer layers for samples 1, 2, 3 and 4 in degree.

Sample No	1	2	3	4
(002)	36.45	36.06	36.22	36.54
(004)	77.29	77.47	76.83	76.57
(006)	136.82	136.52	137.01	137.11

In UDM method, equation (2) is derived from equation (1) by using some mathematical methods.

$$\beta_{hkl} = \beta T + \beta \varepsilon \tag{2}$$

$$\beta_{hkl} \cos(\theta_{hkl}) = \beta T + \beta \varepsilon \tag{3}$$

Because crystal defects are taken into account in this method, strain (ε) value can also be calculated by using equation (3). In Figure 3, $\beta\cos\theta$ versus $4\sin\theta$ were plotted. Slope of linear fit calculates lattice strain value and crystallite size is determined by y-axis intercept of this fit. Because data are away from each other, most points are not fitted together.
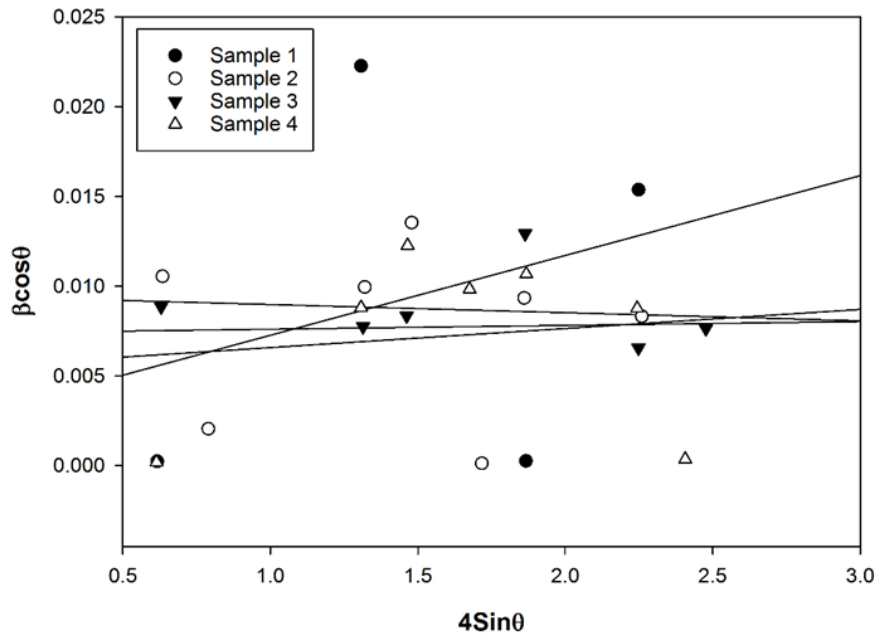
Figure 3. $\beta\cos\Theta$ vs $4\sin\Theta$ plot in modified WH method

In USDM method $\sigma = \varepsilon E_{hkl}$ transformation gives modified Scherrer equation given in equation

$$\beta hkl = \frac{k\lambda}{D} + \frac{4\sigma sin\theta}{Ehkl} \tag{4}$$

If $\beta\cos\Theta$ versus $4\sin\Theta/E_{hkl}$ plot is drawn given in Figure 4, crystallite size can be calculated from y-axis intercept of the fit. Slope of the fit gives us the strain. $\sigma = \varepsilon E_{hkl}$ equation can be used to calculate stress.
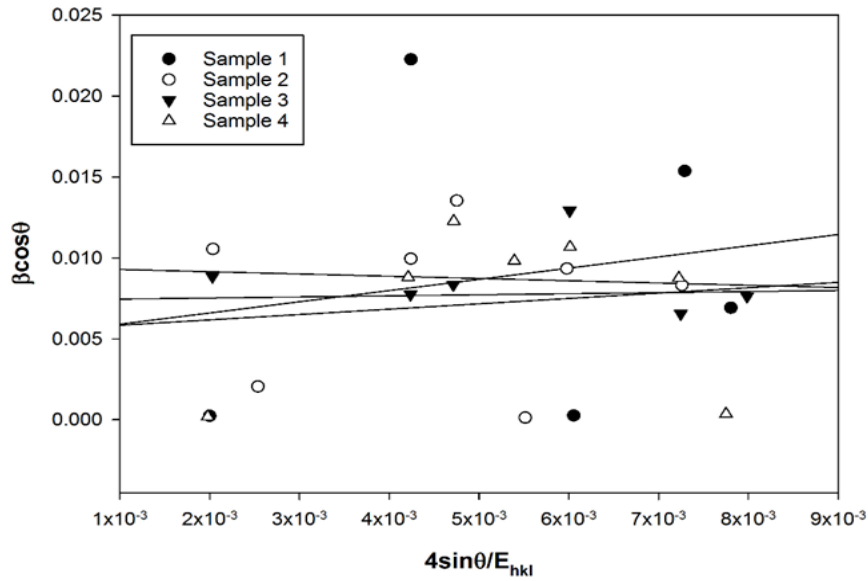
Figure 4. $\beta cos\Theta$ vs ($4sin\Theta/E_{hkl}$) plot for modified WH method

If we compare Figure 3 and Figure 4, x axis data are different from each other. In UDEDM method if $u=\varepsilon 2_{Ehkl}/2$ transformation is made, equation (5) is gained.

$$E_{hkl} = (h^2 + \frac{(h+2k)^2}{3} + \left(\frac{al^2}{c^2}\right)x(s_{11}(h^2 + \frac{(h+2k)^2}{3} + s_{33}\left(\frac{al^4}{c^4}\right)) \tag{5}$$

By using equation (5), if $\beta cos\Theta$ versus $4sin\Theta(2/E_{hkl})0.5$ plot is drawn, y-axis intercept of the fit gives crystallite size and slope of the fit gives UDED. $u=\varepsilon 2E_{hkl}/2$ equation is used for calculating stress. In Figure 5 $\beta cos\theta$ vs $(4sin\theta(2/E_{hkl})^{0.5})$ plot for modified WH method can be seen. Results are shown in Table 3 and it can be noticed that they are in good accordance with results of other models.
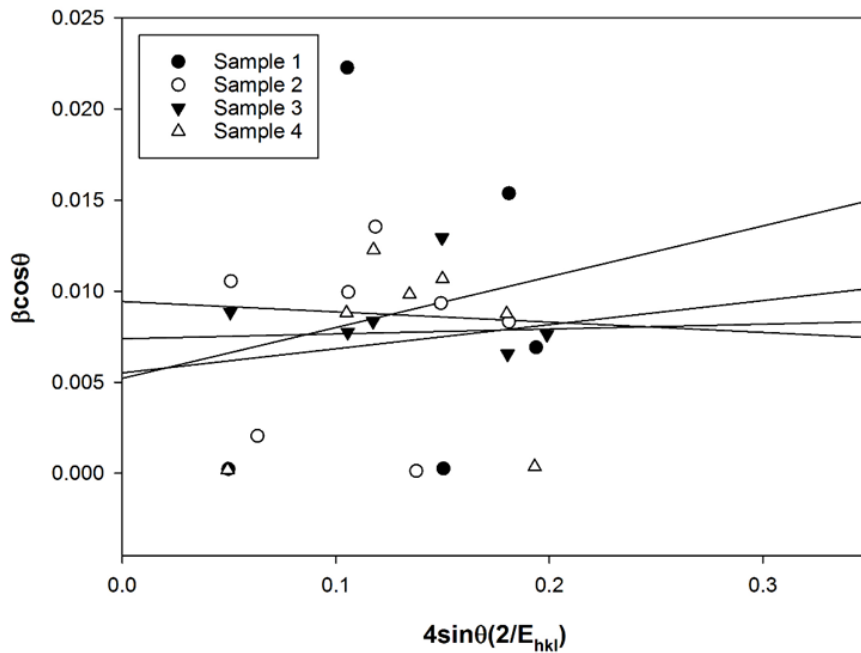
Figure 5. $\beta cos\theta$ vs $(4sin\theta(2/E_{hkl})^{0.5})$ plot for modified WH method

Crystallite size determined by WH and Scherrer methods versus thickness for all samples is given in Table 4. For an optoelectronic device, crystallite of it is expected to be good. In ideal case, mono-crystal structure can be seen but many research showed that mentioned structures present mosaic form including high defects such as dislocation densities. Of course, for these research, using semi-experimental methods is effective. As can be seen in Table 4, crystallite size dependent on thickness increase until 140 nm and later it shows a decreasing behaviour. Crystallite size presents similar behaviour for Scherrer and WH methods.

In crystal structures, maintaining lattice match in c-orientation implies there is no strain. Strain in c-orientation causes cracks. Therefore, it must be examined. In Table 4, it can clearly be seen that strain gained with WH method is found at 10^{-3} level. It shows an increase from tension case to relaxation case. Around 140 nm thickness, near the region which relaxation increase rapidly versus tension, there is minimum critical thickness.

In samples, especially the ones including Al there is stress stemming from Al. In MOCVD technique, in the process of Al growth, forming Al is extremely difficult if proper temperature and pressure conditions are not maintained. Growth of Al is possible on SiC or sapphire but difference in band gaps may not permits to grow desired structures. For this reason, in Al based structures (especially AlN) permanent stress may occur.

Models are in accordance with each other. Table 4 presents a similar behaviour with thickness versus strain. Here relaxation after tension behaviour can be noticed for samples 1, 2 and 3. Also critical minimum around 140 nm can be seen here.

Table 3. *Mosaic defects of samples*

Sample	1	2	3	4
N_{edge} (x10^{10} cm^{-2})	56.19	32.78	8.99	2.98
N_{screw} (x10^{8} cm^{-2})	19.64	6.31	1.41	2.46
L_{ort}(nm)	108.88	1952.62	1405.58	156.85
L_{par}(nm)	45.93	974.49	841.36	81.65
Tilt	0.019	0.011	0.015	0.016
Stress	-1.72x10^{-3}	-2.26x10^{-3}	-2.5x10^{-3}	-2.63x10^{-3}

Table 4. *Samples Scherrer, UDM, USDM, UDEDM part dimensions physical size strain stress results with techniques*

		Scerrer	W-H method									Sin$^2\psi$
ID	Thick.	D(nm)	UDM		USDM			UDEDM				
	nm		D (nm)	ε (x10^{-3})	D (nm)	σ (Gpa)	ε (x10^{-3})	D (nm)	u(k)/m³/(x10^{-3})	σ (Gpa)	ε (x10^{-3})	σ (Gpa)
1	100	12.37	9.16	-2.61	9.44	-0.76	-2.43	9.27	1.01	-0.80	-2.54	-0.79
2	130	10.72	10.72	-2.09	11.48	-0.53	-1.70	10.95	0.56	-0.59	-1.91	-0.73
3	140	15.37	15.37	-2.06	12.71	-0.54	-1.74	12.18	0.57	-0.59	-1.91	-0.78
4	150	10.48	10.48	2.45	10.59	0.61	1.97	10.06	0.78	0.70	2.23	0.49

In Table 4, collected energy density from lattice versus thickness can be seen in UDEDM. In order to maintain the energy needed for tension to relaxation, energy value in this plot presents a sharp decreasing later increasing behaviour. This behaviour in thickness versus energy density implies, stress and strain situations are in good accordance.

Figure 6 shows strain analysis measurements for (00.2) plane of four samples. These measurements are repeated for every Ψ in θ-2θ scans. Ψ measurement range for all samples is -4°/4° with 0.2° unit steps. Scanning is made in this range for (00.2) planes which maintain Bragg condition. It is noticed that there is shift in the peaks for all samples. This situation implies there is stress and strain in the structures. The difference between samples can be seen in tables.
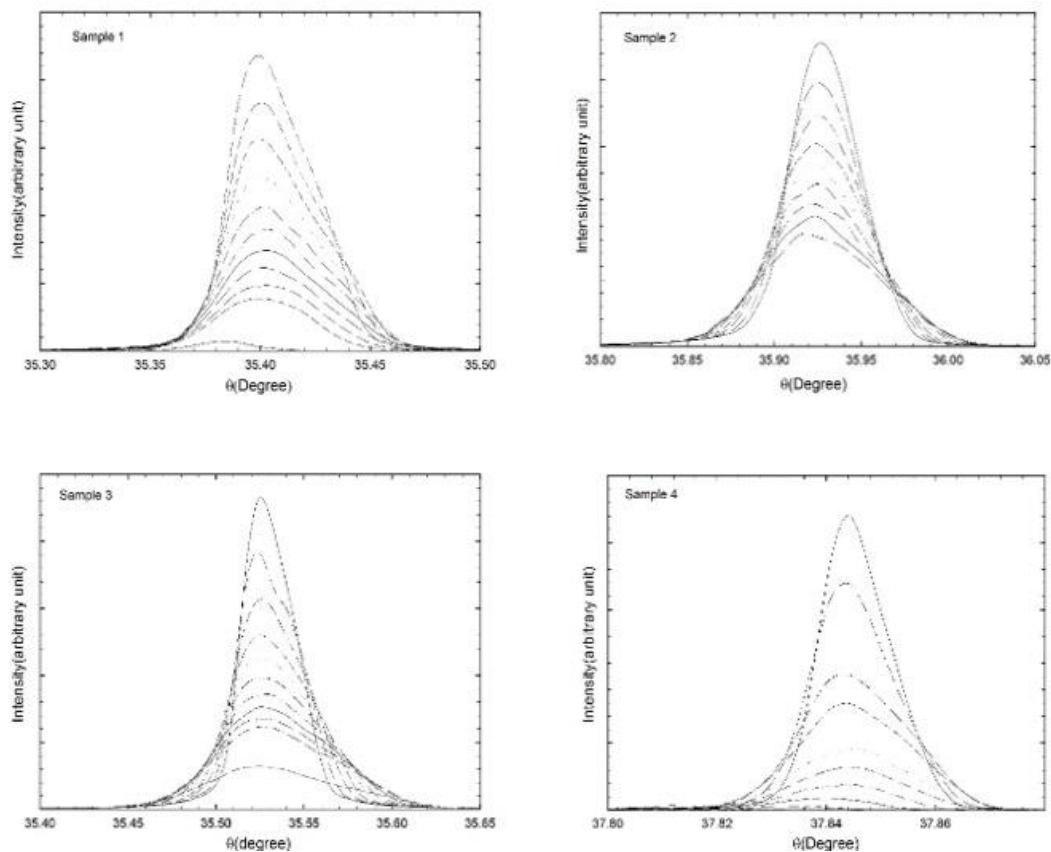
Figure 6. Stress analysis of samples in (002) planes

layer can form two situations: 1- $a_1 < a_{os}$ (relaxation), 2- $a_1 > a_{os}$ (tension). The reason for transmission from tension to relaxation around 140 nm due to critical thickness. If this value is surpassed, lattice coefficients of layers change.

-0.79 GPa (sample-1) (Yang et al., 2011), -0.73 GPa (sample-2), -0,78 GPa (sample-3) and 0,49 GPa (sample-4) (Pandey et al, 2021) values are gained from *sin2Ψ* method and they are in good accordance with WH models.

HR-XRD is a suitable method for investigation of mosaic defects. Because monocromatic Kα1 peak from Cu tube has high resolution (Williamson & William, 1953). Very few studies in literature takes attention with tilt and twist angle. For example, Lafford and co-workers investigated effect of alloy compounds and thickness on twist and tilt (Ayers, 1994). Wang and co-workers examined effect of grain volume on mosaical tilt and twist (Dai et al, 2018). For peak positions and broadening double axis x-ray pattern is used. In order to present quality of hexagonal structure, HR-XRD scans are used for symmetric and asymmetric planes. Surface morphology of samples is investigated with atomic force microscopy (AFM).

Hexagonal GaN and AlN based layers grown on Al_2O_3, SiC or Si presents lattice mismatch. As the result of this mismatch, it shows high dislocation density. There are 3 types of dislocations in such layers. As, edge, screw and mixed type dislocations.

$$D_{edge} = \left(\frac{\beta^2}{9b^2}\right) \tag{6}$$

Two methods are used for investigating tilt stemming from crystallity level and twist. In epitaxial layers it is possible to calculate Dedge and Dscrew (Ambacher, 1998; Speck & Rosner, 1999) with equations (6) and (7). Equation (7) is the same with equation (6). Full width at half maximum (FWHM) measured with HR-XRD states crystallity condition. Here b is the length of Burgers vector. (for AlN bscrew=0,4979 nm, bedge=0.3111 nm) (Chierchia et al., 2003).

Another method for edge and screw type dislocations is related with Burger's vector, plane tilt angle and lateral coherence length. All type of dislocations is dependent on, lateral coherence length of mosaic block, plane tilt and structure twist.

$$N_{(screw)} = \left(\frac{\alpha_{tilt}^2}{4.\ 35\ b\ screw^2}\right) \tag{7}$$

Screw type dislocation density can be calculated with equation (8).

Burger's vector is seen by azimuthal rotating of crystal along normal of c- surface. By measuring twist angle, edge type dislocation density can be calculated (Durukan et al., 2017).

$$N_{edge} = \left(\frac{\alpha\ \emptyset}{2.\ 1\ b_{edge}\ L}\right) \tag{8}$$

In equation (8), $\alpha\emptyset$ is FWHM of asymmetric planes, b is the length of lattice Burger's vector and L_l is the lateral coherence length (Bas et al., 2014).

HRXRD graphic of aluminum nitrate buffer layers grown on silicon carbide substrate is given in Figure 2. Peak positions of AlN buffer layers for (00.2), (00.4) and (00.6) symmetric planes can be explained in Figure 2. For four samples these peak positions show variations in peak broadening. This situation is depended on mosaic crystal structure.

Morphological properties of AlN/n-4H SiC structure is investigated by AFM. AFM scans are made in the range of 5μm x 5μm. Figure 7 shows (3D) AFM surface micrographs of AlN grown on 4H-SiC. AFM images show that layers have uniform and field like surface morphology. In addition to this, root mean square values (RMS) of samples are measured as 4.04, 3.72, 3.64 and 3.23 nm for samples 1, 2, 3 and 4 respectively. According to RMS values, 150 nm thick AlN layer grown with 50 sccm (NH3) flow ratio, has the smoothest surface morphology. It is obvious that if AlN layer is thicker, RMS value is lower for samples grown with the same NH3 flow ratio. This result implies structural quality of films increase with thicker buffer layers in accordance with XRD results. On the other hand, samples 3 which is grown with 1000 sccm NH3 flow ratio has rougher surface morphology than samples 4 which is grown with 50 sccm NH3 flow ratio. This result is in accordance with previous works done by different researchers (Çörekçi et al., 2012).

Figure 7. (3D) AFM surface micrographs of samples4

4. CONCLUSION

AlN buffer layers with different thickness are grown on SiC substrate by using Molecule beam epitaxy technique. Optical and structural properties of samples are investigated by using AFM and HR-XRD systems. Strain calculation is made with symmetric and asymmetric peaks of AlN from HR-XRD. Peak positions are determined versus Ψ. For all samples WH models are applied to calculate strain, stress, crystallite size and energy density. Results are presented in table 4. In this table it is seen that energy value sharply decrease later increase. This behaviour of energy density is in accordance with strain and stress behaviours. It is noticed that AlN buffer layers grown without tension and relaxation are more suitable for optoelectronic devices. For this reason, thickness optimization of AlN buffer layers is important.

ACKNOWLEDGEMENT

AUTHOR CONTRIBUTIONS

O. Bayal, wrote the manuscript, D. Demir, made the measurements, A. K. Bilgili made the calculations, M. K. Ozturk, N. Kaya and S. Kalayci maintained device support.

CONFLICT OF INTEREST

The authors declare no conflict of interest.

REFERENCES

Akbas, S., Oztürk, M. K. (2023). Comparative study of neutronic, mechanical and thermodynamic properties of accident tolerant cladding materials: SiC, TiC and ZrC. *Materials Science and Engineering:* B, *290*, 116352. https://doi.org/10.2139/ssrn.4181421

Akpinar, O., Bilgili, A. K., Baskose, U. C., Ozturk, M. K., Ozcelik, S., & Ozbay, E. (2020). Swanepoel method for AlInN/AlN HEMTs. *Journal of Materials Science: Materials in Electronics*, *31*, 9969-9973. https://doi.org/10.31466/kfbd.954421

Ambacher, O. (1998). Growth and applications of group III-nitrides. *Journal of physics D: Applied Physics*, *31*(20), 2653. https://doi.org/10.1088/0022-3727/31/20/001

Ayers, J.E. (1994). The measurement of threading dislocation densities in semiconductor crystals by X-ray diffraction. *Journal of Crystal Growth*. *135*(1), 71-77. https://doi.org/10.1016/0022-0248(94)90727-7

Baş, Y., Demirel, P., Akın, N., Başköse, C., Özen, Yunus., Kınacı, Barış., & Özbay, E. (2014). Microstructural defect properties of InGaN/GaN blue light emitting diode structures. *Journal of Materials Science: Materials in Electronics*, *25*, 3924-3932.

Chierchia, R., Böttcher, T., Heinke, H., Einfeldt, S., Figge, S., & Hommel, D. (2003). Microstructure of heteroepitaxial GaN revealed by x-ray diffraction. *Journal of Applied physics*, *93*(11), 8918-8925. https://doi.org/10.1063/1.1571217

Çörekçi, S., Öztürk, M. K., Çakmak, M., Özçelik, S., & Özbay, E. (2012). The influence of thickness and ammonia flow rate on the properties of AlN layers. *Materials Science in Semiconductor Processing*, *15*(1), 32-36. https://doi.org/10.1016/j.mssp.2011.06.003

Durukan, İ. K., Öztürk, M. K., Özçelik, S., & Özbay, E. (2017). Analysis of the Mosaic Defects in Graded and Non Graded In x Ga 1-x N Solar Cell Structures. *Süleyman Demirel Üniversitesi Fen Bilimleri Enstitüsü Dergisi*, *21*(1), 235-240. https://doi.org/10.19113/sdufbed.58096

Lester, S. D., Ponce, F. A., Craford, M. G., & Steigerwald, D. A. (1995). High dislocation densities in high efficiency GaN-based light-emitting diodes. *Applied Physics Letters*, *66*(10), 1249-1251.

Lin, M. E., Sverdlov, B., Zhou, G. L., & Morkoc, H. (1993). A comparative study of GaN epilayers grown on sapphire and SiC substrates by plasma-assisted molecular-beam epitaxy. *Applied Physics Letters*, *62*(26), 3479-3481. https://doi.org/10.1063/1.109026

Mote, V.D., Y. Purushothani, & Dole B.N. (2012). Williamson-Hall analysis in estimation of lattice strain in nanometer-sized ZnO particles. *Journal of Theoretical and Applied Physics*, *6*(1). https://doi.org/10.1186/2251-7235-6-6

Nakamura, S. (1995). InGaN/AlGaN Blue-Light-Emitting Diodes. *Journal of Vacuum Science & Technology A*, *13*(3), 705-710. https://doi.org/10.1116/1.579811

Nakamura, S., Mukai, T., & Senoh, M. (1994). Candela-class high-brightness InGaN/AlGaN double-heterostructure blue-light-emitting diodes. *Applied Physics Letters*, *64*(13), 1687-1689. https://doi.org/10.1063/1.111832

Nakamura, S., Senoh, M., Iwasa, N., & Nagahama, S. I. N. S. I. (1995). High-brightness InGaN blue, green and yellow light-emitting diodes with quantum well structures. *Japanese Journal of Applied Physics*, *34*(7A), L797. https://doi.org/10.1143/JJAP.34.L797

Pandey, A., Shankar, D., Janesh, K., Nidhi, G., Garima, G., Raman, R., Davinder, K. (2021). Growth, structural and electrical properties of AlN/Si (111) for futuristic MEMS applications. *Materials Science in Semiconductor Processing*, *123*, 105567. https://doi.org/10.1016/j.mssp.2020.105567

Rong, X., Wang, X., Chen, G., Pan, J., Wang, P., Liu, H., & Shen, B. (2016). Residual stress in AlN films grown on sapphire substrates by molecular beam epitaxy. *Superlattices and Microstructures*, *93*, 27-31. https://doi.org/10.1016/j.spmi.2016.02.050

Sasaki, T., & Matsuoka, T. (1988). Substrate-polarity dependence of metal-organic vapor-phase epitaxy-grown GaN on SiC. *Journal of Applied Physics*, *64*(9), 4531-4535. https://doi.org/10.1063/1.341281

Speck, J. S., & Rosner, S. J. (1999). The role of threading dislocations in the physical properties of GaN and its alloys. *Physica B: Condensed Matter*, *273*, 24-32. https://doi.org/10.1016/S0921-4526(99)00399-3

Uehara, K., Yang, C. M., Furusho, T., Kim, S. K., Kameda, S., Nakase, H., & Tsubouchi, K. (2003). AlN epitaxial film on 6H-SiC (0001) using MOCVD for GHz-band saw devices. In IEEE Symposium on Ultrasonics. Vol. 1, pp. 905-908. IEEE. https://doi.org/10.1109/ULTSYM.2003.1293546

Williamson, G.K. & W.H. Hall. (1953). X-ray line broadening from filed aluminium and wolfram. *Acta Metallurgica*, *1*(1), 22-31. https://doi.org/10.1016/0001-6160(53)90006-6

Yang, S., Reina, M., Hideto, M., Kazumasa, H., & Hiroshi, H. (2011). Raman Scattering Spectroscopy of Residual Stresses in Epitaxial AlN Films. *Applied Physics Express*, 4(3), 031001. https://doi.org/10.1143/APEX.4.031001

Perturbation Augmentation for Adversarial Training with Diverse Attacks

Duygu SERBES[1] İnci M. BAYTAŞ[1*]

[1] Boğaziçi University, Department of Computer Engineering, İstanbul, Türkiye

Keywords	Abstract
Adversarial Attacks Adversarial Training Adversarial Robustness Deep Neural Networks	Adversarial Training (AT) aims to alleviate the vulnerability of deep neural networks to adversarial perturbations. However, the AT techniques struggle to maintain the performance on natural samples while improving the deep model's robustness. The absence of perturbation diversity in generated during the adversarial training degrades the generalizability of the robust models, causing overfitting to particular perturbations and a decrease in natural performance. This study proposes an adversarial training framework that augments adversarial directions from a single-step attack to address the trade-off between robustness and generalization. Inspired by feature scattering adversarial training, the proposed framework computes a principal adversarial direction with a single-step attack that finds a perturbation disrupting the inter-sample relationships in the mini-batch during adversarial training. The principal direction obtained at each iteration is augmented by sampling new adversarial directions within a region spanning 45 degrees from the principal adversarial direction. The proposed adversarial training approach does not require extra backpropagation steps in adversarial direction augmentation. Therefore, generalization of the robust model is improved without posing an additional burden on the feature scattering adversarial training. Experiments on CIFAR-10, CIFAR-100, SVHN, Tiny-ImageNet, and The German Traffic Sign Recognition Benchmark consistently improve the accuracy on adversarial with an almost pristine natural performance.

1. INTRODUCTION

Deep Neural Networks (DNNs) establish the best performances in various fields with challenging problems, including natural language processing (Alzantot, 2018), and image (Goodfellow et al., 2014; Moosavi-Dezfooli et al., 2016) and speech (Carlini et al., 2016) recognition. Although the DNNs are versatile and successful, they are susceptible to imperceptible perturbations named adversarial attacks (Szegedy et al., 2014). Adversarial attacks can force a network into misclassifying an input that was correctly classified before the attack. Such attacks are commonly encountered as additive perturbations that the human eye cannot catch in vision applications (Goodfellow et al., 2014). The vulnerability of deep models against adversarial attacks has raised concerns about their reliability and robustness, specifically in safety-critical applications in the fields, e.g., autonomous driving (Wang et al. 2021), medical diagnostics (Finlayson et al., 2019), and finance (Fursov et al., 2021). As the vulnerability against various adversarial attacks emerges, developing defense mechanisms to fortify deep models against such attacks has become of great interest to the applications employing DNNs.

Adversarial Training (AT) is one of the commonly proposed approaches to defend against adversarial attacks. AT (Madry et al., 2018; Tramer et al., 2018) essentially trains a DNN with a training set augmented or replaced by the adversarial counterparts of training samples. The adversarial samples used in the AT should be generated

at each training iteration. Consequently, AT can be posed as a min-max optimization problem where the inner maximization generates the adversarial perturbation, and the model is updated via the minimization step. Although it is an effective defense, AT has specific challenges and limitations. When adversarial attacks are generated by attacking a supervised loss function with labels, correlations between the perturbations and the ground-truth labels might emerge during the AT leading to label leakage (Kurakin et al., 2017), degrading the model's generalization. Furthermore, the insufficient diversity in adversarial perturbations generated during training causes catastrophic overfitting (Wong et al., 2020; Kim et al., 2021).

Adversarial defense techniques often aim to alleviate the gap between robustness and generalization. Previous studies show that generating more complex (Madry et al., 2018; Schmidt, 2018) and diverse adversarial samples during AT may improve the robustness up to some extent (Jang, 2019). However, strong attacks may hurt the model's generalization to unseen natural samples (Zhang H. et al., 2019). We stress that the goal of adversarial robustness should not be improving the robust accuracy while sacrificing the model's accuracy on the natural test samples. To alleviate this trade-off, mixup (Zhang et al., 2018) and feature scattering-based techniques (Zhang H. et al., 2019; Baytaş & Deb, 2023) are employed in the literature. More recently, augmenting the training set with millions of images synthesized by generative models has also been employed to improve both robust and natural performance (Wang et al., 2023). However, generating millions of images to train a robust model would not be sufficient with limited resources.

This study proposes an adversarial training framework inspired by Zhang & Wang (2019), where adversarial perturbations are generated by disrupting the inter-sample relations in the mini-batch. On the other hand, the proposed approach augments the adversarial perturbations during training to improve the generalization. The primary motivation behind this study is to preserve the natural accuracy and avoid exacerbating the training complexity while enhancing the adversarial robustness. Training with strong but not diverse attacks hurts the model's generalization to different adversarial perturbations and natural samples. On the other hand, robust training with relatively weaker attacks to alleviate overfitting to specific adversarial perturbations improves generalization to natural samples but degrades the adversarial robustness. Therefore, this study proposes Perturbation Direction Augmentation for Adversarial Training (PDA-AT) to increase the attack diversity during training and enhance the robustness and generalization of the DNN. Contributions of the study are outlined below.

- Differing from the standard feature scattering AT (Zhang & Wang, 2019), we generate perturbations that increase the optimal transport distance between different samples of the mini-batch instead of between the natural mini-batch and its randomly perturbed version. We empirically show that we can obtain more diverse adversarial directions at each iteration.
- Adversarial perturbations are augmented by sampling new adversarial directions within a region spanning 45 degrees from the principal adversarial direction obtained from the gradient of the distance between the mini-batch of data points measured by optimal transport.
- Perturbation augmentation can enhance the adversarial robustness compared with the baseline AT methods without synthetic images. Notably, the gap between the natural and adversarial accuracies is substantially reduced.
- The proposed approach addresses the trade-off between robustness and generalization. The augmented perturbations provide robustness without sacrificing the accuracy for the natural test samples.
- Experimental results on CIFAR-10, CIFAR-100, SVHN, Tiny-ImageNet, and The German Traffic Sign Recognition Benchmark (GTSRB) datasets demonstrate consistent performance improvement for PDA-AT with augmented perturbations compared with the baseline AT techniques in the literature.

The following Literature Review presents related studies from the adversarial robustness literature. The Material and Method section explains the proposed framework and deep model architecture in detail. The Experimental Results section presents the performance of PDA-AT and a comparison with the baselines. The experimental results are interpreted in the Discussion section. The Conclusion section summarizes the proposed approach and key findings.

2. LITERATURE REVIEW

Adversarial attacks (Szegedy et al., 2014; Goodfellow et al., 2014) and robustness literature have been growing since it became evident that DNNs are sensitive against imperceptible but adversarially crafted perturbations. AT has become an effective and notable method to defend DNNs against adversarial attacks and improve robustness with the help of various adversarial attack algorithms. Goodfellow et al. (2014) were among the first studies to introduce an AT approach with Fast Gradient Sign Method (FGSM) attack. Their AT scheme augments the training samples in a mini-batch with adversarial samples obtained with FGSM. In other words, they optimize two cross-entropy terms computed with natural and adversarial samples separately. On the other hand, Madry et al. (2018) observed that incorporating natural samples in the AT weakens the robustness. Therefore, they proposed optimizing the model with only adversarial samples, given in Equation 1, generated by an iterative gradient-based adversarial attack named Projected Gradient Descent (PGD).

$$\mathbf{x}^{t+1} = \prod_{\mathbf{x}+S} \left(\mathbf{x}^t + \eta \text{sign} \left(\nabla_{\mathbf{x}^t} \mathcal{L}(\mathbf{x}, y; \theta) \right) \right) \tag{1}$$

where t denotes the attack iteration, S is the allowed perturbations set, η is the attack step size, $\prod_{\mathbf{x}+S}(\cdot)$ is the projection operator of the L-infinity ball, and θ is the parameters of a deep model.

PGD can explore stronger attacks than a single-step adversarial attack such as FGSM. However, robustness literature often discusses that the trade-off between robustness and generalization inevitably grows when the PGD attack is used in AT (Baytaş & Deb, 2023). For this reason, various modifications and improvements are proposed to address the lack of generalization of PGD adversarial training (Wong & Kolter, 2018; Wang et al., 2019; Zhang & Wang, 2019). Nevertheless, there are challenges, such as label leaking (Kurakin et al., 2017) and gradient masking (Athalye et al., 2018), that leads to a misleading robustness. Although training a deep model with powerful adversarial perturbations, such as PGD, boosts robustness more than employing FGSM attacks, training with PGD attacks is impractical for large-scale problems due to its increased number of backpropagation steps.

To alleviate AT's time complexity, researchers attempted to attain state-of-the-art robustness with single-step attacks (Zhang D. et al., 2019; Shafahi et al., 2019; Wong et al., 2020) by adopting accumulative perturbation and perturbation initialization. Shafahi et al. (2019) employed a single backpropagation step to update the model weights and generate the adversarial perturbations. On the other hand, Wong et al. (2020) identified the reasons behind the phenomenon where robust accuracy drops to 0 % during AT with FGSM attacks. Authors claimed that random initializing of the FGSM attack mitigates catastrophic overfitting and attains the desired level of robustness (Wong et al., 2020). On the other hand, Andriushchenko & Flammarion (2020) discussed the correlation between the catastrophic overfitting and local non-linearities. Consequently, the authors proposed a regularizer, GradAlign, to produce stronger adversarial examples by explicitly maximizing the gradient alignment within the attack. Furthermore, Kim et al. (2021) explained that distortions in decision boundaries and a highly curved loss surface due to characteristics of FGSM-based AT cause overfitting, which they address with an appropriate step size. However, the experimental results of these studies show that FGSM-based AT approaches suffer from poor generalization to natural samples while their robustness does not significantly exceed the PGD AT's performance by Madry et al. (2018).

Mixup-based approaches have interested the adversarial robustness domain due to their potential to enhance the generalization of AT. Mixup introduces linear behavior in the data manifold by interpolating inputs and their labels (Zhang et al., 2018). It becomes evident in the literature that the AT with mixup might outperform standard AT while improving the generalization performance (Lee et al., 2020). In the literature, various mixup studies are proposed to support adversarial robustness. For instance, Manifold Mixup (Verma et al., 2019) aims to smooth decision boundaries for multiple levels of hidden representations of deep models that provide robustness against single-step adversarial attacks. Furthermore, Lee et al. (2020) introduced Adversarial Vertex Mixup, a soft-labeled data augmentation approach that interpolates the virtual adversarial vector and the natural input.

This proposed PDA-AT is inspired by the feature scattering AT method of Zhang & Wang (2019). Feature scattering is based on a single-step adversarial attack that concerns the inter-sample relationships between adversarial and natural samples defined by the optimal transport (OT) distance. An unsupervised perturbation is generated by maximizing the OT of the perturbed and natural images. In addition, the authors also designed bilateral adversarial training (Wang & Zhang, 2019), where both images and labels are attacked during training with a single targeted perturbation where the target is the most mistaken class. Although the aforementioned AT frameworks try to address several issues of AT, there is still room for improvement.
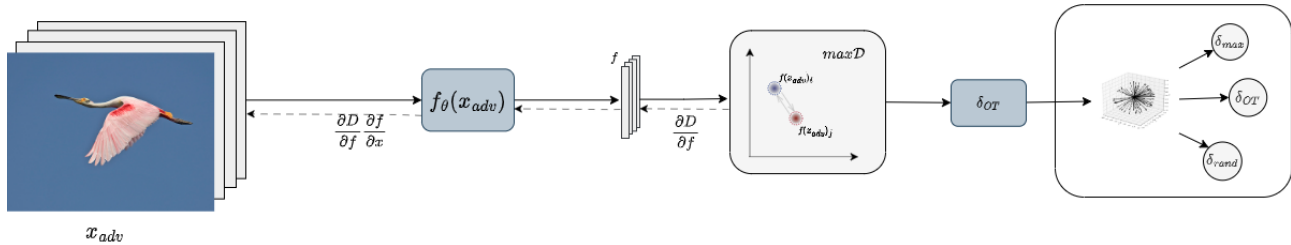
Figure 1. Proposed PDA-AT Adversarial Training Framework

3. MATERIAL AND METHOD

One of the widely discussed causes of the model's susceptibility against adversarial perturbations is explained with overfitting. Since deep models are prone to overfitting to the training data distribution, the model's predictions could be altered by the adversarial samples that can be considered out-of-distribution instances. Therefore, some AT approaches try to augment the training data with possible adversarial samples so that the model can have experience in handling adversarial perturbations. Thus, AT can be posed as the following two-step optimization problem:

$$\min_{\theta} \mathbb{E}_{(\mathbf{x},y)\sim D} \left[\max_{\delta \in S} \mathcal{L}(f(\mathbf{x} + \boldsymbol{\delta}; \theta), y) \right] \qquad (2)$$

where $f(.;\theta)$ is a neural network parametrized by θ, $\mathbf{x}$ is the natural sample, $\boldsymbol{\delta}$ is an adversarial attack, the set S contains the possible perturbations bounded by an L-infinity norm ball with an ϵ maximum amount of perturbation, y is the ground truth, and $\mathcal{L}$ is the loss function, which is cross-entropy for classification tasks.

In the optimization problem above, $\boldsymbol{\delta}$, is the perturbation that maximizes the loss function, where adversarial directions in a single step or multiple steps are obtained. Although AT is expected to contribute to the generalization of the model for adversarial samples, we commonly observe several phenomena, such as catastrophic overfitting (Wong et al., 2020), label leaking (Kurakin et al., 2017), and gradient masking (Athalye et al., 2018; Ilyas et al., 2019) that result in overfitting to certain perturbations and hampering the training. One of the contributing factors to these challenges in AT is the adversarial sample generation based on the gradient of the cross-entropy loss (Baytaş & Deb, 2023). Therefore, the adversarial direction obtained via increasing the cross-entropy loss is insufficient to generate stronger and diverse attacks (Etmann et al., 2019).

One of the most critical weaknesses of the traditional AT approaches is the generalization to natural samples. As the model's adversarial robustness improves, test accuracy on the natural samples drops below what the literature reports, which is unacceptable. We stress that the primary goal of a robust training framework should be preserving the natural performances while enhancing the robustness. Secondly, an AT training framework should be scalable such that the adversarial sample generation procedure should not require multiple costly backpropagation steps.

This study proposes an AT approach, PDA-AT, illustrated in Figure 1, where the adversarial directions are generated using Optimal Transport (OT) distance, and they are augmented to reinforce the generalization. Thus, the goal of PDA-AT is a more generalizable AT regarding robust and natural accuracies. OT distance, also known as Wasserstein distance (Xie et al., 2020) or earth mover's distance, measures the distance between

two distributions based on the minimum cost of transforming one probability distribution into another. OT distance (Villani, 2009; Cuturi, 2013) between two distributions can be defined as:

$$\mathcal{D}(\mu, v) = \inf_{\gamma \in \Pi(\mu, v)} \mathbb{E}_{(x,y) \sim \gamma} c(x, y) \tag{3}$$

where $\Pi(\mu, v)$ represents the joint distributions $\gamma(x, y)$ with marginals of $\mu(x)$ and $v(y)$. The cost function, $c(x, y)$ denotes $K \times K$ transport cost matrix C, where $C_{ij} = c(x_i, y_j)$ indicates how much it costs to transfer the i-th data vector in mini-batch **X** to the j-th data vector in mini-batch **Y**.

Feature Scattering based AT, first introduced by Zhang & Wang (2019), replaces PGD attack on the cross-entropy loss in the standard AT (Madry et al., 2018) with an FGSM attack on OT distance between the natural and the adversarial mini-batches. To be more specific, before the OT loss attack is generated, we need to compute the loss. Since a single-step attack is considered, the mini-batch of adversarial samples is obtained by adding a uniform random matrix sampled within the ϵ-ball to the natural samples to compute the OT loss before the attack. In other words, in the standard feature scattering AT, the adversarial direction is generated by altering the inter-sample relationships between a natural mini-batch and its randomly shifted version to deepen the discrepancy between natural and adversarial distributions.

The standard feature scattering AT obtains a perturbation by computing the gradient of the OT distance between the natural image and its randomly shifted counterpart. Thus, the perturbation aims to maximize the gap between the distributions of the mini-batch of natural and randomly shifted samples at each training iteration. Although training with feature scattering perturbation improves the robustness to an extent, the attack diversity, discussed in Section 4.4, gradually decreases during training, which is detrimental to the model's generalization. Therefore, we argue that maximizing the OT distance between natural and randomly shifted samples may limit the attack diversity since the difference between the two sets in question is the amount and the direction of the random shift at each iteration. Consequently, the OT distance between the same mini-batch given in Equation 4 is preferred.

$$\boldsymbol{\delta}_{\text{OT}} = \arg \max_{\mathbf{X}} \mathcal{D}(\boldsymbol{v}_{\text{adv}}, \boldsymbol{v}_{\text{adv}}) \tag{4}$$

$$\mathcal{D}(\boldsymbol{v}_{\text{adv}}, \boldsymbol{v}_{\text{adv}}) = \min_{\mathbf{T} \in \Pi(\boldsymbol{v}_{\text{adv}}, \boldsymbol{v}_{\text{adv}})} \sum_{i=1}^{n} \sum_{j=1}^{n} \mathbf{T}_{ij} \cdot c\left(f(\mathbf{x}_{\text{adv}})_i, f(\mathbf{x}_{\text{adv}})_j\right)$$

where $c(f(\mathbf{x}_{\text{adv}})_i, f(\mathbf{x}_{\text{adv}})_j)$, given below, is the element of the transport cost matrix which is zero for the same samples.

$$c\left(f(\mathbf{x}_{\text{adv}})_i, f(\mathbf{x}_{\text{adv}})_j\right) = \left\| f(\mathbf{x}_{\text{adv}})_i - f(\mathbf{x}_{\text{adv}})_j \right\|_2^2 \tag{5}$$

The proposed modification aims to facilitate exploring adversarial directions that change the natural sample distribution more freely since we do not force the adversarial direction to specifically deepen the discrepancy between the natural samples and their randomly shifted versions. The proposed perturbation is intended to diverge the adversarial sample distribution from the distribution of the natural samples. Therefore, we claim that the perturbation direction should change at each iteration since the representation distribution will differ after each weight update. Thus, Equation 5 aims to diversify the adversarial direction at each iteration compared with constantly leading the adversarial direction toward increasing the disparity between the natural and randomly perturbed samples. In experiments, we empirically show that the proposed modification increases attack diversity and improves the robustness.
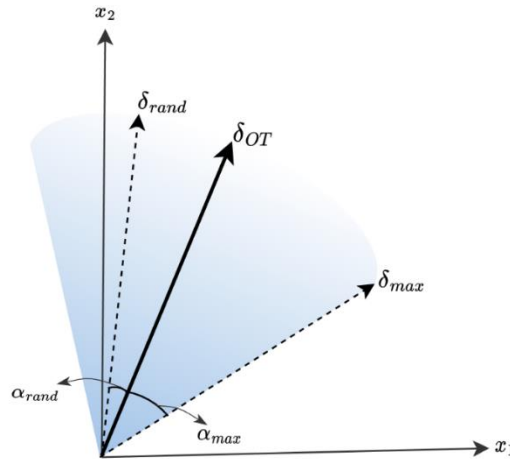
Figure 2. *Adversarial Direction Augmentation in 2-Dimensional Space*

3.1. Adversarial Direction Augmentation

It is evident in adversarial robustness literature that presenting a wide range of perturbations to model training alleviates overfitting to certain perturbations. This study introduces an intuitive and effective adversarial perturbation augmentation approach. The perturbation $\boldsymbol{\delta}_{\mathrm{OT}}$ in Equation 4 denotes the principal adversarial direction that increases the OT loss. This direction contains the most distinctive information about how to increase the gap between the distributions of adversarial and natural data representations. Although relying only on the principal adversarial direction enhances the robustness of the model, the attack diversity could be further improved. However, increasing the attack diversity during training should not create an additional computational overhead since the complexity of AT is already higher than the standard training. Therefore, we propose to benefit from the principal adversarial direction carried in $\boldsymbol{\delta}_{\mathrm{OT}}$ to obtain new adversarial directions without requiring extra backpropagation steps during AT iterations. Particularly, we propose randomly sampling a new adversarial direction within a 45-degree angle from the principal direction as given below:

$$\boldsymbol{\delta}_{\mathrm{rand}} = \cos(\alpha)\boldsymbol{\delta}_{\mathrm{OT}} + \sin(\alpha)\,\boldsymbol{\delta}_{\perp} \tag{6}$$

where α is a random angle between 0 and 45 degrees, and $\boldsymbol{\delta}_{\perp}$ is a randomly generated perturbation vector perpendicular to $\boldsymbol{\delta}_{\mathrm{OT}}$. In addition to $\boldsymbol{\delta}_{\mathrm{rand}}$, we generate one more adversarial direction denoted by $\boldsymbol{\delta}_{45}$ when α is set to 45 degrees. Thus, three adversarial directions, shown in Figure 2, can be obtained to increase the variety of adversarial attacks at each iteration without significantly increasing the computational cost. The fundamental reason behind 45 degrees is to ensure that the new sampled direction maintains its adversarial characteristic. As we move away from the principal adversarial direction that stems directly from the gradient of the OT loss, the perturbation's strength might degrade since the new direction might be toward a decrease in loss. Therefore, we constrain the sampling region at 45-degree from the principal direction so that the sampled perturbations can still decrease the loss up to an extent. We also hypothesize that there should be more than one adversarial direction for each natural sample in the input space. Therefore, we propose to explore more adversarial directions with the sampling approach in Equation 6. it is intuitive to investigate the new potential adversarial attacks obtained from similar directions to the gradient of the loss.

Finally, the mini-batch is augmented with perturbed images to update the model as follows:

$$\min_{\theta} \frac{1}{N} \left[\sum_{i=1}^{N/3} \mathcal{L}(f(\mathbf{x}_i + \boldsymbol{\delta}_{\mathrm{OT}}; \theta), y) + \sum_{i=1}^{N/3} \mathcal{L}(f(\mathbf{x}_i + \boldsymbol{\delta}_{\mathrm{rand}}; \theta), y) + \sum_{i=1}^{N/3} \mathcal{L}(f(\mathbf{x}_i + \boldsymbol{\delta}_{45}; \theta), y) \right] \tag{7}$$

where the mini-batch size is denoted by N. As seen in Equation 7, the model is updated with samples perturbed with the principal and augmented adversarial directions. Clipping is applied to perturbations to stay inside the

ϵ-ball and to the perturbed images to avoid stepping out of the input domain. The proposed PDA-AT framework is given in Algorithm 1.

Algorithm 1 PDA-AT Framework. Robustness for T epochs, D dataset, θ network parameters, ϵ perturbation budget, τ learning rate, n mini-batch size, α_{max} maximum deviation angle

---

Require: $\mathcal{D}$ optimal transport (OT) distance

for $t = 1, \cdots, T$ **do**

    for mini-batch $\{\mathbf{x}_i, y_i\}_{i=1}^{n} \sim D$ **do**

        $\delta_{OT} \leftarrow \arg\max_{\mathbf{x}} \mathcal{D}(\boldsymbol{v}_{adv}, \boldsymbol{v}_{adv})$

        $\alpha \sim \mathcal{U}(0, \alpha_{max})$

        $\boldsymbol{\delta}_{rand} \leftarrow \cos(\alpha)\boldsymbol{\delta}_{OT} + \sin(\alpha)\boldsymbol{\delta}_{\perp}$

        $\boldsymbol{\delta}_{max} \leftarrow \cos(\alpha_{max})\boldsymbol{\delta}_{OT} + \sin(\alpha_{max})\boldsymbol{\delta}_{\perp}$

        $\mathbf{x}' \leftarrow [\mathbf{x} + \boldsymbol{\delta}_{OT}, \mathbf{x} + \boldsymbol{\delta}_{rand}, \mathbf{x} + \boldsymbol{\delta}_{max}]$

        model update:

        $\theta \leftarrow \theta - \tau \frac{1}{n} \sum_{i=1}^{n} \nabla_{\theta} \mathcal{L}(\mathbf{x}', y; \theta)$

    end for

end for

---

4. EXPERIMENTAL RESULTS

The PDA-AT's robustness is evaluated in both white-box and black-box settings. Extensive experiments are conducted on five commonly used benchmark datasets, including CIFAR-10, CIFAR-100 (Krizhevsky & Hinton, 2009), The Street View House Numbers (SVHN) (Yuval et al., 2011), German Traffic Sign Recognition Benchmark (GTSRB) (Houben et al., 2013), and Tiny-Imagenet (Le & Yang, 2015). The selected datasets are widely used benchmarks in the adversarial robustness literature. Furthermore, the datasets have varying characteristics such as the number of categories, background, and scale. Therefore, the datasets of interest are suitable for evaluating the adversarial robustness of the proposed method and compare it with literature.

4.1. Baselines

The PDA-AT's performance is compared with the common AT baseline methods that are based on gradient-based attacks. The proposed method does not utilize synthetically generated data during training, nor do the baselines. Performances of the following baselines are reported:

Natural: Standard training with natural images.

Madry: AT with PGD attack proposed by Madry et al. (2018), accepted as one of the most effective defense methods.

Bilateral: Training with both image and label adversarial perturbations (Wang & Zhang, 2019).

Feature Scattering: Maximizes the OT distance between natural and perturbed images (Zhang & Wang, 2019).

Adv-Interp: Generating of adversarial samples by adversarial interpolation (Zhang & Xu, 2020).

AV-Mixup: Adversarial training of data augmentation-based soft labeling approach (Lee et al., 2020).

4.2. Datasets

Comprehensive experiments are conducted across five publicly available datasets with various configurations. The CIFAR-10 dataset (Krizhevsky & Hinton, 2009) is widely recognized as the benchmark for adversarial training and comprises 32×32 RGB images of ten different object classes. The training set of CIFAR-10 contains a total of 50K images, 5K images per class, whereas the test set has 10K images. Similarly, the CIFAR-100 dataset (Krizhevsky & Hinton, 2009) comprises the same number of images and dimensions as CIFAR-10 but includes 100 object classes, each containing 500 images in a total of 50K images in the training set. CIFAR-10 and 100 datasets are constructed as a subset of 80 million tiny images dataset. The categories in the dataset do not have overlapping samples. The CIFAR-10 and CIFAR-100 are well-known object recognition datasets used for benchmarking in wide-variety of problems. The SVHN dataset (Yuval et al., 2011) is another widely used dataset in computer vision and comprises approximately 100K labeled digit images with varying sizes and orientations collected from Google Street View house numbers. The SVHN dataset is divided into 73,257 training images and 26,032 test images. Although the SVHN dataset also has 10 categories of same sized images as CIFAR-10, the SVHN images has digits in the wild instead of objects. Therefore, the SVHN data characteristics are substantially different from CIFAR-10 and 100 datasets. Tiny-ImageNet (Le & Yang, 2015) consists of 110 K images of 200 classes, each with 500 training images and 50 validation images. The Tiny-ImageNet dataset poses a challenge due to the high number of categories with less number of samples from each category. Thus, we can investigate how the number of classes impact the robustness of AT. The GTSRB (Houben et al., 2013) comprises a collection of 43 different traffic sign classes, featuring a total of 39,209 training images and 12,630 test images. The images in the dataset exhibit diverse lighting conditions and complex backgrounds, complicating the traffic sign recognition models. The GTSRB is also selected since its a large-scale multi-class image dataset of completely different pattern than the above-mentioned datasets.

4.3. Training Scheme

In all experiments, the WideResnet28-10 model (Zagoruyko & Komodakis, 2016) is used for the object recognition task. The number of epochs is set to 200 with a batch size of 60 compatible with the configurations in Feature Scattering AT study (Zhang & Wang, 2019). The optimizer is chosen as the Stochastic Gradient Descent with a weight decay of 2×10^{-4}, a momentum of 0.9, and a learning rate of 0.01 and 0.1 for SVHN and other datasets, respectively. The learning rate decays with 0.1 at the epochs 30 and 60.

PyTorch is used in the experiments. The codebase provided by Zhang & Wang (2019) is modified to implement PDA-AT. In the experiments, the maximum perturbation amount is set to $\epsilon = 8/255$, which is the commonly accepted maximum perturbation amount by the literature for the benchmark datasets considered in this study. Data augmentations, random crops and flips, are used to improve the model generalization for CIFAR and Tiny-ImageNet datasets. Label smoothing is applied with a factor of 0.5. For all datasets except Tiny-ImageNet, the images are randomly cropped into 32×32 with a padding size of 4. Meanwhile, images from Tiny-ImageNet are cropped to 64×64. To calculate the optimal transport (OT) distance, we adopted the Sinkhorn algorithm with a regularization parameter of 0.01 in a one-step attack configuration (Zhang & Wang, 2019).

4.4. Attack Diversity

One of the essential motivations of this study is to enhance the attack diversity during AT. The proposed approach is based on the inter-sample relationship between adversarial samples within the mini-batch to augment the attacks. We investigate the attack diversity by comparing the proposed method with Feature Scattering AT (Zhang & Wang, 2019). In that regard, we first create adversarial directions of CIFAR-10 training images at several epochs. Next, we sample a random direction as a reference point to compute cosine similarities with the generated adversarial directions. The standard deviations of the cosine similarities at various epochs are plotted in Figure 3. Similarly, the change in the standard deviations of the element-wise sum of the gradient direction tensor's elements for each sample can be seen in Figure 3. In both plots, we expect the proposed attack against the OT distance between the inter-samples of the mini-batch given in Equation 4 to generate a higher standard deviation than the standard Feature Scattering attack (Zhang & Wang, 2019).

Figure 3 provides empirical evidence that the proposed approach can generate more diverse attack directions than the standard single-step OT distance attack.
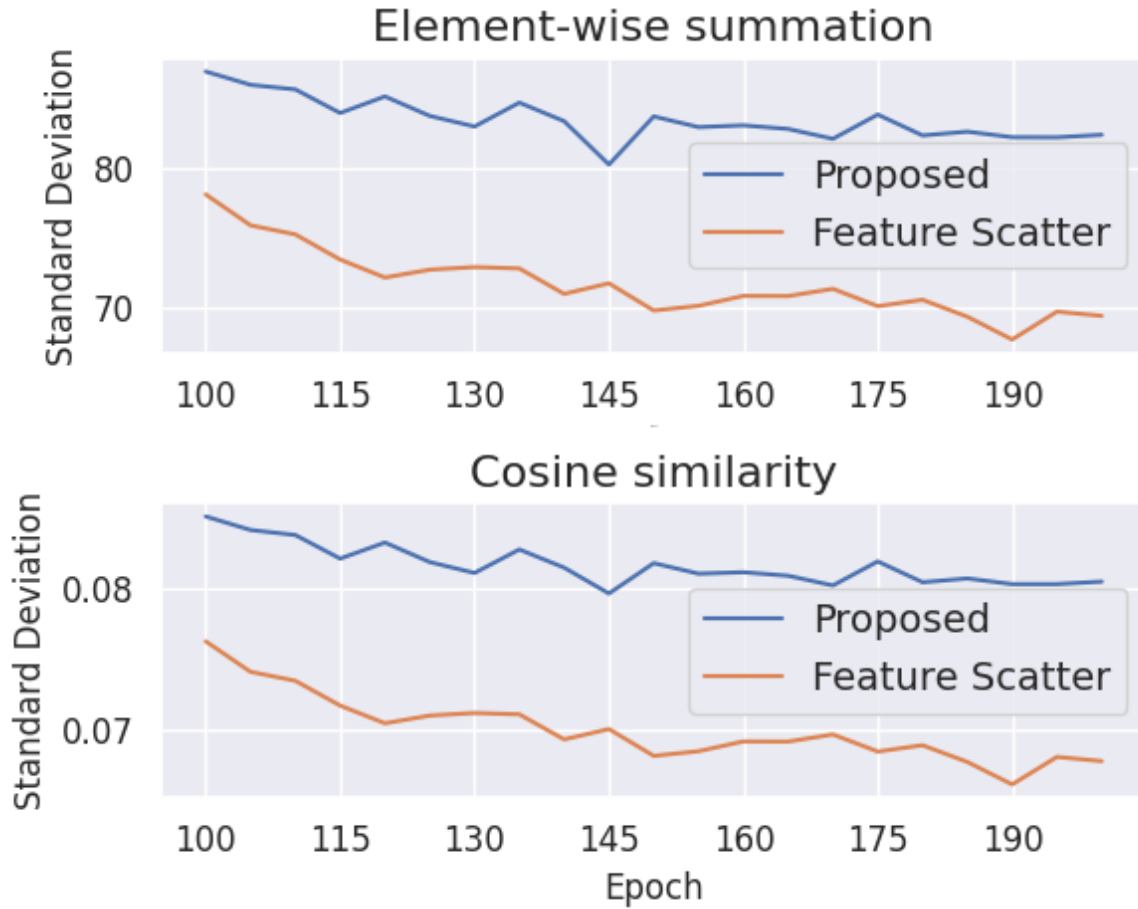
Figure 3. *Diversity of adversarial directions in training*

4.5. Variations of Perturbation Augmentations

This section investigates the optimal combination of the proposed perturbation augmentations. In this experiment, the OT distance between natural and adversarial samples is considered to obtain the primary adversarial direction, δ_{FS}, as in Feature Scattering AT (Zhang & Wang, 2019). Thus, we can observe the independent effect of the perturbation augmentation given in Table 1 below. The table demonstrates natural and robust test accuracies of proposed model trained with augmented adversarial perturbations. Natural column presents the classification accuracy of the robust model on natural test images. FGSM column demonstrates the performance on test images with FGSM attack, which is a single-step attack. On the other hand, PGD20 and CW20 columns are results on test images with PGD and Carlini and Wagner (CW) (Carlini & Wagner, 2017) attacks of 20 steps, respectively. Thus, the Table 1 investigates the contributions of different adversarial direction augmentations to the classification performance.

Table 1. *Performance of the proposed PDA-AT framework with various perturbation augmentations. Results denote classification accuracy in percentages*

Perturbation Augmentation	Natural	FGSM	PGD20	CW20
$\delta_{FS}, \delta_{rand}$	92.98	92.54	62.83	58.60
$\delta_{FS}, \delta_{rand}, \delta_{rand}$	92.44	89.27	59.74	57.40
$\delta_{FS}, \delta_{rand}, \delta_{45}$	93.68	94.33	68.08	61.88

Once the primary direction δ_{FS} is identified, we augment it within a cosine similarity region of 45 degrees. Through various experiments, we determined that the most effective attack perturbation involved a combination of the primary perturbation direction and augmented directions generated by both random and maximum allowed perturbations. Table 1 shows that adding two random perturbation directions, δ_{rand}, could hurt the generalization, while augmentation with the direction within 45 degrees of the principal adversarial direction boosts the adversarial accuracies and brings the natural performance close to state-of-the-art.

4.6. Robustness Against White-Box Attacks

We evaluate the PDA-AT framework's test accuracies for the adversarial samples and baseline methods against the following white-box attacks: FGSM (Goodfellow et al., 2014), PGD (Madry et al., 2018), and Carlini and Wagner (CW) attack (Carlini & Wagner, 2017), as well as black-box variants. We report the accuracy of the natural test images described as natural. Iterative attacks are denoted by PGDT and CWT, where T is the attack iteration. The attack step size in iterative attacks is set to 2/255 and 8/255 for single-step attacks. All the attacks are randomly initialized. The adversarial budget is set to $\epsilon = 8/255$. We summarize the natural and robust accuracies for the CIFAR-10, CIFAR-100, and SVHN datasets in Table 2. In the table, the proposed approaches are denoted by δ_{OT} and $\delta_{\mathrm{OT,rand,45}}$ represent AT with the single-step attack given in Equation 4, and AT with perturbation augmentation obtained by Equation 6, respectively.

Performances in the cells with hyphen symbols in Table 2 are not available. The baseline results without a start sign are the reported results in their corresponding studies. The selected baseline studies do not report results for each test presented in Table 2. Some of the missing results were obtained by training the baseline approach from scratch. However, we prefer to compare the PDA-AT's performance with the original results reported by the studies to reduce the changes in baseline performances due to issues such as random initialization. As a result, unavailable results are denoted by a hyphen in Table 2.

In Table 2, when Feature Scattering (Zhang & Wang, 2019) line is compared with PDA-AT with δ_{OT}, denoted by PDA-AT-δ_{OT}, we can conclude that using perturbations altering the distribution of the mini-batch rather than increasing the gap between mini-batch distributions of the natural and adversarial samples can boost the robustness in CIFAR-10 and SVHN datasets. On the other hand, PDA-AT-δ_{OT} without perturbation augmentation does not contribute to the robustness of CIFAR-100. We discuss that the change in this behavior might be due to the higher number of classes. When the number of classes increases from 10 to 100, perturbing different mini-batches at each iteration might not sufficiently generalize. Moreover, it is evident in Table 2 that the proposed perturbation augmentation significantly improves adversarial and natural accuracies compared with the baselines. Specifically, when comparing the proposed method with the best baseline performance, we can observe an increment of 13.14%, 10.28%, and 5.82% in CIFAR-10, CIFAR-100, and SVHN accuracies against the FGSM attack, respectively.

Performances for Tiny-ImageNet and GTSRB datasets are provided in Table 3. Since performances for the two datasets are not reported by all the baselines, we present their results separately by comparing them with the Feature Scattering model trained from scratch using the implementation in its GitHub repository (HaicHao, 2019). All models used in this comparison were trained with the same training and attack configurations as the other datasets. Since the Tiny-ImageNet dataset is quite challenging, the discrepancy between the robustness provided by Feature Scattering and the proposed method is not significant. However, the improvement in the robustness of GTSRB can be seen in Table 3.

4.7. Results Against Black-Box Attacks

The PDA-AT's performance in transfer-based black-box attack settings is also evaluated (Papernot et al., 2017). For this purpose, the models trained with only natural and adversarial samples with PGD attacks (Madry et al., 2018) are used to generate the gradient-based black-box attacks. The AT model has trained with PGD7. Feature Scattering and the proposed model, PDA-AT, are evaluated with a set of PGD and CW attacks created in the black-box setting. Feature Scattering (Zhang & Wang, 2019) models are trained from scratch using the code provided in (Zhang, 2019). As seen in Table 4 and Table 5, the robustness of the proposed method can generalize against black-box attacks and outperforms the Feature Scattering AT.

Table 2. *Adversarial accuracy comparison of baselines and PDA-AT under white-box attacks. The star, *, symbol indicates result of training from scratch. The dagger, †, symbol denotes results taken from Baytaş and Deb (2023). Other values are the best results reported by the baselines*

CIFAR-10								
Defenses	Natural	FGSM	PGD10	PGD20	PGD100	CW10	CW20	CW100
Natural*	96.08	34.7	0.01	0.00	0.00	0.01	0.00	0.00
Madry et al. (2018) †	87.25	62.64	47.33	45.91	45.29	-	46.99	46.54
Bilateral	91.00	70.70	63.00	57.80	55.20	-	56.20	53.80
Feature Scattering (Zhang & Wang, 2019)	90.0	78.40	70.90*	70.50	68.60	62.60*	62.40	60.60
Adv-Interp (Zhang & Xu, 2020)	90.30	78.00	-	73.50	73.00	-	69.70	68.70
AV-Mixup (Lee et al., 2020)	93.24	78.25	62.67	58.23	-	53.63	-	-
PDA-AT-δ_{OT}	90.24	78.11	73.97	72.29	71.10	62.11	59.66	57.52
PDA-AT-$\delta_{OT,rand,45}$	92.83	91.54	74.16	71.83	66.74	64.35	60.60	53.85
CIFAR-100								
Natural*	79.78	5.57	0.00	0.00	0.00	0.00	0.00	0.00
Madry et al. (2018) †	59.78	32.70	23.49	22.78	22.44	-	23.05	22.87
Bilateral	66.20	31.30	-	-	22.40	-	-	20.00
Feature Scattering (Zhang & Wang, 2019)	73.90	61.00	47.60*	47.20	46.20	30.76*	34.60	30.60
Adv-Interp (Zhang & Xu, 2020)	73.60	58.30	-	41.00	40.20	-	32.40	31.2
AV-Mixup (Lee et al., 2020)	74.81	62.76	-	38.49	-	-	-	-
PDA-AT-δ_{OT}	71.80	49.31	41.50	40.83	25.08	23.18	22.48	24.46
PDA-AT-$\delta_{OT,rand,45}$	75.73	73.04	49.19	48.83	48.77	35.16	34.64	33.86
SVHN								
Natural*	96.33	45.29	1.59	0.62	0.39	1.04	0.63	0.48
Madry et al. (2018) †	90.74	64.50	44.23	41.38	40.37	-	42.46	41.60
Bilateral	94.10	69.80	-	53.90	50.30	-	-	48.90
Feature Scattering (Zhang & Wang, 2019)	96.20	83.50	55.40*	62.90	52.00	58.18*	61.30	50.80
Adv-Interp (Zhang & Xu, 2020)	94.10	81.83	-	-	-	-	-	-
AV-Mixup (Lee et al., 2020)	95.59	91.51	37.97	-	-	-	-	-
PDA-AT-δ_{OT}	96.31	95.78	71.74	66.38	55.43	67.35	60.75	48.43
PDA-AT-$\delta_{OT,rand,45}$	97.15	97.33	72.48	65.02	50.61	65.13	56.58	42.45

Table 3. *The performance comparison for Tiny-ImageNet and GTRSB datasets.*

Tiny-ImageNet								
Defenses	Natural	FGSM	PGD10	PGD20	PGD100	CW10	CW20	CW100
Natural	69.04	2.28	0.02	0.01	0.00	0.00	0.00	0.00
Feature Scattering (Zhang & Wang, 2019)	57.42	24.42	12.54	11.25	10.33	9.11	7.97	7.55
PDA-AT-$\delta_{OT,rand,45}$	57.34	25.31	12.93	11.73	11.24	11.14	10.31	9.97
GTSRB								
Natural	98.62	63.34	19.94	14.31	11.29	17.29	13.22	11.36
Feature Scattering (Zhang & Wang, 2019)	96.5	91.81	87.82	84.56	78.52	76.01	72.02	67.42
PDA-AT-$\delta_{OT,rand,45}$	97.01	94.86	90.46	88.27	82.66	78.56	74.76	69.35

Table 4. *Results against black-box attacks transferred from the naturally trained model on CIFAR-10.*

		Defenses	
		Feature Scattering	**PDA-AT**
Attacks	**PGD20**	89.42	91.94
	PGD100	89.33	92.14
	CW20	89.41	91.87
	CW100	89.34	91.88

Table 5. *Results against black-box attacks transferred from standard AT on CIFAR-10.*

		Defenses	
		Feature Scattering	**PDA-AT**
Attacks	**PGD20**	76.60	78.40
	PGD100	76.46	77.94
	CW20	77.71	78.86
	CW100	77.44	78.76

5. DISCUSSION

The performance of the proposed PDA-AT is investigated from qualitative and quantitative perspectives. Figure 3 indicates that the adversarial direction augmentation improves the attack diversity during training. We also observe that the attack diversity slightly decreases as the training epochs proceed. In Tables 2 and 3, we can see that the augmented attack diversity results in improved robustness and generalization. The proposed PDA-AT does not sacrifice the natural accuracy compared with the baseline robust training approaches. The PDA-AT substantially improves the robustness against the FGSM attack. Adversarial accuracy might decrease for CW attacks compared to the robustness against PGD attacks for some datasets. This result shows that there is still room to alleviate overfitting certain types of attacks. On the other hand, Tiny-ImageNet and GTSRB results in Table 3 show that the PDA-AT can maintain the adversarial performance against the CW attacks better than the Feature Scattering AT. Finally, the adversarial defense techniques are notoriously prone to gradient masking (Papernot, et al., 2017). Robustness against black-box attacks in Tables 4 and 5 is reported particularly to investigate the gradient masking effect. When gradient masking occurs, adversarially trained models perform well against white-box attacks but cannot stand a black-box attack (Papernot et al., 2017). Tables 4 and 5 show that the PDA-AT can maintain its robustness against black-box attacks better than the model trained with Feature scattering AT for the CIFAR10 dataset. Thus, the proposed AT approach does not demonstrate a gradient masking effect (Papernot, et al., 2017).

6. CONCLUSION

This study proposes an adversarial training approach, PDA-AT, with adversarial direction augmentation during training. The PDA-AT employs alternative adversarial directions within a region spanning a 45-degree angle from the principal adversarial direction determined by the gradient of the optimal transport distance between the mini-batch samples. The principal adversarial direction generation differs from the Feature Scattering adversarial training, where the perturbation aims to increase OT distance between a mini-batch of adversarial samples and randomly perturbed natural samples. We empirically show that conditioning the adversarial direction to perturb the mini-batch distribution to differ from random perturbation hampers the attack diversity during training. Therefore, the proposed approach obtains adversarial directions that alter the natural sample distribution with random initializations. The extensive experimental results of the benchmark datasets, CIFAR-10, CIFAR-100, SHVN, GTSRB, and Tiny-ImageNet, against well-known white-box and black-box attacks provide empirical evidence that the PDA-AT improves adversarial robustness and augmenting the adversarial directions further boosts the adversarial accuracy.

AUTHOR CONTRIBUTIONS

D. Serbes and İ. M. Baytaş wrote the manuscript, İ. M. Baytaş developed the approach, D. Serbes conducted the experiments, and D. Serbes and İ. M. Baytaş interpreted the results.

CONFLICT OF INTEREST

The authors declare no conflict of interest.

REFERENCES

Alzantot, M., Sharma, Y., Elgohary, A., Ho, B., Srivastava, M., & Chang, K. (2018). *Generating natural language adversarial examples*. In: Proceedings of the 2018 Conference on Empirical Methods in Natural Language Processing, (pp. 2890–2896).

Andriushchenko, M., & Flammarion, N. (2020). *Understanding and improving fast adversarial training.* In: Proceedings of Advances in Neural Information Processing Systems, *33*, (pp. 16048-16059).

Athalye, A., Carlini, N., & Wagner, D. (2018, July). *Obfuscated gradients give a false sense of security: Circumventing defenses to adversarial examples.* In: International Conference on Machine Learning (pp. 274-283).

Baytaş, İ. M., & Deb, D. (2023). Robustness-via-synthesis: Robust training with generative adversarial perturbations. *Neurocomputing*, *516*, 49-60. https://doi.org/10.1016/j.neucom.2022.10.034

Carlini, N., Mishra, P., Vaidya, T., Zhang, Y., Sherr, M., Shields, C., ... & Zhou, W. (2016). *Hidden voice commands.* In: 25th USENIX security symposium (USENIX security 16), (pp. 513-530).

Carlini, N., & Wagner, D. (2017, May). *Towards evaluating the robustness of neural networks.* In: Proceedings of the IEEE Symposium on Security and Privacy. (pp. 39-57).

Cuturi, M. (2013). Sinkhorn distances: Lightspeed computation of optimal transport. *Advances in neural information processing systems*, *26*.

Etmann, C., Lunz, S., Maass, P., & Schönlieb, C. B. (2019). *On the connection between adversarial robustness and saliency map interpretability.* In: Proceedings of the 36th International Conference on Machine Learning, 97, (pp. 1823-1832).

Finlayson, S. G., Bowers, J. D., Ito, J., Zittrain, J. L., Beam, A. L., & Kohane, I. S. (2019). Adversarial attacks on medical machine learning. *Science*, *363*(6433), 1287-1289. https://doi.org/10.1126%2Fscience.aaw4399

Fursov, I., Morozov, M., Kaploukhaya, N., Kovtun, E., Rivera-Castro, R., Gusev, G., ... & Burnaev, E. (2021). *Adversarial attacks on deep models for financial transaction records.* In: Proceedings of the 27th ACM SIGKDD Conference on Knowledge Discovery & Data Mining, (pp. 2868-2878).

Goodfellow, I. J., Shlens, J., & Szegedy, C. (2014). *Explaining and harnessing adversarial examples.* In: Proceedings of the 3th International Conference on Learning Representations. https://arxiv.org/abs/1412.6572

Houben, S., Stallkamp, J., Salmen, J., Schlipsing, M., & Igel, C. (2013, August). *Detection of traffic signs in real-world images: The German Traffic Sign Detection Benchmark.* In: Proceedings of the 2013 International Joint Conference on Neural Networks, (pp. 1-8).

Ilyas, A., Santurkar, S., Tsipras, D., Engstrom, L., Tran, B., & Madry, A. (2019). *Adversarial examples are not bugs, they are features*. In: Proceedings of Advances in Neural Information Processing Systems, 32.

Jang, Y., Zhao, T., Hong, S., & Lee, H. (2019). *Adversarial defense via learning to generate diverse attacks.* In: Proceedings of the IEEE/CVF International Conference on Computer Vision, (pp. 2740-2749).

Kim, H., Lee, W., & Lee, J. (2021). *Understanding catastrophic overfitting in single-step adversarial training*. In: Proceedings of the AAAI Conference on Artificial Intelligence, (pp. 8119-8127).

Krizhevsky, A., & Hinton, G. (2009). *Learning multiple layers of features from tiny images*. University of Toronto.

Kurakin, A., Goodfellow, I. J. & Bengio, S. (2017). *Adversarial machine learning at scale*. In: Proceedings of the 5th International Conference on Learning Representations. https://arxiv.org/abs/1611.01236

Le, Y., & Yang, X. (2015). *Tiny imagenet visual recognition challenge*. CS 231N, 7(7), 3.

Lee, S., Lee, H., & Yoon, S. (2020). *Adversarial vertex mixup: Toward better adversarially robust generalization.* In: Proceedings of the IEEE/CVF Conference on Computer Vision and Pattern Recognition, (pp. 272-281).

Madry, A., Makelov, A., Schmidt, L., Tsipras, D. & Vladu, A. (2018). *Towards deep learning models resistant to adversarial attacks.* In: Proceedings of the International Conference on Learning Representations. https://arxiv.org/abs/1706.06083

Moosavi-Dezfooli, S. M., Fawzi, A., & Frossard, P. (2016). *Deepfool: A Simple and accurate method to fool deep neural networks.* In: Proceedings of the IEEE Conference on Computer Vision and Pattern Recognition, (pp. 2574-2582).

Papernot, N., McDaniel, P., Goodfellow, I., Jha, S., Celik, Z. B., & Swami, A. (2017, April). *Practical black-box attacks against machine learning*. In: Proceedings of the 2017 ACM on Asia Conference on Computer and Communications Security. (pp. 506-519).

Schmidt, L., Santurkar, S., Tsipras, D., Talwar, K., & Madry, A. (2018). *Adversarially robust generalization requires more data.* In: Proceedings of Advances in Neural Information Processing Systems, (pp. 5019-5031).

Shafahi, A., Najibi, M., Ghiasi, M. A., Xu, Z., Dickerson, J., Studer, C., ... & Goldstein, T. (2019). *Adversarial training for free!*. In: Proceedings of Advances in Neural Information Processing Systems, 32.

Szegedy, C., Zaremba, W., Sutskever, I., Bruna, J., Erhan, D., Goodfellow, I., & Fergus, R. (2014). *Intriguing properties of neural networks.* In: Proceedings of International Conference on Learning Representations. http://arxiv.org/abs/1312.6199

Tramer, F., Kurakin, A., Papernot, N., Goodfellow, I. J., Boneh, D. & McDaniel, P. D. (2018). *Ensemble adversarial training: Attacks and defenses.* In: Proceedings of the 6th International Conference on Learning Representations. https://arxiv.org/abs/1705.07204

Verma, V., Lamb, A., Beckham, C., Najafi, A., Mitliagkas, I., Lopez-Paz, D., & Bengio, Y. (2019, May). *Manifold mixup: Better representations by interpolating hidden states.* In: International Conference on Machine Learning, (pp. 6438-6447).

Villani, C. (2009). *Optimal transport: old and new* (Vol. 338, p. 23). Berlin: Springer.

Wang, J., & Zhang, H. (2019). *Bilateral adversarial training: Towards fast training of more robust models against adversarial attacks.* In: Proceedings of the IEEE/CVF International Conference on Computer Vision, (pp. 6629-6638).

Wang, K., Li, F., Chen, C. M., Hassan, M. M., Long, J., & Kumar, N. (2021). Interpreting adversarial examples and robustness for deep learning-based auto-driving systems. *IEEE Transactions on Intelligent Transportation Systems*, *23*(7), 9755-9764. https://doi.org/10.1109/TITS.2021.3108520

Wang, Y., Zou, D., Yi, J., Bailey, J., Ma, X., & Gu, Q. (2019, September). *Improving adversarial robustness requires revisiting misclassified examples.* In: Proceedings of International Conference on Learning Representations. https://openreview.net/forum?id=rklOg6EFwS

Wang, Z., Pang, T., Du, C., Lin, M., Liu, W., & Yan, S. (2023). *Better diffusion models further improve adversarial training.* In: Proceedings of the 40th International Conference on Machine Learning. (202:36246-36263) https://proceedings.mlr.press/v202/wang23ad.html

Wong, E., & Kolter, Z. (2018, July). *Provable defenses against adversarial examples via the convex outer adversarial polytope.* In: Proceeding of International Conference on Machine Learning, (pp. 5286-5295).

Wong, E., Rice, L., Kolter, J. Z. (2020). *Fast is better than free: Revisiting adversarial training.* In: Proceedings of the 8th International Conference on Learning Representations. https://arxiv.org/abs/2001.03994

Xie, Y., Wang, X., Wang, R., & Zha, H. (2020, August). *A fast proximal point method for computing exact Wasserstein distance*. In: Proceedings of Uncertainty in Artificial Intelligence (pp. 433-453).

Yuval, N., Wang, T., Coates, A., Bissacco, A., Wu, B., & Ng, A. Y. (2011). *Reading digits in natural images with unsupervised feature learning.* In: Proceedings of the NIPS Workshop on Deep Learning and Unsupervised Feature Learning.

Zagoruyko, S., & Komodakis, N. (2016) *Wide residual networks.* In: Proceedings of the British Machine Vision Conference. (pp. 1-12).

Zhang, D., Zhang, T., Lu, Y., Zhu, Z., & Dong, B. (2019). *You only propagate once: Accelerating adversarial training via maximal principle.* In: Proceedings of Advances in Neural Information Processing Systems, 32.

Zhang, H., Cisse, M., Dauphin, Y. N., Lopez-Paz, D. (2018). *Mixup: Beyond empirical risk minimization.* In: Proceedings of the 6th International Conference on Learning Representations. https://arxiv.org/abs/1710.09412

Zhang, H., & Xu, W. (2020). Adversarial interpolation training: A simple approach for improving model robustness. https://openreview.net/forum

Zhang, H., Yu, Y., Jiao, J., Xing, E., El Ghaoui, L., & Jordan, M. (2019). *Theoretically principled trade-off between robustness and accuracy*. In: Proceedings of the International Conference on Machine Learning, (pp. 7472-7482).

Zhang, H., & Wang, J. (2019). *Defense against adversarial attacks using feature scattering-based adversarial training*. In: Proceedings of the Advances in Neural Information Processing Systems, 32.

Zhang, H. (2019). Feature Scattering Adversarial Training (NeurIPS 2019) (Accessed: 24/03/2024) https://github.com/Haichao-Zhang/FeatureScatter

A No-Code Automated Machine Learning Platform for the Energy Sector

Ezgi AVCI[1*] (iD)

[1] TED University, Applied Data Science Department, Ankara, Türkiye

Keywords	Abstract
Auto-ML No-Code Platform AI Energy	This paper presents a No-Code Automated Machine Learning (Auto-ML) platform designed specifically for the energy sector, addressing the challenges of integrating ML in diverse and complex data environments. The proposed platform automates key ML pipeline steps, including data preprocessing, feature engineering, model selection, and hyperparameter tuning, while incorporating domain-specific knowledge to handle unique industry requirements such as fluctuating energy demands and regulatory compliance. The modular architecture allows for customization and scalability, making the platform adaptable across various energy sub-sectors like renewable energy, oil and gas, and power distribution. Our findings highlight the platform's potential to democratize advanced analytical capabilities within the energy industry, enabling non-expert users to generate sophisticated data-driven insights. Preliminary results demonstrate significant improvements in data processing efficiency and predictive accuracy. The paper details the platform's architecture, including data lake and entity-relationship diagrams, and describes the design of user interfaces for data ingestion, preprocessing, model training, and deployment. This study contributes to the field by offering a practical solution to the complexities of ML in the energy sector, facilitating a shift towards more adaptive, efficient, and data-informed operations.

1. INTRODUCTION

The advent of machine learning (ML) has significantly transformed various sectors, with the energy industry standing out as a prime beneficiary of this technological revolution. The deployment of ML in energy encompasses a wide range of applications, from optimizing renewable energy production to predictive maintenance of infrastructure. However, the complexity of developing and deploying effective ML models can be a significant barrier, particularly in an industry that traditionally has not focused on software development. This is where Automated Machine Learning (Auto-ML) comes into play, providing tools and frameworks that automate the ML pipeline from data preprocessing to model selection and tuning.

The need for an Auto-ML platform specifically tailored for the energy sector is driven by unique challenges such as high variability in data types, stringent reliability requirements, and the critical nature of operational efficiency. An effective Auto-ML platform for this sector must not only automate the model development process but also ensure that the models are scalable, robust, and compliant with industry-specific regulations and standards.

Our research question is *Can a No-Code Auto-ML platform specifically tailored for the energy sector effectively address the unique challenges faced by energy industry professionals, thereby enhancing operational efficiency and decision-making processes?* with the hypothesis: *A No-Code Auto-ML platform*

*Corresponding Author, e-mail: ezgi.avci@tedu.edu.tr

designed with domain-specific knowledge and tailored features for the energy sector will democratize access to advanced machine learning capabilities, leading to significant improvements in data processing efficiency, predictive accuracy, and overall operational efficiency, even for users with limited technical expertise.

This paper introduces a novel Auto-ML platform designed specifically for the energy industry. We discuss the core components of the platform, including the architecture, entity-relationship (ER) diagram, data lake architecture, ML approach, and design interfaces for the ML pipeline. The objective is to offer a comprehensive tool that empowers energy sector professionals with little to no ML expertise to leverage predictive analytics, thereby enhancing decision-making and operational efficiency.

2. THEORETICAL BACKGROUND

2.1. Auto-ML Pipeline

2.1.1. Structure

The construction of an ML pipeline begins with establishing its structure. The process starts with cleaning the input data through various steps. Subsequently, feature selection and generation are tailored to the specific domain of application. Ultimately, the model is trained using the processed features. In practice, experienced data scientists often modify and expand this basic structure to suit specific needs.

Most Auto-ML frameworks utilize a fixed pipeline structure (McGushion, 2019): data cleaning, feature selection, and a modeling phase. The preprocessing phase typically involves selecting one of several well-known algorithms, such as matrix decomposition techniques. Although the data cleaning steps often include imputation and scaling, certain steps may be unnecessary depending on the dataset, such as imputation in a dataset without missing values. By adhering to a fixed structure, the complexity of designing a pipeline is reduced, as it primarily involves choosing suitable preprocessing and modeling algorithms. However, this rigidity can sometimes result in suboptimal performance for complex datasets that may require more nuanced preprocessing.

To achieve optimal results, data science experts often design highly customized pipelines for specific ML tasks, which is not feasible with rigid pipeline structures. The initial approach to generating flexible ML pipelines using genetic programming was introduced by Olson & Moore, (2016), where pipelines are treated as tree structures and modified through the combination and mutation of sub-graphs (Koza, 1994; Banzhaf, 2006).

Hierarchical task networks simplify complex problems into smaller, manageable sub-problems until only simple operations remain. This approach reduces pipeline structure design to identifying the optimal endpoint in the network (Mohr et al., 2018). Similarly, Monte-Carlo method, a heuristic search algorithm, progressively builds more complex pipelines, aiming to find the best performing node in the search tree (Kocsis & Szepesvari, 2006; Browne et al., 2012; Rakotoarison et al., 2019).

Self-play, a reinforcement learning strategy popularized by developments like AlphaZero, involves generating training data through self-competition (Lake et al., 2016; Silver et al., 2018). In pipeline structure search, this method treats the process as a game, where actions include adding, removing, or replacing nodes, and pipeline performance dictates the scoring (Drori et al., 2018).

Although these methods offer flexibility, they often overlook dependencies between different stages of the pipeline and overall constraints. To address potential issues, such as the creation of incomplete or inappropriate pipelines, restrictions can be imposed through a defined grammar, ensuring the generation of practical yet adaptable pipelines (Drori et al., 2019).

2.1.2. Automatic Data Preparation

Data collection is essential for creating or expanding datasets. Data cleaning involves filtering out noisy data to ensure it doesn't affect subsequent model training negatively. Data augmentation is crucial for increasing

model robustness and performance, with further details on these stages provided in the following subsections. The significance of high-quality datasets in ML has been widely acknowledged, leading to the development of various open datasets. Finding appropriate datasets for specific tasks, such as those involving medical or privacy-sensitive data, can be challenging. Two approaches to address this are data searching and data synthesis. Web searching is common but faces issues like mismatched search results and poor data labeling. Noise in collected data can be detrimental to model training, necessitating robust data cleaning methods (Jesmeen et al., 2018). Techniques range from crowdsourcing to automated systems like Katara (Chu et al., 2015, 2016) and methods focusing on optimizing cleaning operations for efficiency (Krishnan & Wu, 2019). Continuous data generation poses challenges for ongoing data cleaning, which is crucial for enterprises managing daily data influxes. Systems that adapt from past cleaning experiences to optimize future workflows are being developed (Mahdavi et al., 2019).

Data augmentation (DA) is a significant component of data preparation, discussed separately due to its role in both generating new data and preventing model overfitting. Recent advances in DA focus on automating the selection of optimal DA policies using techniques like reinforcement learning and various optimization strategies (Cubuk et al., 2019; LingChen et al., 2020).

2.1.3. Feature Engineering

It is widely acknowledged that the potential of ML is fundamentally constrained by the quality of data and features, with models and algorithms serving merely to approximate this upper limit. Within this framework, feature engineering is critical for maximizing the utility of raw data for algorithmic and model use. Feature engineering encompasses three distinct phases:

- Feature selection involves creating a subset of features to minimize irrelevance and redundancy, which helps improve model performance and prevent overfitting. The selected features should be diverse and have a strong correlation with the target variables.

- Feature construction is the process of creating new features from basic feature spaces or raw data to improve the model's robustness and generalizability. This typically requires human expertise and includes preprocessing transformations like standardization, normalization, or feature discretization. Due to the impracticality of manually exploring all possible feature combinations, automated methods for feature construction have been developed (Gama, 2004; Zheng, 1998; Vafaie & De Long, 1998). These automated approaches help in searching and evaluating combinations of operations, achieving results that are often comparable to or better than manual techniques.

- Feature extraction focuses on reducing dimensionality by applying specific mapping functions to isolate informative and non-redundant features.

2.1.4. Model Generation and Evaluation

Model generation within AutoML is about automating the selection and configuration of machine learning algorithms. Traditional machine learning model development requires a practitioner to manually select an algorithm suitable for the problem at hand and then experiment with various hyperparameters to find the best configuration. This is a time-consuming and often technically challenging process, particularly in complex datasets and problem domains. AutoML simplifies this by using sophisticated algorithms to explore a wide range of machine learning models. This includes a variety of algorithm types such as:

- Decision Trees: These models perform classification or regression by making decisions based on the data features. They are easy to understand and interpret, making them a popular choice for many applications.

- Support Vector Machines (SVMs): SVMs are effective in high-dimensional spaces and are best known for their use in classification problems.

- Neural Networks: With their ability to model complex nonlinear relationships, neural networks are suited for tasks like image and speech recognition, where they can capture intricate patterns in data.

- Ensemble Methods: Techniques like Random Forests and Gradient Boosting Machines combine multiple models to produce one optimal predictive model, reducing the likelihood of overfitting and improving prediction accuracy.

AutoML tools typically use a search strategy such as grid search, random search, or more advanced methods like Bayesian optimization to systematically explore different models and their configurations. These strategies vary in their efficiency and effectiveness; for example, Bayesian optimization can more quickly generate optimal model parameters by building a probabilistic model of the function mapping hyperparameters to model performance.

Once models are generated, model selection stands as a pivotal stage where the optimal model, from those generated and evaluated earlier, is chosen for deployment. This process involves several intricate steps that ensure the selected model not only performs well statistically but also aligns with practical, operational criteria:

- **Ranking Models Based on Evaluation Metrics**

These metrics differ depending on the type of task—for instance, accuracy, precision, recall, and F1 score for classification tasks, or mean squared error and R-squared for regression tasks. In classification tasks, for instance, while accuracy might give a basic idea of performance, it could be misleading in cases of imbalanced classes, thereby making metrics like F1 score or AUC-ROC more reliable for assessing model quality. AutoML systems often employ sophisticated scoring systems that aggregate these metrics to provide a holistic assessment of each model's performance. This might involve weighting different metrics based on their relevance to the specific application or using statistical techniques to normalize scores across various metrics.

- **Considering Computational Efficiency and Complexity**

Beyond just raw performance metrics, AutoML systems also consider the computational efficiency and complexity of each model. This is crucial because a model that requires excessive computational resources for training or inference may not be practical, especially in environments with limited hardware capabilities.

  - **Computational Efficiency**: This involves evaluating the time and resources required for training and making predictions. A model that is slightly less accurate but much faster may be preferred over a top-performing model that is computationally expensive.

  - **Model Complexity**: Simpler models are often more robust and easier to maintain. They are also less likely to overfit the training data. AutoML systems can evaluate complexity based on the number of parameters, the depth of decision trees, or the architecture of neural networks.

- **Performance Criteria and Thresholds**

Model selection isn't merely about picking the highest-ranked model; it often involves meeting predefined performance criteria or thresholds. These criteria are set based on business objectives or the specific requirements of the task at hand. For example, in a medical diagnosis application, a high recall might be more important than achieving the highest possible accuracy.

- **Further Fine-Tuning**

Once a model or a set of top models is identified, AutoML systems might engage in further fine-tuning. This can involve adjusting hyperparameters, scaling up the model with more data, or simplifying the model to improve computational efficiency without significantly affecting performance. Techniques such as Bayesian optimization are often employed here to find the optimal configuration with fewer iterations.

- **Validation and Testing**

Before deployment, the selected model undergoes rigorous validation and testing to ensure that it performs consistently well on unseen data. This often includes testing on a separate test set that was not used during the

model training or evaluation phases. It helps confirm that the model's performance metrics are genuinely indicative of its real-world capabilities.

- **Deployment Considerations**

Finally, deployment considerations such as integration with existing systems, the need for real-time versus batch processing, and the operational environment (cloud, on-premises, edge devices) are taken into account. The model's architecture might be adjusted to fit into the deployment environment, ensuring that it delivers the expected performance in the real world.

2.2. Auto-ML Tools

In this section, features and functionalities of some widely used Auto-ML platforms such as Auto-sklearn, Auto-Keras, TPOT, Auto-WEKA, H2O Auto-ML,Amazon Sagemaker, and AutoGluon (Thornton et al., 2013; Feurer et al., 2019).

2.2.1. Auto-sklearn

Auto-sklearn is an open-source tool which utilizes the established Scikit-Learn package in Python (Pedregosa et al., 2011). This tool automatically identifies the most suitable learning algorithm for a new dataset and fine-tunes its hyperparameters. Additionally, Auto-sklearn employs Bayesian optimization techniques in its operations.

2.2.2. Auto-keras

Auto-Keras, also open-source, is constructed atop the Keras library and specializes in automatic neural network design, particularly for text and image data (Jin et al., 2019). It simplifies complex tasks such as embeddings and dimensionality reduction, which are typically challenging for novices in deep learning. Auto-Keras also performs automatic neural architecture optimization, adjusting aspects like neuron counts and layer configurations. Models developed with Auto-Keras function as standard TensorFlow/Keras models, handling many preprocessing tasks automatically, such as text data vectorization and cleaning (Jin et al., 2023).

2.2.3. TPOT

TPOT (Tree-based Pipeline Optimization Tool), is an open-source which utilizes genetic programming to determine the most effective model pipelines. It symbolically represents a model's pipeline, including all stages from data preparation to modeling. TPOT emphasizes ease of use with minimal user input, generating sophisticated, high-performance ML pipelines (Olson et al., 2016).

2.2.4. Auto-WEKA

Auto-WEKA leverages the classification and regression algorithms from the WEKA platform, an established open-source ML framework known for its user-friendly interface (Kotthoff et al., 2019). It is designed to help beginners by automatically tuning WEKA's algorithms and hyperparameters using Bayesian Optimization, making it as approachable as other learning algorithms (Kotthoff et al., 2016).

2.2.5. H2O

H2O, both a commercial and open-source tool, excels in detecting data schemas and analyzing results comprehensively (Darren, 2016). It is particularly adept at handling time series data, automating feature engineering, and creating efficient pipelines. H2O Auto-ML performs iterative model comparisons to identify the best model. It also has a recommender that provides data-driven recommendations tailored to business needs (Del & Poirier, 2020).

2.2.6. Amazon sageMaker

Introduced by AWS, Amazon SageMaker Autopilot is a cloud-based platform designed to work seaML essly with well-known deep-learning methods (Iwendi et al., 2022). It automatically identifies the suitable model

for any given dataset. This platform significantly simplifies the process of building ML models by autonomously searching for the best models and providing an explainability report that helps users understand and evaluate the models it develops (Park et al., 2022).

2.2.7. AutoGluon

AutoGluon is an advanced Auto-ML platform known for its automated data preprocessing, model architecture exploration, and hyperparameter tuning, which together enhance model performance and predictive accuracy (Ji et al., 2022; Erickson et al., 2020; UC., 2023). It features a diverse array of ML models. AutoGluon is designed to efficiently determine the most suitable model for specific applications, thereby optimizing performance and accuracy (UC., 2023). AutoGluon employs a multi-layer stacking strategy that uses the output of one layer of models as the input for the next layer, continually building complexity. This methodology not only uses diverse model types within each layer but also combines their outputs to create new feature sets for subsequent layers, enhancing the model's ability to learn from the data. In its final stages, AutoGluon implements ensemble models to prevent overfitting (Ge, 2020).

3. PROPOSED AUTO-ML PLATFORM

3.1. Challenges of Developing Auto-ML Solutions in Energy Sector

Despite advances in Auto-ML, its implementation in the energy sector is still limited. This shortfall is due to specific challenges within the energy domain that obstruct the adoption of Auto-ML Technologies:

- Developing a high-quality dataset:

It's crucial for models to be trained on data that reflects the format and quality expected in real-world applications. However, applying automated feature engineering to energy data, which is often highly noisy, can be challenging and lead to less than optimal outcomes.

- Black-box property of Auto-ML systems:

They do not provide clear visibility into their decision-making processes, such as the exploration of different model configurations, which can lead to mistrust among both expert and novice users. This distrust is especially acute in the critical areas of energy operations and infrastructure, where the clarity and interpretability of algorithms are vital for their integration into existing workflows.

- Big-Data:

The current methods for optimizing ML pipelines struggle to handle the large datasets that are typical in the energy sector, further limiting the presence of Auto-ML solutions in this area.

This paper seeks to overcome these challenges by creating an Auto-ML platform specifically designed for the energy industry, capable of handling the vast and diverse data streams that characterize today's energy data. Through iterative consultations with professional traders and data scientists in the energy field, essential data sources and technical needs have been pinpointed. The ability to efficiently process these data sources at high speeds is critical for improving forecasting accuracy. The proposed platform will focus on streaming data analytics, requiring continuous data access, scalability for handling substantial data volumes, and stringent data quality management.

3.2. Platform Architecture

The platform architecture (Figure 1) describes the key components and how they interact to automate the ML process. It details the data flow from ingestion to model deployment, including the integration of domain-specific modules for handling energy data. The architecture is designed to be scalable and flexible, supporting various types of energy data and ML algorithms.

3.3. Auto-ML Entity-Relationship (ER) Diagram

The ER Diagram (Figure 2) provides a visual representation of the data relationships within the Auto-ML platform. This diagram shows how different data entities such as datasets, models, features, and results are interconnected. The ER diagram serves as a blueprint for database design and helps in ensuring that the data management component of the platform is robust and efficient, catering to the needs of model training, evaluation, and deployment.

3.4. Data Lake Architecture

Although distribution companies actively collect data from different systems and many similar data sources, most of these systems work asynchronously and are stored in independent databases. Therefore, the interaction between the collected data is extremely weak. The proposed data lake architecture (Figure 3) enables many different and discrete types of data sources can be integrated with each other. SQL and NoSQL based hybrid, integrated database infrastructure. Users easily integrate their data, can get started quickly with ML.
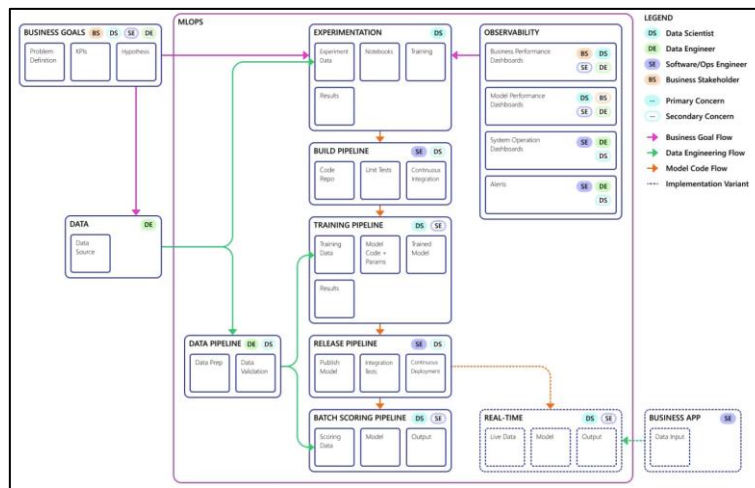
Figure 1. *Platform Architecture*
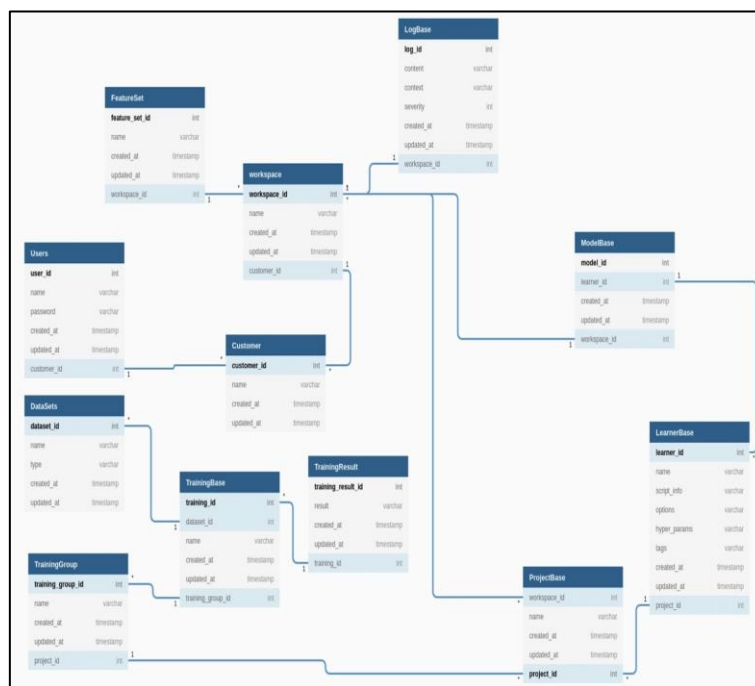
Figure 2. *ER Diagram*
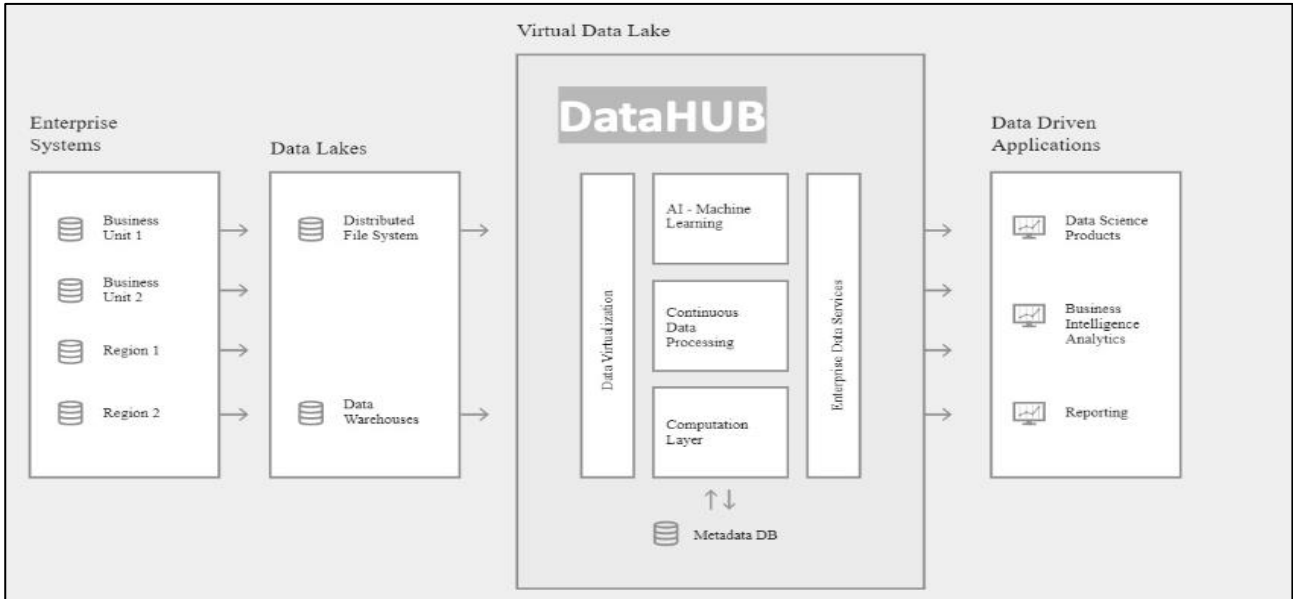
Figure 3. *Data Lake Architecture*

3.5. ML Approach

Our proposed Auto-ML platform, at the macro-level uses a model-centric strategy (Figure 4) to automate the selection, training, and optimization of ML models. This approach focuses on selecting the most appropriate models based on the characteristics of the data and the specific requirements of the energy sector tasks at hand. It includes the use of meta-learning to predict the best models and configurations, and how the platform adapts its strategies based on feedback from ongoing operations.
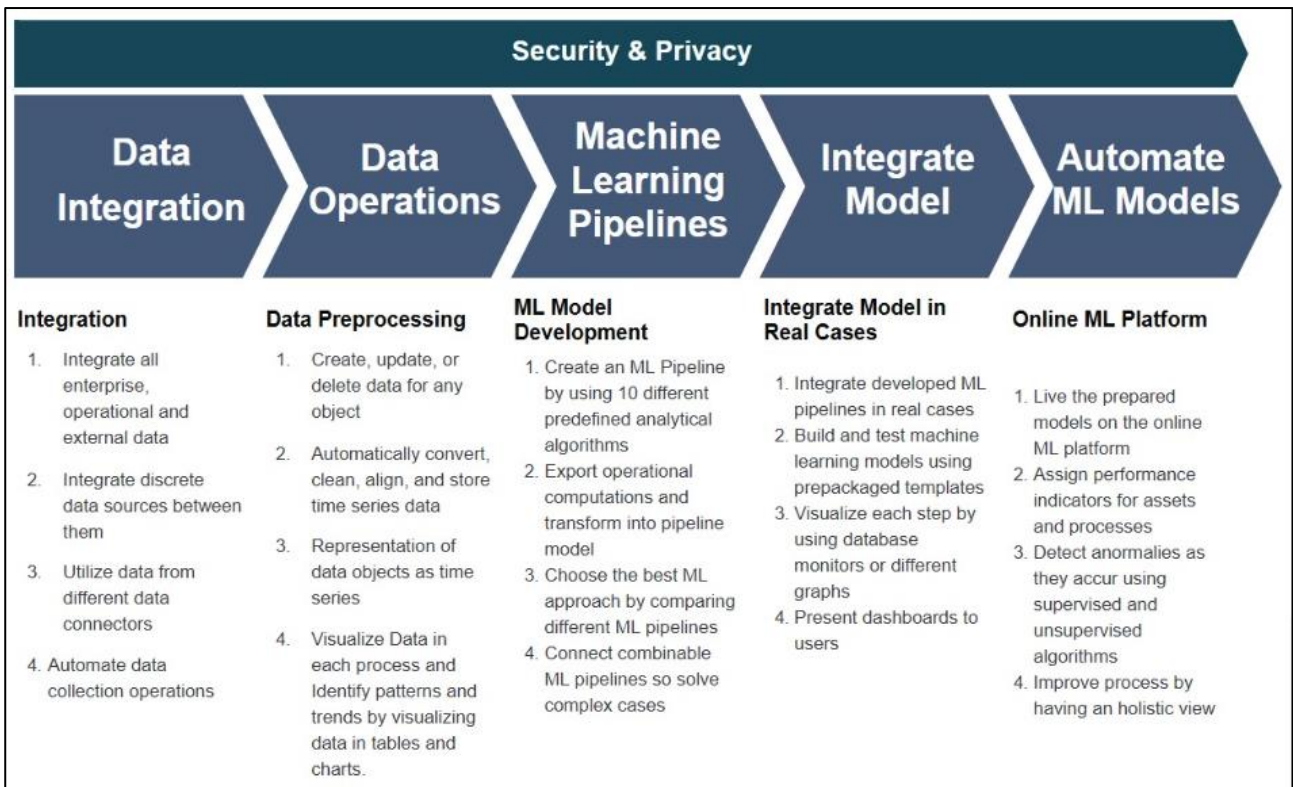
Figure 4. *Model-driven ML Approach (Macro-Level)*

Our ML approach, at the micro-level (Figure 5), enables Utility Users to:

- Integrate data sources from our platform or other data service platforms.
- Easily preprocess raw data without writing code by using predefined blocks.
- Built ML pipelines using predefined ML algorithms.
- Visualize each step of data, input or output of pipeline in preview.
- Deliver AI insights and develop your operations with actionable and qualitative AI insights.
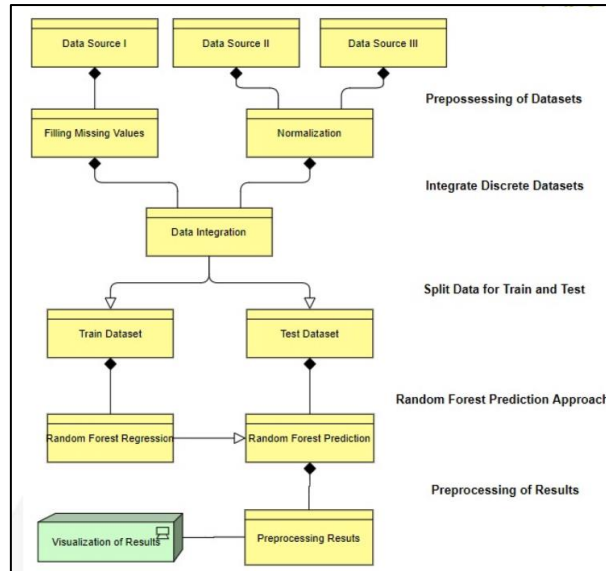
Figure 5. *ML Approach (Micro-Level)*

3.6. Design

3.6.1. Dashboard Interface

The dashboard interface (Figure 6) provides users with an overview of ongoing activities, performance metrics, and system statuses. It is designed for ease of use, allowing users to quickly assess model performances, monitor system health, and make informed decisions about adjustments or deployments.
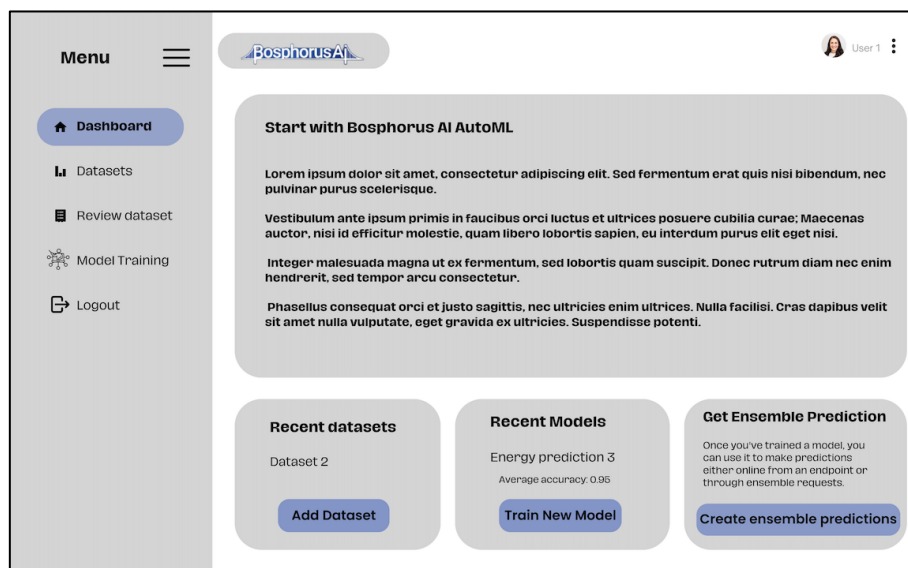
Figure 6. *Dashboard Interface*

3.6.2. Data Viewing and Addition Interface

The data viewing and addition interface (Figure 7) enables users to view existing datasets and add new ones. It explains how users interact with the data, the types of data supported, and how new data can be uploaded to the system. The interface facilitates easy management of data resources, including search, filter, and sort capabilities.
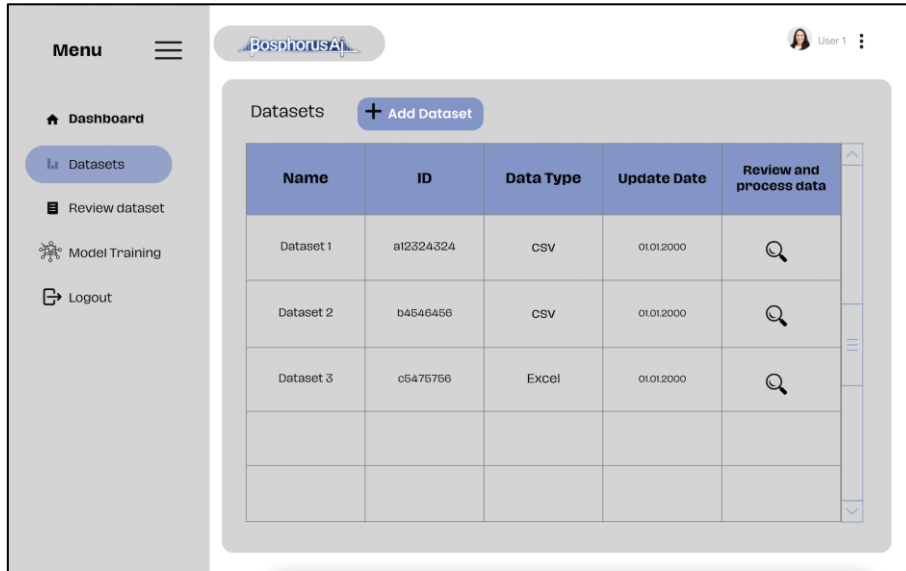
Figure 7. Data Viewing and Addition Interface

3.6.3. Data Preprocessing Interface

The data preprocessing interface (Figure 8) enables users to preprocess data which includes options for cleaning data, handling missing values, normalizing data, and feature engineering. The user-friendly design allows non-experts to perform complex preprocessing tasks with minimal technical knowledge.
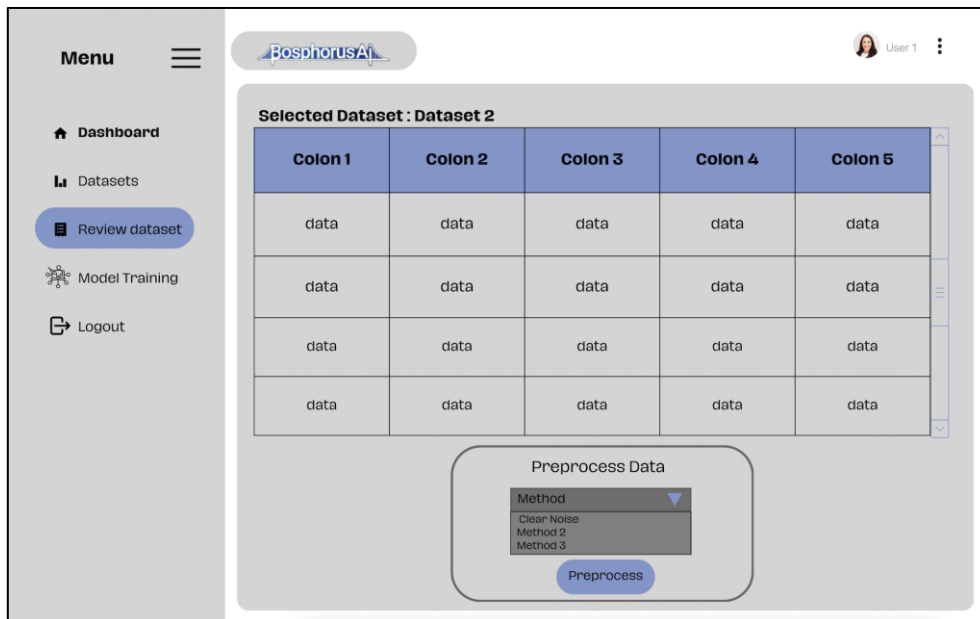
Figure 8. Data Preprocessing Interface

3.6.4. Model Training Interface

The model training interface (Figure 9) enables users to select, configure, and train ML models. It includes tools for setting parameters, choosing algorithms, and initiating training sessions. This screen also provides feedback on model performance and diagnostics to help users optimize their models.
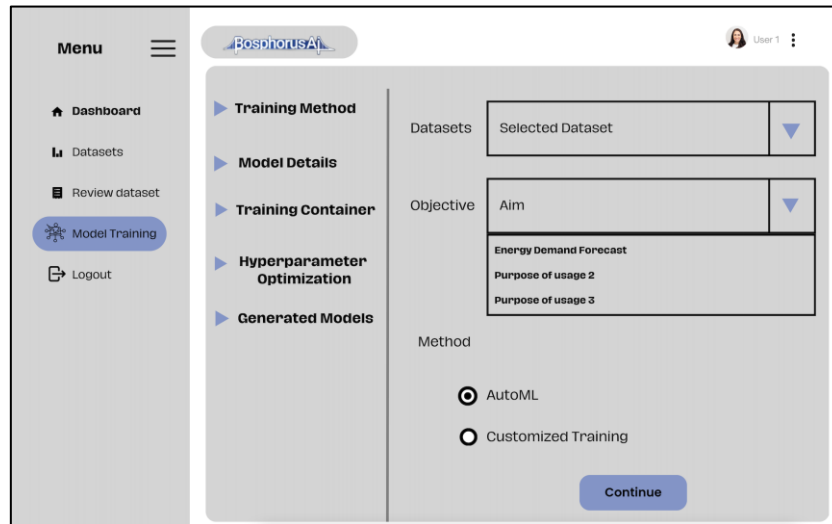
Figure 9. Model Training Interface

3.7. Usability and Preliminary Results

While the proposed No-Code Auto-ML platform for the energy sector presents significant potential, it is crucial to consider and test specific challenges such as the black-box nature of Auto-ML systems and the need for high-quality datasets, providing valuable insights into how these issues may affect the platform's deployment and effectiveness.

3.7.1. Mitigating the Effect of Black-Box Nature of Auto-ML Systems

Trust is essential for the integration of AI-driven solutions into existing workflows, and the opaque nature of Auto-ML models can hinder this trust. To mitigate this issue, the platform incorporates visualization tools aimed at enhancing interpretability and transparency. Advanced visualization tools that graphically represent model behavior and decision pathways, making it easier for users to comprehend complex models.

3.7.2. Robust Data Preprocessing and Cleaning Modules

Energy companies collect data from diverse sources and systems, leading to data silos. Integrating these disparate datasets into a cohesive whole can be challenging and time-consuming. To address these challenges, the platform includes robust data preprocessing and cleaning modules. Tools for automated data cleaning that filter out noise, handle missing values, and standardize data formats to improve dataset quality. Features that facilitate the integration of data from multiple sources, including SQL and NoSQL databases, to create comprehensive and high-quality datasets for model training.

3.7.3. Preliminary Results

Empirical validation is crucial to demonstrate the practical effectiveness of the proposed No-Code Auto-ML platform in real-world energy industry settings. We did a pilot project in collaboration with key stakeholders in the energy sector. The platform is applied to improve the accuracy of energy demand forecasts, allowing better matching of supply and demand dynamics. Accurate forecasting is critical for energy providers to ensure reliability and cost-effectiveness. Initial feedback from the pilot projects has been promising. Users have reported significant improvements in data processing efficiency and predictive accuracy. Key observations include:

- **Data Processing Efficiency**: The platform's automated data preprocessing and feature engineering capabilities have streamlined workflows, significantly reducing the time required for data preparation.

- **Predictive Accuracy**: Enhanced model accuracy has been observed in applications involving high variability in energy demands, leading to more reliable and actionable insights.

- **User Experience**: Non-expert users have found the platform's no-code interface intuitive and easy to use, facilitating broader adoption of machine learning tools within their organizations.

These preliminary results provide a strong foundation for further validation and suggest that the platform can deliver substantial benefits to energy sector professionals.

4. CONCLUSION

In this paper, we presented the design and implementation of a no-code Auto-ML platform tailored specifically for the energy industry, aiming to streamline the development and deployment of ML models. The proposed Auto-ML platform addresses the unique challenges faced by the energy sector, such as high variability in data sources and strict regulatory requirements, by incorporating domain-specific knowledge into every phase of the ML pipeline. The modular architecture of the Auto-ML platform allows for extensive customization and scalability, ensuring that it can be adapted to meet the diverse needs of various energy sub-sectors. This adaptability fosters a wider adoption of advanced analytics across the industry, from large-scale utility companies to renewable energy startups. By reducing the barrier to entry for sophisticated data analysis, our platform empowers industry stakeholders to leverage predictive analytics and ML without the need for deep technical expertise in these areas. In conclusion, our work contributes a significant tool to the energy industry's arsenal, facilitating a shift towards more adaptive, efficient, and data-informed operations. The ongoing development and refinement of such technologies will be crucial in meeting the evolving demands of global energy markets and in tackling the pressing challenges of energy sustainability and management.

While the development of the No-Code Auto-ML platform for the energy sector has shown significant promise, several limitations and challenges were encountered throughout the process. Acknowledging these issues is crucial for understanding the platform's current capabilities and identifying areas for future improvement. One of the primary challenges faced during the development of the Auto-ML platform was ensuring the quality and availability of data. The energy sector generates vast amounts of data, but this data is often noisy, incomplete, or stored in disparate systems. Developing a high-quality dataset that accurately reflects real-world conditions is essential for training effective machine learning models. This challenge was partially mitigated by integrating robust data cleaning and preprocessing modules, but inconsistencies in data sources still posed significant hurdles. Incorporating domain-specific knowledge into the Auto-ML platform to handle unique industry challenges such as fluctuating energy demand and regulatory compliance proved complex. While the platform's modular architecture allows for customization, translating expert knowledge into automated processes and algorithms required extensive collaboration with domain experts. This process was time-consuming and highlighted the need for ongoing refinement and expert input to ensure the platform remains relevant and effective.

The potential for future research and practical applications of this platform has several promising directions to further enhance its impact and utility. Collaborative and federated learning approaches can be explored to enable the platform to learn from decentralized data sources without compromising data privacy. This involves developing algorithms that allow multiple stakeholders to collaboratively train models while keeping their data local. Such approaches can enhance the platform's ability to generate robust models using diverse datasets from different organizations. While the platform is designed for the energy sector, its modular architecture allows for adaptation to other industries. Future research can explore the customization of the Auto-ML platform for different domains such as healthcare, finance, and manufacturing. This includes developing domain-specific modules and algorithms that address the unique challenges and requirements of these sectors, broadening the platform's applicability and impact.

ACKNOWLEDGEMENT

CONFLICT OF INTEREST

The author declares no conflict of interest.

REFERENCES

Banzhaf, W. (2006). Introduction. Genetic Programming and Evolvable Machines, 7(1), 5–6. https://doi.org/10.1007/s10710-006-7015-0

Browne, C. B., Powley, E., Whitehouse, D., Lucas, S. M., Cowling, P. I., Rohlfshagen, P., Tavener, S., Perez, D., Samothrakis, S., & Colton, S. (2012). A Survey of Monte Carlo Tree Search Methods. IEEE Transactions on Computational Intelligence and AI in Games, 4(1), 1–43. https://doi.org/10.1109/tciaig.2012.2186810

Chu, X., Ilyas, I. F., Krishnan, S., & Wang, J. (2016). Data Cleaning. Proceedings of the 2016 International Conference on Management of Data. https://doi.org/10.1145/2882903.2912574

Chu, X., Morcos, J., Ilyas, I. F., Ouzzani, M., Papotti, P., Tang, N., & Ye, Y. (2015). KATARA. Proceedings of the 2015 ACM SIGMOD International Conference on Management of Data. https://doi.org/10.1145/2723372.2749431

Cubuk, E. D., Zoph, B., Mane, D., Vasudevan, V., & Le, Q. V. (2019). AutoAugment: Learning Augmentation Strategies From Data. 2019 IEEE/CVF Conference on Computer Vision and Pattern Recognition (CVPR). https://doi.org/10.1109/cvpr.2019.00020

Darren, C. (2016). Practical ML with H2O: powerful, scalable techniques for deep learning and AI. O'Reilly Media, Inc.

Drori, I., Krishnamurthy, Y., Rampin, R., Lourenco, R. d. P., Ono, J. P., Cho, K., Silva, C., & Freire, J. (2018). AlphaD3M: Machine Learning Pipeline Synthesis. In International Conference on Machine Learning AutoML Workshop.

Drori, I., Krishnamurthy, Y., de Paula Lourenco, R., Rampin, R., Kyunghyun, C., Silva, C., & Freire, J. (2019). Automatic Machine Learning by Pipeline Synthesis using Model-Based Reinforcement Learning and a Grammar. In International Conference on Machine Learning AutoML Workshop.

Erickson, N., Mueller, J., Shirkov, A., Zhang, H., Larroy, P., Li, M., & Smola, A. (2020). AutoGluon-Tabular: Robust and Accurate Auto-ML for Structured Data. arXiv preprint arXiv:2003.06505.

Feurer, M., Klein, A., Eggensperger, K., Springenberg, J. T., Blum, M., & Hutter, F. (2019). Auto-sklearn: Efficient and Robust Automated Machine Learning. The Springer Series on Challenges in Machine Learning, 113-134. https://doi.org/10.1007/978-3-030-05318-5_6

Gama, J. (2004). Functional Trees. Machine Learning, 55(3), 219–250. https://doi.org/10.1023/b:mach.0000027782.67192.13

Ge, P. (2020). Analysis on Approaches and Structures of Automated Machine Learning Frameworks. 2020 International Conference on Communications, Information System and Computer Engineering (CISCE). https://doi.org/10.1109/cisce50729.2020.00106

Iwendi, C., Huescas, C. G. Y., Chakraborty, C., & Mohan, S. (2022). COVID-19 health analysis and prediction using machine learning algorithms for Mexico and Brazil patients. Journal of Experimental & Theoretical Artificial Intelligence, 1–21. https://doi.org/10.1080/0952813x.2022.2058097

Z. H, J. M., Hossen, J., Sayeed, S., Ho, C., K, T., Rahman, A., & Arif, E. M. H. (2018). A Survey on Cleaning Dirty Data Using Machine Learning Paradigm for Big Data Analytics. Indonesian Journal of Electrical Engineering and Computer Science, 10(3), 1234. https://doi.org/10.11591/ijeecs.v10.i3.pp1234-1243

Ji, Z., He, Z., Gui, Y., Li, J., Tan, Y., Wu, B., Xu, R., & Wang, J. (2022). Research and Application Validation of a Feature Wavelength Selection Method Based on Acousto-Optic Tunable Filter (AOTF) and Automatic Machine Learning (AutoML). Materials, 15(8), 2826. https://doi.org/10.3390/ma15082826

Jin, H., Song, Q., & Hu, X. (2019). Auto-Keras: An Efficient Neural Architecture Search System. Proceedings of the 25th ACM SIGKDD International Conference on Knowledge Discovery & Data Mining. https://doi.org/10.1145/3292500.3330648

Jin, H., Chollet, F., Song, Q., & Hu, X. (2023). Autokeras: an Auto-ML library for deep learning. Journal of Machine Learning Research, 24(6), 1-6. https://www.jmlr.org/papers/volume24/20-1355/20-1355.pdf

Kocsis, L., & Szepesvári, C. (2006). Bandit Based Monte-Carlo Planning. Machine Learning: ECML 2006, 282–293. https://doi.org/10.1007/11871842_29

Kotthoff, L., Thornton, C., Hoos, H. H., Hutter, F., & Leyton-Brown, K. (2019). Auto-WEKA: Automatic Model Selection and Hyperparameter Optimization in WEKA. The Springer Series on Challenges in Machine Learning, 81–95. https://doi.org/10.1007/978-3-030-05318-5_4

Kotthoff, L., Thornton, C., & Hutter, F. (2017). User guide for auto-WEKA version 2.6. Department of Computer Science, University of British Columbia, BETA Lab, Tech Report 2, 1-15. Vancouver, BC, Canada.

Koza, JohnR. (1994). Genetic programming as a means for programming computers by natural selection. Statistics and Computing, 4(2). https://doi.org/10.1007/bf00175355

Krishnan, S., & Wu, E. (2019). AlphaClean: Automatic generation of data cleaning pipelines. https://doi.org/10.48550/arXiv.1904.11827

Lake, B. M., Ullman, T. D., Tenenbaum, J. B., & Gershman, S. J. (2016). Building machines that learn and think like people. Behavioral and Brain Sciences, 40. https://doi.org/10.1017/s0140525x16001837

LeDell, E., & Poirier, S. (2020). H2o Auto-ML: scalable automatic machine learning. In 7th ICML Workshop on Automated Machine Learning. https://www.automl.org/wp-content/uploads/2020/07/AutoML_2020_paper_61.pdf

LingChen, T. C., Khonsari, A., Lashkari, A., Nazari, M. R., & Sambee, J. S. (2020). UniformAugment: A search-free probabilistic data augmentation approach. arXiv preprint arXiv:2003.14348. https://doi.org/10.48550/arXiv.2003.14348

McGushion, H. (2019). HyperparameterHunter. Available at https://github.com/HunterMcGushion/hyperparameter_hunter.

Mahdavi, M., Neutatz, F., Visengeriyeva, L., & Abedjan, Z. (2019). Towards automated data cleaning workflows. Machine Learning, 15, 16.

Mohr, F., Wever, M., & Hüllermeier, E. (2018). ML-Plan: Automated machine learning via hierarchical planning. Machine Learning, 107(8–10), 1495–1515. https://doi.org/10.1007/s10994-018-5735-z

Olson, R. S., Bartley, N., Urbanowicz, R. J., & Moore, J. H. (2016). Evaluation of a Tree-based Pipeline Optimization Tool for Automating Data Science. Proceedings of the Genetic and Evolutionary Computation Conference 2016. https://doi.org/10.1145/2908812.2908918

Park, J. B., Lee, K. H., Kwak, J. Y., & Cho, C. S. (2022). Deployment Framework Design Techniques for Optimized Neural Network Applications. 2022 13th International Conference on Information and Communication Technology Convergence (ICTC). https://doi.org/10.1109/ictc55196.2022.9952771

Pedregosa, F., Varoquaux, G., & Gramfort, A. (2011). Scikit-learn: ML in python. Journal of Machine Learning Research, 12, 2825-2830.

Rakotoarison, H., Schoenauer, M., & Sebag, M. (2019). Automated Machine Learning with Monte-Carlo Tree Search. Proceedings of the Twenty-Eighth International Joint Conference on Artificial Intelligence. https://doi.org/10.24963/ijcai.2019/457

Silver, D., Hubert, T., Schrittwieser, J., Antonoglou, I., Lai, M., Guez, A., Lanctot, M., Sifre, L., Kumaran, D., Graepel, T., Lillicrap, T., Simonyan, K., & Hassabis, D. (2018). A general reinforcement learning algorithm

that masters chess, shogi, and Go through self-play. Science, 362(6419), 1140–1144. https://doi.org/10.1126/science.aar6404

Thornton, C., Hutter, F., Hoos, H. H., & Leyton-Brown, K. (2013). Auto-WEKA. Proceedings of the 19th ACM SIGKDD International Conference on Knowledge Discovery and Data Mining. https://doi.org/10.1145/2487575.2487629

UC Irvine ML Repository. (2023). Epileptic Seizures Dataset. https://www.kaggle.com/datasets/chaditya95/epileptic-seizures-dataset.

Vafaie, H., & Jong, K. (1998). Evolutionary Feature Space Transformation. Feature Extraction, Construction and Selection, 307–323. https://doi.org/10.1007/978-1-4615-5725-8_19

Zheng, Z. (1998). A Comparison of Constructing Different Types of New Feature For Decision Tree Learning. Feature Extraction, Construction and Selection, 239￼255. https://doi.org/10.1007/978-1-4615-5725-8_15

IoT-Based Energy Consumption Prediction Using Transformers

Abdul Amir ALIOGHLI[1*] iD   Feyza YILDIRIM OKAY[2] iD

[1] Gazi University, Department of Computer Science, Ankara, Türkiye
[2] Gazi University, Department of Computer Engineering, Ankara, Türkiye

Keywords	Abstract
Transformers Time-Series Prediction IoT	With the advancement of various IoT-based systems, the amount of data is steadily increasing. The increase of data on a daily basis is essential for decision-makers to assess current situations and formulate future policies. Among the various types of data, time-series data presents a challenging relationship between current and future dependencies. Time-series prediction aims to forecast future values of target variables by leveraging insights gained from past data points. Recent advancements in deep learning-based algorithms have surpassed traditional machine learning-based algorithms for time-series in IoT systems. In this study, we employ Enc & Dec Transformer, the latest advancements in neural networks for time-series prediction problems. The obtained results were compared with Encoder-only and Decoder-only Transformer blocks as well as well-known recurrent based algorithms, including 1D-CNN, RNN, LSTM, and GRU. To validate our approach, we utilize three different univariate time-series datasets collected on an hourly basis, focusing on energy consumption within IoT systems. Our results demonstrate that our proposed Transformer model outperforms its counterparts, achieving a minimum Mean Squared Error (MSE) of 0.020 on small, 0.008 on medium, and 0.006 on large-sized datasets.

1. INTRODUCTION

The latest Internet of Things (IoT), Analytics 'State of IoT—Spring 2023' report indicates a significant surge in global IoT connections, marking an 18% increase in 2022, with 14.3 billion active IoT endpoints. Projections by IoT Analytics suggest a further 16% growth in 2023, pushing the global number of connected IoT devices to an expected 16.7 billion active endpoints (IoT Analytics, 2023). This continual rise indicates an ongoing expansion of IoT device connections, with these devices increasingly found in homes, businesses, factories, and hospitals (Pashamokhtari, 2020). With the rapid proliferation of the IoT, there is an exponential generation of extensive time-series data (Hu et al., 2023). This data, characterized by repeated observations of various variables over time, is a product of IoT, significantly contributing to the vastness and velocity of big data applications (Adhikari & Agrawal, 2013). It encompasses diverse predictions such as energy consumption, temperature fluctuations, light intensity measurements, among other factors.

Mathematically, a time-series is defined as $\{x_1, x_2, x_3 \ldots x_T\}$, where $t = 1, 2, \ldots, T$ denotes time, ranging from 1 to T, and x_T signifies a vector of random variables (Cochrane, 1997). The significance of time-series data derived from IoT in scientific and technological research cannot be overstated. Analysis of this data reveals hidden patterns and laws, enabling its application in environmental contexts. This analysis further aids in uncovering correlations and periodicities between events, fostering a deeper understanding of their nature and mechanisms. The insights derived provide robust support across various disciplines engaged in related research

(Hu et al., 2023). With the vast array of data generated by IoT, accurate analysis and prediction of energy-related data have emerged as critical areas. The role of such analysis is pivotal in curbing energy wastage (Shapi et al., 2021). According to the international energy agency, global energy demand is declining by 3.8% to 6% each year in developed countries, while it is increasing in developing countries due to their escalating energy usage, ranging between 4% and 7% (Raheem et al., 2022). This imbalance in energy consumption necessitates an accurate forecast more than ever before.

Time-series prediction expects the future distribution of target variables by analyzing past observations within the time-series. This approach has been applied to various temporal inferencing problems, such as filtering, smoothing, and predicting unobserved past events or alternative histories (Russell & Norvig., 2020). The models utilized for energy consumption included time-series prediction, spanning from the past to the present, can be categorized into three distinct groups based on their abilities and advancements (Shi et al., 2022): traditional models, classical machine-learning, and deep learning models. Models such as ARIMA and SARIMA (Hipel & McLeod, 1994; Box et al., 2015) were initially employed as traditional for linear and non-linear time-series analysis, addressing stationary and non-stationary data, respectively. As machine learning algorithms progressed, researchers ventured into implementing standard algorithms like SVM (Cao, 2003) in this domain. Additionally, hybrid techniques combining ARIMA and SVM have been employed specifically for short-term time-series prediction (Nie et al., 2012). neural networks and artificial neural networks have demonstrated superior performance compared to classical machine learning and traditional techniques in energy consumption IoT-based generated data (Nor et al., 2017) (Masum & Chiverton, 2018). Among the widely used deep learning algorithms for time-series prediction are 1D-CNN (Markova, 2022), RNN (Coulibaly & Baldwin, 2005), LSTM (Sahoo et al., 2019), and GRU (Afanasieva & Platov, 2019).

The literature review on deep learning for time-series prediction (Tealab, 2018; Torres et al., 2021), indicating that all previous recurrent neural network-based algorithms have problems detecting relationships between input features of time-series data, as well as being unable to capture long sequences. A recent significant advancement in deep learning is the multi-head attention-based approach, which has shown remarkable results in Natural Language Processing (NLP), introduced (Vaswani et al., 2017), this technique has found successful applications in various domains, including computer vision and speech recognition (Carion et al., 2020), (Zeyer et al., 2019). Various variations of Transformers have been implemented based on a survey on time-series for transformers, as conducted (Wen et al., 2023). The transformer network comprises a sequence of encoder and decoder blocks, with each block featuring a residual connection employed in the time-series data. Additionally, each layer of transformers is utilized independently in various areas of time-series forecasting problems. To the best of our knowledge, there are currently no studies incorporating the dataset we utilized and analyzing it with Enc&Dec Transformer and its variants, including Encoder-only and Decoder-only Transformer models. Our dataset contains smart home energy data, and the precise predictions made by these efficient algorithms aid consumers in balancing their consumption and determining appropriate pricing strategies. Furthermore, there is a lack of a defined methodology for assessing the performance of transformer-based neural networks across varying volumes of time-series data, spanning low, medium, and high quantities, particularly concerning multi-step predictions.

Therefore, in this paper, our approach involves using vanilla transformers to predict univariate multi-step time series energy consumption data generated by IoT devices, as well as employing encoder-only and decoder-only transformer layers separately. In particular, our aim is to demonstrate the superior success of our proposed model, the Enc&Dec transformer, in analyzing IoT time series data compared to leading deep learning methods in other literature. We evaluate our models on three dataset sizes in the energy domain: small, medium, and large.

Motivated by our contributions to the literature, our study aims to achieve the following objectives:

- Implementation of the Enc & Dec Transformer in its fundamental form, specifically targeting univariate time-series prediction within the energy domain data.
- implementing the Encoder-only and Decoder-only blocks of Transformers separately for the time-series prediction problem.
- Comparison of the obtained results with prevalent deep learning-based algorithms commonly utilized in time-series prediction across datasets of varying sizes, low, medium and high data volumes.

The remaining sections of the paper are organized as follows: In Section 2, the existing studies in the literature are discussed. Section 3 gives background information about recurrent-based neural network algorithms. Section 4 presents and explains our developed model. Section 5 covers experimental analysis, including dataset, hyperparameter optimization, experimental setup, and evaluation metrics, all of which are detailed. In Section 6, the experimental results of models are discussed. Finally, in Section 7, the study is summarized, and key points are emphasized. Furthermore, the detailed acronyms and their abbreviations used throughout the entire study are listed in Table 1.

Table 1. List of Abbreviations and Acronyms

Abbreviation	Definition	Abbreviation	Definition
1D-CNN	One-Dimensional Convolutional Neural Network	MIMIC-II	Multiparameter Intelligent Monitoring in Intensive Care II
ARIMA	Autoregressive Integrated Moving Average	MLP	Multi-Layer Perceptron
ATM	Automated Teller Machine	MMC	MovieLens
C-MAPSS	Commercial Modular Aero-Propulsion System Simulation	MSE	Multi-Layer Perceptron
DUQ	Duquesne Light Company	MW	Megawatts
EKPC	East Kentucky Power Cooperative	NLP	Natural Language Processing
FD001	Flight Degradation Simulation 001,002,003,004	ReLU	Rectified Linear Unit
GPU	Graphics Processing Unit	RMSE	Root Mean Squared Error
GRU	Gated Recurrent Unit	RNN	Megawatts
IoT	Internet of Things	RT	Reuters-21578 Text Categorization Collection
KDD	Knowledge Discovery in Databases	RUL	Remaining Useful Life
LSTM	Long Short-Term Memory	SARIMA	Seasonal Autoregressive Integrated Moving Average
MAE	Mean Absolute Error	SOF	Stack Overflow
MHA	Multi-head Attention	SVM	Support Vector Machine

2. RELATED WORK

The original Transformer architecture is a multifaceted model comprising an encoder and a decoder. However, drawing inspiration from NLP, within the expansive domain since its introduction for time-series data, literature has found value in either utilizing both or just one of these components. According to Table 2, summarized related works of transformers for time-series prediction are from modifications of structure-based categorized into three parts including: Enc & Dec Transformer, Encoder-only Transformer, and Decoder-only Transformer in different applications.

An initial application of the self-attention concept in time-series forecasting is Cross-Dimensional Self-Attention, which is tailored for multivariate, geo-tagged time-series imputation (Ma et al., 2019). The proposed novel approach aims to jointly capture self-attention across multiple dimensions, such as time, location, and sensor measurements, while keeping computational complexity low. It processes each dimension sequentially, yet in a manner that is independent of order, as presented in the study. Extensive experiments conducted on four real-world datasets show that this method surpasses state-of-the-art imputation and forecasting techniques in performance. In another extensive investigation, an encoder-decoder Transformer architecture is employed for time-series forecasting, with a focus on influenza-like illness prediction (Wu et al., 2020). The study introduces a vanilla Transformer architecture for both univariate and multivariate time-series predictions. The findings demonstrate that the forecasting outcomes achieved by their method are notably comparable to the current state-of-the-art approaches. Subsequently, an upgraded iteration of the Transformer was introduced (Li et al., 2019), incorporating causal convolution within the self-attention module to enhance the model's responsiveness to local context. Additionally, adjustments were made to mitigate the memory overhead of Transformers, rendering them more adept at handling lengthy time series. A pioneering Temporal Fusion

Transformer emerged (Lim et al., 2020), combining recurrent and attention layers to discern temporal dependencies across various scales within numerous real-world datasets. At this time, the transformer-based neural networks predominantly featured an encoder-decoder architecture.

***Table 2**. Summary of Related Works of Transformers for Time-Series Prediction*

Model	Reference Title	Year	Dataset	Data Type
Enc&Dec Transformer	CDSA: Cross-Dimensional Self-Attention for Multivariate, Geo-tagged Time Series Imputation	2019	Traffic, KDD cup 2015&2018	Multivariate
	Deep Transformer Models for Time Series Forecasting: The Influenza Prevalence Case	2020	ILI reports from Centers for Disease Control and Prevention	Univariate & Multivariate
	Enhancing the Locality and Breaking the Memory Bottleneck of Transformer on Time Series Forecasting	2020	Real-worlds (Traffic and Electricity) and Synthetic dataset	Univariate & Multivariate
	Temporal Fusion Transformers for Interpretable Multi-horizon Time Series Forecasting	2020	Real-world datasets (Traffic, Electricity, Volatility, and Favorita)	Multivariate
Encoder-only Transformer	Self-Attentive Hawkes Process	2020	Real-world datasets (RT, SOF, and MMC) and Synthetic dataset	Multivariate
	Transformer Hawkes Process	2021	Retweets, MemeTrack, Finanial, MIMIC-II, SOF, 911-Calls, Earthquake datasets	Univariate & Multivariate
	Remaining useful life estimation via transformer encoder enhanced by a gated convolutional unit	2021	C-MAPSS datasets (FD001, FD002, FD003, and FD004)	Multivariate
	A Transformer-based Framework for Multi-variate Time Series: A Remaining Useful Life Prediction Use Case	2023	C-MAPSS datasets (FD001, FD002, FD003, and FD004)	Multivariate
Decoder-only Transformer	Evaluation of the Transformer Architecture for Univariate Time Series Forecasting	2021	Traffic, Tourism, Financial (Exchange rate, Daily ATM's cash, and artificially generated) M4, M3, and Solar Energy datasets	Univariate
	Persistence Initialization: a novel adaptation of the Transformer architecture for time series forecasting	2022	M4 dataset	Univariate & Multivariate
	A Decoder-Only Foundation Model for Time-Series Forecasting	2024	Google Trends, Wiki Pageviews, M4	Univariate & Multivariate

Despite outperforming recurrent-based and convolutional-based neural networks on time-series data, they have problems including the requirement for high computational resources, time-consuming inference, and complex architectures that are challenging to employ in real-world scenarios. Therefore, to overcome these issues more effectively, some studies utilize the Encoder layer (Encoder-only Transformer), as well as the Decoder layer (Decoder-only Transformer), to sought solutions to various time-series prediction problems.

Self-Attentive Hawkes Processes and Transformer Hawkes Process models are proposed as Encoder-only Transformers for event forecasting problem (Zhang et al., 2019; and Zuo et al., 2020). Both methods utilize a Transformer encoder architecture to capture the impact of past events and calculate the intensity function for event prediction, representing a modification at the architecture level to an Encoder-only structure. They adjust

the positional encoding by converting time intervals into sinusoidal functions, enabling the utilization of event intervals. A hybrid approach has been proposed for the prediction of Remaining Useful Life (RUL), employing a transformer encoder architecture combined with a gated convolutional unit. This approach utilizes the gated convolution to extract local features and employs the encoder transformer to capture global features (Mo et al., 2021). Furthermore, in the domain of RUL prediction, a recent comprehensive method has been introduced. This method is based on an encoder-transformer architecture for multivariate time series prediction (Ogunfowora & Najjaran, 2023). The study employs a basic transformer encoder block, which comprises four main sub-modules: multi-head attention, positional encoding, layer normalization, skip connections, and feed-forward neural network layers.

A Decoder-only Transformer structure-based method, geared towards univariate time-series forecasting, is introduced (Lara-Benítez et al., 2021). In this investigation, the conventional Transformer Decoder blocks were adhered to, wherein each decoder block comprises a masked self-attention module followed by multi-head attention and a feed-forward block. Additionally, all sub-modules incorporate a residual connection, followed by dropout and batch normalization layers, to enhance the network's generalization capacity. Similarly, the Persistence Initialization framework is outlined, consisting of four components: normalization, linear projections, a decoder-only Transformer incorporating Rotary positional encodings and ReZero normalization, and Persistence Initialization (Haugsdal et al., 2023). Finally, in a recent work, a decoder-only pretrained attention-based model for time-series forecasting is proposed (Das et al., 2024). It serves as a foundation for decoder-only pretrained applications for time-series forecasting, consisting of an input layer, stacked transformer decoder blocks, and an output layer.

3. BACKGROUND INFORMATION

3.1. Recurrent neural network (RNN)

RNN is particularly well-suited for sequential data and is commonly employed in time-series analysis (Javaid, 2019). RNN's employ recurrent neural architectures to grasp the functional relationships between input characteristics from the immediate past and a future target variable (Coulibaly & Baldwin, 2005). The computational procedure defining each hidden state (hidden unit or hidden cell) can be mathematically define, as demonstrated in Equation (1) within our framework.

$$S_t = \tanh(W_{xs} \cdot (x_t \oplus S_{t-1}) + b_s) \ \& \ y_t = \sigma(W_y \cdot S_t + b_y) \tag{1}$$

where $x_t \in R^m$ represents input vector comprising m input features at time t; $W_{xs} \in R^{n \times (m+n)}$ and $W_y \in R^{n \times m}$ are parameter matrices; n denotes number of neurons in the RNN; $b_s \in R^n$ and $b_y \in R^n$ are bias vectors for internal state and output, respectively; σ denotes the sigmoid activation; S_t represents the internal (hidden) state; and $x_t \oplus S_t$ shows concatenation of vectors x_t and S_{t-1}.

One of the significant drawbacks of RNNs is their susceptibility to the gradient vanishing problem, stemming from repeated multiplication of the recurrent weight matrix. This issue leads to diminishing gradients over time, causing the RNN to retain information effectively only for shorter durations (Sahoo et al., 2019).

3.2. Long short-term model (LSTM)

LSTM network is a variation of RNN, offer partial mitigation of the vanishing gradient problem (Sahoo et al., 2019). and excel in capturing longer-term dependencies within time-series data. LSTMs utilize gates—forget gate, input gate, addition gate, and output gate—to manage the removal, multiplication, addition, and filtering of information. The computational procedures implementing these functions, in our context $f_t, i_t, \hat{C}_t$ and O_t, respectively are described in Eq. (2).

$$
\begin{aligned}
f_t &= \sigma\big(W_f \cdot (x_t \otimes S_{t-1}) + b_f\big); \\
i_t &= \sigma(W_i \cdot (x_t \otimes S_{t-1}) + b_i) \\
\hat{C}_t &= tanh(W_c \cdot (x_t \otimes S_{t-1}) + b_c); \\
C_t &= f_t \cdot C_{t-1} \cdot i_t \cdot \hat{C}_t; \\
O_t &= \sigma(W_o \cdot (x_t \otimes S_{t-1}) + b_o); \\
S_t &= tanh(C_t) \cdot O_t \ \& \ y_t = \sigma(W_y \cdot S_t + b_y)
\end{aligned}
\tag{2}
$$

where $x_t \in R^m$ represents input vector comprising m input features at time t; $W_f, W_i, W_c, W_o \in R^{n \times (m+n)}$ and $W_y \in R^{n \times m}$ are parameter matrices; n denotes number of neurons in LSTM layer; $b_f, b_i, b_c, b_o \in R^n$ are bias vectors; σ denotes the sigmoid activation; and S_t represents the internal (hidden) state. The functions $f_t, i_t, \hat{C}_t$ and O_t correspond to the forget gate, input gate, addition gate, and output gate, respectively.

3.3. Gated recurrent unit (GRU)

GRU represent a variation of LSTM network aimed at further mitigating the vanishing gradient problem (Afanasieva & Platov, 2019). In the computational process described by Eq. (3), the distinctive aspect of this approach lies in utilization of gets including: update, reset, and a third get, which implement the functions z_t, r_t and $\check{S}_t$, respectively. Each gate serves a distinct role in regulating how prior information is filtered, utilized, and amalgamated. The initial element in the formula for the next state, expressed as $(1 - z_t) \cdot S_{t-1}$, determines the information retained from the past, while $z_t \cdot \check{S}_t$ decides the content to be included from the current memory.

$$
\begin{aligned}
r_t &= \sigma(W_r \cdot (x_t \otimes S_{t-1}) + b_r) \\
z_t &= \sigma(W_z \cdot (x_t \otimes S_{t-1}) + b_z) \\
\check{S}_t &= tanh(W_s \cdot (x_t \otimes S_{t-1} \cdot r_t) + b_s) \\
S_{t-1} = (1 - z_t) \cdot S_{t-1} + z_t \cdot \check{S}_t &\quad \& \quad y_t = \sigma(W_y \cdot S_t + b_y)
\end{aligned}
\tag{3}
$$

where $x_t \in R^m$ represents the input vector with m input features at time t; $W_r, W_z, W_s, \in R^{n \times (m+n)}$ and $W_y \in R^{n \times m}$ are parameter matrices; n denotes the number of neurons in the GRU layer; $b_r, b_z, b_s \in R^n$ are bias vectors; σ represents the sigmoid activation function; and S_t signifies the internal (hidden) state. The functions z_t, r_t, and $\check{S}_t$ correspond gets to the update, reset, and third gate, respectively.

3.4. One-dimensional convolution neural network (1D-CNN)

A CNN falls within the class of deep neural networks capable of automatically extracting features and generating informative representations from time-series data, eliminating the need for manual feature engineering (Markova, 2022). It serves as a modification of the 2D-CNN architecture. The 1D-CNN architecture introduces two distinct layer types:

1. 'CNN-layers' where 1D convolutions, activation functions, and sub-sampling (pooling) operations occur.
2. Fully-connected (dense) layers, akin to those found in a standard Multi-Layer Perceptron (MLP), hence referred to as 'MLP-layers.'

In our case, the computational process of a 1D-CNN can be represented as demonstrated in Eq. (4).

$$
\begin{aligned}
Z &= Conv1D(X, Y) + b \\
Z_i &= \sum_{j=0}^{F-1} (x_{i+j} \cdot w_j) + b \\
A_i &= activation(Z_i) \\
MaxPooling(A_i, i) &= max \, x_0 \leq w \, A_i, i + j \times s
\end{aligned}
\tag{4}
$$

The input sequence, denoted as X is defined with dimensions $N \times C \times L$ where N is the batch size, C is represent the number of channels (features) and L is the number of sequence; In 1D convolution, a filter slides over the input sequence, performing convolution at each position i, yielding the output Z_i is the value of the output at position i, x_{i+j} represents the input values at positions $i + j$ (for j from 0 to $F - 1$), W_j represents the weights of the filter at position j, b_i represents the bias term for the output at position i; Following it is applied an activation function element-wise to the output of the convolution operation. *Max Pooling* operation with a window size W and stride S in a 1D setting is represented in above x_i, i represents the input value at position i in channel c.

4. DEVELOPED MODEL: ENC&DEC TRANSFORMER

The Env&Dec Transformer follows the recent competitive advancement in deep learning introduced by google researchers (Vaswani et al., 2017), aligns with the majority of cutting-edge neural sequence models, featuring

an encoder-decoder architecture. Illustrated in Figure 1, both the encoder and decoder comprise numerous identical blocks. In detail, each encoder block includes a multi-head self-attention module and a position-wise feed-forward network, whereas each decoder block integrates cross-attention mechanisms between the multi-head self-attention module and the position-wise feed-forward network. Within the input, w denotes the dimension of the look-back window, while k represents the count of future prediction steps. The decoder segment employs a masked attention module, and within the decoder, a cross attention mechanism is employed to choose output of encoder layer, which serve as the feature vector.

In Enc&Dec, attention is a mechanism that assigns weights to each word in a sentence based on its importance. In this context, we have a feature vector that includes query, key, and value, which conceptually are used to perform this operation. The query represents the sought-after information, while the key signifies the context or reference, and the value denotes the content under scrutiny. Multiplying the query and key yields attention scores, which are subsequently utilized to compute the weighted sum of the values (Haugsdal et al., 2023). This weighted sum, in turn, is employed to compute the model's output.

The model's recursive definition can be established by denoting X_i as the output of the i-th block, as depicted in Eq. (5-7).

$$X_i(X_i - 1) = FF_i(SA_i(X_i - 1))$$
$$SA_i(X) = LayerNorm(X + SelfAttention_i(X))$$
$$FF_i(X) = LayerNorm(X + FeedForward_i(X))$$

(5)

The matrix X_i has dimensions $L \times d_{model}$, where L represents the sequence or time dimension and d_{model} represents the feature dimension. X_0 acts as the base case of the recursion, representing the initial input to the model. The hyperparameter N, determines the number of blocks, and subsequently the final output of the model denoted as, X_n. Before delving into self-attention, it's crucial to establish multi-head attention.
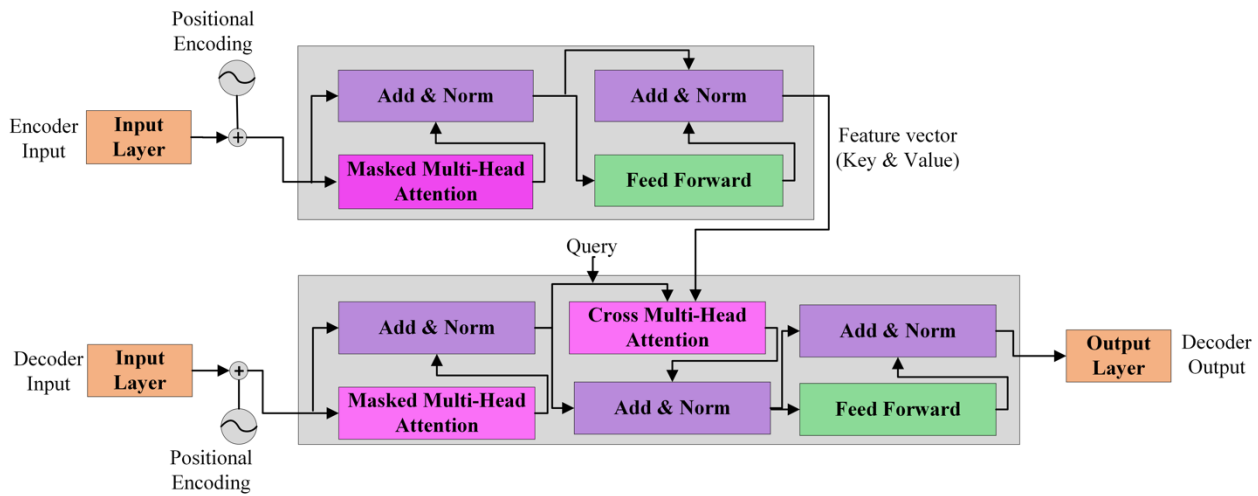
Figure 1. Structure of Enc & Dec Transformer-based prediction model

Multi-head attention aggregates multiple attention heads, each equipped with its unique set of learnable weights, enabling them to perform simultaneous computations.

Self-attention arises as a particular case of multi-head attention, wherein the keys, queries, and values are identical.

$$SelfAttention(X) = MHA(X, X, X)$$

$$MHA(Q, K, V) = Concat(head_1, \dots, head_h)W_o$$

$$head_j = Attention(QW_Q^{(j)}, KW_K^{(j)}, VW_V^{(j)})$$

(6)

$$Attention(Q, K, V) = softmax\left(\frac{QK^T}{\sqrt{d_{model}}} + M\right)V$$

where, h represents the number of attention heads, and d_{heads} is calculated as d_{model} divided by the number of heads ($d_{head} = \frac{d_{model}}{h}$). The learnable weight matrices $W_Q^{(j)}, W_K^{(j)}$ and $W_V^{(j)}$ have a shape of $d_{model} \times d_{head}$, while W_O is a learnable weight matrix with a shape of $d_{model} \times d_{model}$. W_O is responsible for combining the outputs from each attention head. M denotes an upper triangular masking matrix that prevents the model from attending to future time steps.

The feed-forward layer functions in a point-wise manner, concentrating exclusively on information from the present time step, akin to a 1-D convolution. It consists of two linear transformations interspersed with a ReLU activation function, representing non-linearity.

$$FeedForward(X) = ReLU(XW_1 + b_1)W_2 + b_2 \tag{7}$$

where W_1 and W_2 denote learnable weight matrices with dimensions $d_{model} \times d_{ff}$ and $d_{ff} \times d_{model}$ respectively. Similarly, b_1 and b_2 represent learnable bias vectors with dimensions d_{ff} and d_{model}.

In Figure 1, we can observe the composition of an encoder and decoder block. During training, the decoder receives a feature vector (key and $value$) from the encoder output and utilizes it to predict the future point. The $query$ is involved in the calculation of the masked attention.

Unlike other recurrent neural network that process sequence tokens sequentially, self-attention favors parallel computation over sequential operations. It is important to note that self-attention itself doesn't maintain sequence order. To retain token order information, the prevalent approach involves providing the model with additional inputs known as positional encodings. These encodings, associated with each token, can be either learned or pre-defined. In this study, we utilized a straightforward approach: fixed positional encodings utilizing sine and cosine functions (Vaswani et al., 2017), as per Eq. (8).

$$PE_{(pos,2i)} = \sin(\frac{pos}{1000^{\frac{2i}{d_{model}}}})$$
$$PE_{(pos,2i+1)} = \cos(\frac{pos}{1000^{\frac{2i}{d_{model}}}}) \tag{8}$$

4.1. Encoder-only transformer

The encoder-only is the encoder block of the Enc&Dec Transformer. According to Figure 1, it has a multi-head module without masking operation, a residual connection with normalization, and a feed-forward layer. To serve the prediction purpose by the encoder layer, we feed the output of the encoder layer to an output layer. The mathematical computations and positional encoding are the same as Eq. (5-8), respectively.

4.2. Decoder-only transformer

The decoder-only block is a component of the Enc&Dec Transformer, distinct from the decoder in the standard transformer. In contrast to the transformer decoder, which obtains the key and value from the encoder block, the decoder-only block generates a feature vector through its masked multi-head attention layer. Illustrated in Figure 1, the decoder comprises two primary elements: initially, windowed data is fed into the model's input layer, followed by the application of fixed positional embedding. Next, the raw positional encoded matrix is fed into masked multi-head attention mechanisms. After applying self-attention (according to Eq. (6)) on each split matrix, the data is further separated into three matrices: Query, Key, and Value. Layer normalization is then implemented, followed by feeding the output of the initial masked multi-head attention, which comprises the three matrices, into the subsequent non-masked multi-head attention. The mathematical calculations and positional encoding remain consistent with Eq. (5-8), respectively.

5. EXPERIMENTAL EVALUATION

5.1. Dataset

PJM Interconnection LLC (PJM) functions as a regional transmission organization within the United States, operating as a component of the Eastern Interconnection grid and managing an electric transmission system

that serves multiple cities across the country. It produces their power sensor devices generated hourly energy consumption data as benchmark datasets (Mulla, 2019). We downloaded three univariate publicly available datasets from PJM's website, including PJM, DUQ, and EKPC, with large, medium and small size. Their sizes are 145,392; 119,088; and 45,336 observations respectively, and they are collected hourly in megawatts (MW).

5.2. Hyperparameter optimization

Hyperparameter tuning stands as one of the most arduous tasks within machine learning projects. As the complexity of deep learning methods continues to surge in popularity, the demand for an efficient automatic hyperparameter tuning framework has escalated significantly (Akiba et al., 2019). Numerous techniques exist to optimize hyperparameters in deep learning. While previous literature emphasizes grid search and random search as primary methods for machine learning models, recently Optuna has become very popular hyperparameter tuning technique in machine learning problems. Grid search, though widely used, can become time-consuming and computationally expensive, particularly with a large number of hyperparameters or potential values. Optuna distinguishes itself as a more advanced approach, leveraging Bayesian optimization to efficiently explore and pinpoint the best set of hyperparameters (Shekhar et al., 2021).

In this study, we employed the Optuna to identify optimal parameters suitable for our dataset and model complexity. Specifically, we configured Optuna to conduct 100 trials with 20 internal epochs. Parameters were set within defined ranges: the number of layers varied from 1 to 10, hidden layers spanned from 16 to 2048, drop probabilities ranged between 0 and 1, and learning rates fell within the range of 0 to 1, consistent across all five models. However, certain models necessitated additional hyperparameters; for instance, in the case of the 1D-CNN, we specified the $kernel\ size$ between $3 - 7$ and $padding$ as $(kernel\_size - 1) // 2$. Similarly, for the transformers, the required number of $heads$ set from 1 to 8, and the number of dimensions from 32 to 1024. Additionally, we manually set the activation function as linear, the number of $epochs$, $batch\ size$ and $optimizer$ in Table 3.

As seen in Table 3, we summarized the optimal result for transformer-based networks, including Enc&Dec, Encoder-only, as well as Decoder-only architectures, due to their similarity in data flow within modules and the mechanism of assigning weight and bias values, we utilize the same parameters for training for our proposed models. The algorithm recommended the best range of values for each parameter based on the outcomes from Optuna trials.

Table 3. Hyperparameter settings through Optuna

Model	Hyperparameters								
	# of layers	# of hidden layers	Drop rate	Learning rate	Activation function	Kernel size	Padding	# of heads	# of dimension
RNN	6	1710	0.0055353	0.0001863781	tanh				
LSTM	3	2048	0.2075485	0.0002399395	tanh				
GRU	8	74	0.0206139	8.00205811e-05	tanh				
1D-CNN		1995	0.1614444	1.64786113e-05	ReLU	5	2		
Transformers	1	1998	0.0009843	1.04834920e-05				6	501
Optimizer	Adam		Batch size			32			

5.3. Experimental setup

Deep learning models utilize past data to identify a functional connection between input characteristics and the forthcoming values of the target variable. These trained models offer forecasts for the target variable in subsequent time periods. In a time-series $\{x_1, x_2, x_3 \dots x_T\}$, where x_t denotes a set of m input features recorded at time t, the aim is to construct a model that predicts a target variable y_{t+k} at a future time point t + k, utilizing insights derived from historical data up to time $t - 1$ ($\{\dots, x_{t-2}, x_{t-1}\}$). To ensure consistency in the model's input, we adopted a fixed-length sliding time window of magnitude w, as depicted in Figure 2. In our case, the

look-back size w is set to 168 hours, equivalent to one week in hourly collected data, while the look-ahead size k is set to 48 hours to forecast two days ahead based on the given w size.

The mathematical representation of the functional relationship learned by machine learning models can be illustrated through Eq. (9), as shown.

$$\hat{y}_{t+k} = f_k(x_{t-w}, \dots, x_{t-1}, y_{t-w}, \dots, y_{t-1}) \tag{9}$$
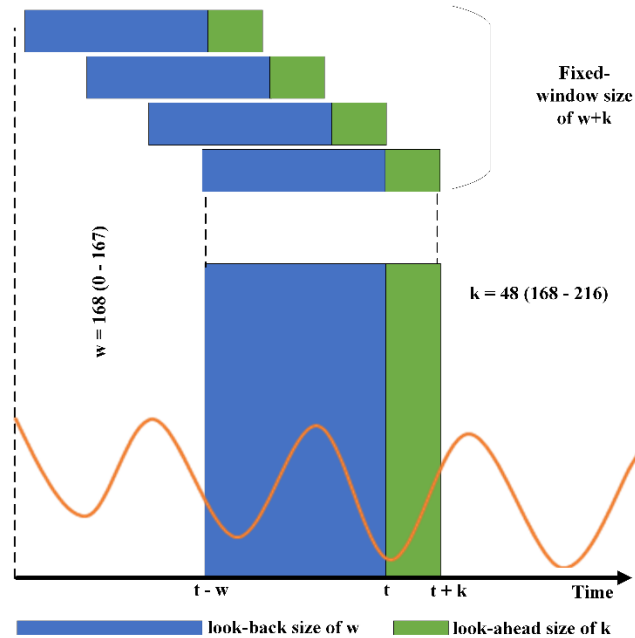
Figure 2. Sliding window forecasting next 48 observation based on 168 data points

where $\hat{y}_{t+k}$ represents the forecasted target variable for time $t + k$; k represents the future time duration for which the target variable is predicted; $y_{t-w}, \dots, y_{t-1}$ represent the observed target values spanning from time $t - w$ to $t - 1$; $x_{t-w}, \dots, x_{t-1}$ represent the vector of m observed input features observed from time $t - w$ to $t - 1$. The function f_k denotes the learned function by deep learning models with a step size of 1. In our context, m denotes the number of input features, defaulted to 1 as it is univariate, and w indicates the size of the window utilized as input. As well as we utilized the StandardScaler to transform our data, normalize it within the range of 0 to 1, as illustrated in Eq. (10).

$$z = \frac{x - \mu}{\sigma} \tag{10}$$

Leveraging the GPU for accelerated computing with high-dimensional matrices, we implemented our data and models using PyTorch. For coding, we utilized Python 3.12, ensuring compatibility with various essential libraries such as NumPy, PyTorch, Matplotlib, among others. To maintain a robust evaluation process, we partitioned our dataset into three segments. We trained all our models on the initial 80% of the dataset, validated their performance on the subsequent 10%, and finally tested each model on the last 10%—ensuring that the test data remained unseen during training and validation. To optimize computational efficiency, we organized data input to the models in batches according to specifications outlined in Table 3 hyperparameter setting. Moreover, in order to prevent overfitting and underfitting, we implemented regularization techniques. Specifically, we set the patience parameter to 3 and applied early stopping if the validation metric did not improve for 20 or more epochs.

5.4. Evaluation metrics

To evaluate the performance of proposed models, we utilized the MAE (Mean Absolute Error), MSE (Mean Squared Error), and RMSE (Root Mean Squared Error) metrics according to Eq. (11-13), respectively.

$$MAE = \frac{1}{n}\sum_{i=1}^{n}|y_i - \tilde{y}_i| \tag{11}$$

$$MSE = \frac{1}{n}\sum_{i=1}^{n}(y_i - \tilde{y}_i)^2 \tag{12}$$

$$RMSE = \sqrt{\frac{\sum_{i=1}^{n}(y_i - \tilde{y}_i)^2}{N-P}} \tag{13}$$

where, y_i indicate individual observed values in the dataset, $\tilde{y}_i$ predicted values corresponding to y_i and μ the mean of the observed values.

6. EXPERIMENTAL RESULTS AND DISCUSSION

The training and testing losses were calculated based on the epochs to identify potential overfitting, we utilize the MSE as our chosen loss function computation for both training and testing. In Table 4, a summary of our model results is presented and organized based on high, medium and low volume datasets. Notably, the MSE values are observed to be lower than both MAE and RMSE, influencing our decision-making process.

This table highlights that RNN consistently demonstrates a high MSE score across all evaluated univariate datasets. LSTM, a variant of RNN tailored to tackle the vanishing gradient problem, exhibits a lower MSE score compared to RNN. Moreover, the GRU, addressing issues inherent in both RNN and LSTM, achieves the best results with a minimum MSE of 0.24 when compared with the MSE of 0.36 for RNN and 0.30 for LSTM. While 1D-CNN, leveraging automatic feature extraction, has a minimum MSE of 0.15 in univariate time-series prediction, it outperforms recurrent-based models, including RNN, LSTM, and GRU, as well as Transformer-based models, including Encoder-only and Decoder-only models.

Table 4. *The performance metrics for experimented models across three different sizes of datasets*

Dataset	Data size	Model	Evaluation Metrics		
			MAE	MSE	RMSE
PJME_hourly	Large	RNN	0.49	0.40	0.63
		LSTM	0.43	0.31	0.56
		GRU	0.36	0.24	0.47
		1D-CNN	0.27	0.14	0.38
		Encoder-only Transformer	0.40	0.27	0.52
		Decoder-only Transformer	0.33	0.19	0.44
		Enc&Dec Transformer	0.06	0.006	0.08
DUQ_hourly	Medium	RNN	0.46	0.36	0.60
		LSTM	0.41	0.30	0.55
		GRU	0.38	0.24	0.49
		1D-CNN	0.28	0.15	0.39
		Encoder-only Transformer	0.38	0.26	0.51
		Decoder-only Transformer	0.31	0.19	0.43
		Enc&Dec Transformer	0.07	0.008	0.09
EKPC_hourly	Small	RNN	0.55	0.61	0.78
		LSTM	0.52	0.54	0.73
		GRU	0.53	0.56	0.75
		1D-CNN	0.40	0.34	0.58
		Encoder-only Transformer	0.54	0.58	0.76
		Decoder-only Transformer	0.47	0.45	0.67
		Enc&Dec Transformer	0.11	0.020	0.14

Utilizing the Encoder-only and Decoder-only models with minimum MSE of 0.26 and 0.19 respectively in energy prediction outperforms RNN, LSTM, and GRU. However, when comparing these results with those in Table 4, the performance falls short compared to 1D-CNN and Enc & Dec Transformer models, which is not satisfactory. Decoder-only outperforms Encoder-only due to its ability to perform masking operations for handling data and employing more attention layers. In another aspect, the Enc & Dec Transformer model, composed of both encoder and decoder, outperforms all models evaluated in this study for univariate time-

series by achieving a minimum MSE of 0.006 for small, 0.008 for medium, and 0.020 for large datasets in predicting energy consumption.

Figure 3 illustrates the performance of RNN, LSTM, GRU, 1D-CNN, Encoder-only, Decoder-only, and Enc & Dec Transformer across three large, medium and small size datasets. The results indicate a clear trend: as our dataset size increases, the corresponding loss decreases. The size difference between the DUQ and PJME datasets is not substantial. However, the variance between the EKPC (small) and PJME (large) dataset is extremely high. This leads to more noticeable fluctuations in results across all models. This observation underscores the conventional wisdom that larger datasets often lead to enhanced model generalization. Across all dataset sizes, the Enc & Dec Transformer consistently demonstrates superior performance, yielding minimal loss values. This trend suggests its remarkable capability to capture long-range dependencies and complex patterns within the data. Consequently, Enc & Dec Transformers exhibit superior performance compared to recurrent and convolutional architectures, especially when dealing with increased data size. Among the recurrent models (RNNs, LSTMs, and GRUs), there's comparable performance observed, even though with slight variations depending on the dataset. This consistency indicates their stable capacity to model sequential relationships. However, 1D-CNNs exhibit a noticeable performance increase with low MAE, MSE and RMSE scores, particularly on the smallest dataset (EKPC hourly). This suggests that these models might require a larger dataset to effectively learn and harness meaningful convolutional filters. In essence, 1D-CNNs might face challenges and show diminished performance with smaller datasets, similar to other deep learning algorithms. The performance of Encoder-only remains the same in both large and medium-size datasets, but the loss is going high in the small dataset. However, the Decoder-only outperforms in the medium-size dataset. Overall, our results suggest that for training such deep learning algorithms, we must have enough data to reach the best result.
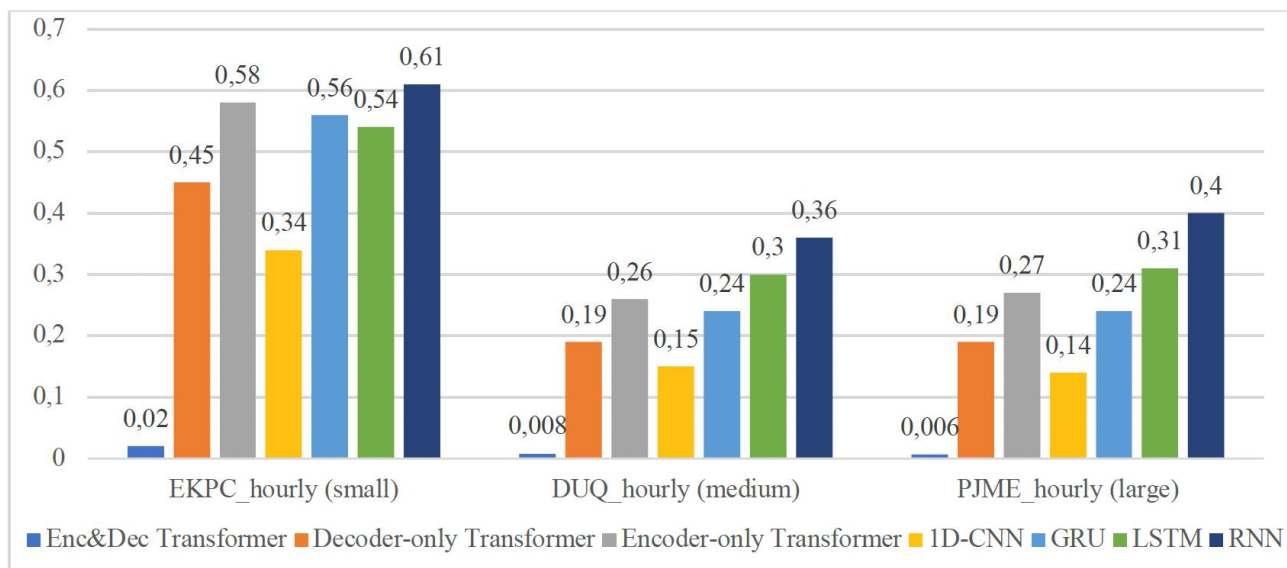
Figure 3. *Model performance in terms of MSE scores with varying sizes of datasets*

The existing literature studies we summarized in Table 2 categorized the employed Enc&Dec Transformer models in energy consumption and other domains (Mat et al. 2019, Wu et al. 2020, Li et al. 2019, Lim et al. 2020). In the studies, researchers also compared their findings with those of state-of-the-art machine learning and deep learning models. For instance, the findings of Li et al. (2019) showed that the proposed Enc&Dec Transformer models outperformed ARIMA, ETS, TRMF, DeepAR, DeepState, and even LSTM. The efficiency of the proposed Enc&Dec Transformer models by Lim et al. (2020) was demonstrated by comparing their proposed methods with state-of-the-art DL methods as well as hybrid techniques, including ConvTrans and Seq2Seq, and finding them to be superior. Since the dataset in this study differs from the studies, we could not directly compare our results with those in the literature. Nevertheless, our study, consistent with these studies, demonstrates that our Enc&Dec Transformer outperforms DL methods in predicting energy consumption. Furthermore, we distinguish our study by comparing the results of the Enc&Dec Transformer with those of Encoder-only and Decoder-only Transformer models.
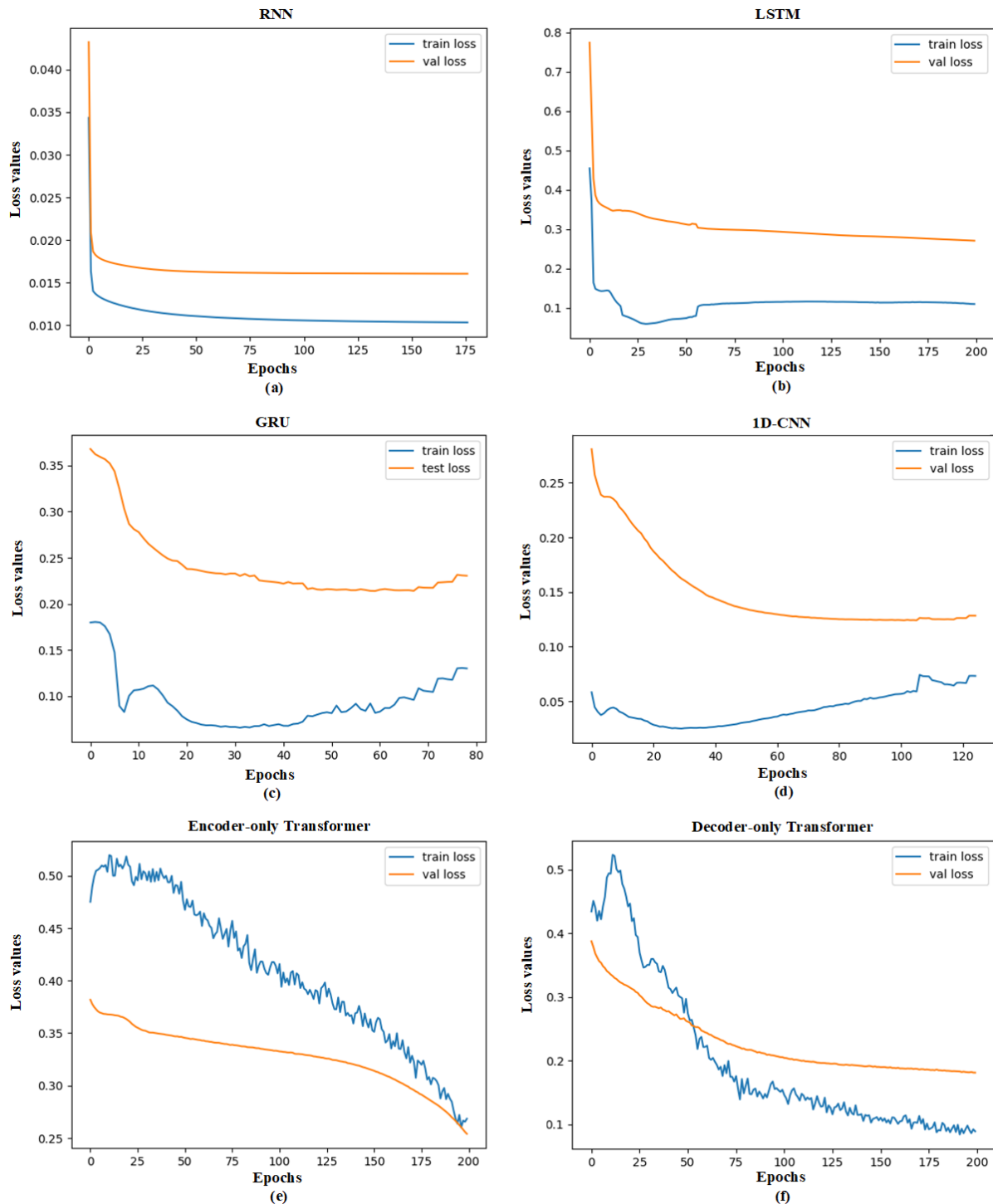
Figure 4. *Training and validation losses for* **(a)** *RNN,* **(b)** *LSTM,* **(c)** *GRU,* **(d)** *1D-CNN,* **(e)** *Encoder-only Transformer, and* **(f)** *Decoder-only Transformer models using the medium (DUQ) dataset in terms of MSE score*

In Figure 4, the graphs depict the train losses vs. validation losses of RNN, LSTM, GRU, 1D-CNN, Encoder-only, and Decoder-only, respectively evaluated only for medium (DUQ_hourly) dataset. The figures show the models' generalizing performance, indicating overfitting, underfitting, and the fitting capability of each model. Figures 4 (a), (b) and (c) depict the train vs. validation losses of RNN, LSTM and GRU networks. The training loss remains high throughout the training process, never dipping below the validation loss. This suggests that the model is not effectively learning from the training data. Additionally, the gap between the training and validation loss remains significant throughout the training process, indicating that the model is not generalizing well to unseen data. Neither the training nor the validation loss shows a significant decrease over time,

suggesting that the model is not making progress during training. These are all indicators of underfitting, implying that the models are not complex enough to capture the underlying patterns in the data. As a result, the model is unable to make accurate predictions on new data. In Figure 4(d) graph displays the 1D-CNN training vs. validation loss. This graph shows that the training loss starts off much higher than the validation loss, but then steadily decreases and crosses over the validation loss around epoch 60. This is a positive sign, suggesting that the model is learning from the training data and generalizing well to unseen data. However, after the crossover, the training loss continues to decrease while the validation loss starts to increase slightly. In Figures 4(e) and Figure 4(f) illustrate the training losses and validation losses of Decoder-only and Encoder-only, attention-based neural networks. The graphs show that the training loss is initially higher than the validation loss, but it quickly decreases and crosses over the validation loss around epoch 50. This is a positive sign, suggesting that the model is learning from the training data and generalizing well to unseen data. The validation loss also starts to decrease after epoch 50, but it remains slightly higher than the training loss throughout the rest of the training process. This could be an indication of underfitting. The Encoder-only graph displays the training loss and validation loss over the course of training epochs. The validation loss decreases initially, indicating that the model is generalizing well to unseen data. There is no indication of overfitting in this graph, as the validation loss never increases after decreasing, and the gap between the training and validation loss remains relatively constant throughout the training process. This could be an indication of overfitting.

Figure 5. *Training and validation losses of Enc&Dec Transformer model in terms on MSE score using **(a)** small (EKPC), **(b)** medium (DUQ) and **(c)** large (PJME) datasets*

Figure 5 shows the training and validation loss curves for a time series prediction model trained with an Enc&Dec Transformer on small, medium, and large datasets. In Figure 5(a), for the small dataset, the training loss is considerably higher before epoch 50. However, after epoch 60, the validation loss decreases while the training loss increases; overall, the difference is not very significant. In Figure 5(b), for the medium dataset,

the training loss curve consistently remains lower than the validation loss curve, indicating a positive sign. This suggests that the model effectively learns the training data without overfitting. The validation loss curve initially decreases rapidly but then plateaus around epoch 25. Figure 5(c) demonstrates the performance of the Enc&Dec Transformer model on a large dataset. Initially, the validation loss is lower than the training loss, but this trend is not consistent throughout. Again, after epoch 100, the validation loss starts to decrease, indicating that the model is beginning to generalize well to unseen data.
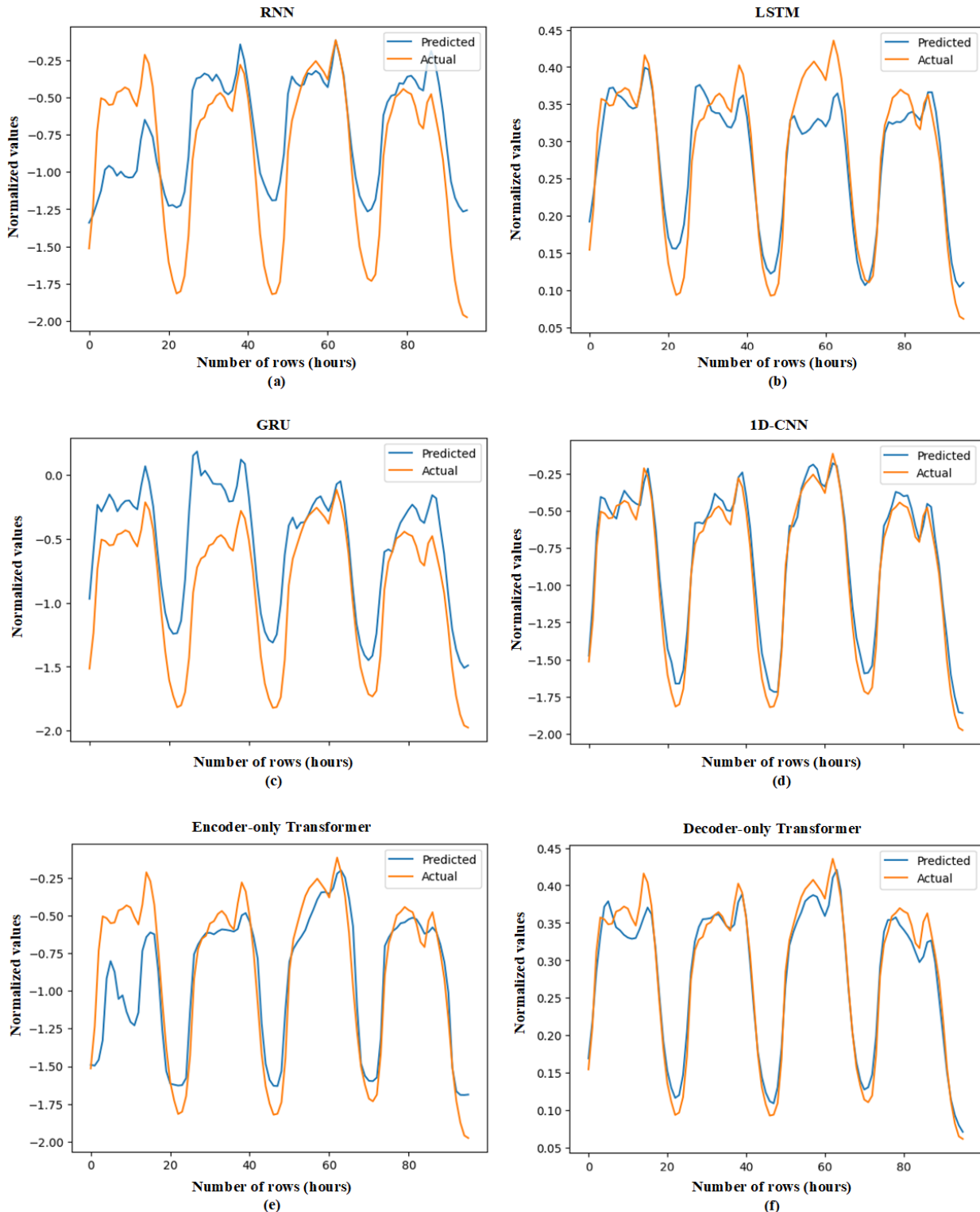
Figure 6. *Predicted and actual values of for (**a**) RNN, (**b**) LSTM, (**c**) GRU, (**d**) 1D-CNN, (**e**) Encoder-only Transformer, and (**f**) Decoder-only Transformer models using medium (DUQ) dataset in terms of MSE score*

Figure 6 illustrates the ground truth data for RNN, LSTM, GRU, 1D-CNN, Encoder-only, and Decoder-only models, plotting the deviation between predicted and actual values, specifically for the medium dataset (DUQ_hourly), with the aim of comprehensively assessing model performance. Across all graphs, the blue line corresponds to predicted values, whereas the orange line represents actual values. For prediction, a fixed-length window size is employed. As demonstrated in Figure 2, a fixed look-back window size of 168 hours is utilized to forecast a look-ahead size of 48 hours during training. To validate our models, we conducted testing on the last 10% of unseen data, predicting the subsequent four days ahead. This testing involved targeting and comparing 96 hours of data for predictions and the evaluation of the model. Each graph is plotted based on the MSE loss scores, and the comparison is specifically conducted on the medium dataset. The result of Figure 6(a) confirms that the RNN model exhibits a significant difference between predicted and actual values, primarily due to the vanishing gradient problem, impacting its ability to memorize previous data effectively. Comparatively, LSTM and GRU in Figures 6(b) and Figure 6(c), respectively, demonstrate better predictive capabilities than RNN. Particularly in our proposed domain data, GRU outperforms both LSTM and RNN. Additionally, both the 1D-CNN and Decoder-only in Figures 6(d) and Figure 6(f) surpass the performance of recurrent-based models. They predict values very close to the actual ones, but there are instances, particularly between 58 and 60, where the maximum wavelength incurs higher losses. Beyond point 60, the predicted values align more closely with the actual ones. However, in the case of 1D-CNN, the minimum point of the wavelength exhibits better performance. In Figure 6(e), where the Encoder-only is plotted, the model seems to be learning well and generalizing decently, but there might be room for improvement.
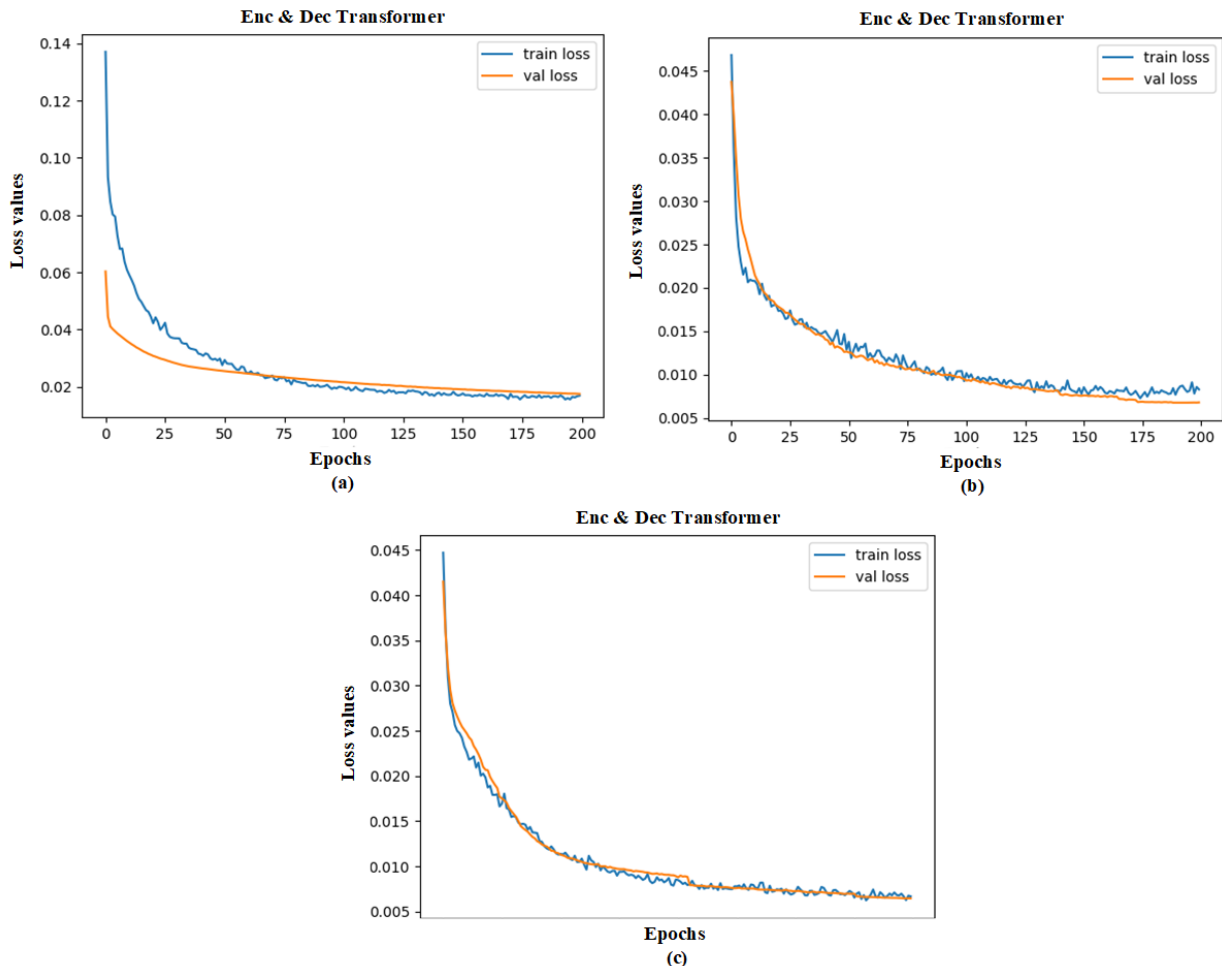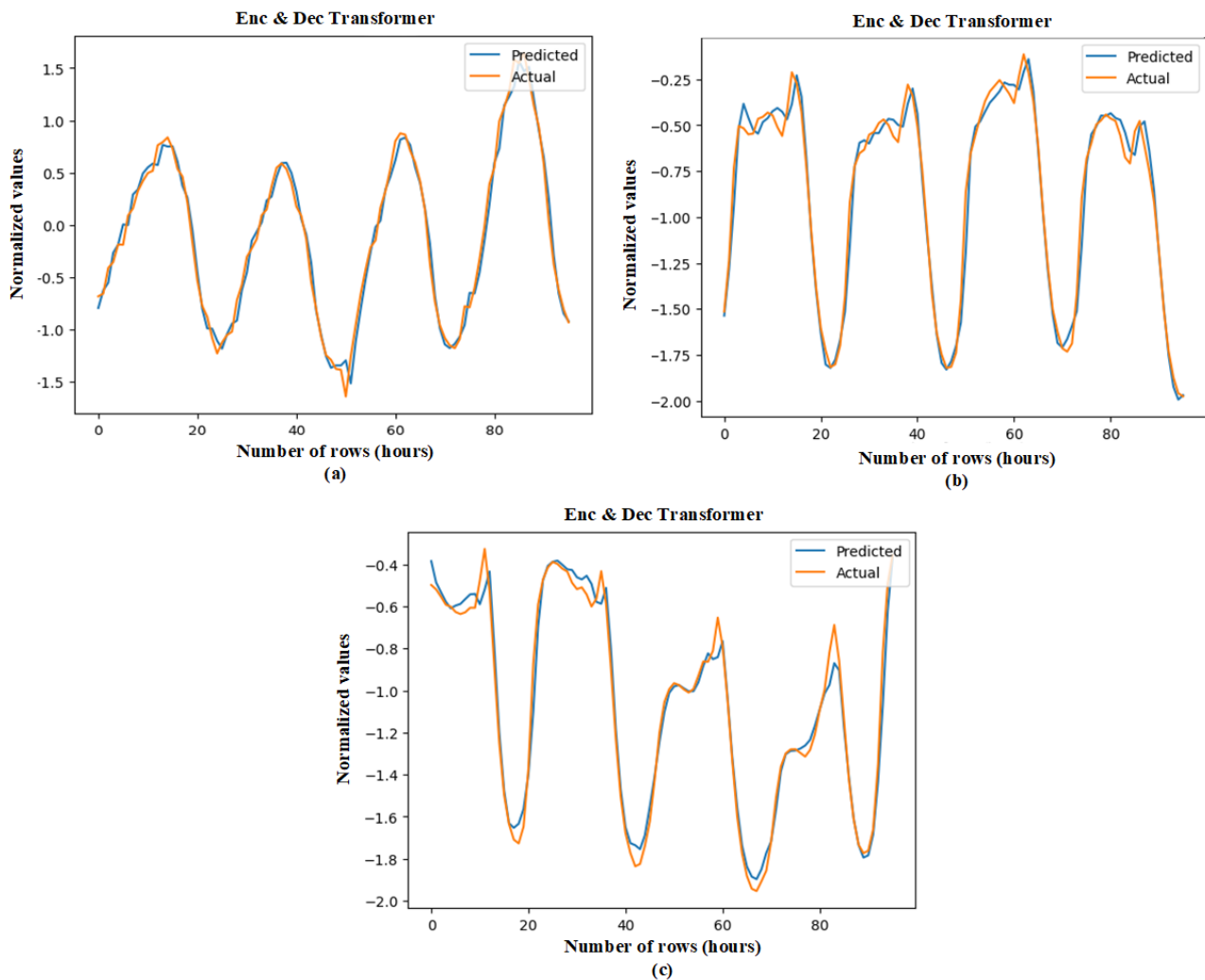

Figure 7. *Predicted and actual values of Enc&Dec Transformer model in terms on MSE score using (a) small (EKPC), (b) medium (DUQ,), and (c) large (PJME) datasets*

Figure 7 depicts the predicted and actual values of the first 96 hours ahead for small, medium, and large datasets, utilizing our proposed approach, Enc&Dec Transformer. In Figure 7(a), the difference between predicted values and actual values for the small size of data indicates in the initial stage a lesser height. In Figure 7(b), the points for the medium size of data in the scatter plot are generally close to the blue line, indicating that the model is performing well in predicting the actual values. Many points cluster around the ideal line, suggesting that the model is generally accurate. There are very few outliers, as the model points out. This implies that the model's predictions were very close to the actual values for the majority of the Enc&Dec Transformer. In Figure 7(c), it shows the growth trend for the large size of data, in which the difference between actual and predicted values is very close; at sometimes, they are the same. There is no trend of underestimation at high values; in fact, there is a slight trend of overestimation at high values, with the red circles positioned slightly above the blue line on the higher values of the x-axis. The graph exhibits that in the case of high volume of data Enc&Dec Transformer is good at predicting the actual value.

7. CONCLUSION

In this study, we propose utilizing the Enc & Dec Transformer having encoder-decoder architecture to forecast univariate time-series in IoT device-generated energy consumption data. The performance of our proposed models is compared with recurrent-based models, including RNN, LSTM, GRU, convolutional-based 1D-CNN, as well as self-attention-based Encoder-only and Decoder-only. To determine optimal hyperparameters, we utilized Optuna, optimizing network complexity efficiently with minimal resource and memory usage. We evaluated the performance of our proposed model alongside other deep learning models on datasets of varying sizes: small, medium, and large. Our experimental results indicate that all models perform admirably well on large time-series datasets. Among the recurrent-based models, GRU demonstrated superior performance compared to RNN and LSTM, particularly in understanding the relationships between features within the univariate energy domain data. The 1D-CNN model, leveraging automatic feature engineering properties, outperformed all models in the case of medium-sized data. For the comparison of self-attention-based models, Decoder-only outperforms Encoder-only as well as recurrent-based algorithms. Our proposed Enc & Dec Transformer model showcased superior performance on small, medium, and very large datasets. As dataset sizes increased, the performance gaps widened, highlighting the transformer's advantage in handling large-scale data. However, it is essential to note that while transformers achieve higher scores, they also incur higher computational expenses during training. Depending on specific applications and available computational resources, separated Transformer models like Encoder-only and Decoder-only transformers or simpler model like RNNs or 1D-CNNs might be more viable, especially for smaller datasets. Our results show that attention mechanisms, especially those composed of Enc & Dec Transformer which composed of encoder and decoder layers, represent the state-of-the-art in time-series prediction. This interpretation method is inspired by human recognition and allows neural networks to focus on how various inputs influence outputs at each step of inference in the model development process, providing a quantitative explanation of these influences. One of the important components that can improve the efficiency of Encoder-only Transformer, Decoder-only Transformer, and Enc & Dec Transformer models is positional encoding. Attention modules may not understand the exact location of each data point, which is why positional encodings are utilized to represent the location of each time-dependent data point in a precise manner. In this study, we trained models using one of the traditional positional encodings (absolute). Therefore, it is suggested to evaluate the performance of transformers by employing different types of positional encoding to demonstrate efficiency in energy consumption prediction.

AUTHOR CONTRIBUTIONS

Methodology and writing-reviewing, A.A. and F.Y.O; editing, F.Y.O.; conceptualization and software, A.A. All authors have read and legally accepted the final version of the article published in the journal.

CONFLICT OF INTEREST

The authors declare no conflict of interest.

REFERENCES

Adhikari, R., & Agrawal, R.K. (2013). An Introductory Study on Time Series Modeling and Forecasting. *ArXiv, abs/1302.6613*. https://doi.org/10.48550/arXiv.1302.6613

Afanasieva, T., & Platov, P. (2019). The Study of Recurrent Neuron Networks based on GRU and LSTM in Time Series Forecasting. *In ITISE 2019. Proceedings of papers. Vol 1 (pp. 12). Granada, Spain: International Conference on Time Series and Forecasting.* https://itise.ugr.es/ITISE2019_Vol1.pdf

Akiba, T., Sano, S., Yanase, T., Ohta, T., & Koyama, M. (2019). Optuna: A Next-generation Hyperparameter Optimization Framework. *In Proceedings of the 25th ACM SIGKDD International Conference on Knowledge Discovery & Data Mining* (pp. 2623–2631). *Association for Computing Machinery.* https://doi.org/10.1145/3292500.3330701

Box, G. E. P., Jenkins, G. M., Reinsel, G. C., & Ljung, G. M. (2015). Time Series Analysis: Forecasting and Control (5th ed.). *Hoboken, NJ: John Wiley & Sons Inc.* https://doi.org/10.1111/jtsa.12194

Cao, L. (2003). Support vector machines experts for time series forecasting. *Neurocomputing*, 51, 321-339. https://doi.org/10.1016/S0925-2312(02)00577-5

Carion, N., Massa, F., Synnaeve, G., Usunier, N., Kirillov, A., & Zagoruyko, S. (2020). End-to-End Object Detection with Transformers. *CoRR, abs/2005.12872*. https://doi.org/10.48550/arXiv.2005.12872

Cochrane, J. H. (1997). Time Series for Macroeconomics and Finance. *Graduate School of Business, University of Chicago.* Retrieved from http://www.fsb.miamioh.edu/lij14/672_notes_Cochrane

Coulibaly, P., & Baldwin, C. K. (2005). Nonstationary hydrological time series forecasting using nonlinear dynamic methods. *Journal of Hydrology*, 307(1–4), 164-174. https://doi.org/10.1016/j.jhydrol.2004.10.008

Das, A., Kong, W., Sen, R., & Zhou, Y. (2024). A decoder-only foundation model for time-series forecasting. *ICML.* https://doi.org/10.48550/arXiv.2310.10688

Haugsdal, E., Aune, E., & Ruocco, M. (2023). Persistence Initialization: a novel adaptation of the Transformer architecture for time-series prediction. *Applied Intelligence*, 53, 26781–26796. https://doi.org/10.1007/s10489-023-04927-4

Hipel, K. W., & McLeod, I. (1994). Time series modelling of water resources and environmental systems. *In Proceedings of the International Conference on Systems, Man and Cybernetics* (pp. 1-6). https://doi.org/10.1016/s0167-5648(08)x7026-1

Hu, C., Sun, Z., Li, C., Zhang, Y., & Xing, C. (2023). Survey of time-series data generation in IoT. *Sensors,* 23(15), 6976. https://doi.org/10.3390/s23156976

IoT Analytics (2023). state of IoT 2023: number of connected IoT devices growing 16% to 16.7 billion *globally.* https://iot-analytics.com/number-connected-iot

Javaid N., Jul 12, 2019. Implementing an RNN from scratch in Python: towards data science. https://towardsdatascience.com/recurrent-neural-networks-rnns-3f06d7653a85

Lara-Benítez, P., Gallego-Ledesma, L., Carranza-García, M., & Luna-Romera, J. M. (2021). Evaluation of the Transformer Architecture for Univariate Time Series Forecasting. *In E. Alba et al. (Eds.), Advances in Artificial Intelligence. CAEPIA 2021.* Lecture Notes in Computer Science (Vol. 12882). *Springer,* Cham. https://doi.org/10.1007/978-3-030-85713-4_11

Li, S., Jin, X., Xuan, Y., Zhou, X., Chen, W., Wang, Y.-X., & Yan, X. (2019). Enhancing the Locality and Breaking the Memory Bottleneck of Transformer on Time Series Forecasting. *CoRR, abs/1907.00235.* https://doi.org/10.48550/arXiv.1907.00235

Lim, B., Arık, S. Ö., Loeff, N., & Pfister, T. (2021). Temporal Fusion Transformers for interpretable multi-horizon time series forecasting. *International Journal of Forecasting*, 37(4), 1748–1764. https://doi.org/10.1016/j.ijforecast.2021.03.012

Ma, J., Shou, Z., Zareian, A., Mansour, H., Vetro, A., & Chang, S. (2019). CDSA: Cross-Dimensional Self-Attention for Multivariate, Geo-tagged Time Series Imputation. *ArXiv, abs/1905.09904.* https://doi.org/10.48550/arXiv.1905.09904

Markova, M. (2022). Convolutional neural networks for forex time series forecasting. *AIP Conference Proceedings*, 2459(1), 030024. https://doi.org/10.1063/5.0083533

Masum, S., Liu, Y., & Chiverton, J. (2018). Multi-step Time Series Forecasting of Electric Load Using Machine Learning Models. In L. Rutkowski, R. Scherer, M. Korytkowski, W. Pedrycz, R. Tadeusiewicz, & J. M. Zurada (Eds.), *Artificial Intelligence and Soft Computing* (pp. 148-159). Springer International Publishing. https://doi.org/10.1007/978-3-319-91253-0_15

Mo, Y., Wu, Q., Li, X., et al. (2021). Remaining useful life estimation via transformer encoder enhanced by a gated convolutional unit. *Journal of Intelligent Manufacturing*, 32, 1997–2006. https://doi.org/10.1007/s10845-021-01750-x

Mulla, R. (2019). Hourly Energy Consumption. PJM Interconnection LLC in *Kaggle.*

Nie, H., Liu, G., Liu, X., & Wang, Y. (2012). Hybrid of ARIMA and SVMs for Short-Term Load Forecasting. *Energy Procedia*, 16, 1455-1460. https://doi.org/10.1016/j.egypro.2012.01.229

Nor, M. E., Mohd Safuan, H., Md Shab, N. F., Asrul, M., Abdullah, A., Mohamad, N. A. I., & Lee, M. H. (2017). Neural network versus classical time series forecasting models. *AIP Conference Proceedings*, 1842(1), 030027. https://doi.org/10.1063/1.4982865

Ogunfowora, O., & Najjaran, H. (2023). A Transformer-based Framework for Multi-variate Time Series: A Remaining Useful Life Prediction Use Case. https://doi.org/10.48550/arXiv.2308.09884

Pashamokhtari, A. (2020). Dynamic inference on IoT network traffic using programmable telemetry and machine learning. In Proceedings of the 2020 19th *ACM/IEEE International Conference on Information Processing in Sensor Networks (IPSN)* (pp. 371–372). https://doi.org/10.1109/IPSN48710.2020.00006

Raheem, I., Mubarak, N. M., Karri, R. R., et al. (2022). Forecasting of energy consumption by G20 countries using an adjacent accumulation grey model. *Scientific Reports*, 12, 13417. https://doi.org/10.1038/s41598-022-17505-4

Russell, S. J., & Norvig, P. (2020). (4th ed.). *Artificial Intelligence: A Modern Approach*. Prentice Hall Publishing.

Sahoo, B. B., Jha, R., Singh, A., et al. (2019). Long short-term memory (LSTM) recurrent neural network for low-flow hydrological time series forecasting. *Acta Geophysica*, 67, 1471–1481. https://doi.org/10.1007/s11600-019-00330-1

Shapi, M. K. M., Ramli, N. A., & Awalin, L. J. (2021). Energy consumption prediction by using machine learning for smart building: Case study in Malaysia. *Developments in the Built Environment*, 5, 100037. https://doi.org/10.1016/j.dibe.2020.100037

Shekhar, S., Bansode, A., & Salim, A. (2021). A Comparative study of Hyper-Parameter Optimization Tools. *In 2021 IEEE Asia-Pacific Conference on Computer Science and Data Engineering (CSDE)* (pp. 1-6). Brisbane, Australia. https://doi.org/10.1109/CSDE53843.2021.9718485

Shi, J., Jain, M., & Narasimhan, G. (2022). Time Series Forecasting (TSF) Using Various Deep Learning Models. *arXiv, 2204.11115.* https://doi.org/10.48550/arXiv.2204.11115

Tealab, A. (2018). Time series forecasting using artificial neural networks methodologies: A systematic review. *Future Computing and Informatics Journal,* 3(2), 334-340. https://doi.org/10.1016/j.fcij.2018.10.003

Torres, J. F., Hadjout, D., Sebaa, A., Martínez-Álvarez, F., & Troncoso, A. (2021). Deep Learning for Time Series Forecasting: A Survey. *Big Data,* 9(1), 3-21. https://doi.org/10.1089/big.2020.0159

Vaswani, A., Shazeer, N., Parmar, N., Uszkoreit, J., Jones, L., Gomez, A. N., Kaiser, L., & Polosukhin, I. (2017). Attention Is All You Need. *CoRR, abs/1706.03762*. https://doi.org/10.48550/arXiv.1706.03762

Wen, Q., Zhou, T., Zhang, C., Chen, W., Ma, Z., Yan, J., & Sun, L. (2023). Transformers in time series: A survey. *In Proceedings of the Thirty-Second International Joint Conference on Artificial Intelligence* (pp. 759). Macao, P.R. China: International Joint Conferences on Artificial Intelligence. https://doi.org/10.24963/ijcai.2023/759

Wu, N., Green, B., Ben, X., & O'Banion, S. (2020). Deep Transformer Models for Time Series Forecasting: The Influenza Prevalence Case. *CoRR, abs/2001.08317*. https://doi.org/10.48550/arXiv.2001.08317

Zeyer, A., Bahar, P., Irie, K., Schlüter, R., & Ney, H. (2019). A Comparison of Transformer and LSTM Encoder Decoder Models for ASR. *In 2019 IEEE Automatic Speech Recognition and Understanding Workshop (ASRU)* (pp. 8-15). Singapore. https://doi.org/10.1109/ASRU46091.2019.9004025

Zhang, Q., Lipani, A., Kirnap, Ö., & Yilmaz, E. (2019). Self-Attentive Hawkes Processes. *CoRR, abs/1907.07561*. https://doi.org/10.48550/arXiv.1907.07561

Zuo, S., Jiang, H., Li, Z., Zhao, T., & Zha, H. (2020). Transformer Hawkes Process. *CoRR, abs/2002.09291*. https://doi.org/10.48550/arXiv.2002.09291

Diagnosis of Pneumonia from Chest X-ray Images with Vision Transformer Approach

Emrah ASLAN[1*] iD

[1] Dicle Üniversitesi, Silvan Meslek Yüksekokulu, Diyarbakır, Türkiye

Keywords	Abstract
ViT Pneumonia Artificial Intelligence CNN	People can get pneumonia, a dangerous infectious disease, at any time in their lives. Severe cases of pneumonia can be fatal. A doctor would usually examine chest x-rays to diagnose pneumonia. In this work, a pneumonia diagnosis system was developed using publicly available chest x-ray images. Vision Transformer (ViT) and other deep learning models were used to extract features from these images. Vision Transformer (ViT) is an attention-based model used for image processing and understanding as an alternative to the convolutional neural networks traditionally used for this purpose. ViT consists of a series of attention layers, where each attention layer models the relationships between input pixels to represent an image. These relationships are determined by a set of attention heads and then fed into a classifier. ViT performs effectively in a variety of visual tasks, especially when trained on large datasets. The study shows that the ViT model's classification procedure has a high success rate of 95.67%. These results highlight how deep learning models can be used to quickly and accurately diagnose dangerous diseases such as pneumonia in its early stages. The study also shows that the ViT model outperforms current approaches in the biomedical field.

1. INTRODUCTION

Recently, significant progress has been made in computer vision thanks to the introduction of deep learning (DL) algorithms. Convolutional Neural Networks (CNNs) have long dominated image processing tasks (Aslan & Özüpak, 2024). They have demonstrated outstanding performance in numerous applications, including photo classification, object identification, and segmentation. Nevertheless, the reliance on CNNs for visual tasks has led researchers to investigate alternative architectures that could provide improvements in effectiveness and efficiency. One viable option that has received much interest is the Vision Transformer (ViT) model. In ViT, spatial features are extracted from images using a transformer-based architecture first introduced for natural language processing tasks, as opposed to typical CNNs that use convolutions. This departure from CNNs represents a paradigm shift in image understanding, providing a novel approach to capture long-range dependencies and semantic relationships within visual data (Berliner et al., 2016).

The basic idea of the ViT model is the self-attention mechanism, which allows the model to capture global contextual information while focusing on relevant areas of the input image. By decomposing the input image into patches and processing them through a sequence of transform blocks, ViT learns to extract hierarchical representations of visual content, effectively leveraging both local and global information for downstream tasks. To extract high-level information from the input image, ViT's architecture consists of multiple layers of self-attention blocks followed by feedforward neural networks. Most importantly, ViT eliminates the need for

manually constructed features, allowing the model to self-train on massive datasets and learn discriminative features directly from raw pixel values. Through this comprehensive review, we aim to provide researchers and practitioners with a comprehensive understanding of ViT's capabilities, potential areas for improvement, and future research directions in the evolving landscape of computer vision (Salehinejad et al., 2018).

Vision Transformer (ViT) has significant potential in medical imaging and can be applied to critical health issues such as the diagnosis of pneumonia. Pneumonia is a disease resulting from infection in the lungs and can lead to serious complications. Traditionally, pneumonia is diagnosed by examining chest X-rays. Within these images, specific clues are searched for. However, deep learning models like ViT can be employed to extract information from such images and diagnose the disease. When trained on large datasets, ViT can perceive complex patterns in images and detect symptoms of specific illnesses like pneumonia. For the diagnosis of pneumonia, ViT can extract features from chest X-rays. Based on these features, it can classify the disease. This approach could support the diagnosis process of human doctors or contribute to the development of automated diagnostic systems. However, before implementing such a system, the accuracy and reliability of ViT need to be thoroughly validated. Additionally, strict compliance with regulations and standards for medical devices and applications is necessary. As a result, deep learning models like ViT could play an important role in the early diagnosis and treatment of pneumonia, but careful evaluation is essential (Pacal, 2023).

Image processing refers to a technology that rapidly performs various tasks similar to those performed by the human eye within a computerized environment, using various interface software. A plethora of models have been developed within this domain, with accompanying scientific research contributing significantly. Recently, the predominant model emerging from the analytical results is deep learning, an integral component of machine learning. Deep learning has gained popularity due to its multi-layered design, which distinguishes it from typical machine learning techniques. Its inspiration comes from the complex functioning of the human brain (Koitka & Friedrich, 2016). The focus of deep learning models in the field of image processing includes biomedical applications, where their integration has heralded remarkable successes (Ravi et al., 2017). Throughout history, infectious diseases have emerged as a major threat to human well-being. Pneumonia, medically known as pneumonias, reigns supreme in the hierarchy of infectious diseases (Bakator & Radosav, 2018). Characterized by inflammation of lung tissue due to microbial invasion, pneumonia takes a heavy toll, affecting approximately 7% of the global population annually and resulting in an estimated 4 million deaths (Akter et al., 2015). Timely diagnosis is paramount to mitigating the impact of such diseases. Recognizable symptoms include chest pain, dyspnea, and cough, among others, with diagnostic modalities including sputum cultures and chest radiographs (Berliner et al., 2016).

Much research has attempted to apply various computer vision techniques to the interpretation of human chest X-rays to detect pneumonia. In 2017, Rajpurkar and colleagues presented a framework called "ChexNet" that demonstrated the ability to diagnose pneumonia from chest X-rays with a level of accuracy exceeding that of expert radiologists (Rajpurkar et al., 2017). With over 100,000 frontal view X-rays labeled with 14 diseases, the ChestXray14 dataset serves as the training set for ChexNet, a 121-layer CNN. This repository is currently the largest of its kind in the public domain. In another study, Tatiana Gabruseva and colleagues developed a computational method based on augmentation, multi-task learning, squeeze-and-excitation deep convolutional neural networks, single-shot detectors, and multi-task learning for pneumonia area detection (Gabruseva et al., 2020). When the suggested method was assessed in the context of the Radiological Society of North America Pneumonia Detection Project, it produced good results within the project framework.

For the purpose of analyzing abnormal and normal chest X-rays, Varshni et al. (2019) evaluated the effectiveness of pre-trained CNN models used as feature extractors followed by different classifiers. The best CNN model for this purpose was then analytically determined and the accuracy was 80.02% (Varshni et al., 2019). To diagnose pneumonia more accurately than individual models, Chouhan et al. (2020) proposed an ensemble model that incorporates results from multiple pre-trained models. Their ensemble model achieved excellent recall of 99.62% and accuracy of 96.4% on unknown data from the Guangzhou Women and Children's Medical Center dataset. Salehinejad et al. (2018) used GAN-generated images to improve the original chest X-ray images in order to overcome the absence of medical data. The dataset was subsequently subjected to DCNN, which produced considerable improvements in classification performance (Salehinejad et

al., 2018). A text-image embedding network for feature extraction was proposed by Wang et al. (2017) Subsequently, an automatic annotation framework was created, which demonstrated an amazing accuracy of 0.9 (Wang et al., 2017). Toğaçar et al. (2022) used CNN as a feature extractor along with a variety of convolutional neural network models such as VGG-16, VGG-19, and AlexNet. They also used a feature selection approach (mRMR) to reduce combined features (Toğaçar et al., 2020). Using VGG16 with Bi-directional LSTM, Suganya G et al. extracted characteristics from chest X-ray pictures. This resulted in a notable accuracy of 97.76% in tuberculosis detection (Chowdary et al., 2021). With the help of cytological imaging, Guan et al. (2019) were able to discriminate between benign thyroid nodules and papillary thyroid cancer with a reasonable accuracy of 95% in their patient base. In the contemporary landscape of medical practice, reliance on manual interpretation of chest X-rays by clinicians presents a cumbersome process amidst the era of technological advancements. Leveraging extant technological resources and software applications to facilitate diagnosis represents a commendable stride in terms of efficiency and cost-effectiveness. By harnessing deep learning models, particularly in training with chest X-ray images sourced from pneumonia patients, superior diagnostic outcomes can be achieved compared to conventional methodologies. This study, employing publicly available chest X-ray imagery, has harnessed ViT, a prominent deep learning methodology, with ensuing results showcasing its efficacy and proficiency.

2. MATERIAL AND METHOD

A well-liked method in the deep learning family, transformers have shown remarkable results in natural language processing (NLP) applications. Transformers have been used in image processing activities recently, a significant development that was started by Dosovitskiy and associates. Demonstrating success in image processing, transformers have swiftly gained prominence across various domains. Characterized by a simple network architecture based on attention mechanisms, transformers enable focused processing of input elements. Similar to operations in natural language processing, inputs are divided into multiple patches, akin to words, and undergo a series of linear transformations (Dosovitskiy et al., 2021).

In the realm of image processing, inputs are fragmented into multiple patches, resembling words, which are then utilized as input elements. The Vision Transformer (ViT) stands as the pioneering attempt to apply a pure transformer architecture to process images. While the original transformer model encompasses both encoder and decoder components, the ViT model solely incorporates an encoder. The operational principles of image transformers closely parallel those observed in NLP. In the ViT architecture, the input image I is represented as R^{HxWxC} of dimensions. Subsequently, this image is partitioned into N patches of dimensions $PxPxC$. The value of N is mathematically expressed as shown in Equation 1.

$$N = \frac{HW}{P^2} \tag{1}$$

Flattening and Embedding Process: In this context, H represents the height, P the patch size, W the width, and C the number of channels in the image. The fragmented image patches, divided into N parts, are flattened and subjected to a linear embedding process. Subsequently, a positional embedding process is applied to retain positional information of the patches. The functioning of vision transformers proceeds akin to natural language processing. Three layers typically make up the ViT architecture: the classifier, encoder, and embedding layers. This structure is illustrated in Figure 1.

Embedding Layer: Each patch is handled separately in this layer, and a learnable linear projection is used to map the patches to the embedding dimensions E and D. The embedded projections are combined with a learnable class token U_{class}, which serves as a trainable token completing the classification process. Positional embedding, E_{pos}, tracks the arrangement of each patch, ensuring their maintenance to facilitate the recognition of the actual image. The patch-encoded series, denoted as Z_0, is mathematically expressed as shown in Equation 2 below.

$$Z_0 = \left[U_{class}; X_p^1 E;\ X_p^2 E;\ ......X_p^N E\right] + E_{pos} \tag{2}$$

Encoder Layer: The transformer encoder is employed to process the previously obtained series of embedded patches Z_0. In vision transformers, the encoder unit comprises L identical layers. Each identical layer consists of a multi-head self-attention (MSA) block and a fully connected feed-forward dense block (MLP) structure (Equations 3 and 4). In the transformer encoder, the MSA block serves as the fundamental component, incorporating self-attention and merging layers. These blocks consist of the GeLU activation function after two dense layers. Skip connections are used in the encoder, and layer normalization (LN) is used prior to the output layer.

$$Z'_1 = MSA(LN)(Z_1 - 1) + (Z_1 - 1), 1 = 1 .... L \tag{3}$$

$$Z'_1 = MLP(LN)(Z'_1) + Z'_1, 1 = 1 .... L \tag{4}$$

Within the transformer encoder, the output of the multi-head self-attention (MSA) is obtained through the aggregation of several self-attention heads. Mathematically, self-attention is represented as shown in Equation 5.

$$H = Atten(Q, K, V) = softmax\left(\frac{QK^T}{\sqrt{D_K}}\right)V \tag{6}$$

In Equation 5, the query obtained after matrix multiplications is represented by Q, the key by K, and the value matrix by V. In vision transformers, the final output of the MSA is obtained by passing the concatenation of all self-attention heads through a linear layer. This linear layer is mathematically expressed in Equation 6.

$$MSA(Q, K, V) = [H_1, H_2, ... H_h]W_0 \tag{7}$$

Where, W_0 represents the learnable output transformation matrix, while H denotes the number of self-attention heads.

2.1. Vision Transformer Approach

The Vision Transformer (ViT) technique is now a helpful tool for work involving NLP. In the area of computer vision, ViT offers a pure transformer model devoid of any convolutional blocks (Vaswani et al., 2017). Convolutional Neural Networks (CNN) have historically dominated image recognition efforts. Nevertheless, CNNs have several drawbacks. Most notably, because of processes like max pooling, they process information more slowly, and large datasets are required for efficient processing and neural network training (Zhou et al., 2021). The suggested model uses a dataset of chest X-rays to classify pneumonia using the Vision Transformer (ViT) approach. Notably, when it comes to managing massive computer vision datasets, the Vision Transformer has lately gained favor over CNNs. Data integration across the full image is made possible by ViT's usage of a transformer architecture with self-attention. The operating principle of ViT is visualized in Figure 1.

As required by the algorithm, the image is split up into tokens, or patches, of similar size. These patches go through a 2D flattening process to become a vector format. The patch embedding is then combined with a position embedding to preserve positional information. Layers for self-attention and multi-head attention make up the transformer encoder. The multi-layer perceptron blocks are connected to a second layer normalization, and the embedded patches are connected to layer normalization within the multi-head arrangement. Each X-ray image was resized to a consistent pixel dimension of 250 by 250. Subsequently, each image was partitioned into 25 identical patches, each with dimensions of 50 by 50 pixels. These patches were vectorized and flattened in order to be input into the transformer encoder network, where positional encoding was applied to the picture vectors. Among the six transformer blocks, the multi-head attention layer utilized eight heads.
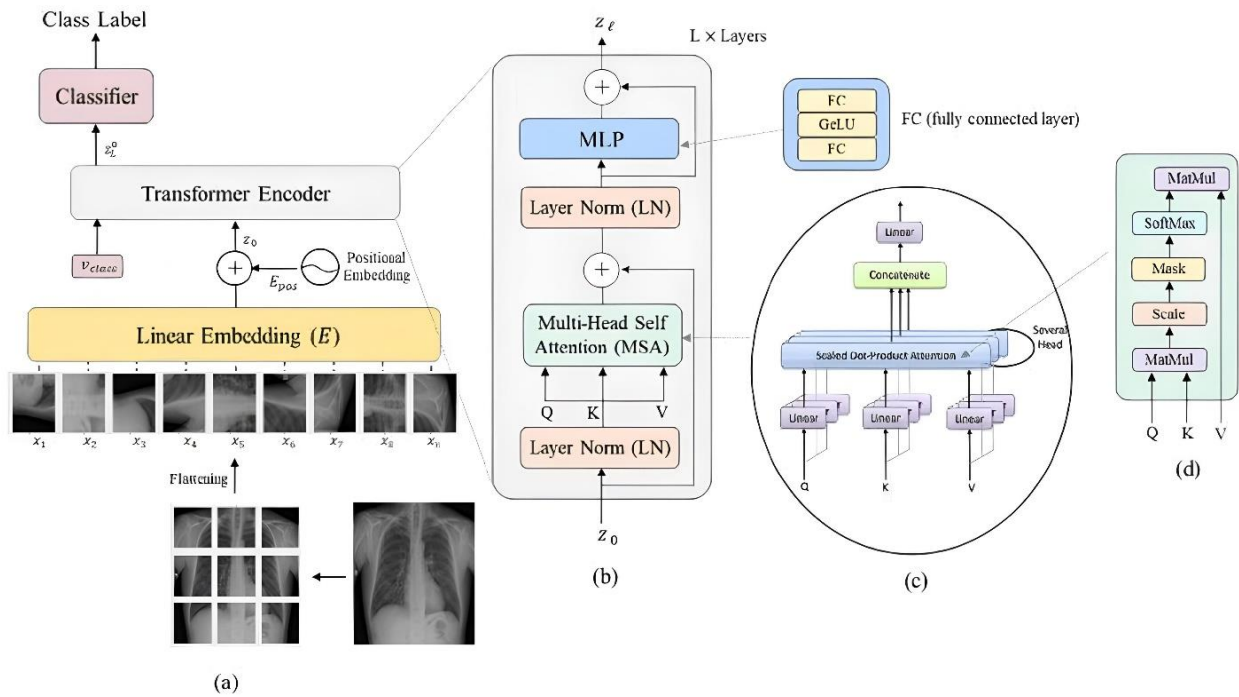
Figure 1. Overview of the design of the vision transformer

2.2. Classification layer

Within this unit dedicated to the classification process, the entity Z_l^0 is initially retrieved and subsequently input into an external auxiliary head classifier to forecast the ultimate layer of the encoder for classification. This procedure is formally delineated in Equation 7, wherein y symbolizes the model's output and Z_l^0 denotes the initial element utilized for decision-making (Pacal, 2023).

$$y = layer\_normalization\ (Z_l^0) \tag{8}$$

In this study, three different transformer-based models were applied for pneumonia diagnosis from chest X-ray images. Table 1 displays each vision transformer model's specifics. The ViT-B model consists of two different models, ViT-B16 and ViT-B32. Actually, the ViT-B model, or the base model, is obtained by changing the patch sizes to 16x16 or 32x32, resulting in two models, but there is no change in the number of layers, which remains at 12. Similarly, in the ViT-L, or large model, ViT-L16 and ViT-L32 models are obtained by changing the number of patches. However, the ViT-H model, or the larger model, was not used in the study due to its unavailability on the RTX-2080-TI graphics card. Despite selecting the lowest batch size of 1, the GPU proved inadequate for operation. As seen in Table 1, the MLP size increased from 3072 in the base model to 5120 in the high model. It is well known that larger models provide more effective results, especially with large-scale data.

2.3. Dataset

The dataset is divided into three subdirectories, one for each of the three photo categories (Pneumonia/Normal): train, test, and validation. It includes 5,863 X-ray images (JPEG) in total, divided into two categories: pneumonia and normal. Anterior-posterior chest X-ray pictures were selected from a retrospective cohort of pediatric patients (aged one to five) from Guangzhou Women and Children's Medical Center in Guangzhou. The patients' regular clinical care included the acquisition of these chest X-rays. Prior to commencing the analysis of chest X-ray images, all radiographs underwent meticulous quality control, wherein any scans deemed of subpar quality or unreadable were eliminated. Subsequently, two board-certified medical experts evaluated the images prior to training the AI system for diagnosis. A third specialist validated the assessment set to ensure absence of grading discrepancies. The dataset's specifics are depicted in Figure 2.
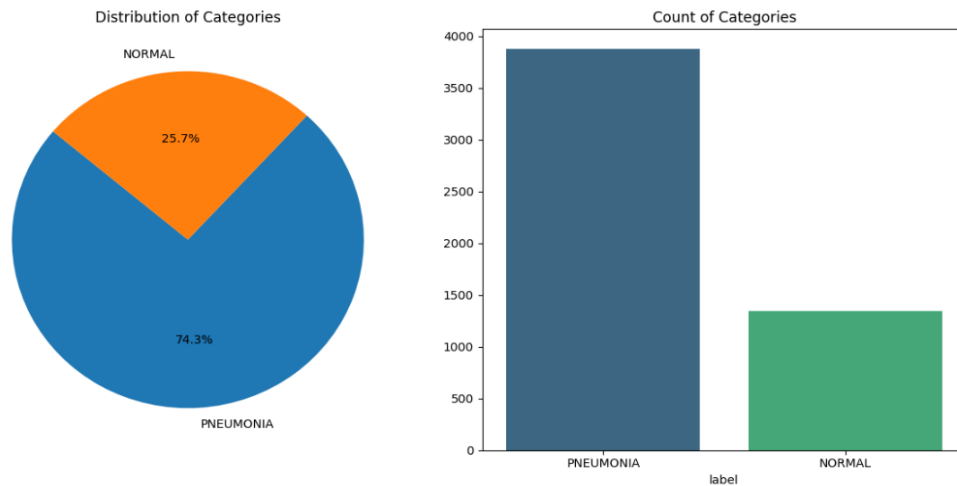
Figure 2. Representation of values in the dataset

In the pneumonia dataset, the training and evaluation images of the deep learning approaches come pre-separated. The main advantage of such a situation is that the study is easily comparable to other studies and the actual performance of the model can be measured. The dataset is an extended publicly available dataset consisting of images from different datasets. Train, Test, and Validation are the three primary folders into which the dataset is arranged. Pneumonia and Normal are two subfolders that correspond to different image categories in each of these directories. There are 5,863 JPEG-formatted X-ray images in total, divided into two groups: normal and pneumonia. Here, the class distributions in the training, validation and test data are well-adjusted and there is no data imbalance. Thus, the model will try to learn each class in the dataset in a better way, and the bias towards any one class will be reduced. Some random sample images from the pneumonia dataset are shown in Figure 3.

Figure 3. Random sample images from the pneumonia dataset.

2.4. Proposed Method

There are essentially three parts to the suggested technique for automatically detecting pneumonia. Figure 4 displays the primary parts of the suggested system. By using the achievements of deep learning techniques in medical image processing to chest X-ray pictures, a more efficient system is suggested. The first part of this deep learning based system, which consists of three parts, is the data set unit. The next unit after the dataset is the unit where data pre-processing and data augmentation techniques are combined. This unit's primary goal is to use some fundamental data augmentation techniques and shrink all of the dataset's photos to the same size. The most fundamental data augmentation methods, including translation, rotation, and panning, were used during training as there are enough images in the dataset. For large-scale datasets, data augmentation is not very effective, but it contributes to the performance, while for small-scale and less diverse datasets, data augmentation is very effective. The last unit of the proposed method is the unit where deep learning approaches are used. This unit includes learning transfer and a vision transformer for classification. The technique of moving the weights of a model trained in one domain to another is known as transfer learning or learning

transfer. For the pneumonia dataset in this study, the weights of the vision transformers trained on the ImageNet dataset were utilized. Significant performance is obtained by learning transfer, particularly with small-scale datasets. In this dataset, it resulted in both better performance and faster convergence than training from scratch. After learning transfer, we used vision transformers for classification. This architecture is described in detail in the materials and methods section.

2.5. Evaluation Metrics

Important measures including accuracy, F1 score, precision, and recall are used to evaluate the suggested model. Four parameters are used in the calculation of these metrics: true positive (TP), false negative (FN), false positive (FP), and true negative (TN). The following definitions apply to the parameters in these equations: Examples of data that the model correctly categorized as positive are called True Positives (TP). Examples of negative outcomes that the model correctly detects are called True Negatives (TN). False positives (FP) are instances in which something was mistakenly categorized as positive by the model. Examples of negative numbers that the model misinterpreted are called False Negatives (FN) (Özüpak, 2024).

These indicators provide a comprehensive evaluation of the model's efficacy, accounting for both positive and negative classifications. The F1-score finds a compromise between precision and recall, even though both indicate details about the model's capacity to accurately identify positive and negative samples, respectively. The accuracy measure gives an overall evaluation of the model's prediction accuracy.

$$Accuracy \ = \frac{TP + TN}{(TP + TN + FP + FN)} \tag{9}$$

$$Recall = \frac{TP}{(TP + FN)} \tag{10}$$

$$Precision = \frac{TP}{(TP + FP)} \tag{11}$$

$$F_1 = 2 * \frac{Precision * Recall}{(Precision + Recall)} \tag{12}$$

3. RESULTS AND DISCUSSION

The model's initial values were used for training and evaluation in the experimental investigation. Figure 4 shows the confusion matrix for the study's model. The expected class is shown on the x-axis of the confusion matrix, and the actual class is shown on the y-axis. The confusion matrix allows us to see both true and false positives and negatives for each class, which improves our ability to observe. The model's experimental findings are shown in Table 1.

In the Figure 4, the confusion matrix shows that the model correctly classified 208 patients as normal (TP) and 389 patients as pneumonia (TN). The model misclassified 26 patients as pneumonia (FP) and 1 patient as not pneumonia (FN). The overall test accuracy of the model was 95.67%.

Table 1. *Metrics showing the performance of the trained model on the test data*

Model	Accuracy	Recall	Precision	F_1 Score
Proposed Model	0.9567	0.9952	0.8888	0.9390

This table shows that the accuracy rate of the suggested model is 95.67%. This indicates that the model makes accurate predictions in general. The recall rate is quite high at 99.52%, indicating that the model can effectively recognize positive class instances. However, the Precision rate is 88.88%, which indicates how many of the cases that the model predicts as positive are actually positive. If the precision is lower than the true positive rate, it may indicate that the model is making false positive predictions and classifying some negative samples as positive. The F1 score was calculated as 0.9390. In this instance, the model's success is gauged by the F1

score, which illustrates the trade-off between precision and the capture rate of true positives. These results show that the model performs well overall but could be improved in specific cases. A comparison of the suggested model with a few findings from the literature is presented in Table 2.
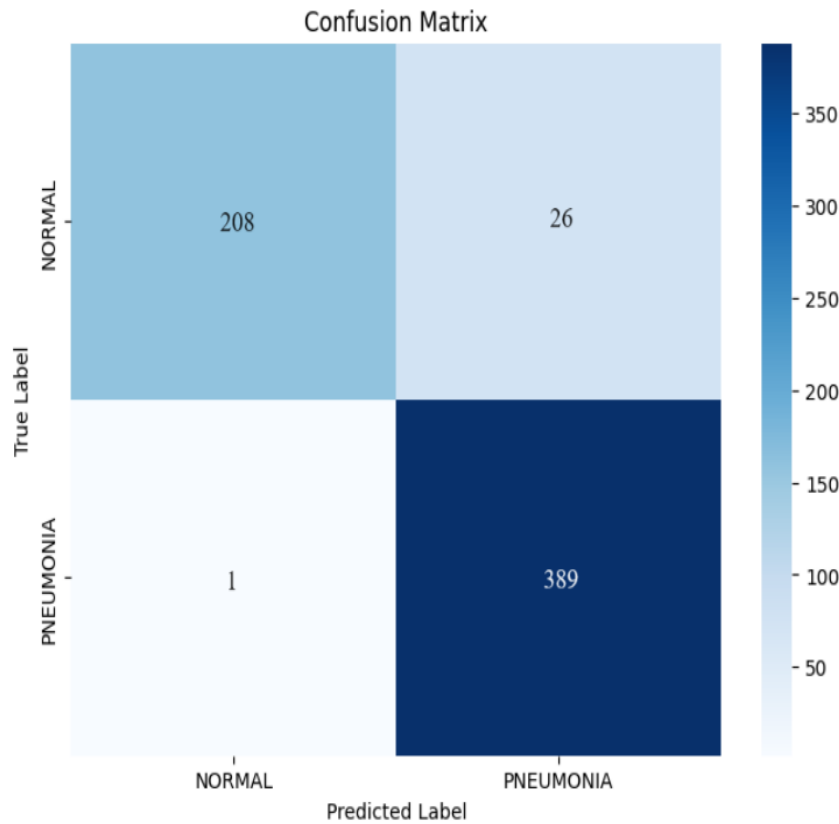
Figure 4. Confusion matrix for the suggested architecture

Table 2. Metrics showing the performance of the trained model on the test data

Model	Accuracy	F_1 Score
(Hassan, 2018)	0.9214	0.9234
(Dey et al., 2021)	0.9012	0.8999
(Singh & Tripathi, 2022)	0.9375	**0.9405**
(Singh & Tripathi, 2022)	0.8814	0.8812
Proposed Model	**0.9567**	0.9390

According to Table 2, we analyzed the performance of five different models and obtained accuracy and F1 score values for each of them, including the proposed model. In this work, we assessed how well several machine learning models performed in diagnosing pneumonia. First, we analyzed the results obtained for Model (Hassan, 2018), where we obtained an accuracy of 92.14% and an F1 score of 92.34%. Although this model performed well overall, we observed that it had a lower F1 score compared to the other models. Model (Dey et al., 2021) performed slightly lower than Model (Hassan, 2018) with an accuracy of 90.12% and an F1 score of 89.99%. We observed that this model was less accurate in diagnosing pneumonia and tended to make more false positive and negative classifications. However, Model (Singh & Tripathi, 2022) did rather well, scoring an F1 score of 94.05% and an accuracy of 93.75%. It is noteworthy that this model is quite effective in diagnosing pneumonia, despite its high accuracy rate and F1 score. When we examined the results obtained

for model (Singh et al., 2022), we obtained an accuracy rate of 88.14% and an F1 score of 88.12%. We observed that this model performs poorly compared to the other models and is less reliable in pneumonia diagnosis. Finally, our proposed model performed the best with an accuracy rate of 95.67% and an F1 score of 93.90%. This model provided more reliable results for pneumonia diagnosis with a higher accuracy rate and a balanced F1 score compared to the other models. These findings demonstrate how well the suggested model diagnoses pneumonia in comparison to the other models. Therefore, we suggest that the proposed model may be a more effective tool for pneumonia diagnosis in clinical applications. While this analysis evaluates the performance of each model separately, it highlights that the proposed model achieves a higher accuracy and F1 score than the others. This indicates that the proposed model is a more reliable option for diagnosing pneumonia.

Figure 5 displays the model's accuracy following testing and training. Figure 6 provides several instances comparing the values predicted by the model with the actual values in the dataset.
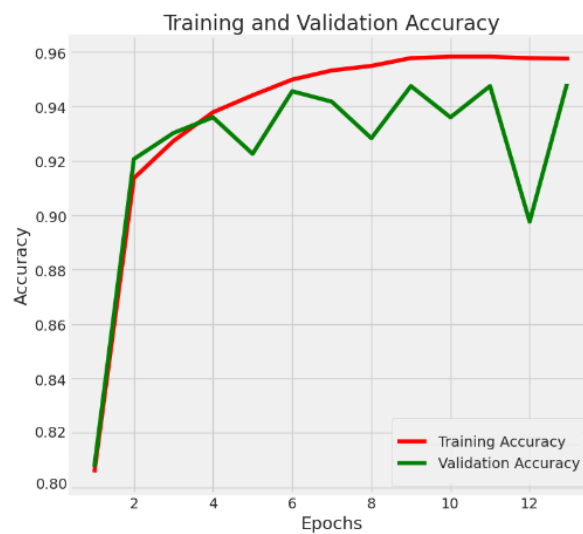
Figure 5. *Training and validation accuracy results*
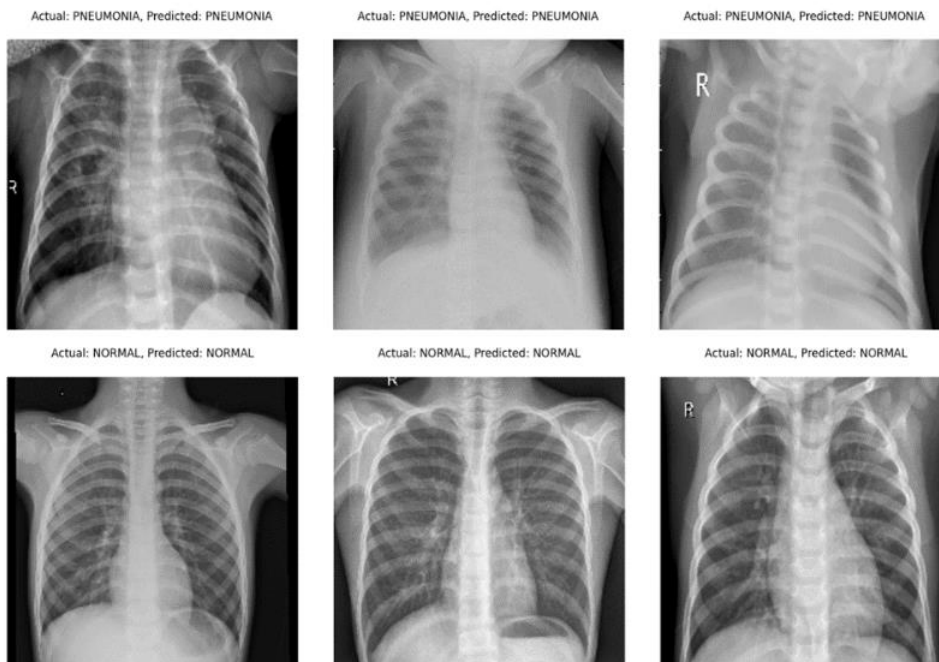
Figure 6. *Some examples showing actual and predicted values*

4. CONCLUSION

In this work, we evaluate the pneumonia diagnosis performance of a DL model. The tremendous potential of transfer learning in the field of medical imaging is demonstrated by the use of the ViT for the classification of chest X-rays. ViT, which has its origins in NLP, has successfully transferred to computer vision through self-supervised learning, offering a workable method for determining the presence of pneumonia from X-rays. The versatility of the Vision Transformer is shown by its distinct method of segmenting images for processing. Its fundamental design, which was first created for NLP tasks, has been skillfully modified for challenging computer vision tasks. A steady reduction in training loss is seen during the training period. This demonstrates how well the model learns from the data and adjusts its parameters to minimize errors. Not only could the model learn, but it also showed excellent generalization abilities. The 95.67% test accuracy indicates that the model performs well. A detailed examination of the confusion matrix demonstrated the model's excellent ability to distinguish between chest X-rays labeled as "Pneumonia" and "Normal." The low rate of misclassifications strengthened trust in the model's predictions. Its excellent accuracy, versatility, and capacity for self-supervised learning bode well for its further applications in medical imaging.

CONFLICT OF INTEREST

The author declares no conflict of interest.

REFERENCES

Akter, S., Shamsuzzaman, & Jahan, F. (2015). Community Acquired Pneumonia. *International Journal of Respiratory and Pulmonary Medicine*, *2*(1). http://doi.org/10.23937/2378-3516/1410016

Aslan, E., & Özüpak, Y. (2024). Classification of Blood Cells with Convolutional Neural Network Model. *Bitlis Eren Üniversitesi Fen Bilimleri Dergisi*, 13(1), 314–326. https://doi.org/10.17798/bitlisfen.1401294

Bakator, M., & Radosav, D. (2018). Deep Learning and Medical Diagnosis: A Review of Literature. *Multimodal Technologies and Interaction*, *2*(3), 47. https://doi.org/10.3390/mti2030047

Berliner, D., Schneider, N., Welte, T., & Bauersachs, J. (2016). The differential diagnosis of dyspnoea. *Deutsches Ärzteblatt International*, *113*(49), 834–844. https://doi.org/10.3238%2Farztebl.2016.0834

Chouhan, V., Singh, S. K., Khamparia, A., Gupta, D., Tiwari, P., Moreira, C., Damaševičius, R., & de Albuquerque, V. H. C. (2020). A novel transfer learning based approach for pneumonia detection in chest X-ray images. *Applied Sciences*, *10*(2), 559. https://doi.org/10.3390/app10020559

Chowdary, G. J., Suganya, G., Premalatha, M., & Karunamurthy, K. (2021). Class dependency-based learning using Bi-LSTM coupled with the transfer learning of VGG16 for the diagnosis of tuberculosis from chest X-rays. In: M. Sabharwal, B. B. Balusamy, S. R. Kumar, N. Gayathri, & S. Suvanov (Eds.), *Applications of Artificial Intelligence in E-Healthcare Systems*, (pp. 37-54). https://doi.org/10.1049/PBHE040E_ch3

Dey, N., Zhang, Y.-D., Rajinikanth, V., Pugalenthi, R., & Raja, N. S. M. (2021). Customized VGG19 architecture for pneumonia detection in chest X-rays. *Pattern Recognition Letters*, *143*, 67–74. https://doi.org/10.1016/j.patrec.2020.12.010

Dosovitskiy, A., Beyer, L., Kolesnikov, A., Weissenborn, D., Zhai, X., Unterthiner, T., Dehghani, M., Minderer, M., Heigold, G., Gelly, S., Uszkoreit, J., Houlsby, N. (2021, May 3-7). An Image is Worth 16x16 Words: Transformers for Image Recognition at Scale. In: Proceedings of the Ninth International Conference on Learning Representations (ICLR 2021), (pp. 1-21). https://iclr.cc/virtual/2021/poster/3013

Gabruseva, T., Poplavskiy, D., & Kalinin, A. (2020, June 14-19). *Deep Learning for Automatic Pneumonia Detection*. In: Proceedings of the IEEE/CVF Conference on Computer Vision and Pattern Recognition (CVPR) Workshops (pp. 1436-1443), Seattle, WA, USA. https://doi.org/10.1109/CVPRW50498.2020.00183

Guan, Q., Wang, Y., Ping. B., Li, D., Du, J., Qin, Y., Lu, H., Wan, X., & Xiang, J. (2019). Deep convolutional neural network VGG-16 model for differential diagnosing of papillary thyroid carcinomas in cytological images: a pilot study. *Journal of Cancer*, *10*(20), 4876–4882. https://doi.org/10.7150/jca.28769

Hassan, M. (2018, November 20). VGG16–Convolutional Network for Classification and Detection. https://neurohive.io/en/popularnetworks/vgg16

Koitka, S., & Friedrich, C. M. (2016, September 5-8). *Traditional feature engineering and deep learning approaches at medical classification task of imageCLEF 2016*. In: K. Balog, L. Cappellato, N. Ferro, & C. Macdonald (Eds.), Proceedings of the Conference and Labs of the Evaluation Forum (vol. 1609, pp. 304-317), Évora, Portugal.

Özüpak, Y. (2024). Detection of Malaria with Convolutional Neural Network (CNN) Architectures Using Cell Images. *Cukurova University Journal of the Faculty of Engineering*, *39*(1), 197-210. https://doi.org/10.21605/cukurovaumfd.1460434

Pacal, I. (2023). A Vision Transformer-based Approach for Automatic COVID-19 Diagnosis on Chest X-ray Images. *Journal of the Institute of Science and Technology*, *13*(2), 778–791. https://doi.org/10.21597/jist.1225156

Rajpurkar, P., Irvin, J., Zhu, K., Yang, B., Mehta, H., Duan, T., Ding, D., Bagul, A., Ball, R. L., Langlotz, C., Shpanskaya, K., Lungren, M. P., & Ng, A. Y. (2017). CheXNet: Radiologist-Level Pneumonia Detection on Chest X-Rays with Deep Learning. https://doi.org/10.48550/arXiv.1711.05225

Ravi, D., Wong, C., Deligianni, F., Berthelot, M., Andreu-Perez, J., Lo, B., & Yang, G.-Z. (2017). Deep Learning for Health Informatics. *IEEE Journal of Biomedical and Health Informatics*, *21*(1), 4-21. https://doi.org/10.1109/jbhi.2016.2636665

Salehinejad, H., Valaee, S., Dowdell, T., Colak, E., & Barfett, J. (2018, April 15-20). *Generalization of Deep Neural Networks for Chest Pathology Classification in X-Rays Using Generative Adversarial Networks*. In: Proceedings of the IEEE International Conference on Acoustics, Speech and Signal Processing (ICASSP) (pp. 990–994), Calgary, AB, Canada. https://doi.org/10.1109/ICASSP.2018.8461430

Singh, S., & Tripathi, B. K. (2022). Pneumonia classification using quaternion deep learning. *Multimedia Tools and Applications*, *81*, 1743–1764. https://doi.org/10.1007/s11042-021-11409-7

Toğaçar, M., Ergen, B., Cömert, Z., & Özyurt, F.(2020). A deep feature learning model for pneumonia detection applying a combination of mRMR feature selection and machine learning models. *IRBM*, *41*(4), 212–222. https://doi.org/10.1016/j.irbm.2019.10.006

Varshni, D., Thakral, K., Agarwal, L., Nijhawan, R., & Mittal, A. (2019, February 20-22). *Pneumonia Detection Using CNN based Feature Extraction*. In: Proceedings of the IEEE International Conference on Electrical, Computer and Communication Technologies (ICECCT) (pp. 1–7), Coimbatore, India. https://doi.org/10.1109/ICECCT.2019.8869364

Vaswani, A., Shazeer, N., Parmar, N., Uszkoreit, J., Jones, L., Gomez, A. N., Kaiser, Ł, Polosukhin, I.(2017, December 4-9). *Attention is all you need*. In: I. Guyon, U. Von Luxburg, S. Bengio, H. Wallach, R. Fergus, S. Vishwanathan, & R. Garnett (Eds.), Proceedings of the Advances in Neural Information Processing Systems 30 (NIPS 2017), Long Beach CA. https://doi.org/10.48550/arXiv.1706.03762

Wang, X., Peng, Y., Lu, L., Lu, Z., Bagheri, M., & Summers, R. M. (2017, July 21-26). *ChestX-ray8: Hospital-scale Chest X-ray Database and Benchmarks on Weakly-Supervised Classification and Localization of Common Thorax Diseases*. In: Proceedings of the IEEE Conference on Computer Vision and Pattern Recognition (CVPR) (pp. 3462-3471). https://doi.org/10.1109/CVPR.2017.369

Zhou, D., Kang, B., Jin, X., Yang, L., Lian, X., Jiang, Z., Hou, Q., & Feng, J. (2021). Deepvit: Towards deeper vision transformer. https://doi.org/10.48550/arXiv.2103.11886

Designing of 0.9 MWp Solar Power System Project for Kastamonu University

Coskun KARATAS[1] Secil KARATAY[1*] Osman CICEK[1]

[1] Kastamonu University, Department of Electrical Electronics Engineering, Kastamonu, Türkiye

Keywords	Abstract
Solar System PV System Grid-Connected PV System Power Plant Renewable Energy	Today, with increasing consumption costs, costs and needs in the field of energy are increasing exponentially. In this study, a Solar Power System project has been designed at Kastamonu University in order to meet the increasing demand for electrical energy and because it is more advantageous than other power plants, has a shorter depreciation period and a shorter installation and commissioning time. Solar Energy Systems, or Solar Power Systems are cutting-edge devices made to capture solar radiation and transform it into electrical energy that can be used. Solar Power Systems are essential for creating a greener and more sustainable energy landscape as the world community continues to emphasize sustainability. It is envisaged to use 8 inverters with 1632 panels on various roofs within the Kastamonu University campus area in order to supply the energy demand. Energy costs, power plant installation fees, depreciation process and exemptions are also cost within the scope of this study. It is concluded that approximately one third of the energy needs of Kastamonu University will be met with the proposed project.

1. INTRODUCTION

Electricity is a necessity for both daily living and the energy sector. Electrical energy is a crucial prerequisite in order to address the majority of human demands and to further improve technology worldwide. The production of resources required to meet necessities and the advancement of humankind are both significantly impacted by the absence of electricity. From the start of the 21st century to the present, the global and national energy landscapes have been impacted by advancements in the energy industry, rising living standards, and an exponential expansion in the global population. The energy industry has been considerably spurred by rising global temperatures, damaging ecosystems, excessive use, and changing climate patterns. According to researches, the world's energy needs are expected to increase and non-renewable energy resources will start to run out after around 2040. Natural resources are utilized to provide sustainable and ecologically friendly energy through renewable energy sources. To supply the energy demands of civilization, these resources make use of natural processes like solar, wind, water, geothermal, and bioenergy (Weiss, 1962; Park & Allaby, 2017). One of the most important of these resources is solar energy. Solar energy is a technology that uses solar radiation to create electrical energy. The solar radiation sun is converted into electricity by solar panels, making them an environmentally benign energy source. By lowering carbon emissions, this technology not only distinguishes itself as an unstoppable substitute for fossil fuels but also aids in the battle against climate change. Renewable energy sources are crucial in order to achieve the goals of sustainable development and energy security (Foster et al., 2009; Nelson, 2011).

Solar Power Systems provide a clean and sustainable substitute for conventional energy sources by using the sun's abundant and renewable energy to create electricity. Usually, these systems are made up of different

Coskun KARATAS, Secil KARATAY, Osman CICEK

tracking and mounting methods, inverters, and solar panels. Photovoltaic cells, which make up solar panels, absorb solar radiation and transform it into Direct Current (DC) electricity. Once the DC electricity is converted to Alternating Current (AC) by the inverter, it can be used in residences, commercial buildings, and industrial settings (Dunlop, 2012; Solanki, 2013; Cicek et al., 2019). Since Solar Power Systems do not release any greenhouse gases or other pollutants during the electricity production process, this is one of their main environmental benefits. With the cost of solar technology coming down and efficiency gains driving widespread adoption, solar power is becoming a more practical and affordable way to meet the world's expanding energy needs while reducing its environmental impact. Solar Power Systems are essential for creating a greener and more sustainable energy landscape as the world community continues to emphasize sustainability (Duffie & Beckman, 2013).

In the literature, there are a lot of studies dealing with the solar photovoltaic (PV) energy systems. Thomas et al. (2007) has dealt with the technology, plans, administration, and regulations that support these fascinating advancements in solar PV electricity. In the related study, it is suggested that even though Very Large-Scale photovoltaic (VLS-PV) technology looks highly promising, a comprehensive life cycle analysis of the technology is urgently needed if it is to become truly sustainable. VLS-PV is a photovoltaic power generation system that has capacities ranging from several megawatts to gigawatts. In Zheng and Kammen (2014), a thorough dataset covering the years 2000–2012 is constructed for the PV industries in China, Japan, Germany, and the United States in order to build up a model that explains the relationships between innovation, manufacturing, and market dynamics. In the related study, it is concluded that a change in policy in the studied countries is required to fortify the industry by striking a balance between the enthusiasm and emphasis on market forces and a greater commitment to sponsoring research and development. In Ma et al. (2014), five-parameter model has been chosen for modeling PV system power generation for an island in Hong Kong. The model's simulation performance has been compared to that of other models and outside testing have been used to further validate it. This study shows that the PV simulation model created for the study is straightforward but incredibly useful for PV system engineers to precisely forecast the power generation of PV systems outdoors. In Lupangu and Bansal (2017), a variety of modeling, scaling, and maximum power point tracking (MPPT) techniques have been reviewed for grid-connected PV systems to operate efficiently. Energy regulations, different cell technologies, MPPT and converter/inverter technology, energy management and scheduling strategies, dependability, power quality, and control system concerns are among the technological obstacles that have been reviewed and discussed in the related study. In Soomar et al. (2022), the most recent developments in solar power generation equipment are examined to serve as a resource for global decision-makers involved in solar plant construction. This study suggests that the major objectives of optimization techniques are to lower emissions, operating and maintenance expenses, and investment in order to increase system reliability. In Aksoy and Ispir (2023), a PV system with a 300 kWp installed power is developed using PVsyst software in Konya province, Turkey. The system's ability to generate power has been measured and contrasted with various PV systems. The findings in this study have showed that the ratios of income values to investment costs have been 253%, 244.77%, and 126.6%. For small and medium-sized PV systems, it is concluded that mono-Si and poly-Si are quite economically feasible; however, a-Si is still not practicable because of its lower efficiency and higher prices. Benjamins et al. (2024) discusses and assesses the many potential environmental effects of introducing floating photovoltaic arrays into aquatic (freshwater and marine) environments based on the current status of floating photovoltaic technology and the known effects of related businesses. It has been suggested in this study that the utilization of Floating photovoltaic test sites will be essential to establish suitable environmental mitigation and monitoring strategies for the industry, society, and environment.

Multidisciplinary stakeholders with a range of goals and objectives are involved in the complex process of distributed solar PV design and management in buildings. These goals and objectives include achieving higher solar insolation in a specific location, producing energy efficiently, and operating and maintaining the PV system economically. Many studies that present the design and calculation of solar PV systems for buildings have been published in the literature in recent years. Similar to this study, in Sharma and Gidwani (2017), a study for solar PV system has been designed and calculated for Hostel buildings in the campus of Rajasthan Technical University (RTU), Kota, Rajasthan, India. According to this study, a 234 kW grid-connected solar photovoltaic system can provide enough electricity to offset its use, lessen reliance on the grid, and minimize energy consumption from grid supply. In another study Hamoodi et al. (2021), a solar PV system has been

designed and sized for Qayyarah General Hospital south of Mosul city. When the PV*SOL program and mathematical computations have been compared, it has been observed that the solar system's components are roughly identical. Also, in a study Kavitha et al. (2021) similar to this study, a PV system has been designed with PV*SOL simulation software the results have been then utilized to determine and adjust the projected system's design. As a consequence of the simulation analysis in this study, the global irradiance of the Dual Axis Solar Tracking System is found to be 1.3 times greater than that of the other tracking systems. Some PV tools have been tested and compared in Milosavljević et al. (2022). By evaluating the most popular PV tools, this study explores which PV software is most suited for designing of PV systems. Unlike our study, it has been observed that the lowest deviation of the simulation results compared to experimental measurements has been obtained by SolarPro and PVGIS. Similar to our study, Muqeet et al. (2022) have dealt with the campus microgrids' energy management system in detail. This study also presents the research directions and related difficulties that should be taken into account in future studies on microgrid scheduling. Similar to our study, electric energy cost with using renewable energy sources in Gökceada, Turkey has been calculated in Demiroren and Yilmaz (2010). Differently, the HOMER program has been used to determine the best system design for a hybrid or non-hybrid renewable energy system in this study. It has been observed that energy costs can be lowered by selling the excess energy that is produced when the energy source is larger than the load to the grid. The findings of the simulation show that Gökceada has lower energy costs for wind energy installations. In

The Environmental Assessment Report (EIA) published by the Republic of Turkiye Ministry of Energy and Natural Resources in Turkey focuses on the environmental impacts related to the construction and operation activities of solar power plants (URL1, 2022). Solar power plants contribute to the use of solar energy instead of fossil fuels and the reduction of greenhouse gas emissions. In this project designed for Kastamonu University, it is planned to prevent 570.553 kg of carbon dioxide emissions annually. According to the EIA report (EIA, 2024), electricity production in power plants with a capacity of up to 1.000 kW based on renewable resources is exempt from the obligation to obtain a license. According to 2023 data, 679 solar power plants are actively operating, providing a total installed power of 8.335 MW. 37 of these power plants are licensed and 642 are exempt from license. Solar power plants with a project area of 2 hectares or more or an installed power of 1 MW or more (excluding roof and facade systems) are considered exempt from the EIA Regulation. The designed project in this study is exempt from the EIA regulation since the project area is larger than 2 hectares and the installed power is 0.9 MWp.

2. SOLAR ENERGY POTENTIAL IN TURKEY AND KASTAMONU

Turkey is located in a region called the sun belt, which is rich in solar energy. Turkey, which has a high solar energy potential due to its geographical location, has an average annual total sunshine duration of 2.640 hours (total of 7,2 hours per day) and an average total radiation intensity of 1.311 kWh/m²-year (total of 3.6 kWh per day). m²). The solar energy potential is 380 billion kWh/year (EIGM, n.d.). In 2023, 679 solar power plants are actively operating, providing a total installed power of 8.335 MW (URLx, n.d.) (EA, n.d.). In Figure 1, the Total Solar Radiation is shown for all of Turkiye.

Kastamonu located in the Western Black Sea part of the Black Sea Region has a surface area of 13.108,1 km². Total energy consumption in Kastamonu with a population of 372.633, is 778.497 MWh. With this rate, the province has a rate of 0.39% in energy consumption in Turkey. While the installed power (production) of power plants in the province is 41 MW, the installed power share in energy in Turkey is 0.06%. The only source of energy production in the province is hydroelectric power plants (Arslan, 2016). In Figure 2, total solar radiation is given for Kastamonu. Figure 3 shows global radiation values in KWh/m2-day, sunshine times in hours and PV type-area-produced energy in kWh-year for Kastamonu.

When it comes to total sun radiation, the Black Sea region, which includes Kastamonu, is one of the less promising areas. When Figure 2 is investigated, it is observed that the annual total solar radiation in no region within the borders of Kastamonu is more than 1650 kWh/m². The annual solar radiation rate throughout the province is mostly at the level of 1400-1450 kWh/m². This situation shows that the potential for solar energy production in Kastamonu is quite low on a provincial basis.
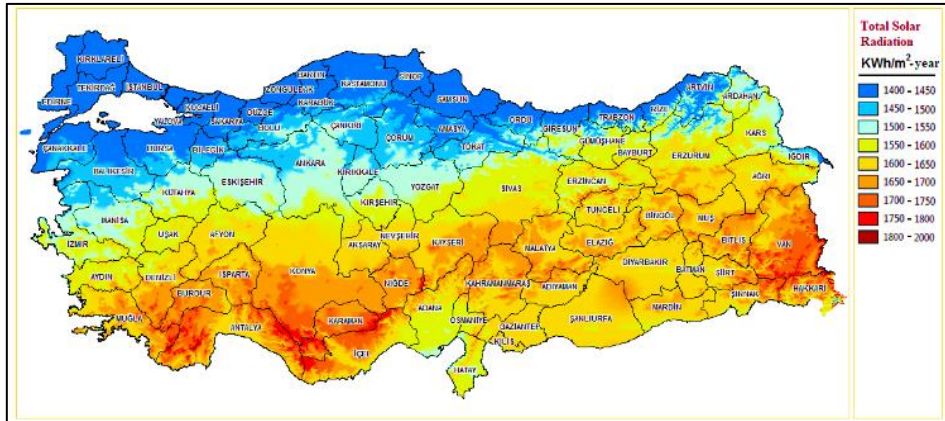
Figure 1. *Solar energy potential atlas for Turkiye (Mudurlugu, n.d.)*
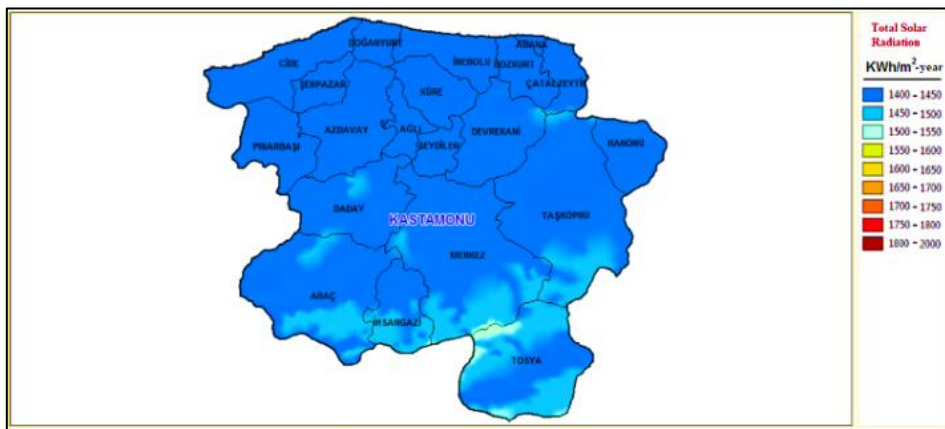
Figure 2. *Solar energy potential atlas for Turkiye (Mudurlugu, n.d.)*
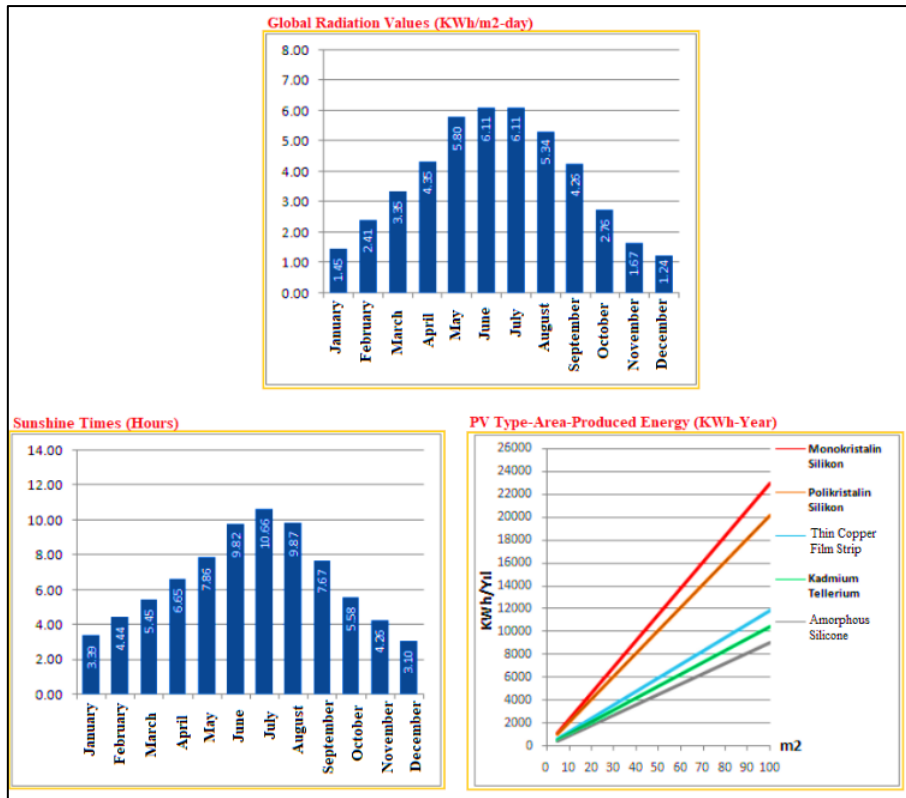
Figure 3. *Global radiation values, sunshine times and PV type-area-produced energy (Mudurlugu, n.d.)*

3. THE DESIGN

Solar Power Systems technologies hold an important place among clean and sustainable energy sources. Universities play an important role in the development and implementation of these technologies. Solar Power Systems project design allows researchers to evaluate solar energy potential, perform system design and optimization, plan solar panel placement and work on energy storage solutions. These projects have the potential to increase society's access to sustainable energy by both contributing to academic knowledge production and enabling the development of new technologies for industrial applications. In this context, universities that focus on Solar Power Systems are of great importance for both scientific progress and social benefit. In this study, 0.9 MWp Solar Power System project is designed to meet the increasing energy needs of Kastamonu University from renewable energy sources. The roof area of the sports complex that can benefit from maximum solar radiation throughout the day is selected for this purpose. In Figure 4, the view of the project aligned to north, the west-oriented and the east-oriented panel placement of the roof are given for this roof, respectively. The panels selected within the scope of the study are PERC monocrystalline panels. Modified silicon cells with an extra layer on the back are called PERC panels. This additional layer can provide more energy by reflecting wasted light back across the n-type and p-type junctions. Furthermore, by keeping longer wavelengths from producing heat and reducing rear recombination, this reflecting surface further improves the performance of the cell. The electrical properties of the panel selected within the scope of the study are given in Table 1.
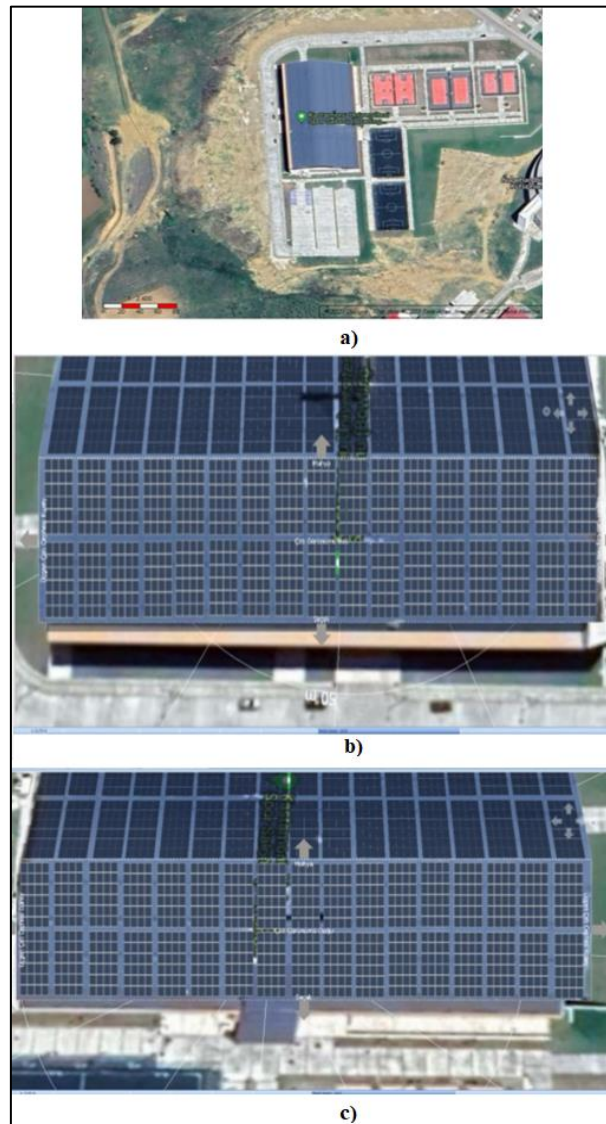
Figure 4. a) the view of the project aligned to north, b) the west-oriented panel placement of the roof, c) east-oriented panel placement of the roof

Table 1. *Electrical properties of the chosen panel*

Maximum Power (P_{max})	545 WP
Module Efficiency	21,29
Maximum Power Voltage (V_{mp})	31,3
Maximum Power Current (I_{mp})	17,42
Open Circuit Voltage (V_{OC})	37,7
Short Circuit Current (I_{SC})	18,45
Power Tolerance	0~+5 W
Max System Voltage	1500V DC
Operating Temperature Range	-40°C~85°C
Max Series Fuse Current	30A

Three-Phase inverter is used in the project. Devices called three-phase inverters are used to convert three phases of direct current (DC) electricity into alternating current (AC). They are frequently employed in commercial and industrial settings where three-phase electricity is necessary. Some features such as power capacity, efficiency, protection features, monitoring and control, grid connectivity, enclosure and cooling and modularity and scalability are typical in three-phase inverters. The technical properties of the chosen inverter is given in Table 2.

Table 2. *Technical properties of the chosen inverter*

Maximum Input Voltage (V)	1100
Minimum Input Voltage (V)	200
Operating Voltage Range (V)	550 ~ 850
Maximum Input Current (A)	26
Maximum Short-Circuit Current (A)	40
Rated Output Power (kW)	100
Maximum Output Current (A)	166,7
Maximum Efficiency (%)	98,6
Operating Ambient Temperature Range (°C)	-30 ~ 60
Communication	RS485 / USB / Wi-Fi+LAN /

As the number and power of panels increases, the cost decreases. In Table 3, the detailed cost calculation of the project on a unit basis is given in Dollars.

Table 3. *Detailed cost calculation based on piece*

	PIECE	PRICE	TOTAL
Inverters	8	$3.957,83	$31.662,87
PV Panels	1632	$180,72	$294.940,06
PV Cable		$133,98	
Transformer	1	$17.978,83	$17.978,83
Roof Mounting Apparatus		$5.328,21	Note: 1,2m $7
Cable Tray*			
Solar Power System Panel*			
36KV Breaker Cell*			
XLPE CABLE after Transformer*			
Profile Foot and Spacer Holder Apparatus*			
Workmanship*			
Grand Total		$344.581,7662	

*Above, prices of prices that may vary depending on the project are left blank.

According to the statement of the Republic of Turkiye Ministry of Energy and Natural Sources, 648 Kg of carbon emission measurement is taken as basis for 1 MWh of solar energy (URL1, 2022). The European Union Carbon Emission price is 86,77 €/Ton in 2023 and increases by 2-3 € every year. Today it corresponds to 95 dollars. It is estimated to be $100 next year. So, 1 MWh = 648 Kg 100 x 0,648 = $64,8. When the dollar exchange rate is taken as 32,09, it is 64,8 x 32,09 = 2.079,432 ₺/1 MWh. The cost and depreciation amounts calculated in the project are also given in Table 4. When calculating Table 4, the hourly production of the power plant installed power has been taken as 889,44 kWp and the current dollar exchange rate has been taken as 28,90 during the time period when the study has been carried out. With the current dollar exchange rate, the roof installation cost of the power plant is calculated as 15.422.889 ₺.

Table 4. Cost and depreciation account values

	ANNUAL	**MONTHLY**	**DAILY**	**HOURLY**
Average electricity partial consumption of the campus (₺)	13.365.508	1.113.792,41	36.617,8	1.525,7
Average electricity partial consumption amount of the campus (kWh)	3.091.695,82	257.641,33	8.470,40	352,93
Average electricity production amount of the power plant (kWh)	955.272,57	79.606,05	2.653,53	110,56
Average electricity production amount of the power plant (₺)	3.362.559,44	280.213,29	9.340,42	389,17
Kastamonu radiation value	1.364 kWh/m^2			
Electricity sales price*	3,52 ₺/kWh			
Power plant roof installation cost	$600			
Loss production power of the power plant	700,35 kWh			
Annual Electricity consumption coverage	30,89%			
	2024	2025	2026	
Central Bank (OVP) estimated dollar exchange rate	36,78	43,94	47,80	
Earnings of the power plant (₺)	4.672.945	5.582.631	6.073.049	Total Earnings
				16.328.626

*Electricity Sales Price= 3,52 ₺ (January-Energy Market Regulatory Authority (EMRA))

The simulation results using the PV*SOL application are presented in the next section. PV*SOL is a software application used for PV system design and simulation that was developed by Valentin Software. Users of PV*SOL can precisely calculate and assess how solar PV systems function in a range of scenarios.

4. SIMULATION OF THE PROJECT WITH PV*SOL APPLICATION

PV*SOL is an all-inclusive solution for solar PV system design and analysis for engineers, installers, and consultants involved in the design and execution of solar energy projects. Users can design PV systems by defining characteristics including site, system size, orientation, tilt angle, shading objects, and PV module and inverter types. The software makes use of intricate algorithms to model the PV system's performance over time while accounting for variables including temperature, shade, solar radiation, and electrical losses. Energy yields, feed-in tariffs, self-consumption rates, payback durations, and return on investment can all be calculated by users performing financial analysis of the PV system. PV*SOL also provides PV module optimization in terms of tilt angle, orientation, and layout. It also helps choose the best components based on cost and performance standards. In this study, the designed project is simulated using the PV*SOL application (PV*SOL, n.d.). Inverter configurations 1 and 2 for the bay window roof area east and west are presented in Figure 5a and 5b, respectively. A device that changes Direct Current (DC) in an electrical circuit to Alternating Current (AC) is arranged in an inverter configuration. This configuration is frequently utilized in numerous applications, including industrial power systems, electric automobiles, and solar energy systems. A typical inverter will efficiently convert energy and adjust to the demands of AC power.

Figure 5. *Inverter configurations for **a)** bay window-roof area east and **b)** bay window-roof area west*

Figure 6 shows the monthly generation forecast for the AC grid. When Figure 6 is investigated, it is observed that the generation forecast for Kastamonu is maximum in June and minimum in December. Similarly, the generation forecast for Kastamonu is highest in summer and least in winter. These forecasts are also correlated with the global radiation values and sunshine times in Figure 3. Looking at Figure 3, it is observed that both global radiation values and sunshine times are larger in June and July, as in Figure 6. Also, similarly, the global radiation values and the sunshine times have the greatest values in summer and have the smallest values in winter. It is observed that the simulation results obtained in this study are compatible with global radiation values and the sunshine times. The energy consumption of Kastamonu University campus in 2022 was approximately 3092MWh. Approximately, 1260MWH of energy can be generated annually in the simulated project that is observed in Figure 6. Thus, one third of the energy needs of Kastamonu University will be met with the designed project.

In Figure 7, global radiation, PV generator output and energy and performance ratio values are given for the bay window-roof area east and the bay window-roof area west. When the two roof areas are compared with each other, it is observed that the PV generator energy values are greater for the west bay window-roof area.
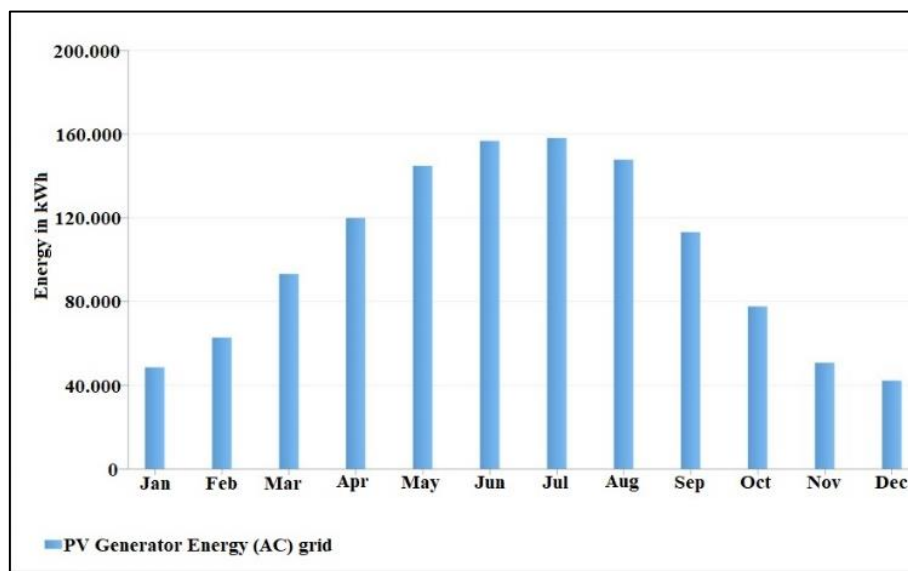
Figure 6. *Monthly generation forecast for the AC grid*

In this study, PV*SOL software is used to more accurately and consistently anticipate energy generation from PV systems. Through the integration of meteorological data, geographical factors, and sophisticated modeling algorithms, PV*SOL enables precise forecasting of solar irradiance and PV system performance under a range of environmental circumstances. The study aims to evaluate the prediction accuracy taking into account the position, tilt angle, orientation of the modules, shading, and other aspects. This study also aims to provide valuable information for optimizing PV system design and operational planning through comprehensive analysis and validation with real-world data.

Bay window-roof area east	
PV Generator Output	444,72 kWp
PV Generator Surface	2.089,28 m²
Global Radiation at the Module	1513,29 kWh/m²
Global Radiation on Module without reflection	1534,05 kWh/m²
Performance Ratio (PR)	88,62 %
PV Generator Energy (AC grid)	604874,07 kWh/Year
Spec. Annual Yield	1360,12 kWh/kWp
Bay window-roof area west	
PV Generator Output	444,72 kWp
PV Generator Surface	2.089,28 m²
Global Radiation at the Module	1526,66 kWh/m²
Global Radiation on Module without reflection	1547,39 kWh/m²
Performance Ratio (PR)	88,50 %
PV Generator Energy (AC grid)	609312,18 kWh/Year
Spec. Annual Yield	1370,10 kWh/kWp

Figure 7. *PV generator output, performance ratio, PV generator energy values for the bay window-roof area east and the bay window-roof area west*

5. CONCLUSION

In this study, a 0.9 MWp Solar Power System is designed to meet the energy demand of Kastamonu University Campus. A sports complex building with a roof area of 4.178,56 m² is chosen as the installation site. Annual production forecasts are simulated with the PV*SOL application. It has been noted that the generation forecast for Kastamonu peaks in June and troughs in December. Additionally, there is a correlation between these forecasts and Kastamonu's sunshine hours and global radiation values. It is concluded that approximately one third of the energy needs of Kastamonu University, whose annual consumption is 30,89% of the 3092 MWh consumption could be met by the designed system. It is concluded that the designed system will amortize itself in approximately three years. These results have important ramifications for encouraging the broad use of solar energy as an affordable and sustainable replacement for traditional power sources.

AUTHOR CONTRIBUTIONS

Methodology, all authors; writing-reviewing, S.K. and O.C.; editing, S.K.; conceptualization and software, C.K. All authors have read and legally accepted the final version of the article published in the journal.

ACKNOWLEDGEMENT

CONFLICT OF INTEREST

The authors declare no conflict of interest.

REFERENCES

Aksoy, M. H., & Ispir, M. (2023). Techno-Economic Feasibility of Different Photovoltaic Technologies. *Applied Engineering Letters*, *8*(1), 1-9. https://doi.org/10.18485/aeletters.2023.8.1.1

Arslan, F. (2016, May 20-21). *The Renewable Energy Potential in Kastamonu*. In: E. Turan, A. Çağlar, O. Y. Bayraktar, G. Sağlam Çitoğlu (Eds.), Proceedings of the 1st International Abana Symposium, (pp. 321-335), Kastamonu.

Benjamins, S., Williamson, B., Billing, S.-L., Yuan, Z., Collu, M., Fox, C., Hobbs, L., Masden, E. A., Cottier-Cook, E. J., & Wilson, B. (2024). Potential environmental impacts of floating solar photovoltaic systems. *Renewable and Sustainable Energy Reviews*, *199*, 114463. https://doi.org/10.1016/j.rser.2024.114463

Cicek, O., Millad, M. A. M., & Erken, F. (2019). Energy Prediction Based on Modelling and Simulation Analysis of an Actual Grid-Connected Photovoltaic Power Plant in Turkey. *European Journal of Technique*, *9*(2), 159-174. https://doi.org/10.36222/ejt.593250

Demiroren, A., & Yilmaz, U. (2010). Analysis of change in electric energy cost with using renewable energy sources in Gökceada, Turkey: An island example. *Renewable and Sustainable Energy Reviews*, *14*(1), 323-333. https://doi.org/10.1016/j.rser.2009.06.030

Duffie, J. A., & Beckman, W. A. (2013). *Solar Engineering of Thermal Processe.* (Fourth Edition). Hoboken: John Wiley & Sons.

Dunlop, J. P. (2012). *Photovoltaic Systems* (Third Edition). Illinois: American Technical Publishers.

EIA (2024, June 11). Short-Term Energy Outlook. Texas. U.S. Energy Information Administration. https://www.eia.gov/outlooks/steo/

EIGM (n.d.). Güneş Enerjisi Potansiyel Atlası. Enerji İşleri Genel Müdürlüğü. (Accessed:03/06/2024) https://gepa.enerji.gov.tr/MyCalculator/

Foster, R., Ghassemi, M., & Cota, A. (2009). *Solar Energy: Renewable Energy and the Environment*. Boca Raton: CRC Press Taylor & Francis. https://doi.org/10.1201/9781420075670

Hamoodi, A. N. H., Abdulla, F. S., & Mezher, S. (2021, September 24-25). Design and sizing of solar plant for Qayarah general Hospital and simulation with the PV-SOL program. *NTU Journal of Engineering and Technology*, *1*(1), 67-71. https://doi.org/10.56286/ntujet.v1i1.89

Kavitha, M., Immanuel, D. G., Rex, C. R. E. S., Meenakshi, V., Pushpavalli, M., Singari, S., & Baskaran, V. (2021). *Energy Forecasting of Grid Connected Roof Mounted Solar PV Using PV*SOL*. In: Proceedings of the 2021 International Conference on Innovative Computing, Intelligent Communication and Smart Electrical Systems (ICSES), (pp. 1-6). Chennai, India. https://doi.org/10.1109/ICSES52305.2021.9633888

Lupangu, C., & Bansal, R. C. (2017). A review of technical issues on the development of solar photovoltaic systems. *Renewable and Sustainable Energy Reviews*, *73*, 950-965. https://doi.org/10.1016/j.rser.2017.02.003

Ma, T., Yang, H., & Lu, L. (2014). Solar photovoltaic system modeling and performance prediction. *Renewable and Sustainable Energy Reviews*, *36*, 304-315. https://doi.org/10.1016/j.rser.2014.04.057

Milosavljević, D. D., Kevkić, T. S., & Jovanović, S. J. (2022). Review and validation of photovoltaic solar simulation tools/software based on case study. *Open Physics*, *20*(1), 431-451. https://doi.org/10.1515/phys-2022-0042

Muqeet, H. A., Javed, H., Akhter, M. N., Shahzad, M., Munir, H. M., Nadeem, M. U., Bukhari, S. S. H., & Huba, M. (2022). Sustainable Solutions for Advanced Energy Management System of Campus Microgrids: Model Opportunities and Future Challenges. *Sensors*, *22*(6), 1-26. https://doi.org/10.3390/s22062345

Nelson, V. C. (2011). *Introduction to Renewable Energy*. A. Ghassemi (Eds.), Energy and the Environment. Boca Raton: CRC Press Taylor&Francis. https://doi.org/10.1201/9781439891209

Park, C., & Allaby, M. (2017). A Dictionary of Environment and Conservation (Third Edition). Oxford: Oxford University Press. https://doi.org/10.1093/acref/9780191826320.001.0001

PV*SOL. (n.d.). PV*SOL. (Accessed:14/03/2024) https://pvsol.software/en/

Sharma, R., & Gidwani, L. (2017, April 20-21). *Grid connected solar PV system design and calculation by using PV*SOL premium simulation tool for campus hostels of RTU Kota*. In: Proceedings of the 2017 International Conference on Circuit, Power and Computing Technologies (ICCPCT), (pp. 1-5). Kollam, India. https://doi.org/10.1109/ICCPCT.2017.8074315

Solanki, C. S. (2013). So*lar Photovoltaic Technology and Systems: A Manual for Technicians, Trainers and Engineers*. Delhi: PHI Learning.

Soomar, A. M., Hakeem, A., Messaoudi, M., Musznicki, P., Iqbal, A., & Czapp, S. (2022). Solar Photovoltaic Energy Optimization and Challenges. *Frontiers in Energy Research*, *10*, 1-18. https://doi.org/10.3389/fenrg.2022.879985

Thomas, C., Jennings, P., & Singh, D. (2007*). New Markets for Solar Photovoltaic Power Systems*. In: P. Jennings, G. Ho, K. Mathew, & C. V. Nayar (Eds.), Proceedings of the International Conference on Renewable Energy for Sustainable Development, Vol. 941, Issue: 1, (pp. 142-153). Fremantle, Western Australia. https://doi.org/10.1063/1.2806080

URL1 (2022, June 29). Çevresel Etki Değerlendirmesi Yönetmeliği. Official Journal of Turkish Republic (Resmî Gazete), Number: 31907.

URL2 (n.d.). Güneş Enerji Santralleri. Enerji Atlası. (Accessed:03/04/2024) https://www.enerjiatlasi.com/gunes/

Weiss, P. (1962). Renewable Resources, A Report to the Committee on Natural Resources of the National Academy of Sciences-National Research Council. Washington: National Academy of Science.

Zheng, C., & Kammen, D. M. (2014). An innovation-focused roadmap for a sustainable global photovoltaic industry. *Energy Policy*, *67*, 159-169. https://doi.org/10.1016/j.enpol.2013.12.006

Evaluating the Spatial-Temporal Dynamics of Urbanization in Prefecture Cities of China Using SNPP-VIIRS Nighttime Light Remote Sensing Data

Neel Chaminda WITHANAGE[1,2*]   Jingwei SHEN[2]

[1] University of Ruhuna, Faculty of Humanities and Social Sciences, Department of Geography, Matara 81000, Sri Lanka
[2] Southwest University, School of Geographical Sciences, Bebei District 400715, Chongqing Province, China

Keywords	Abstract
China Nighttime Light Prefectures Cities Remote Sensing SNPP-VIIRS Urbanization	Ensuring the well-being of urban communities hinges on sustainable urban planning strategies informed by current data, particularly in China since urbanization has been one of the most significant demographic shifts in recent decades. Therefore, our research aimed to evaluate the spatio-temporal dynamics of urbanization and sub urbanization across prefecture and provincial levels in China by utilizing consistent SNPP-VIIRS-like and NPP-VIIRS nighttime data spanning the years 2000 to 2020. The k-means method was applied to derive urban and sub urban features from above datasets. The findings uncovered a significant expansion of urban entities at the prefecture level, escalating from 16,209 km^2 to 89,631 km^2 over the specified period showing a 5% growth. Among five main urban agglomerations, the Yangtze River Delta stands out with the highest urbanization rate, witnessing a remarkable expansion of urban entities from 2,684 km^2 to 41,465 km^2. This growth reflects an average growth rate of 72.2% per annum. The analysis revealed that the overall area of suburbs expanded from 59,151 km^2 to 120,339 km^2 between 2012 and 2020 indicating a proportional growth rate ranging from 0.4% to 1.9%. The peak growth rate of suburbs was recorded between 2012 and 2014, reaching 18%. Guizhou, Hunan, and Hubei provinces have exhibited growth rates of 334%, 258%, and 246% respectively while Beijing, Guangdong, Tianjin, and Shanghai have experienced relatively low growth rates of 50%, 56%, 46%, and 17%. The analysis of urban growth with GDP, population, and electricity consumption revealed an inverse relationship during the specified period. Therefore, the findings of this research can provide immense support to sustainable urban planning initiatives at both the provincial and prefecture-level cities in China. The findings can assist city planning authorities in making informed decisions regarding optimizing resource distribution, all while prioritizing the preservation of ecological footprint within urban environments. Also, the limitations addressed in our study must be taken into account in future research works aimed at deriving reliable urban extraction results using nighttime light remote sensing data.

1. INTRODUCTION

In recent times, urbanization has experienced substantial growth, becoming a notable spatial phenomenon worldwide. According to the UN-Habitat report by 1950, approximately one-fourth of the global population resided in cities (Habitat et al., 2006). As of the present day, that figure has doubled, and currently, half of the world's total population resides in cities (Thapa & Murayama, 2009). The UN World Population Prospect (2019) has reported that by 2030, approximately 57% of the total population of the global south will reside in cities. Spatio-temporal changes in urban growth and related aspects have been monitored and evaluated in various countries and regions using geo-informatics techniques, especially remote sensing coupled with

various machine learning techniques. This approach allows for the derivation of reliable and consistent urban information (Schneider et al., 2010; Zhang & Seto, 2011; Zhou Y. et al., 2014).

Continuous assessment of city growth and geographical patterns is essential for understanding and addressing the exacerbation of escalating socio- environmental issues in urban environments, including traffic congestion, urban crimes, air pollution, and ecological degradation (Thapa & Murayama, 2009). Additionally, understanding the geographical dynamics in urban land use and land cover (LULC) is vital for long-term resource management perspectives (Wijesinghe & Withanage, 2021; Withanage et al., 2024). In this context, multi-temporal and multi-spectral satellite information serves as an effective source for predicting and simulating urban expansion and growth. Therefore, geo-informatics techniques and tools can play a decisive role in sustainable urban planning initiatives, facilitating a win-win situation for both urban development and environmental conservation efforts (Fan et al., 2014). China has undergone rapid urbanization over the past two decades, leading to a diverse array of socio-environmental issues. Consequently, urban and regional planning authorities are actively seeking effective and reliable measures to overcome and mitigate the negative outcomes associated with the urbanization process. According to statistics from the population census in 2010, nearly 50% of the total population in China resided in cities (Lu et al., 2014). As urbanization rapidly progresses in China, farmlands and other land use classes in countryside areas surrounding urban areas are gradually being encroached upon by built-up areas. These land use classes are often delineated from urban areas and commonly referred to as "suburbs" in urban planning and related doctrines (Liu S. et al., 2022). Also, urbanization and sub urbanization have accelerated a diverse array of socioeconomic and environmental issues, affecting both urban and rural environments. Indeed, the demarcation of urban areas and suburbs, coupled with an understanding of their spatial and temporal patterns, plays a pivotal role in achieving sustainable resource management, especially in urban areas in China.

Impervious surfaces in cities are covered by various concrete structures, including roads and other transport networks, a diverse range of buildings such as houses, industrial plants, and other man-made structures that overlay the natural landscape (Zhou Y. et al., 2014; Zhang X. et al., 2020). The MODIS, Sentinel, and Landsat remote sensing images are commonly utilized to detect the geographical dynamics of impervious surfaces in cities. Indeed, evaluating only these structures does not provide an accurate picture of the urbanization process and dynamics. Assessing only these physical structures is inadequate for understanding the geographical evolution of human activity surfaces in the complex urban environment (Ellison et al., 2010). Because of the complex nature of human activities and land utilization in cities, relying solely on changes in impervious structures using multi-source remote sensing data is inadequate for urbanization monitoring (Grove et al., 2015). Indeed, Operational Line-scan System (OLS) nighttime light (NTL) images from the Defense Meteorological Satellite Program (DMSP) and the Suomi National Polar Partnership Visible Infrared Imaging Radiometer Suite (SNPP-VIIRS) NTL data provide a unique proxy for measuring urban dynamics, as they capture both impervious surfaces and human activity surfaces based on NTL brightness value (Imhoff et al., 1997; Xu et al., 2014).

In recent years, monitoring of urbanization and related phenomena, including city size dynamics, spatial structures, and the effect of urban growth on CO_2 emissions, has been a primary focus of research using nighttime light data in China. Most researchers have evaluated urban expansion using stable NTL data, while some have attempted to introduce correction techniques to improve the reliability of their assessments (Elvidge et al., 2009; Zheng et al., 2021). Past scholars have utilized a new generation of NTL data as well as new methods and techniques for urban area delineation and extraction (Liu Z. et al., 2012; Ma T. et al., 2012; Fan et al., 2014; Xu et al., 2014). Those methods included neighborhood statistics, NDVI, and local-optimized thresholds, which were used to extract urban areas based on pixel brightness variations of NTL images (Xiao et al., 2014; Ma T et al., 2015; Su et al., 2015; Shi et al., 2016). Another focal technique used by some researchers was k-means classification to extract built-up areas (Lin et al., 2019; Shi et al., 2023; Withanage et al., 2023). In their analysis, Tian and Qian (2021) endeavored to address the challenge of accurately identifying suburbs in China by leveraging multi source data and integrating multi-logistic regression (MLR) with geographically weighted regression techniques. Furthermore, Feng et al. (2020) employed a k-means algorithm to develop a methodology for delineating the urban-rural fringe in Beijing city, utilizing DMSP/OLS NTL data. Sun and Zhao (2018) endeavored to quantify and compare urban expansion across 13 cities within the Jing-Jin-Ji Urban Agglomeration. They scrutinized the relationship between urban structure and growth

from 1978 to 2015, uncovering considerable variations in expansion patterns attributable to political and other socioeconomic influences. Tian (2020) delineated the suburbs of Jiangsu by estimating spatial interactions through a regression model and a radiation model, evaluating such interactions at a grid level. Consequently, the suburban expansion of Jiangsu over the span of 20 years was found to be noteworthy. Dai et al. (2021) assessed the spatial mutation characteristics of the urban fringe area in Jiangyin city, China by integrating multi-index fusion and wavelet transform techniques. They corroborated their findings by comparing them with results derived from other studies employing the information entropy model and the comprehensive index model. Huang et al. (2020) introduced a quantile method to extract the structure of urban-suburban-rural areas utilizing consistent NTL data from DMSP/OLS. They applied this approach in the Beijing-Tianjin-Hebei region of China using the NTL threshold. Jia et al. (2021) employed an urban-rural gradient approach to investigate the impact of urbanization on land surface phenology across 343 cities in China. They utilized VIIRS Land Surface Phenology in conjunction with MODIS Land Surface Temperature (LST) products for their analysis.

As the k-means algorithm was not commonly applied for delineating urban areas in complex urban environments, we have utilized it as a novel method for extracting both urban and suburban areas in China. This effort assessed the reliability and effectiveness of SNPP-VIIRS-like and SNPP-VIIRS NTL data for urban area identification, addressing this identical flaw. Using both datasets, we aimed to extract and evaluate the geographical dynamics of cities and suburban areas in both provincial and prefecture-level cities using data spanning the period from 2000 to 2020. We structured this paper into five sections. Section one is dedicated to the introduction, encompassing the rationale, objectives of the study, and literature survey. Section two describes the materials and methods, along with the study area description. The third section focuses on the results, with two subsections including urbanization and suburbanization in China. Section four delves into the discussion, comprising the role of SNPP-VIIRS data for urban mapping, the relationship between urban growth and socioeconomic growth, as well as limitations and future research focus. The final section is the conclusion.

2. MATERIALS AND METHODS

2.1. Study Area

China ranks as the world's fourth-largest country by land area, boasting diverse and extensive landscapes, climates, and ecosystems. Spanning from approximately 73.5°E to 135°E longitude and 4°N to 53.5°N latitude it encompasses a wide territory that showcases a wide range of geographical features and environmental conditions. The Country is bordered by the rugged terrain of the Himalayas and the Tibetan Plateau to the west. In the central and eastern regions, it features fertile plains, including the Yangtze River basin. The country also features diverse climatic zones, ranging from arid and semi-arid regions in the northwest to humid subtropical and tropical climates in the south. The country hosts maritime resources and shipping routes along its coastline, which stretches over approximately 18,000 km along the Pacific Ocean.

Urbanization in China has been a significant phenomenon, featuring accelerated growth and transformation. Over the last few decades, millions of people have migrated from the countryside to urban centers in search of better economic opportunities and lifestyles. This great migration has led to the growth of cities and the development of new cities across the country. Several causes have contributed to the rapid urban growth, including industrialization, economic reforms, and government policies aimed at promoting urban development. As a result, China now has some of the largest and most populous cities in the world, such as Shanghai, Beijing, and Guangzhou. As of 2021, the urbanization rate in China stood at 63.8%. In 2016, urban and suburban areas occupied approximately 2.15 million square kilometers, which is equivalent to a considerable portion of the country's total land area (He et al., 2017; Liu S. et al., 2022).

China has been divided into 23 provinces, 5 autonomous regions, 4 direct-controlled municipalities, and 2 Special Administrative Regions (SARs) for ease of administration. Guangxi, Inner Mongolia, Ningxia, Tibet, and Xinjiang are autonomous regions. Beijing, Chongqing, Shanghai, and Tianjin are designated as direct-controlled municipalities. Hong Kong, Taiwan, and Macau are designated as SARs (National Bureau of Statistics, 2021; Withanage et al., 2023). In China, prefectures are administrative divisions that are below the provincial level but above the county level. Prefectures typically encompass several counties. The number of prefectures in China can change over time due to administrative reforms and adjustments. As of January 2022,

there were over 330 prefecture-level divisions. However, our study area is limited to provinces and prefecture-level divisions within mainland China due to data availability constraints. For the study, the selected provinces and prefecture-level cities were categorized into eight groups based on their geographical coverage: east, west, central, south, north, northeast, northwest, and southwest (Figure 1).
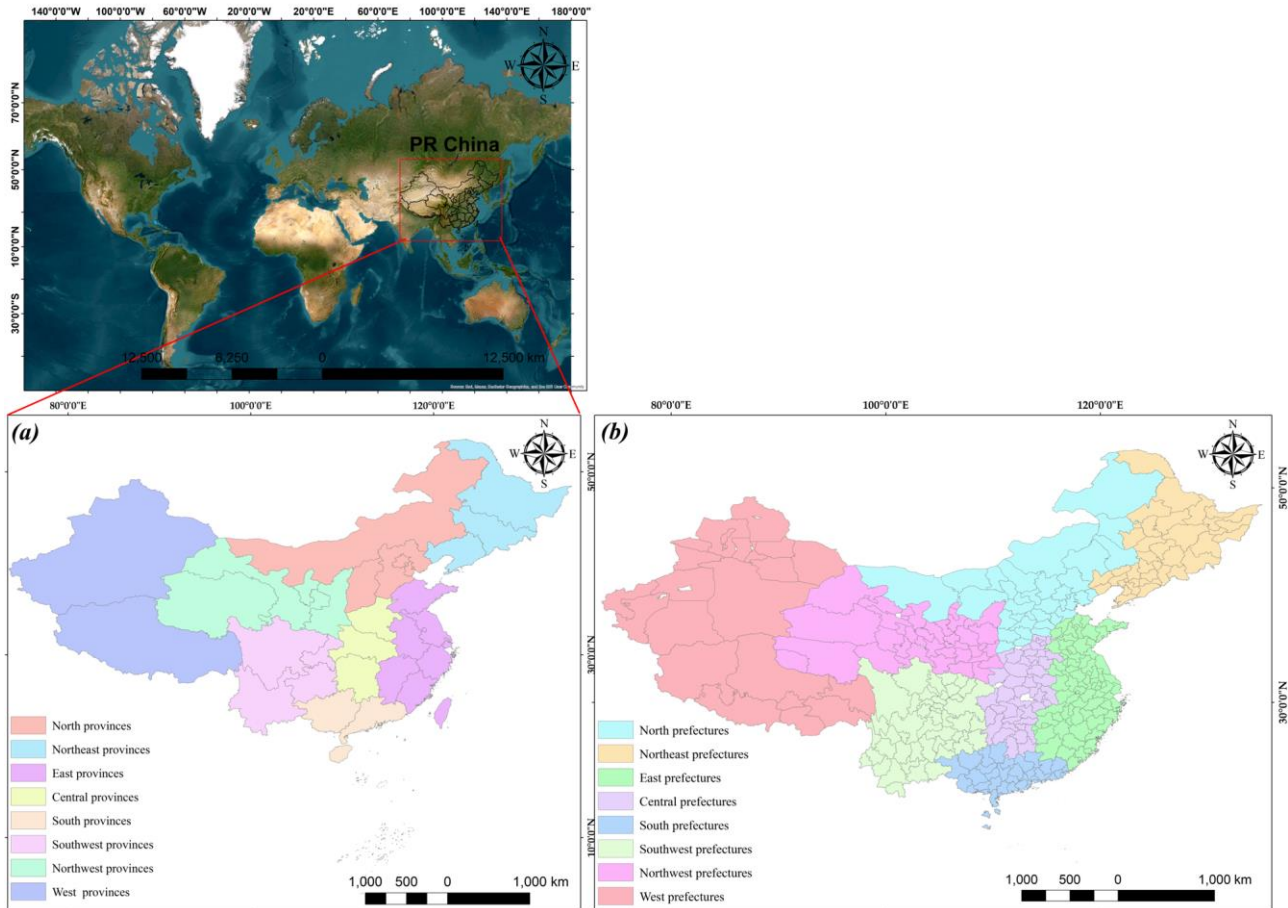
Figure 1. a) provinces in PR China, b) prefecture divisions in PR China

2.2 Materials

Two main spatial data sources were utilized to extract urban and suburban areas: Newly generated SNPP-VIIRS-like data, which covers the period from 2000 to 2023 (Chen et al., 2020). The dataset provides a comprehensive view of NTL emissions and urbanization trends over two decades, facilitating the identification of urban growth trends and changes in human activity and provides valuable insights into NTL emissions and urbanization trends over two decades; SNPP-VIIRS data spanning from 2012 to 2020 (Chen et al., 2021). This dataset offers more recent and detailed information on NTL emissions, enabling researchers to assess urban development and changes in built-up areas over the past nine years. Both datasets are freely available for research purposes from (https://dataverse.harvard.edu/dataset.xhtml). SNPP-VIIRS-like data was generated by merging SNPP-VIIRS and DMSP-OLS datasets, providing consistent and prolonged temporal coverage with 1000 m spatial resolution (30 arc second) and SNPP-VIIRS data have a 500 m (15 arc-second) spatial resolution (Liu S. et al., 2022). The shapefile data of national, provincial, and prefecture boundaries was obtained from the National Geomatics Center of China (http://ngcc.sbsm.gov.cn/). Collecting data on GDP, population, and electricity consumption (EPC) values at the provincial level from the China Statistical Yearbook is a standard practice in research related to socio-economic analysis and urbanization studies. The City Statistical Yearbook is a comprehensive and authoritative source of statistical data published annually by National Bureau of Statistics (https://data.cnki.net/).

2.3 Methodology

2.3.1 Deriving Urban and Suburban Areas

Performing the k-means algorithm in the image classification stage allowed for the segmentation of the datasets into distinct clusters based on nighttime light emissions. This step was essential for delineating urban and suburban areas from the satellite imagery. Various spatial data clustering algorithms, such as threshold, mutation detection, and ordering points to identify the clustering structure (OPTICS), as well as k-means, are at one's disposal. Because OPTICS is sensitive to parameters, it may fail to provide more accurate results when density declines between clusters are not present. Moreover, the mutation detection method exhibits several limitations when it comes to extracting urban areas and boundaries within heterogeneous urban environments. The Threshold method accurately extracts urban areas by considering the differences in brightness values within an image. But, k-means is a prominent algorithm since it can support large datasets, simple processes, and fast-running procedures in the computer system compared to other algorithms (Delmelle, 2015; Li et al., 2015; Yang et al., 2017; Hu et al., 2020; Shi et al., 2023; Withanage et al., 2023). The extraction of urban entities (2000-2020) and suburbs (2012-2020) entailed the utilization of k-means unsupervised classification following the acquisition of two datasets. In the case of urban entity extraction, the algorithm divided the dataset into two classes (urban and non-urban) upon the brightness values. In the context of suburbs, the number of extraction clusters was defined as three, comprising urban, suburban, and rural categories. Additionally, three initial prime centers were randomly selected for the clustering process. Below is the calculation formula (Shi et al., 2023; Withanage et al., 2023);

$$\mu_i^{j+1} = \frac{1}{|C_i|} \sum_{x \in C_i} x \tag{1}$$

$$E_i = \sum_{i=1}^{k} \sum_{x \in C_i} |x_{it} - \mu_i^{j+1}|^2 \tag{2}$$

E denotes the minimum square error of a cluster. For the sample x as C= {Cl, C2, C3... C$_k$} of the dataset. The similarity among all samples inside the cluster increases when smaller its value. -μ_i^{j+1} denotes the center of cluster C$_i$ in the j+1 iteration. As the clustering criterion, we used the sum of the square error criterion function, as outlined by Shi et al. (2023) and Withanage et al. (2023).

$$J_C = \sum_{i=1}^{k} \sum_{P \in C_i} \|P - M_i\|^2 \tag{3}$$

In cluster C$_i$ p denotes all pixels in the cluster, arithmetic mean of all pixels in C$_i$ denotes by M$_i$. Mapping between cluster centers and data objects represented by J_C. The urban and non-urban feature types of each pixel within an image are identified through cluster analysis. After running the algorithm iteration, urban, suburban, and rural areas were discerned from the two datasets on the variations of color.

2.3.2 Image Post Processing

Following the image classification stage, image post-processing techniques were applied to enhance the reliability and accuracy of the derived urban and suburban outputs. These techniques included noise reduction, and spatial filtering to refine the classification results and remove any inconsistencies. We performed image post-processing techniques to ensure the logical consistency of the extracted urban areas and suburban features. Here we followed three main steps: iterative temporal filtering, logical reasoning, and the elimination of unreasonable urban features (Shi et al., 2023; Withanage et al., 2023). This approach aimed to derive more precise and reliable results both in spatial and temporal dimensions.

2.3.3 Accuracy Assessment

Accuracy assessment involves comparing the classified urban and suburban areas to evaluate the reliability of the classification method and outputs. To assess the reliability of urbanization and sub urbanization pixels produced by the k-means algorithm, We computed accuracy of classification for each class over the pertinent

years. Four commonly utilized accuracy metrics were calculated: Overall Accuracy (OA), Producer's Accuracy (PA), User's Accuracy (UA), and Kappa Coefficients. OA stands for the overall percentage of correctly classified pixel classes, which is computed by dividing the number of accurately classified urban and non-urban pixels by the total number of pixels in the datasets (Zhou Q. et al., 2008; Yuh et al., 2023) and can be represented is as;

$$OA = \frac{1}{N} \sum_{ii=1}^{n} P_{ii} \tag{4}$$

OA stands for overall accuracy while N is total samples number and n denotes the total categories number, and Pii is correct classifications number of ith sample. PA measures the percentage accuracy of individual classes within a map. It's calculated by dividing the number of correctly classified pixels in a specific class by the total number of pixels belonging to that class in the reference data. The calculation formula is as;

$$PA = \frac{Correctly\ classified\ number\ pixel\ in\ each\ category}{Correctly\ classified\ total\ number\ pixels\ in\ that\ category (column\ total)} \tag{5}$$

UA, assesses the reliability of a given pixel class by evaluating its agreement with ground observations. It's also calculated by dividing the number of correctly classified pixels in a specific class by the total number of pixels classified within that class as below;

$$UA = \frac{Correctly\ classified\ number\ pixel\ in\ each\ category}{Correctly\ classified\ total\ number\ pixels\ in\ that\ category (row\ total)} \tag{6}$$

The Kappa Coefficient indicates the level of agreement between test and validation data in generated maps. It's based on the probability of the test data closely matching the validation data during the urban area extraction process and is highly correlated with overall accuracy. Overall mean accuracy and Kappa values for the urban features were within acceptable ranges as from 0.80 to 0.92% for OA and from 0.75 to 0.88 for Kappa (Table 1). For suburbs, the identification accuracy, measured by OA, ranged from 0.77 to 0.84, while Kappa coefficients ranged from 0.77 to 0.86 for selected years (Table 2).

***Table 1**. Overall mean accuracy for urban entity identification*

Year	2000		2005		2010		2015		2020	
	OA	Kappa	OA	Kappa	OA	Kappa	OA	Kappa	OA	Kappa
	0.84	0.80	0.80	0.75	0.92	0.81	0.80	0.82	0.88	0.88
	PA	UA	PA	UA	PA	UA	PA	UA	PA	UA
Urban	0.82	0.79	0.79	0.74	1.00	0.93	0.79	0.86	0.92	0.91
Non-urban	0.87	0.82	0.81	0.76	0.84	0.88	0.82	0.78	0.84	0.85

***Table 2**. Overall mean accuracy for suburban area identification*

Year	2012		2014		2016		2018		2020	
	OA	Kappa	OA	Kappa	OA	Kappa	OA	Kappa	OA	Kappa
	0.84	0.77	0.78	0.79	0.78	0.86	0.80	0.83	0.77	0.80
	PA	UA	PA	UA	PA	UA	PA	UA	PA	UA
Sub-urban	0.79	0.81	0.78	0.79	0.82	0.84	0.77	0.75	0.74	0.73
Urban	0.82	0.77	0.76	0.74	0.76	0.81	0.80	0.81	0.79	0.82
Rural	0.93	0.74	0.81	0.85	0.78	0.94	0.83	0.94	0.80	0.86

3. RESULTS

3.1 Urbanization in China

Statistically significant positive trends in digital number values of NTL images in the prefecture-level cities indicated that China has experienced rapid urban growth from 2000 to 2020 (Figure 2). The highest rate of urban growth could be identified in the five national-level agglomerations: Pearl River Delta (PRD); Beijing-Tianjin-Hebei; Yangtze River Delta (YRD); Middle Yangtze; and Chengdu-Chongqing. Variations in DN values in SPNS VIIRS-like imagery reveal greater changes in urbanization, particularly in the eastern region of the country, from 2000 to 2020.
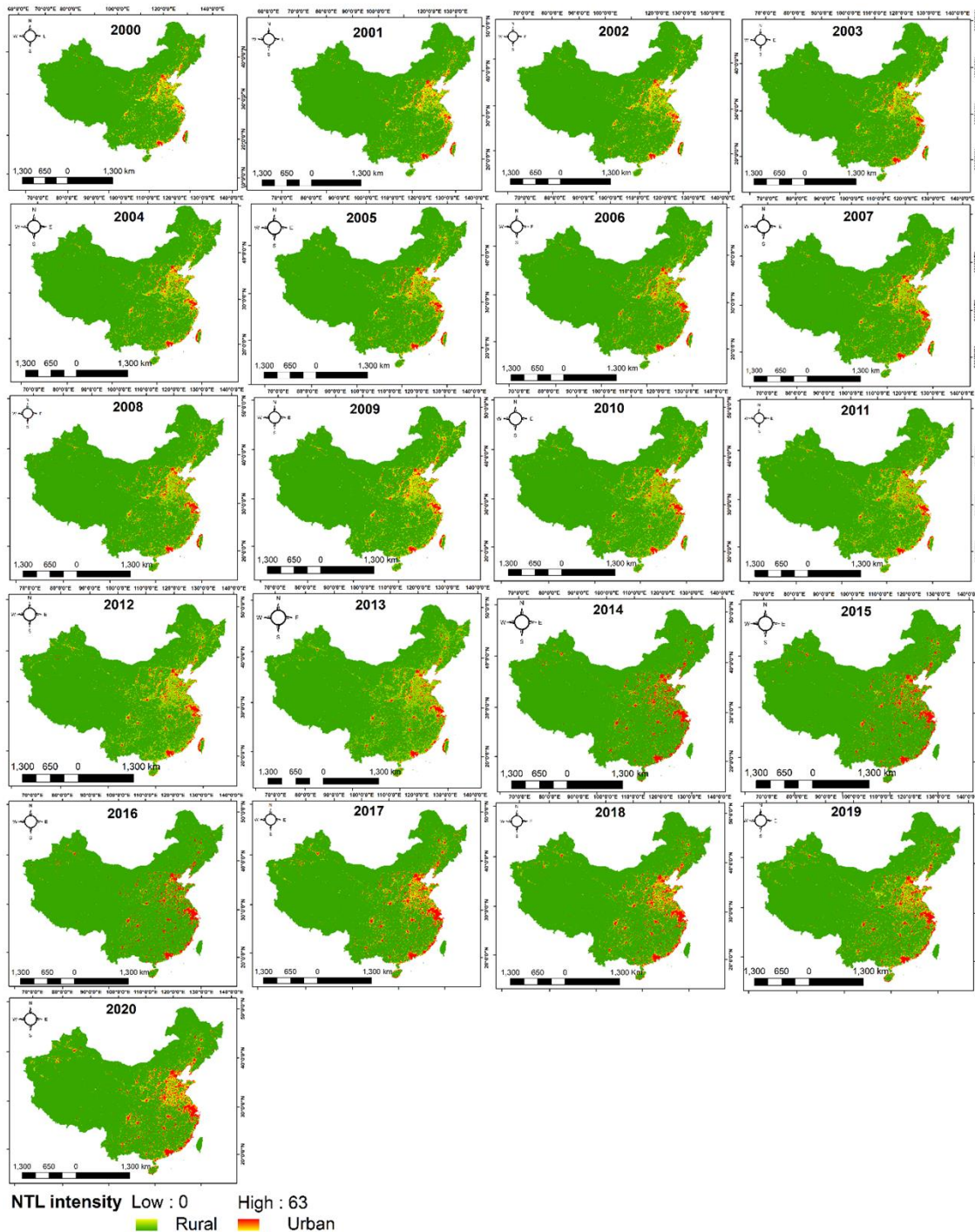
Figure 2. *Urban Growth in China, 2000-2020*

Based on the variations in DN values in SPNS VIIRS imagery, significant changes in urbanization are notably evident, particularly in the eastern region of the country, from 2000 to 2020. The DN values of inter-calibrated SNPP VIIRS NTL signals in the prefecture cities indicate a substantial inverse pattern into enhanced light areas in cities. Varied spatial and temporal trends in urban entities may suggest that light signals from NTL images could be a marker of urban expansion during significant urbanization in China at the prefecture level. Based on Figure 2, the brightly illuminated areas (highlighted in red with DN values >56 in this case) likely represent the developed sections of cities with dense human activities and a high percentage of impermeable surfaces. The yellow areas, which are moderately to highly illuminated, seem to be associated with the outskirts of the central area and suburban regions with significant human activity. The green areas, characterized by low nighttime lighting, mainly cover rural areas with farmland and small communities with low human activity. Most prefecture cities with well-developed urban areas and human activities have shown a significant positive trend in highly illuminated areas at the city level, indicating significant growth outward from the core region and an increase in the spatial extent of urban entities. However, during the period in concern, notable spatial variations in the expansion of urban entities can be observed across distinct regions (Figure 3).
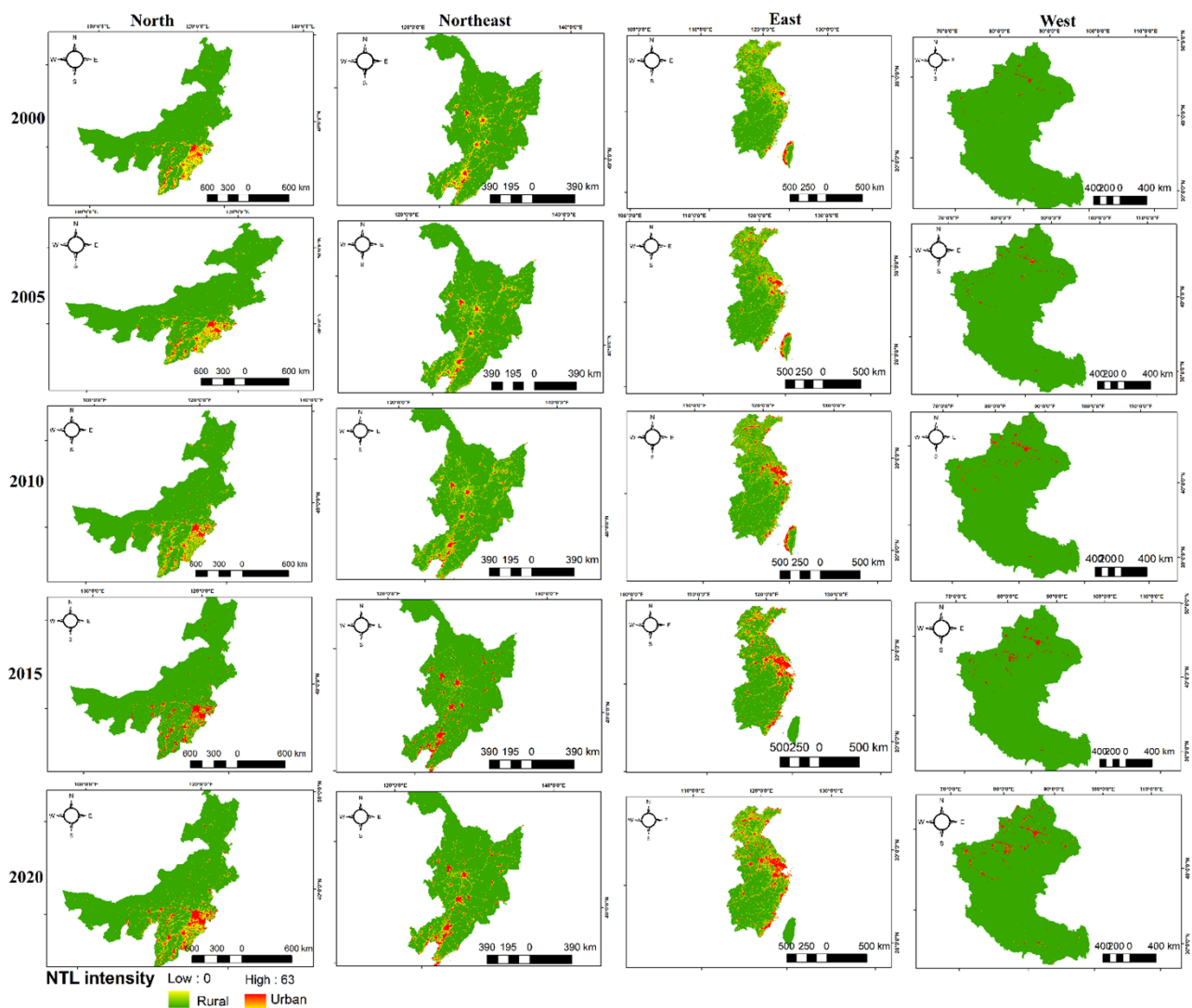
Figure 3. *Expansion of urban areas in China during 2000-2020*
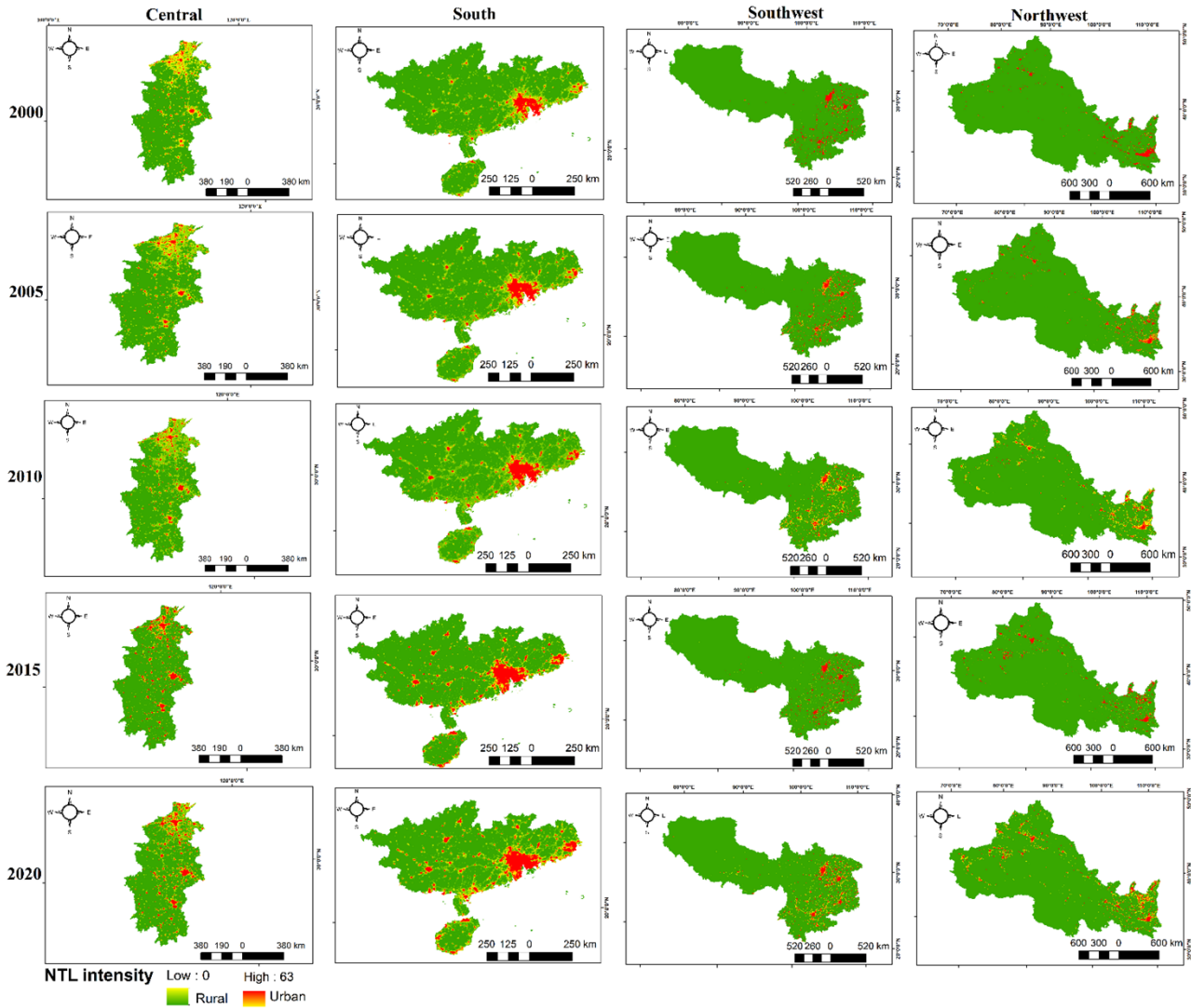
Figure 3. *(continued)*

3.2. Spatial Variations in Regional Scale

At the individual urban scale, especially most large and extra-large cities in the southern and eastern regions have experienced a distinct reduction of the areas with low NTL over the concerned period, while expanding high NTL areas. The eastern region has demonstrated a notable expansion compared to others, driven by socioeconomic factors and other forces of urban growth. This region includes the Yangtze River Delta (YRD) agglomeration.

The Beijing–Tianjin agglomeration (Figure 4a) has experienced a notable expansion during the last two decades in its geographical scope, accompanied by a heightened level of economic activity. From 2000 to 2020, the total urban entity of the agglomeration increased from 2438 km^2 to 12,970 km^2, indicating an average annual growth rate of 21.6%. During the specified period, the Beijing-Tianjin agglomeration exhibited a contrasting trend to the growth observed in the YRD, showing a decline in urban sprawl.

The Chengdu–Chongqing agglomeration (Figure 4b) sits in the Southwest sector of China, situated upstream along the Yangtze River. The collective urban entity within the region saw an increase from 204 km^2 to 5036 km^2, reflecting an average annual growth rate of 118.4%. This agglomeration spans approximately 185,000 km^2 and includes 15 prefecture-level cities in Sichuan Province and 29 district/county-level administrative units in Chongqing Province. With an urbanization rate of 63.01% among its permanent population, this agglomeration stands as a pivotal demonstration area for the nation's advancement of new urbanization (Luo et al., 2023).

As a key agglomerations for development, the YRD (Figure 4c) encompasses Shanghai, Jiangsu, Zhejiang, and Anhui provinces, comprising fifty-one cities, including 26 prefecture cities, including Shanghai (Anhui 8, Zhejiang 8, Jiangsu 9), covering about 225,000 km^2 (Zhang H. et al., 2022). The urban entities in all prefecture cities in the eastern provinces have significantly expanded, including provincial capitals like Shanghai, Hangzhou, Fuzhou, Jinan, Nanchang, Nanjing, and Hefei. The urban entities within the YRD region expanded significantly from 2684 km^2 to 41465 km^2 between 2000 and 2020, indicating an annual average growth rate of 72.2%. As a key urban centre in the Eastern region Shanghai has risen greatly from 660 km^2 to 2852 km^2 demonstrating a 45% growth rate. Land urbanization is more pronounced in the southeast prefectures of the YRD agglomeration compared to those in the northwest. Higher levels of land urbanization have occurred over the specified period, particularly in the core areas of Shanghai, Nanjing, and Hangzhou, as depicted in the Figure 4c. Nevertheless, land urbanization in certain mountainous prefectures in southern Anhui and Zhejiang has shown a low level of development.

During the specified period, prefecture cities in southern provinces experienced significant growth, with a notable expansion observed in those within the Pearl River Delta (PRD) urban agglomeration (Figure 4d). The urban entity in the Pearl River Delta (PRD) increased from 4147 km^2 to 12,962 km^2, illustrating a growth rate of 213%. Despite comprising only 0.58% (56,000 km^2) of the total land area, the PRD urban agglomeration significantly contributes to 9.2% of the GDP (Zhang H. et al., 2022). Among the seventeen cities in the PRD, nine prefectures serve as crucial urban hubs in the region. These include Guangzhou, Shenzhen, Zhuhai, Foshan, Jiangmen, Zhaoqing, Huizhou, Dongguan, and Zhongshan. Based on the NTL imagery retrieval data, Shenzhen, situated in the southern part of the PRD, has exhibited significant growth in urban development from 2000 to 2020. Following closely behind is Guangzhou, which is the second most rapidly expanding urban entity in the region. Nevertheless, several adjacent cities, such as Zhaoqing, Huizhou, and Jiangmen, have shown relatively modest urban growth over the specified period.

3.3 Spatial Variations in Prefecture Scale

During the specified period, the total urban entity in mainland China expanded from 16,209 km^2 to 89,631 km^2 indicating a growth rate of 5% during the last 20 years. However, the rates and patterns of growth in urban entities (UEs) exhibited significant variations across eight regions undergoing diverse economic and urban development stages. The eastern and southern prefectures contributed the highest growth in urban expansion, with 27,640 km^2 and 9,340 km^2, respectively, while the northeast and northwest prefectures showed lower spatial extents of 2,897 km^2 and 5,207 km^2, respectively.

Shanghai, located in the eastern prefectures (Figure 5), has experienced dramatic growth over the last 20 years, expanding from 660 km^2 to 2,852 km^2 (Figure 5y). As fast growing prefecture in the southern provinces, Guangzhou expanded its urban area from 375 km^2 to 1,635 km^2 (Figure 5v). In Beijing, urban areas expanded from 783 km^2 to 2,150 km^2, making it the fastest-growing prefecture in the northern regions (Figure 5q). From a temporal perspective, certain provincial capitals like Chongqing and Chengdu exhibited rapid expansion after 2015 (Figure 5m, n). However, some provincial capitals like Xining, Lhasa, Haikou, and Hohhot have demonstrated comparatively slower spatial expansion during the target period (Figure 5h, l, x, u). The temporal patterns and trends of the 31 provincial capitals growth has illustrated in Figure 6.

3.4 Growth of Suburbs

Over the past two decades, significant spatial and temporal changes in land use have occurred in suburban areas, acting as bridges amid urban and rural areas. The k-means method was utilized to discern and assess the spatial-temporal patterns of sub-urbanization in China mainland using SNPP VIIRS data from 2012 to 2020. The suburbs underwent a proportional expansion attributed to factors such as population density, urban GDP growth, and the development of the road network. The analysis revealed that the overall area of suburbs expanded from 59,151 km^2 to 120,339 km^2 between 2012 and 2020 (Figure 7), indicating a proportional growth rate ranging from 0.6% to 1.2%. The peak growth rate of suburbs was recorded between 2012 and 2014, reaching 18%. Urban areas and suburbs experienced integrated growth during the specified period, with both entities mutually benefiting from each other for their area growth. Consequently, the spatial and temporal urban-suburb development sequences are accurate. Figure 8 illustrates the proportions of suburbs and urban

entities in the years 2012, 2014, 2016, 2018, and 2020. Figure 8 demonstrates a notable increase in the proportional contribution of suburbs compared to urban entities.
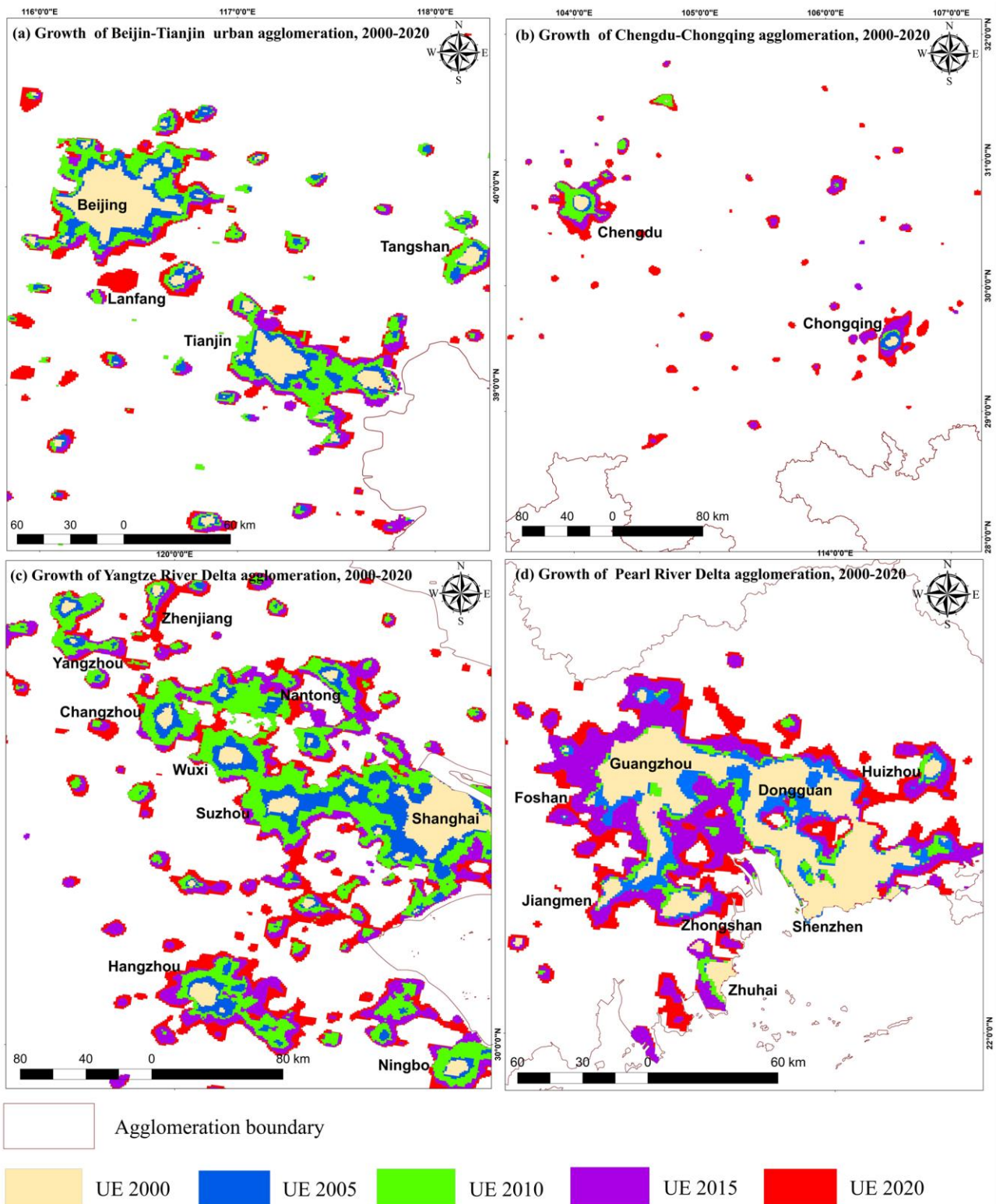
Figure 4. *Growth of urban entities, 2000-2020* ***a)*** *Beijin-Tianjin agglomeration,* ***b)*** *Chengdu-Chongqing agglomeration,* ***c)*** *Yangtze River Delta agglomeration,* ***d)*** *Pearl River Delta agglomeration*
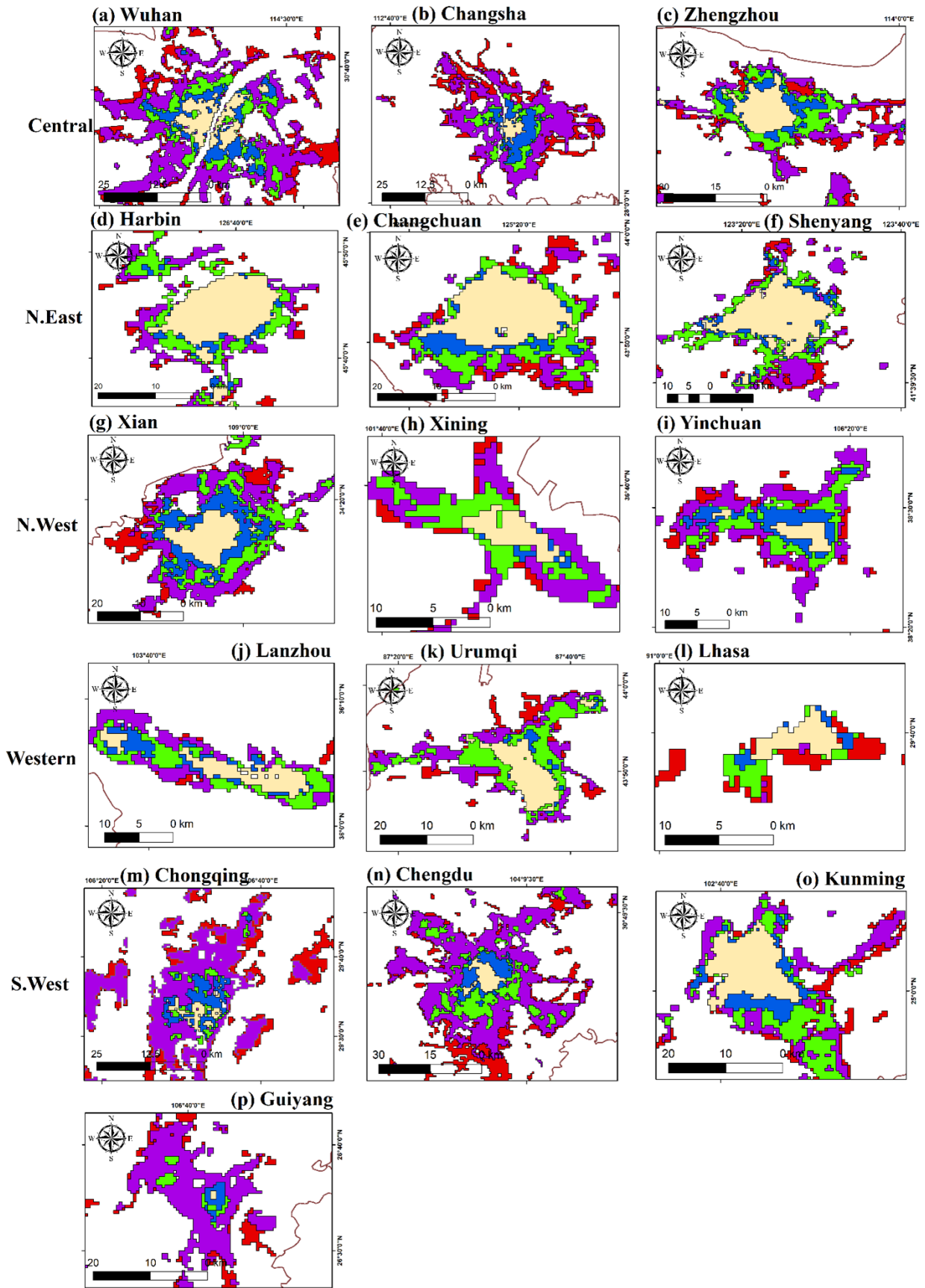
Figure 5. *Growth of provincial capitals, 2000-2020*
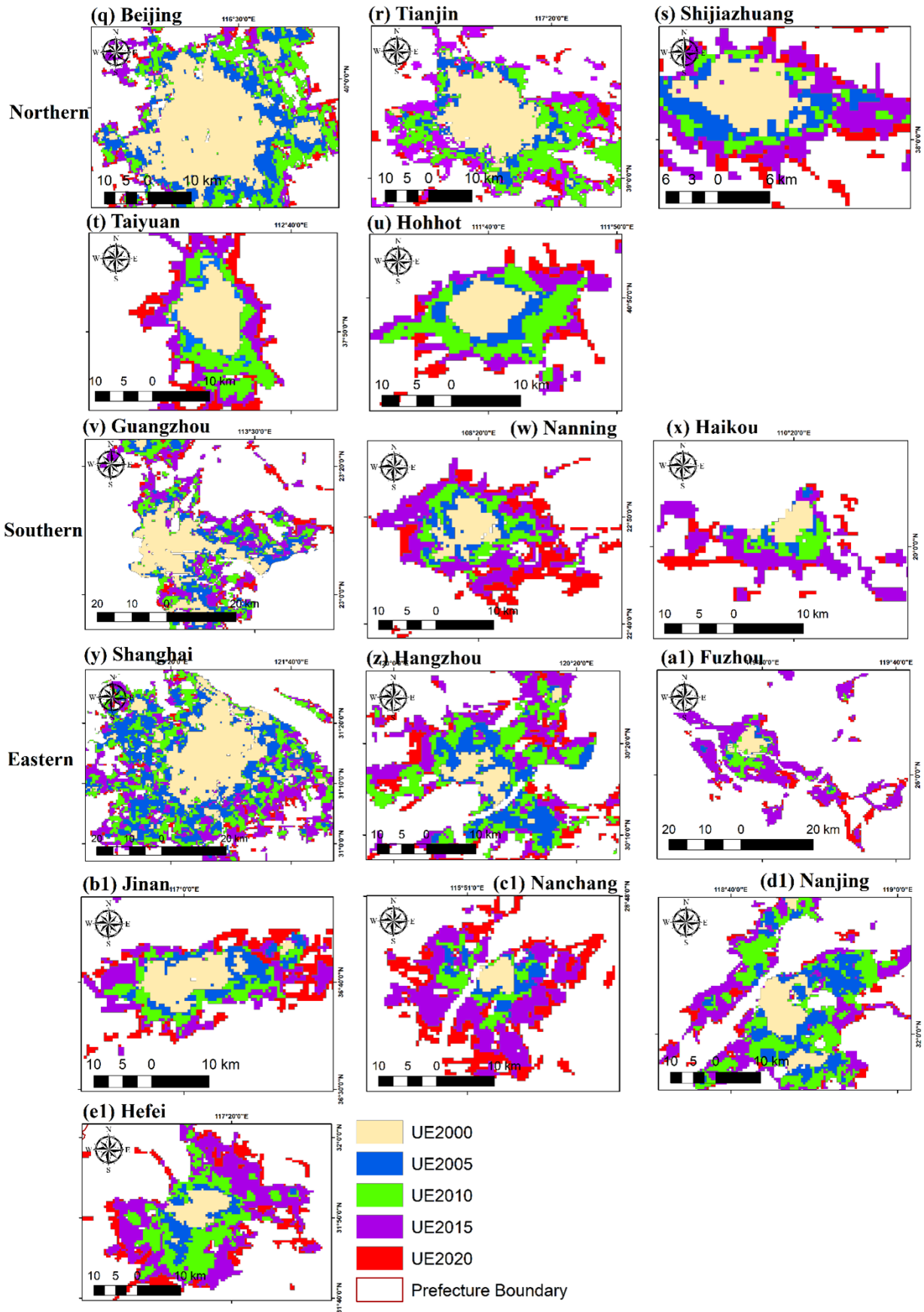
Figure 5. *(continued)*
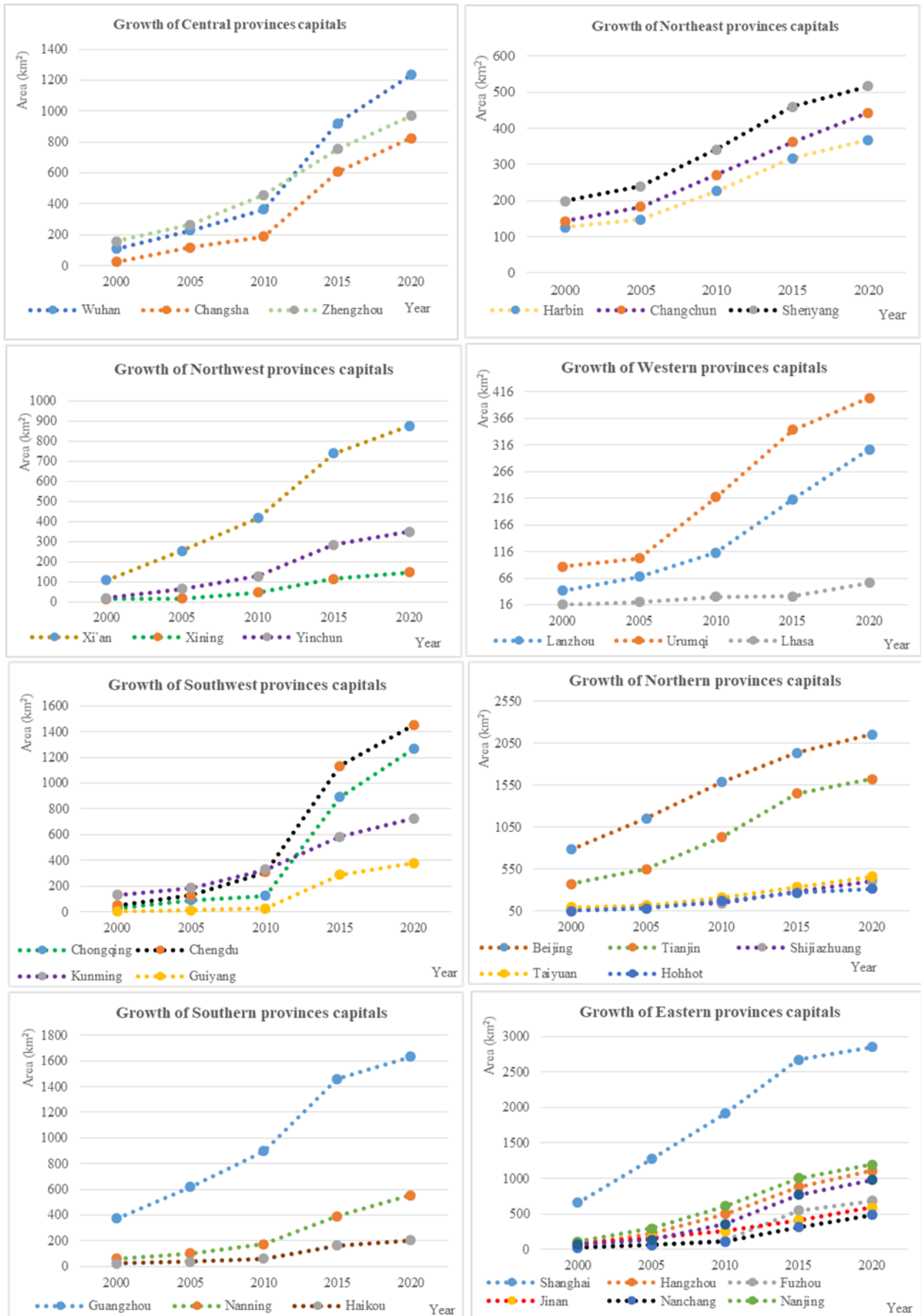
Figure 6. *Growth patterns of urban entities in provincial capitals, 2000-2020*
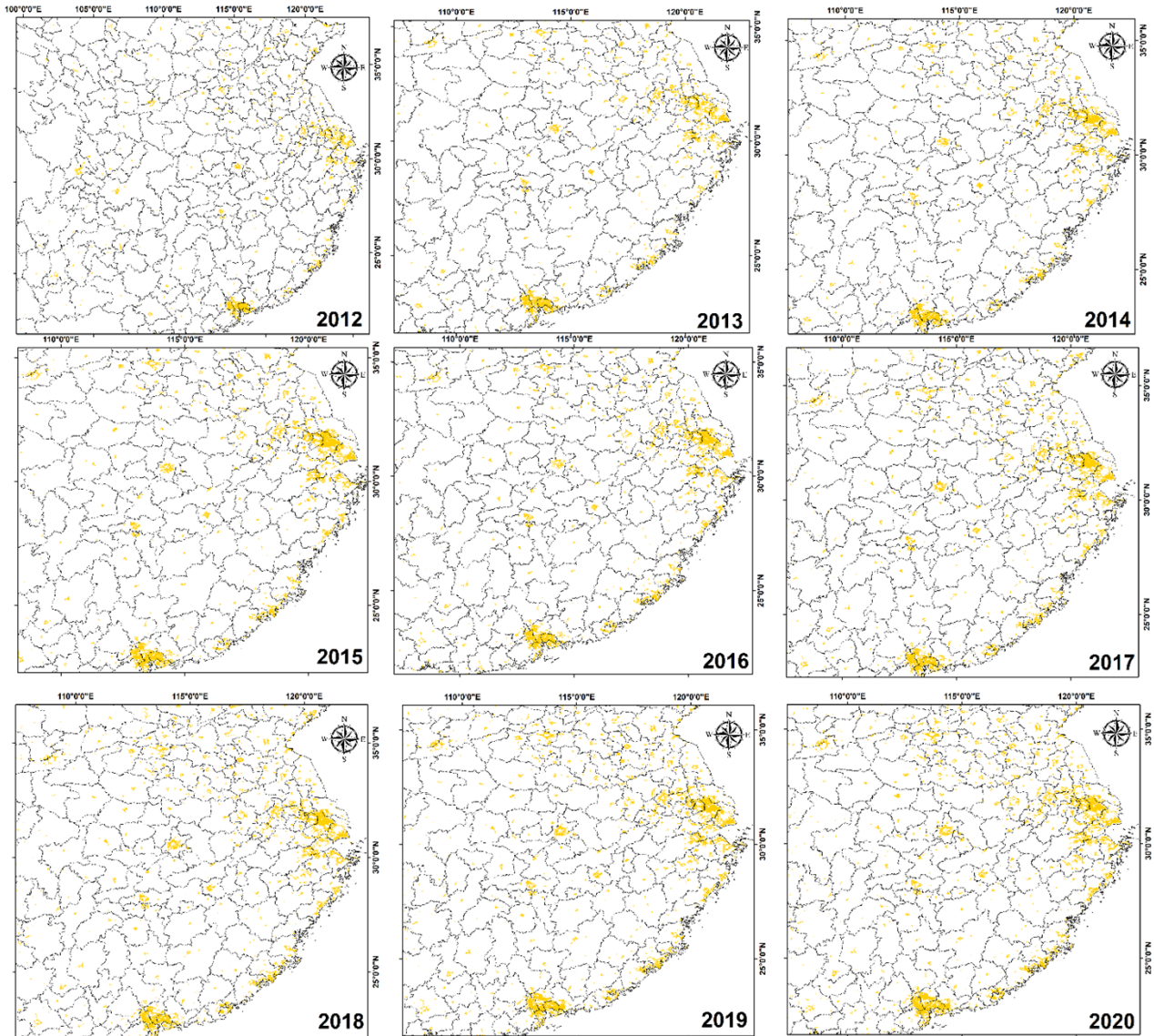
Figure 7. Growth patterns of suburbs in China, 2012-2020
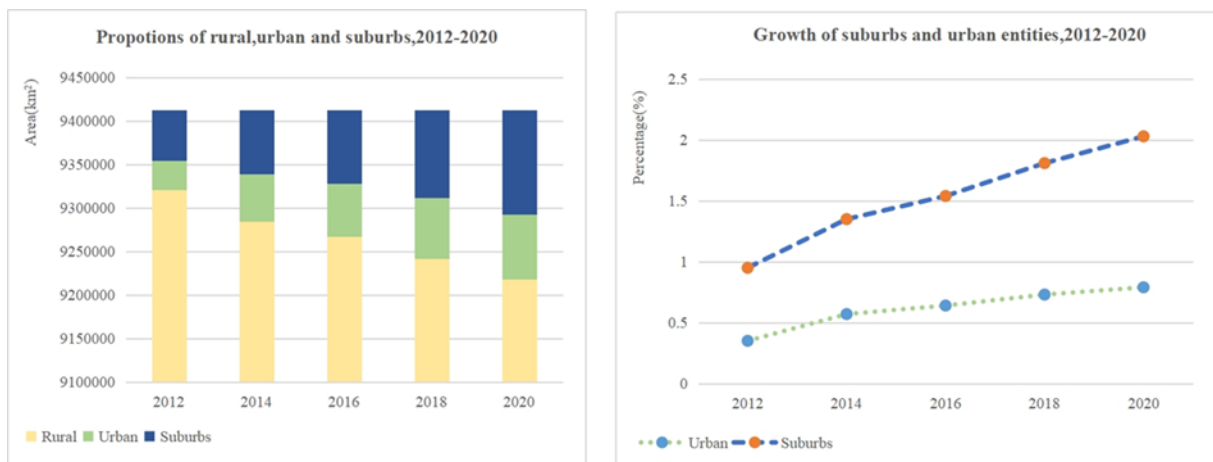
Figure 8. Proportion of rural, urban, and suburbs in China and growth rates of urban entities and suburbs, 2012-2020

When examining the provincial landscape of suburban development, each province exhibits distinct growth trends and patterns. Guizhou, Hunan, and Hubei have exhibited growth rates of 334%, 258%, and 246% respectively throughout the specified period, indicating their status as suburban areas in the intermediate phase of the urbanization process. However, the provinces of Beijing, Guangdong, Tianjin, and Shanghai, which are in the advanced stage of urbanization, have experienced relatively low growth rates of 50%, 56%, 46%, and 17% respectively. This is because these provinces have already established and stabilized as urban areas. Additionally, in Heilongjiang, Liaoning, and Inner Mongolia, slow economic growth has negatively affected urbanization. Thus, the growth rate of suburbs in those provinces is low, with growth rates of 45% and 89% respectively. The spatial and temporal patterns of suburban growth in China can be best illustrated using provincial capitals such as Beijing, Tianjin, Shanghai, Wuhan, Chengdu, Chongqing, Nanjing, Guangzhou, and Xi'an (Figure 9 and Table 3).
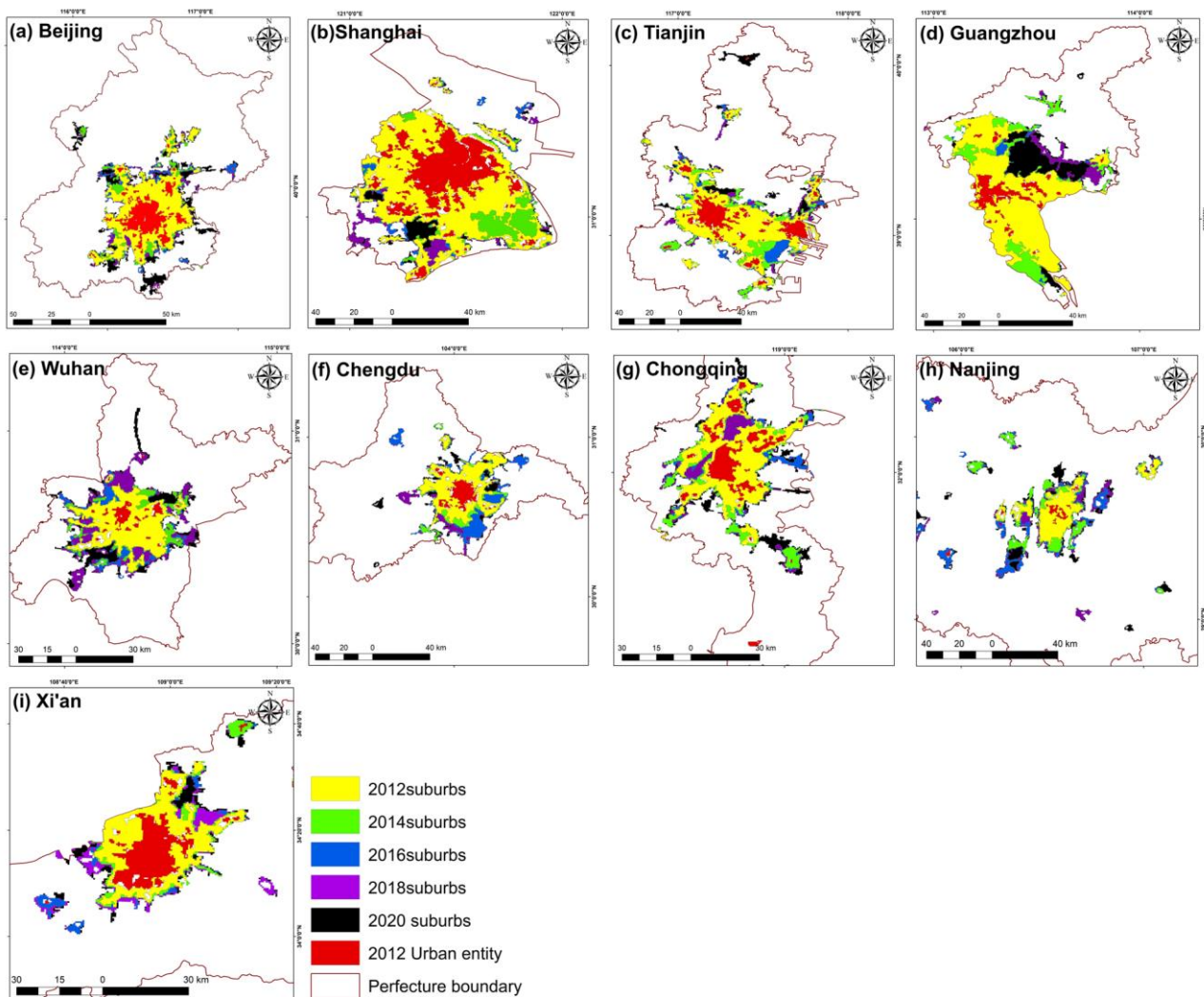
Figure 9. *Suburban growth during 2012-2020 **a**) Beijing, **b**) Shanghai, **c**) Tianjin, **d**) Guangzhou, **e**) Wuhan, **f**) Chengdu, **g**) Chongqing, **h**), Nanjing, **i**) Xi'an*

***Table 3.** Top 10 suburbs in the years 2012, 2016, and 2020*

City	2012	City	2016	City	2020
	Area (km^2)		Area (km^2)		Area (km^2)
Qingyuan	2103	Suzhou	4119	Suzhou	4363
Shanghai	2074	Shanghai	2390	Guangzhou	2671
Foshan	1869	Guangzhou	2085	Shanghai	2404
Guangzhou	1858	Qingyuan	1988	Foshan	2175
Suzhou	1619	Foshan	1915	Qingyuan	1945
Beijing	1535	Beijing	1697	Tianjin	1718
Tianjin	1171	Tianjin	1639	Hangzhou	1593
Shenzhen	1100	Hangzhou	1390	Wuhan	1528
Hangzhou	975	Wuxi	1310	Chengdu	1457
Chengdu	941	Chengdu	1291	Quanzhou	1394

3.5 Growth Patterns and Driving Factors in Suburb Development

Suburban expansion in cities such as Beijing and Wuhan, it becomes evident that there has been growth in all directions. However, the expansion of Tianjin's suburbs occurred predominantly in a southeasterly direction. Upon analyzing the situation of Shanghai city, it becomes apparent that the suburbs initially expanded on the eastern side. However, thereafter, they expanded in a southern direction. Similarly, the suburbs in Chongqing have been consistently expanding towards the southwest. The suburbs of Guangzhou have experienced a significant trend of northward development from 2012 to 2020. These spatial variations are a result of the effect of several political, economic, and geographical factors. This pattern is better evident from the expansion of suburbs in the Pearl River Delta (PRD).

Therefore, these variables significantly contribute to the process of sub urbanization in China throughout the concerned period. Urban growth in major cities has led to a rise in environmental difficulties such as noise, air, and water pollution in metropolitan regions. As a result, people are increasingly moving from urban areas to suburban areas due to lower land prices and more favorable living conditions. Urban-suburb commuter communities have emerged as a result of the recent growth of road networks and other advantages in suburbs, leading to daily changes. Urban policy making has also significantly contributed to the growth of suburbs in China.

The development of suburbs is closely correlated with the expansion of road networks, population growth, and other socioeconomic development indicators. Provincial-level socioeconomic variables such as Gross Domestic Product (GDP) and Electricity Consumption (EPC) exhibit a higher spatial consistency with sub urbanization according to the regression analysis performed (Figure 10). Observing the R^2 values between population, GDP, EPC, and the suburban area, they were not less than 0.3594, 0.6214, and 0.6252 respectively. According to the regression results among the three socioeconomic variables, higher consistency is exhibited in suburban growth with GDP, as it derived an R^2 value of 0.8758 (Figure 10r). The second-highest R^2 value was reported for EPC as 0.7982 (Figure 10y), while population and suburban area show a comparatively low inverse relationship, reporting an R^2 of 0.6115 as higher (Figure 10i).
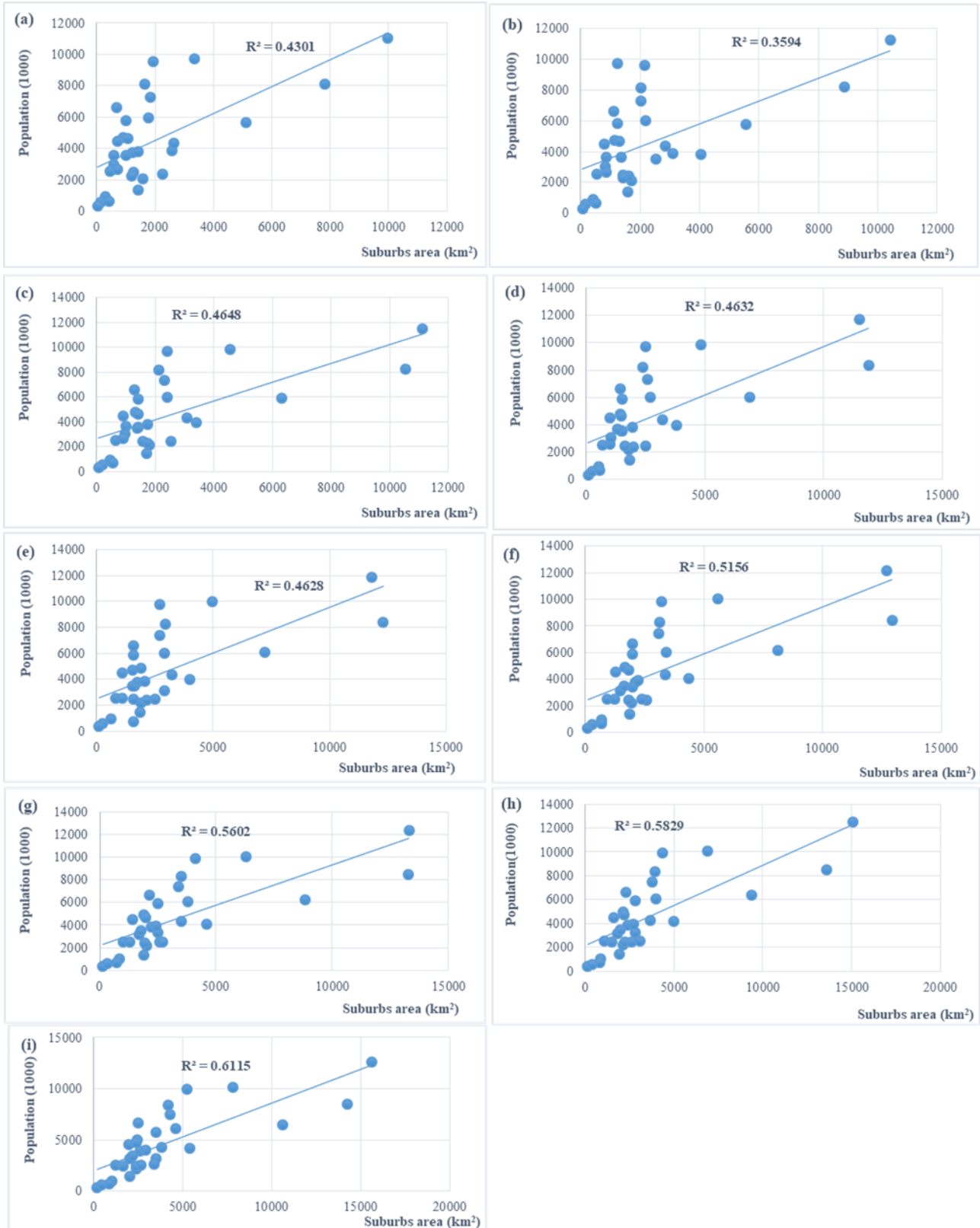
Figure 10. *Correlation between the growth of suburban areas and **a-i**) provincial level population,*
j-r) *GDP, **s-x1**) EPC*
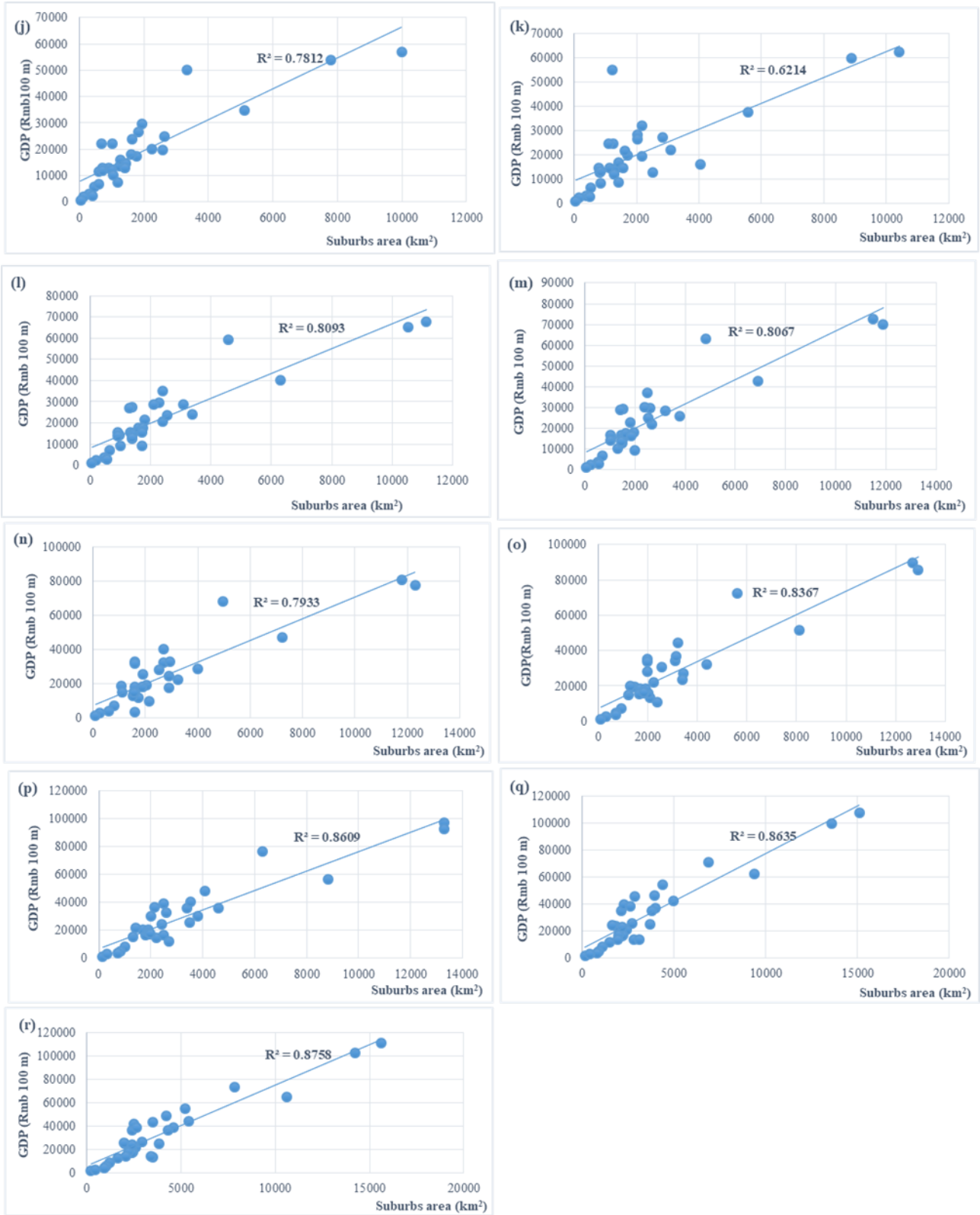
Figure 10. *(continued)*
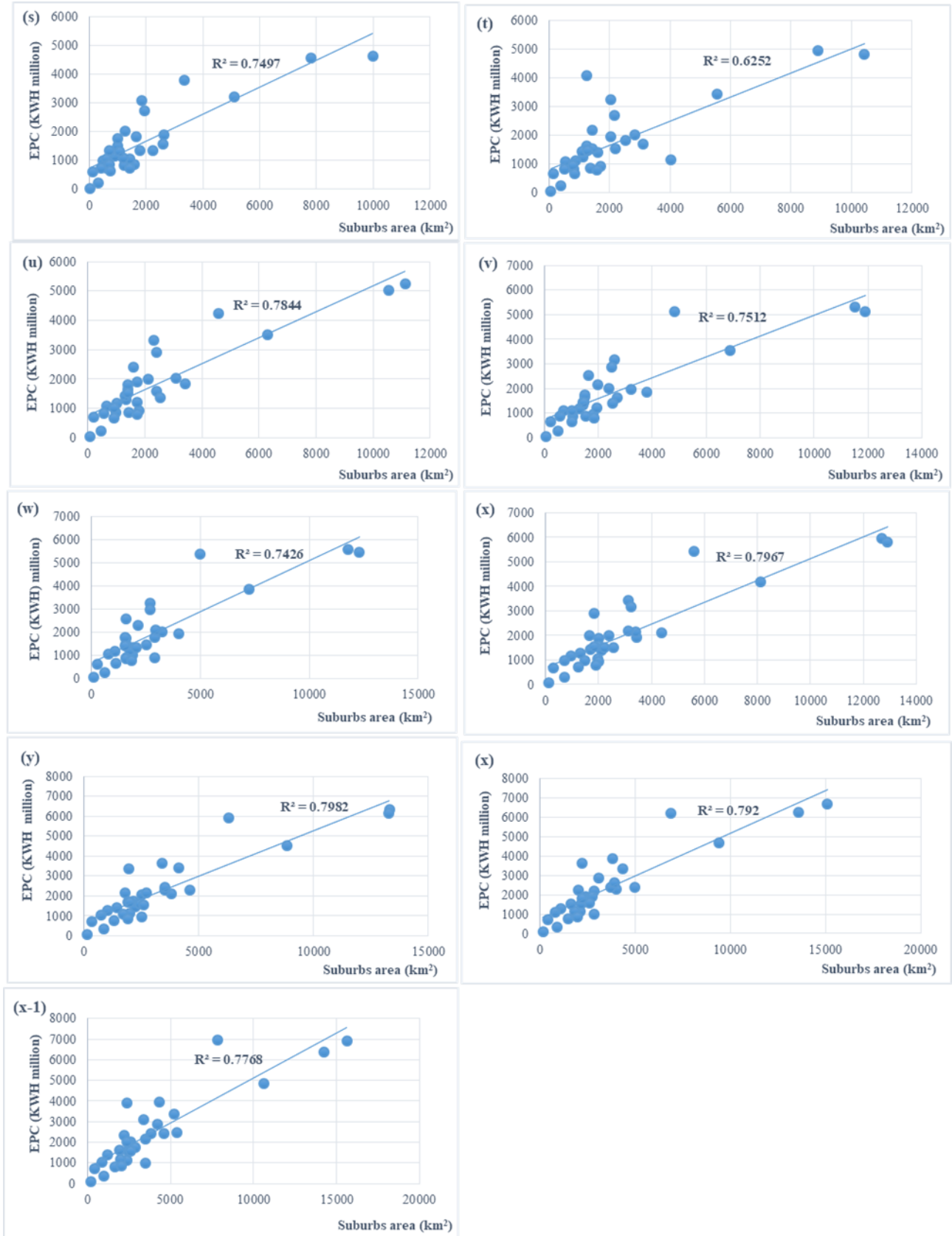
Figure 10. *(continued)*

4. DISCUSSION

4.1 Role of SNPP-VIIRS Data for Urban Mapping

Demarcating clear urban boundaries solely based on results derived from other remote sensing data such as Landsat and MODIS can be challenging, particularly when considering impervious surfaces. Therefore, it is essential to utilize reliable data that also captures human activity surfaces. Ma M. et al. (2020) demonstrated a positive correlation between nighttime lights and human activity surfaces. We employed the k-means algorithm to extract urban and suburban areas, aiming to evaluate their spatiotemporal evolution using SNPP-VIIRS data. Yu et al. (2018) also confirmed that NTL data is a reliable data source for extracting built-up areas. They revealed that various methods can be employed for reliable urban area extraction, including threshold, watershed segmentation, Sobel-based edge detection, and neighborhood statistics. Shi et al. (2023) and Withanage et al. (2023) similarly employed the k-means method to extract cities utilizing SNPP-VIIRS NTL data. However, Shi et al. (2023) emphasized the importance of integrating NTL data with other sensing data for urban area extraction to attain higher accuracy. Liu S. et al. (2022) have also demonstrated that the results of suburban area extraction derived from SNPP-VIIRS data are more accurate compared to DMSP-OLS. They also revealed that suburban areas have experienced a growth rate from 0.6% to 1.3% from 2012 to 2020, which aligns closely with our findings.

4.2 Urbanization and Socioeconomic Development

Through our correlation analysis, it was discovered that there exists an almost inverse relationship between urban growth and urban socioeconomic indicators. Our findings revealed a higher R^2 value, exceeding 0.621, for GDP and electricity consumption, although it resulted in a lower R^2 value for population growth. Similar findings by Shi et al. (2023) confirmed the inverse relationship between urban entity growth and population density. The R^2 value for their correlation results between urban entity and population density was higher than 0.564. Liu S. et al. (2022) discovered that suburban development is closely associated with factors such as GDP, road network expansion, and population growth. Especially, Liu S. et al. (2022) found a higher consistency in suburban development with population density and road network expansion within the Pearl River Delta (PRD) agglomeration during the period from 2012 to 2020. The R^2 value of their correlation analysis was also higher than 0.500 for three variables: GDP, population density, and road network.

4.3 Limitations and Future Research Directions

At a larger spatial scale, errors in NPP-VIIRS data may arise due to atmospheric turbidity, distortion, and variations in satellite views (Ma Q. et al., 2014; Li & Li, 2015). Indeed, these factors can also have adverse effects on the accuracy of urban extraction results of our study. Also, in future research, it is essential to address the challenges associated with light emissions across different wavelengths. Moreover, the time bias in NPP-VIIRS data acquisition can have a detrimental impact on urban extraction results, particularly considering that a significant portion of artificial lights in Chinese cities are turned off after late nights (Ma Q. et al., 2014). Therefore, conducting a comparative study that utilizes LuoJia1-01 data for future research may offer advantages, as it has the potential to compensate for the limitations present in NPP-VIIRS data.

Although NTL data is valuable for evaluating urbanization, it's essential to recognize that the brightness of lights varies among cities based on their respective levels of urbanization, industrial structure, and development status (Ma Q. et al., 2014; Pan & Li, 2016). Hence, our study's findings may be adversely influenced to some extent by these factors. Certain cities in China utilize artificial lighting to attract tourists and improve the aesthetic appeal of their nighttime skyline. This can impact or elevate the brightness levels recorded for these cities (Cao, 2008; Ma Q. et al., 2014). Therefore, further research is needed to differentiate the unit values of NTL based on varying socioeconomic status. Additionally, previous research has demonstrated that NTL in industrial areas can influence and supplant peak pixel values within cities (Li & Li, 2015). Hence, adopting advanced image processing techniques to mitigate the influence of concentrated industrial plants within cities and the edges of cities on light brightness differentiation could potentially yield more reliable results, as also suggested by Ma Q. et al. (2014). Furthermore, while nighttime light data provides insight into human activity at the city scale, it may not fully account for peak pixel variations at the agglomeration scale. Therefore, in future research, it is essential to give due consideration to minimizing the impact of this limitation.

5. CONCLUSION

Using SNPP-VIIRS-like data (2000-2020) and NPP-VIIRS (2012-2020), we applied a novel k-means technique to extract urban and suburban entities in China. The research findings indicate a substantial expansion of urban entities at the prefecture level, increasing from 16,209 km^2 to 89,631 km^2 during the specified period. However, the total areas of urban entity features in our study differ from the findings of Shi et al. (2023), who reported urban areas ranging from 9,435 km^2 to 78,546 km^2.This discrepancy may be attributed to variations in the minimum distance decision rule employed in the k-means classification. The highest growth in urban entities was reported in the east and south prefectures, totaling 27,640 km^2 and 9,340 km^2, respectively. Conversely, the lowest growth was reported in the northeast (2,897 km^2) and northwest (5,207 km^2) prefectures. Yangtze River Delta exhibited the highest urbanization rate, experiencing a significant expansion of built-up areas from 2,684 km^2 to 41,465 km^2. The urban entities in all prefecture cities in the eastern provinces have significantly expanded, including provincial capitals like Shanghai, Hangzhou, Fuzhou, Jinan, Nanchang, Nanjing, and Hefei. As a key urban center in the Eastern region, Shanghai has experienced significant growth, expanding from 660 km^2 to 2852 km^2, demonstrating a growth rate of 45%. Further analysis revealed that the overall area of suburbs expanded from 59,151 km^2 to 120,339 km^2 between 2012 and 2020, indicating a proportional growth rate ranging from 0.4% to 1.9%. These results closely resemble the findings of Liu S. et al. (2022), who also used k-means classification algorithm for suburbs extraction and observed fluctuating trends in China, reporting growth rates ranging from 0.6% to 1.6% over nine years. Guizhou, Hunan, and Hubei provinces have exhibited suburban growth rates of 334%, 258%, and 246% respectively while Beijing, Guangdong, Tianjin, and Shanghai have experienced relatively low growth rates of 50%, 56%, 46%, and 17%. These findings are considered reliable, given that the OA and Kappa values of the outputs were within acceptable ranges, ranging from 77.2% to 92.3% for OA and from 0.77 to 0.88 for Kappa. Additionally, our study revealed a strong correlation between urban growth, urban GDP, and electricity consumption on a provincial scale. However, the limitations identified in our study must be carefully considered in future research focused on obtaining accurate urban extraction results. Indeed, incorporating alternative methods that are superior to the k-means algorithm or conducting comparative studies with other techniques would be highly beneficial in addressing these challenges and advancing the reliability of urban extraction from NTL remote sensing data in the future.

AUTHOR CONTRIBUTIONS

Conceptualization, N.C. and J.S.; methodology, N.C.; title, N.C.; formal analysis, N.C.; data curation, N.C.; manuscript-original draft, N.C.; manuscript-review and editing, J.S.; visualization, N.C.; supervision, J.S. All authors have read and legally accepted the final version of the article published in the journal.

ACKNOWLEDGEMENT

CONFLICT OF INTEREST

The authors declare no conflict of interest.

REFERENCES

Cao, X. (2008). Research on the countermeasures for developing night tourism in Chinese cities. *Exploration of Economic Issues*, *8*, 125-128. (in Chinese) https://doi.org/10.3969/j.issn.1006-2912.2008.08.025

Chen, Z., Yu, B., Yang, C., Zhou, Y., Yao, S., Qian, X., Wang, C., Wu, B., & Wu, J. (2021). An extended time series (2000–2018) of global NPP-VIIRS-like nighttime light data from a cross-sensor calibration. *Earth System Science Data*, *13*(3), 889-906. https://doi.org/10.5194/essd-13-889-2021

Chen, Z., Yu, B., Yang, C., Zhou, Y., Yao, S., Qian, X., Wang, C., Wu, B., & Wu, J. (2020). An extended time-series (2000-2023) of global NPP-VIIRS-like nighttime light data [dataset]. Harvard Dataverse. https://doi.org/10.7910/DVN/YGIVCD

Dai, J., Dong, J., Yang, S., & Sun, Y., (2021). Identification method of urban fringe area based on spatial mutation characteristics. *Journal of Geo-Information Science*, *23*(8), 1401–1421. https://doi.org/10.12082/dqxxkx.2021.200502

Delmelle, E. C. (2015). Five decades of neighborhood classifications and their transitions: A comparison of four US cities, 1970–2010. *Applied Geography*, *57*, 1–11. https://doi.org/10.1016/j.apgeog.2014.12.002

Elvidge, C. D., Sutton, P. C., Ghosh, T., Tuttle, B. T., Baugh, K. E., Bhaduri, B., & Bright, E. (2009). A Global Poverty Map Derived from Satellite Data. *Computers & Geosciences*, *35*(8), 1652-1660. https://doi.org/10.1016/j.cageo.2009.01.009

Ellison, G., Glaeser, E. L., & Kerr, W. R. (2010). What causes industry agglomeration? Evidence from coagglomeration patterns. *American Economic Review*, *100*(3), 1195-1213. https://doi.org/10.1257/aer.100.3.1195

Fan, J., Ma, T., Zhou, C., Zhou, Y., & Xu, T. (2014). Comparative estimation of urban development in China's cities using socioeconomic and DMSP/OLS night light data. *Remote Sensing*, *6*(8), 7840-7856. https://doi.org/10.3390/rs6087840

Feng, Z., Peng, J., & Wu, J. (2020). Using DMSP/OLS nighttime light data and K–means method to identify urban–rural fringe of megacities. *Habitat International*, *103*, 102227. https://doi.org/10.1016/j.habitatint.2020.102227

Grove, J. M., Cadenasso, M. L.,Pickett, S. T. A., Machlis, G. E., & Burch Jr. W. R. (2015). *The Baltimore School of Urban Ecology*. Yale University Press.

Habitat, UN., Arctic Public Academy of Sciences, & FGUP "Russian State Scientific Research and Design Institute of Urbanistics". (2006, April 26-27). *ANNOTATION of the concept of the United Nations Human Settlements Programme (UN-HABITAT) project: "Sustainable Development of Cities in Arctic Region through the Improvement of their Engineering and Transportation Infrastructure and Personnel Training for Good Urban Governance"*. In: 3rd SAO Meeting, Syktyvkar, Russia. https://hdl.handle.net/11374/681

He, Z., Xu, S., Shen, W., Long, R., & Chen, H. (2017). Impact of urbanization on energy-related CO_2 emission at different development levels: regional difference in China based on panel estimation. *Journal of Cleaner Production*, *140*(Part 3), 1719-1730. https://doi.org/10.1016/j.jclepro.2016.08.155

Hu, X., Qian, Y., Pickett, S. T. A., & Zhou, W. (2020). Urban mapping needs up-to-date approaches to provide diverse perspectives of current urbanization: A novel attempt to map urban areas with nighttime light data. *Landscape Urban Planning*, *195*, 103709. https://doi.org/10.1016/j.landurbplan.2019.103709

Huang, Y., Wu, C., Chen, M., Yang, J., & Ren, H., (2020). A Quantile Approach for Retrieving the "Core Urban-Suburban-Rural" (USR) Structure Based on Nighttime Light. *Remote Sensing*, *12*(24), 4179. https://doi.org/10.3390/rs12244179

Imhoff, M. L., Lawrence, W. T., Stutzer, D. C., & Elvidge, C. D. (1997). A technique for using composite DMSP/OLS "City Lights" satellite data to map urban area. *Remote Sensing of Environment*, *61*(3), 361-370. https://doi.org/10.1016/S0034-4257(97)00046-1

Jia, W., Zhao, S., Zhang, X., Liu, S., Henebry, G. M., & Liu, L. (2021). Urbanization imprint on land surface phenology: The urban-rural gradient analysis for Chinese cities. *Global Change Biology*, *27*(12), 2895-2904. https://doi.org/10.1111/gcb.15602

Li, D., & Li, X. (2015). An overview on data mining of nighttime light remote sensing. *Acta Geodesy and Cartography Sinica*, *44*(6), 591-601.

Li, X., Gong, P., & Liang, L.A. (2015). A 30-year (1984–2013) record of annual urban dynamics of Beijing City derived from Landsat data. *Remote Sensing of the Environment*, *166*, 78-90. https://doi.org/10.1016/j.rse.2015.06.007

Lin, Z., Xu, H., & Huang, S. (2019). Monitoring of the Urban Expansion Dynamics in China's East Coast Using DMSP/OLS Nighttime Light Imagery. *Journal of Geographical Information Science*, *21*(7), 1074-1085.

Liu, S., Shi, K., & Wu, Y. (2022). Identifying and evaluating suburbs in China from 2012 to 2020 based on SNPP–VIIRS nighttime light remotely sensed data. *International Journal of Applied Earth Observation and Geoinformation*, *114*, 103041. https://doi.org/10.1016/j.jag.2022.103041

Liu, Z., He, C., Zhang, Q., Huang, Q., & Yang, Y. (2012). Extracting the dynamics of urban expansion in China using DMSP-OLS nighttime light data from 1992 to 2008. *Landscape and Urban Planning*, *106*(1), 62-72. https://doi.org/10.1016/j.landurbplan.2012.02.013

Lu, L., Zhang, Y., & Luo, T. T. (2014). Difficulties and Strategies in the Process of Population Urbanization: A Case Study in Chongqing of China. *Open Journal of Social Sciences*, *2*(12), 90-95. https://doi.org/10.4236/jss.2014.212013

Luo, T., Zeng, J., Chen, W., Wang, Y., Gu, T., & Huang, C. (2023). Ecosystem services balance and its influencing factors detection in China: A case study in Chengdu-Chongqing urban agglomerations. *Ecological Indicators*, 151, 110330. https://doi.org/10.1016/j.ecolind.2023.110330

Ma, M., Lang, Q., Yang, H., Shi, K., & Ge, W. (2020). Identification of Polycentric Cities in China Based on NPP-VIIRS Nighttime Light Data. *Remote Sensing*, *12*(19), 3248. https://doi.org/10.3390/rs12193248

Ma, Q., He, C., Wu, J., Liu, Z., Zhang, Q., & Sun, Z. (2014). Quantifying spatiotemporal patterns of urban impervious surfaces in China: An improved assessment using nighttime light data. *Landscape Urban Planning*, *130*, 36-49. https://doi.org/10.1016/j.landurbplan.2014.06.009

Ma, T., Zhou, C., Pei, T., Haynie, S., & Fan, J. (2012). Quantitative estimation of urbanization dynamics using time series of DMSP/OLS nighttime light data: A comparative case study from China's cities. *Remote Sensing of Environment*, *124*, 99-107. https://doi.org/10.1016/j.rse.2012.04.018

Ma, T., Zhou, Y., Zhou, C., Haynie, S., Pei, T., & Xu, T. (2015). Night-time light derived estimation of spatiotemporal characteristics of urbanization dynamics using DMSP/OLS satellite data. *Remote Sensing of Environment*, *158*, 453-464. https://doi.org/10.1016/j.rse.2014.11.022

National Bureau of Statistics. (2000-2020). *City Statistical Yearbook*. China Statistics Press: Beijing, China (Accessed:17/09/2023). https://data.cnki.net/yearBook/single?id=N2022040095

Pan, J., & Li, J. (2016). Estimate and Spatio-Temporal Dynamics of Electricity Consumption in China Based on DMSP/OLS Images. *Geographical Research*, *35*(4), 627-638.

Schneider, A., Friedl, M. A., & Potere. D. (2010). Mapping global urban areas using MODIS 500-m data: New methods and datasets based on urban ecoregions. *Remote Sensing of Environment*, *114*(8), 1733-1746. https://doi.org/10.1016/j.rse.2010.03.003

Shi, K., Chen, Y., Yu, B., Xu, T., Li, L., Huang, C., Liu, R., Chen, Z., & Wu, J. (2016). Urban Expansion and Agricultural Land Loss in China: A Multi-scale Perspective. *Sustainability*, *8*(8), 790. https://doi.org/10.3390/su8080790

Shi, K., Wu, Y., Liu, S., Chen, Z., Huang, C., & Cui, Y. (2023). Mapping and evaluating global urban entities (2000–2020): A novel perspective to delineate urban entities based on consistent nighttime light data. GIScience & Remote Sensing, *60*(1), 2161199. https://doi.org/10.1080/15481603.2022.2161199

Su, Y, Chen, X., Wang, C., Zhang, H., Liao, J., Ye, Y., & Wang, C. (2015). A new method for extracting built-up urban areas using DMSP-OLS nighttime stable lights: A case study in the Pearl River Delta, southern China. GIScience & Remote Sensing, *52*(2), 218-238. https://doi.org/10.1080/15481603.2015.1007778

Sun, Y., & Zhao, S. (2018). Spatiotemporal dynamics of urban expansion in 13 cities across the Jing-Jin-Ji urban agglomeration from 1978 to 2015. *Ecological Indicators*, *87*, 302-313. https://doi.org/10.1016/j.ecolind.2017.12.038

Thapa, R. B., & Murayama, Y. (2009). Examining Spatiotemporal Urbanization Patterns in Kathmandu Valley, Nepal: Remote Sensing and Spatial Metrics Approaches. *Remote Sensing*, *1*(3), 534-556. https://doi.org/10.3390/rs1030534

Tian, Y. (2020). Mapping suburbs based on spatial interactions and effect analysis on ecological landscape change: A case study of Jiangsu province from 1998 to 2018, eastern China. *Land*, *9*(5), 159. https://doi.org/10.3390/land9050159

Tian Y., & Qian, J. (2021). Suburban identification based on multi-source data and landscape analysis of its construction land: A case study of Jiangsu Province, China. *Habitat International*, *118*, 102459. https://doi.org/10.1016/j.habitatint.2021.102459

United Nations, Department of Economic and Social Affairs, Population Division (2019). World Urbanization Prospects: The 2018 Revision (ST/ESA/SER.A/420). New York: United Nations. https://population.un.org/wup/publications/Files/WUP2018-Report.pdf

Wijesinghe, W. M. D. C., & Withanage, W. K. N. C. (2021). Detection of the changes in land use and land cover using remote sensing and GIS in Thalawa DS Division. *Prathimana Journal*, *14*(1), 72–86

Withanage, W. K. N. C., Mishra, P. K., & Jayasinghe, B. C. (2024). An Assessment of Spatio-temporal Land Use/Land Cover Dynamics Using Landsat Time Series Data (2008-2022) in Kuliyapitiya West Divisional Secretariat Division in Kurunagala District, Sri Lanka. *Journal of Geospatial Surveying*, *4*(1), 12-23. https://doi.org/10.4038/jgs.v4i1.52

Withanage, N. C., Shi, K., & Shen, J. (2023). Extracting and Evaluating Urban Entities in China from 2000 to 2020 Based on SNPP-VIIRS-like Data. *Remote Sensing*, *15*(18), 4632. https://doi.org/10.3390/rs15184632

Xiao, P., Wang, X., Feng, X., Zhang, X., & Yang, Y. (2014). Detecting China's Urban Expansion over the Past Three Decades Using Nighttime Light Data. *IEEE Journal of Selected Topics in Applied Earth Observations and Remote Sensing*, *7*(10), 4095-4106. https://doi.org/10.1109/JSTARS.2014.2302855

Xu, T., Ma, T., Zhou, C., & Zhou, Y. (2014). Characterizing Spatio-Temporal Dynamics of Urbanization in China Using Time Series of DMSP/OLS Night Light Data. *Remote Sensing*, *6*(8), 7708-7731. https://doi.org/10.3390/rs6087708

Yang, Y., Ma, M., Tan, C., & Li, W. (2017). Spatial Recognition of the Urban-Rural Fringe of Beijing Using DMSP/OLS Nighttime Light Data. *Remote Sensing*, *9*(11), 1141. https://doi.org/10.3390/rs9111141

Yu, B., Tang, M., Wu, Q., Yang, C., Deng, S., Shi, K., Peng, C., Wu, J., & Chen, Z. (2018). Urban Built-Up Area Extraction From Log- Transformed NPP-VIIRS Nighttime Light Composite Data. *IEEE Geoscience and Remote Sensing Letters*, *15*(8), 1279-1283. https://doi.org/10.1109/LGRS.2018.2830797

Yuh, Y. G., Tracz, W., Matthews, H. D., Turner, S. E. (2023). Application of machine learning approaches for land cover monitoring in northern Cameroon. *Ecological Informatics*, *74*, 101955. https://doi.org/10.1016/j.ecoinf.2022.101955

Zhang, Q., & Seto, K. C. (2011). Mapping urbanization dynamics at regional and global scales using multi-temporal DMSP/OLS nighttime light data. *Remote Sensing of Environment*, *115*(9), 2320-2329. https://doi.org/10.1016/j.rse.2011.04.032

Zhang, H., Liang, C., & Pan, Y. (2022). Spatial Expansion of Built-Up Areas in the Beijing-Tianjin-Hebei Urban Agglomeration Based on Nighttime Light Data: 1992-2020. *International Journal of Environmental Research and Public Health*, *19*(7), 3760. https://doi.org/10.3390/ijerph19073760

Zhang, X., Liu, L., Wu, C., Chen, X., Gao, Y., Xie, S., & Zhang, B. (2020). Development of a global 30 m impervious surface map using multi-source and multi-temporal remote sensing datasets with the Google Earth Engine platform. *Earth System Science Data*, *12*(3), 1625-1648. https://doi.org/10.5194/essd-12-1625-2020

Zheng, Y., Tang, L., & Wang, H. (2021). An improved approach for monitoring urban built-up areas by combining NPP-VIIRS nighttime light, NDVI, NDWI, and NDBI. *Journal of Cleaner Production*, *328*, 129488. https://doi.org/10.1016/j.jclepro.2021.129488

Zhou, Q., Li, B., & Sun, B. (2008, July 3-11). *Modelling spatio-temporal pattern of landuse change using multi-temporal remotely sensed imagery*. In: Proceedings of the 21st Congress of the International Society for Photogrammetry and Remote Sensing, ISPRS 2008, (Vol. 37, Part B7), (pp. 729-734), Beijing, China.

Zhou, Y., Smith, S. J., Elvidge, C. D., Zhao, K., Thomson, A., & Imhoff, M. (2014). A cluster-based method to map urban area from DMSP/OLS nightlights. *Remote Sensing of Environment*, *147*, 173-185. https://doi.org/10.1016/j.rse.2014.03.004

Analysis of Frequency and Voltage Dependent Electrical Features of Au/Si3N4/p-GaAs (MIS) Device at Room Temperature

Raziye ERTUĞRUL UYAR[1*] iD

[1] Gazi University, Faculty of Sciences, Department of Physics, Ankara, Türkiye

Keywords	Abstract
Silicon Nitride (Si3N4)	The investigation presented here deals with the comprehensive analysis of the C-V-f and G/ω-V-f characteristics of the Au/Si3N4/p-GaAs (MIS) device. These measurements were performed at 300 K and covered a frequency of between 10 kHz–1 MHz. The determination of the Rs was facilitated by the use of the conductance method, while the evaluation of the Nss of the MIS device was performed according to the Hill-Coleman method. A noteworthy observation concerns the significant frequency dispersion observed in the C-V-f and G/ω-V-f features of the MIS devices, particularly noticeable at low frequencies, which is attributable to the influence of Rs and Nss. Furthermore, the determination of the high-frequency Cm and Gm/ω involved measurements under both reverse and forward-biased conditions, followed by careful adjustments to mitigate the effects of Rs. This meticulous procedure culminated in the derivation of the true capacitance values inherent in semiconductor structure.
MIS Device	
Capacitance	
Conductance	
Series Resistance	
Interface States	

1. INTRODUCTION

The metal-insulator semiconductor structure, frequently referred to as MIS structure, is an essential constituent in semiconductor devices used for various purposes. This structure is fundamental in MISFET/MOSFET transistors mostly used in integrated circuits for electronic devices (Sze, 1981; Rhoderick & Williams, 1988). Understanding surface physics and device functionality is crucial through the assistance of MIS structure, as semiconductor junctions are intricately linked to their surface structures (Reddy et al., 2011). The unquestionable key factor influencing the electrical, optical, and dielectric features of MIS device is the preference for an interfacial layer. This layer may form naturally at the interface between M and S, or it can be deliberately generated at the M/S interface by employing a range of techniques. Additionally, the material's thickness, permittivity and homogeneity equally play crucial roles in determining the mentioned properties (Sevgili et al., 2020; Güneşer et al., 2023). Moreover, the real MIS structure, the semiconductor-insulator interface, has many lattice defects, traps, impurities and interface states. Within the crystalline framework of a semiconductor, the presence of a foreign atom or decomposition, known as interface states, along the insulator-semiconductor boundary results in the emergence of numerous permissible energy levels within the forbidden bandgap (Nicollian & Brews, 1982). This phenomenon exerts a substantial influence on the electronic properties and behavior exhibited by the semiconductor material, manifesting in notable effects across various aspects of its functionality and performance in electronic devices.

The series resistance (R_s) of this MIS device and the density of interface trap/states (N_{ss}) are the other two crucial factors significantly impacting the measurements (Tataroğlu B. et al., 2006; Güçlü et al., 2024). The changes in capacitance within this structure typically do not rely on frequency and are anticipated to rise with

the utilized voltage. Nonetheless, against what was expected to these changes vary significantly in practices, especially at low and medium frequencies, owing to the presence of N_{ss} at the interfacial layer, the influence of R_s, and the selection of the semiconductor interface. N_{ss} typically arise from surface features, lattice defects, surface processing and impurity in the semiconductor. Additionally, R_s arises due to a combination of factors, including the presence of ohmic and back contacts, coupling connections to the gate, and the inherent resistivity of the semiconductor material itself (Osiris et al., 2011).

Silicon nitride (Si_3N_4) constitutes a chemical compound formed through the combination of silicon and nitrogen elements, forming a stable and commonly utilized material in various applications. It exhibits ionic-covalent bonding (70% covalent) and manifests three distinct crystal structures: α, β, and c. While α- Si_3N_4 and β- Si_3N_4 can be acquired under typical nitrogen pressure, the c- Si_3N_4 structure is attainable only under extremely high pressure and temperature. Additionally, Si_3N_4 is a hard, dense refractory material (Riley, 2000). Moreover, silicon nitrate (Si_3N_4), is unremarkably used as an insulator in various electronic and semiconductor devices due to its excellent electrical insulating properties. Known for its exceptional thermal stability, robust mechanical strength and remarkable resistance to chemical corrosion, Silicon Nitride stands out as a reliable material option in a wide range of applications. These properties make it particularly suitable for use in integrated circuits and microelectronics, where reliability and performance are paramount (Buyukbas-Ulusan & Tataroğlu, 2020). Additionally, silicon nitride boasts several noteworthy properties, including but not limited to a low leakage current, a high dielectric permittivity, and a significantly larger energy gap compared to other materials (Jhansirani et al., 2016; Buyukbas-Ulusan & Tataroğlu, 2020).

In this context, the primary aim was to carry out a thorough experimental investigation of the frequency dependency of the C-V and G/ω-V properties in MIS devices, with a major emphasis on the influence of N_{ss} and R_s. In order to deepen our understanding of how N_{ss} and R_s influence these characteristics, a comprehensive series of forward and reverse bias C-V and G/ω-V measurements was meticulously performed over a broad frequency from 10 kHz to 1 MHz, as well as over a wide voltage range from -4 V to +4 V. Moreover, the C and G/ω values were carefully adjusted at elevated frequencies to mitigate the influence of R_s. In addition, careful adjustments were made to the C and G/ω values at higher frequencies to mitigate the effects of R_s, thereby establishing the authentic MIS configuration. The density of interfacial states, which is frequency dependent, was extracted from the C-V and G/ω-V datas by use of the Hill-Coleman technique (Hill & Coleman, 1980).

2. MATERIAL AND METHOD

In this work, Au/Si_3N_4/p-GaAs (MIS) structure was fabricated on p-type gallium arsenide (GaAs). The employed substrate was a 500 μm thick, (100) float zone single crystal wafer of zinc (Zn) loaded p-type gallium arsenide (GaAs) possessing a carrier concentration of 10^{17-18} cm^{-3}. The p-GaAs wafer was chemically cleaned in ammonium peroxide prior to the deposition process. Contaminants on the surface were eliminated by washing the wafer for one minute in a $5H_2SO_4$:H_2O_2:H_2O acidic solution, and then by etching it in an H_2O:HCl solution. After the wafer had been cleaned with 18 MΩ cm ultra-pure water, it was subjected to a dry cleaning process using pure nitrogen. Following the cleaning and etching processes, an ohmic contact was established using high-pure Au metal. A 2000 Å back contact was created on the p-GaAs wafer via thermal evaporation of Au at 375 °C under a vacuum of $3×10^{-6}$ Torr. Next, the wafer underwent a 7-minute annealing process in a nitrogen atmosphere at 475 °C. Following ohmic contact preparation, the wafer was heated to 400 °C in a radio frequency (RF) reactive magnetron sputtering system. Subsequently, the wafer was moved to the storage chamber for silicon nitride (Si_3N_4) film deposition. The Si_3N_4 target was used for the deposition, along with a specific Ar/O_2 reactive gas mixture, both regulated by mass flow controllers. The deposition of the Si_3N_4 thin film was performed by maintaining the wafer temperature at 200 °C and the chamber pressure at $3 × 10^{-6}$ mbar. Following the Si_3N_4 coating, a 2000 Å rectifying contact was established by thermally evaporation of Au as dots onto the Si_3N_4/p-GaAs. The dot's contact area measured at $7.85×10^{-3}$ cm^2 at a temperature of 30°C. This led to the fabrication of the Au/Si_3N_4/p-GaAs (MIS) device. The HP 4192ssoA LF impedance analyzer was utilized to measure the fabricated MIS structure across a broad frequency range at room temperature.

3. RESULTS AND DISCUSSION

Using a parallel RC circuit, the total admittance of the equivalent circuit is determined as $Y = G + i\omega C$ (Sze, 1981; Nicollian & Brews, 1982; Tataroğlu A. et al., 2020). The capacitance-voltage characteristics of MIS/MOS devices to which bias voltage is applied vary according to the accumulation, depletion, and inversion regions. Furthermore, capacitance-voltage (C-V) measurements rely on the interface film's characteristics, the types and electrical features of the MIS device.

The evaluation of the C and G/ω displayed by the $Au/Si_3N_4/p$-GaAs (MIS) device spanned a diverse frequency spectrum, with variations observed alongside changes in bias voltage. Figure 1a and 1b display the C-V and G/ω-V graphs, respectively. It is worth noting that the C-V graphs indicate behaviour consistent with the expected C-V properties of a p-type MIS device. Distinct zones representing accumulation, depletion and inversion phases can be found in each C-V and G/ω-V plot.

Additionally, in the accumulation zone, the C and G/ω values decline as the frequency increases. Conversely, in the inversion region, the C and G/ω values remain constant regardless of frequency. The capacitance-frequency variation is accounted for by the manifestation of interface states at the semiconductor/interface, which has been identified through meticulous analysis (Türkay & Tataroğlu, 2021; Demirezen et al., 2023). The carriers' capacity to track the ac signal is immediately influenced by the specified capacitance worth, which fluctuates with variations in the dielectric constant. Observations indicate that at lower frequencies, the interface states have the tendency to effectively track the alternating current (ac) signal, thus resulting in additional contributions to the capacitance. Nevertheless, as the frequency increases, their ability to track the ac signal diminishes, thereby precluding any further augmentation of the overall capacitance.

The correlation between the capacitance, the conductance, and the frequency at several positive voltages is shown in Figure 2a and 2b. These diagrams reveal that not only C but also G/ω values decline as the voltage and frequency increase. Therefore, this observation is a proof of the presence of states of the interface. Additionally, the outcomes suggest a pronounced reliance between the measures C and G/ω concerning both the applying bias voltage and frequency.
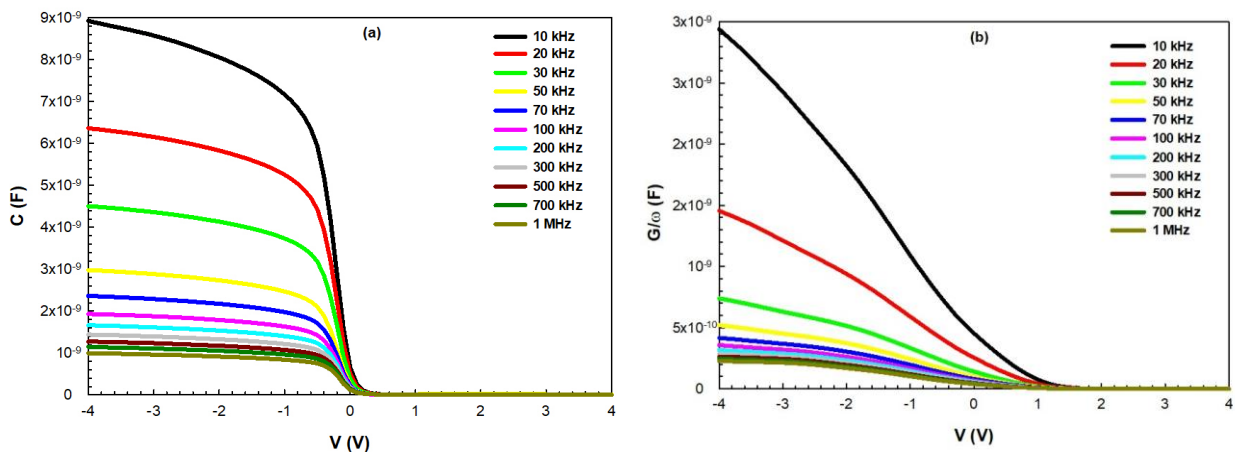
***Figure 1.** a) C-V graphs, b) G/ω-V graphs at various frequencies*

Numerous approaches and techniques have been proposed and investigated to establish the series resistance (R_s) associated with the MIS device. This variety of methods underscores the ongoing efforts within the field to develop comprehensive and accurate means of evaluating this crucial parameter in MIS device characterization and analysis (Nicollian & Brews, 1982). In this investigation, we have utilized the approach established by Nicollian and Goetzberger. The conductivity method was invented by Nicollian and Goetzberger stands out as notably sensitive among the various techniques employed for discerning the interfacial density of states, as well as for determining the time constant of majority carriers and fluctuations in surface potential, especially in regions characterized by weak reversal and depletion (Nicollian & Goetzberger, 1967). The measurement of capacitance (C_{ma}) and conductance (G_{ma}) can be used to define the series resistance (R_s) of the MIS device. The equation for R_s is provided below,

$$R_S = \frac{G_{ma}}{(G_{ma}^{\;2} + C_{ma}^2 w^2)} \tag{1}$$

where ω represents the angular frequency. Figure 3a exhibit the R_s-V graphs for a range of frequencies and Figure 3b exhibit the R_s-Log f graphs for a range of voltages. In Figure 3a, a decrease in R_s values is observed as the frequency increases, a behavior that is related to trapped charges. Additionally, Figure 3b depicts the variation in series resistance (R_s) as it fluctuates with frequency across different positive voltage levels. The graph presents a decrease in R_s values as the frequency increases, whereas the R_s values rise as the voltage increases.
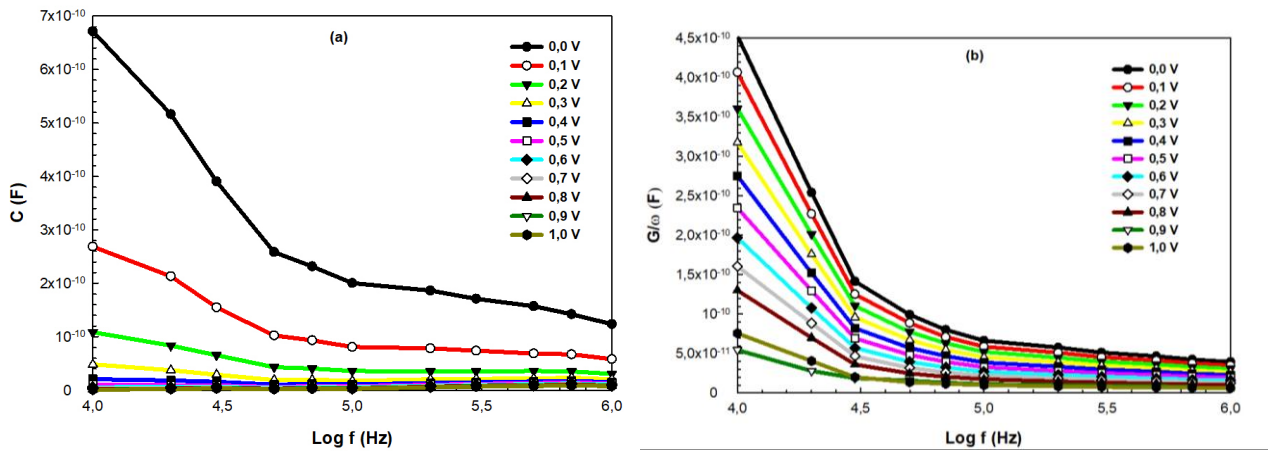
Figure 2. a) C-Log f graphs, b) G/ω-Log f graphs at different positive voltages

In cases where the series resistance (R_s) is present and notably high, it should be noted that the measured conductivity (G_m) and the measured capacitance (C_m) might not accurately represent their true values. In this case the corrected capacitance and conductivity are expressed by C_c and G_c, respectively. Consequently, in order to mitigate the impact of series resistance (R_s) in not only accumulation but also depletion zones, adjustments were made to the capacitance (C_c) and conductance (G_c) by recalibrating the measurements of C and G/ω. Subsequently, the corrected values of capacitance (C_c) and conductance (G_c) were derived using the provided equations (Nicollian & Brews, 1982),

$$C_c = \frac{\left[G_{ma}^2 + (\omega C_{ma})^2\right] C_{ma}}{a^2 + (\omega C_{ma})^2} \tag{2}$$

$$G_c = \frac{G_{ma}^2 + (\omega C_{ma})^2 \, a}{a^2 + (\omega C_{ma})^2} \tag{3}$$

where a is a constant that can be expressed in the form of,

$$a = G_{ma} - \left[G_{ma}^2 + (\omega C_{ma})^2\right] R_s \tag{4}$$

Figure 4a illustrates the variations in both uncorrected and corrected capacitance in response to changes in gate bias at a frequency of 1 MHz, while Figure 4b depicts the corresponding variations in both uncorrected and corrected conductance. This graphical representation provides a comprehensive comparison of the effects of gate bias on capacitance and conductance in both their uncorrected and corrected forms. Within Figure 4a, a

distinct pattern emerges wherein the corrected capacitance values exhibit a notable decrease as the voltage is progressively increased within the accumulation region. Conversely, both uncorrected and corrected capacitance values demonstrate a lack of significant alteration within the depletion and inversion regions. This observation highlights the effectiveness of the correction procedures applied in refining the accuracy of capacitance measurements, particularly in regions where changes were expected to be minimum. Furthermore, upon careful examination of Figure 4b, it becomes apparent that the corrected conductance values exhibit a discernible decline as the voltage decreases within both the accumulation and depletion zones. This trend highlights the sensitivity of the corrected measurements to variations in voltage levels across different operating regions. Additionally, the G_c/ω-V curve depicted in Figure 4b reveals a pronounced peak centered around 0 V within the depletion zone. This particular peak in the data is ascribed to the distribution pattern of charge carriers that occurs specifically at the interface between silicon nitride (Si_3N_4) and p-type gallium arsenide (p-GaAs). In other words, the interface traps can be held accountable for the corrected conductance peak.
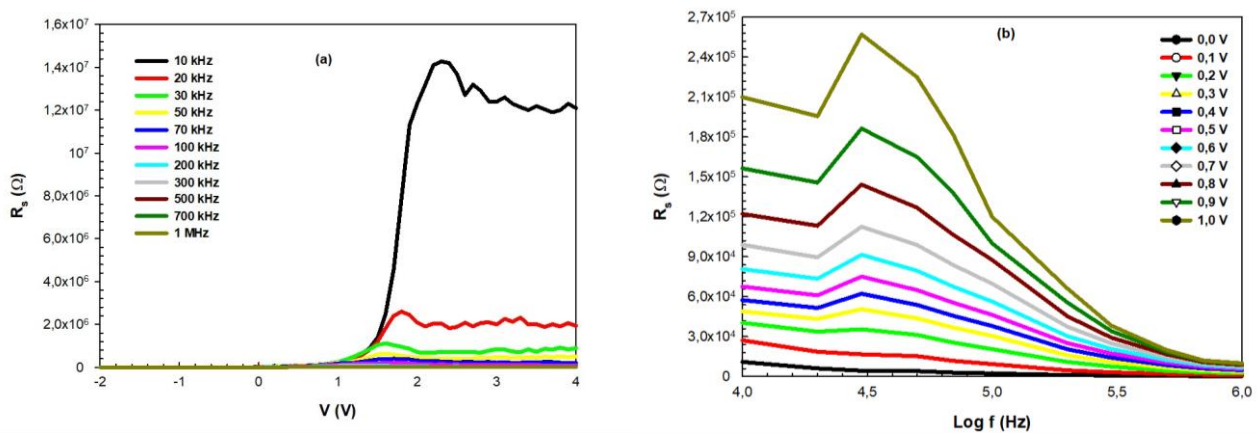
Figure 3. a) R_s-V graphs for a range of frequencies, **b)** R_s-Log f graphs for a range of voltages
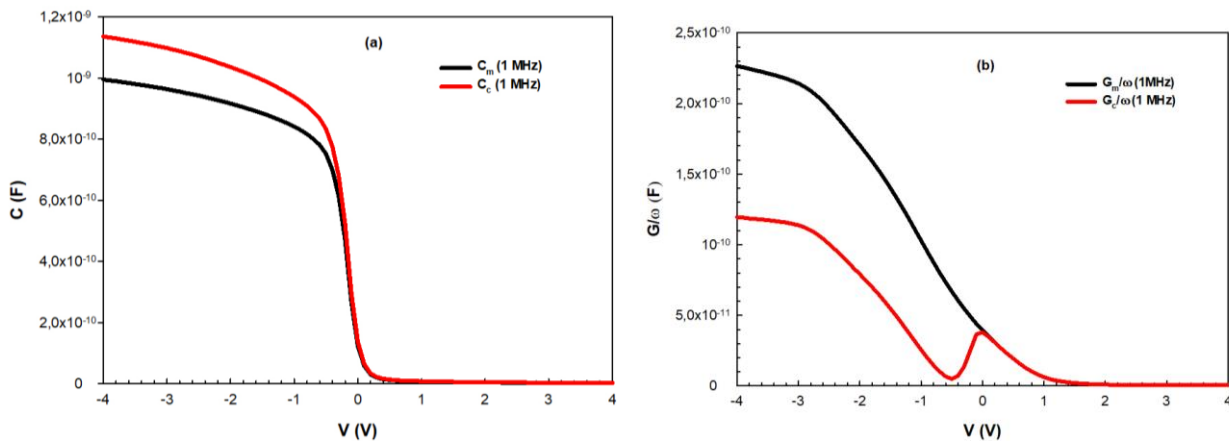
Figure 4. The fluctuations in both the uncorrected and corrected values of **a)** C and **b)** G/ω were examined over a range of gate bias voltages at a frequency of 1 MHz

The calculation of the interface trap/state density (N_{ss}) for the the $Au/Si_3N_4/p$-GaAs (MIS) structure was based on the Hill-Coleman method. With this approach, N_{ss} is expressed as follow (Hill & Coleman, 1980),

$$N_{ss} = \frac{2}{qA} \frac{(G_m/\omega)_{max}}{((G_m/\omega)_{max} C_{ox})^2 + (1 - C_m/C_{ox})^2} \tag{5}$$

where A represents the area of the rectifying contact. The N_{ss} values were derived from Equation (5) and are illustrated in Figure 5. As depicted in Figure 5, as the frequency rises, there is a concurrent decrease in the N_{ss} value. This decline is a consequence of the behavior exhibited by interface charge carriers.
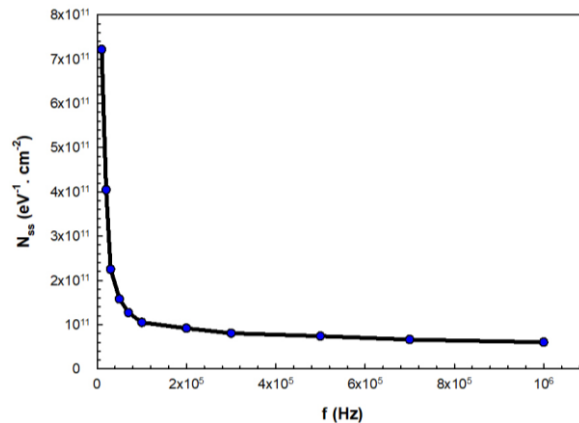
Figure 5. *The changes in N_{ss} with frequency*

4. CONCLUSION

The current research extensively delves into the analysis of the C-V-f and G/ω-V-f properties observed in the Au/Si$_3$N$_4$/p-GaAs (MIS) device. Throughout the investigation, careful attention was paid to the impact of R_s on the C and G/ω parameters, ensuring their accurate representation. It was noted that the R_s values exhibited a decreasing trend with the increase in frequency, while conversely, they showed an upward trend with increasing voltage levels. Hill-Coleman method was used to evaluate the N_{ss}. The obtained results underscore the significant impact of both N_{ss} and R_s on the electrical features of the device. Particularly noteworthy is the inverse relationship observed between N_{ss} values and frequency, indicating a reduction in interface state density as frequency increases. This phenomenon may be ascribed to the behavior of interface charge carriers, shedding light on the intricate dynamics governing the device's performance.

CONFLICT OF INTEREST

The author declares no conflict of interest.

REFERENCES

Buyukbas-Uluşan, A., & Tataroğlu, A. (2020). Electrical characterization of silicon nitride interlayer-based MIS diode. *Journal of Materials Science: Materials in Electronics*, *31*(12), 9888-9893. https://doi.org/10.1007/s10854-020-03533-1

Demirezen, S., Dere, A., Çetinkaya, H. G., Al-Sehemi, A. G., Al-Ghamdi, A.A, & Yakuphanoğlu, F. (2023). Hybrid photonic device based on Graphene Oxide (GO) doped P3HT-PCBM/p-Silicon for photonic applications. *Physica Scripta*, *98*(11), 115916. https://doi.org/10.1088/1402-4896/acfce2

Güçlü, Ç. Ş., Erbilen Tanrıkulu, E., Ulusoy, M., Azizian Kalandargh, Y., & Altındal, Ş. (2024). Frequency-dependent physical parameters, the voltage-dependent profile of surface traps, and their lifetime of Au/(ZnCdS-GO:PVP)/n-Si structures by using the conductance method. *Journal of Materials Science: Materials in Electronics*, *35*(5), 348. https://doi.org/10.1007/s10854-024-12111-8

Güneşer, M. T, Elamen, H., Badali, Y., & Altíndal, Ş. (2023). Frequency dependent electrical and dielectric properties of the Au/(RuO2:PVC)/n-Si (MPS) structures. *Physica B: Condensed Matter*, *657*, 414791. https://doi.org/10.1016/j.physb.2023.414791

Hill, W. A., & Coleman, C. C. (1980). A single-frequency approximation for interface-state density determination. *Solid-State Electronics*, *23*(9), 987-993. https://doi.org/10.1016/0038-1101(80)90064-7

Jhansirani, K., Dubey, R. S., More, M. A., & Singh, S. (2016). Deposition of silicon nitride films using chemical vapor deposition for photovoltaic applications. *Results in Physics*, *6*, 1059-1063. https://doi.org/10.1016/j.rinp.2016.11.029

Nicollian, E. H., & Brews, J. R. (1982). *MOS (Metal Oxide Semiconductor) Physics and Technology*. Wiley, New York.

Nicollian, E. H., & Goetzberger, A. (1967). The Si-SiO₂ Interface - Electrical Properties as Determined by the Metal-Insulator-Silicon Conductance Technique. *Bell System Technical Journal*, *46*(6), 1055-1133. https://doi.org/10.1002/j.1538-7305.1967.tb01727.x

Osiris, W. G., Farag, A. A. M., & Yahia, I. S. (2011). Extraction of the device parameters of Al/P3OT/ITO organic Schottky diode using J–V and C–V characteristics. *Synthetic Metals*, *161*(11-12), 1079-1087. https://doi.org/10.1016/j.synthmet.2011.03.019

Reddy, V. R., Reddy, M. S. P., Lakshmi, B. P., & Kumar, A. A. (2011). Electrical characterization of Au/n-GaN metal-semiconductor and Au/SiO₂/n-GaN metal-insulatorsemiconductor structures. *Journal of Alloys and Compounds*, *509*(31), 8001-8007. https://doi.org/10.1016/j.jallcom.2011.05.055

Rhoderick, E. H., & Williams, R. H. (1988). *Metal-Semiconductor Contacts (Monographs in Electrical and Electronic Engineering* (2nd Ed.). Oxford: Clarendon Press.

Riley, F. L. (2000). Silicon Nitride and Related Materials. *Journal of the American Ceramic Society*, *83*(2), 245-265. https://doi.org/10.1111/j.1151-2916.2000.tb01182.x

Sevgili, Ö., Azizian-Kalandaragh, Y., & Altındal, Ş. (2020). Frequency and voltage dependence of electrical and dielectric properties in metal-interfacial layer-semiconductor (MIS) type structures. *Physica B: Condensed Matter*, *587*, 412122. https://doi.org/10.1016/j.physb.2020.412122

Sze, S. M. (1981). *Physics of Semiconductor Devices* (2nd Ed.). Newyork: Wiley.

Tataroğlu, A., Altındal, Ş., & Azizian-Kalandaragh, Y. (2020). C-V-f and G/ω-V-f characteristics of Au/(In2O3-PVP)/n-Si (MPS) structure. *Physica B: Condensed Matter*, *582*, 411996. https://doi.org/10.1016/j.physb.2020.411996

Tataroğlu, B., Altındal Ş., & Tataroğlu A. (2006). The C–V–f and G/ω–V–f characteristics of Al/SiO2/p-Si (MIS) structures. *Microelectronic Engineering*, *83*(10), 2021-2026. https://doi.org/10.1016/j.mee.2006.04.002

Türkay, S., & Tataroğlu A. (2021). Complex dielectric permittivity, electric modulus and electrical conductivity analysis of Au/Si3N4/p-GaAs (MOS) capacitor. *Journal of Materials Science: Materials in Electronics*, *32*(9), 11418-11425. https://doi.org/10.1007/s10854-021-05349-z

Estimation of Organ Doses in Pediatric Patients for Different Imaging Protocols and Examinations

Turan ŞAHMARAN[1*] iD

[1] Hatay Mustafa Kemal University, Kırıkhan Vocational School, Hatay, Türkiye

Keywords	Abstract
CT $CTDI_{vol}$ VirtualDose Pediatric Dose	In this study, the Volume Computed Tomography Dose Index (CTDIvol) Dose Length Product (DLP), effective patient doses (ED), and organ doses were calculated for pediatric patients aged 0, 1, 5, and 10 years undergoing computed tomography (CT) examinations using the VirtualDose program, a software designed for reporting such doses. The study utilized a Toshiba Aquilion 16 CT scanner. Head, chest, and pelvis CT scans were simulated with commonly used kVp, mAs, and pitch values. The results indicated a significant difference in organ doses between standard and low-dose protocols. When kVp and mAs values were increased, ED and organ doses increased by an average of 2.5 times. Conversely, when kVp and mAs values were held constant and pitch value was increased, ED and organ doses decreased by an average of 2 times. Physicians requesting pediatric CT scans should continuously evaluate the requested examinations based on their benefits and risks. To reduce organ doses, scanning protocols should be reviewed, and low-dose protocols should be preferred. Additionally, newer generation devices that provide lower dose scanning should be utilized.

1. INTRODUCTION

Effective pediatric radiology necessitates proper equipment, specialized safety measures, and expertise in ionizing radiation. This poses significant challenges, particularly for developing countries, regarding the acquisition of equipment and implementation of precautions (Kamdem et al., 2021). Today, rapid and accurate imaging techniques are extremely important for the diagnosis and treatment of diseases. One of these techniques is computed tomography (CT). CT is an X-ray imaging method that visualizes the internal structure of the body in detail, facilitating the diagnosis of diseases and guiding treatment processes (AAPM, 2010; Çakmak et al., 2015). X-rays are absorbed at different intensities as they pass through body tissues. CT detects these differences in absorption to produce detailed cross-sectional images. This allows for a detailed map of organs, tissues, and even blood vessels. It is especially widely used for examining internal organs such as the head, chest, abdomen, and pelvis. CT is of vital importance in the diagnosis and monitoring of a wide range of conditions, from cancer diagnosis to post-trauma injuries, brain hemorrhages, and heart diseases. According to the NCRP (2009) report, data obtained in 2006 indicate that CT usage in the United States increased by 8-15% annually over the past 7-10 years. In 2006, approximately half of the total medical radiation exposure was attributed to CT scans (Zhang et al., 2012). During this process, body tissues are exposed to radiation, which can damage organs (Power et al., 2016; Gul et al., 2024). Children are at a higher risk than adults for developing radiation-induced malignancies due to their longer life expectancies and increased tissue radiosensitivity in certain organs (UNSCEAR, 2013; Kost et al., 2015; Power et al., 2016; Journy et al., 2017; Habib Geryes et al., 2019; Gul et al., 2022). Moreover, the lesser amount of fat between organs in children

results in a higher absorbed dose than in adults when using the same technical parameters (Malchair & Maccia, 2020). The UNSCEAR (2013) report recommends avoiding the use of generalized radiation risk estimates for children (UNSCEAR, 2013). Leukemia and brain tumors are among the most common radiation-induced malignancies in children (Pearce et al., 2012; Meulepas et al., 2019). More frequent use of CT scans raises the overall radiation dose (Tahmasebzadeh et al., 2022). Research indicates that pediatric exposed to CT scan radiation have a higher cancer risk compared to their who are not exposed to CT (Mathews et al., 2013; Huang et al., 2014). Therefore, the optimization of imaging parameters to obtain diagnostic information at the lowest possible dose has become a primary goal in pediatric CT imaging (Lee C. et al., 2016; Pace & Borg, 2018; Strauss et al., 2019). Dose optimization in pediatric CT imaging depends on many parameters, including the patient's age, weight, tube voltage (kVp), current (mAs), and pitch factor (Al Mahrooqi et al., 2015; Olgar & Şahmaran, 2017; Priyanka & Sukumar, 2024). The variation of these factors is an effort to balance image quality with radiation dose. To expedite the dose optimization process, it is necessary to continuously evaluate dose levels in hospitals and medical facilities. Therefore, the optimal pitch, kVp, and mAs values for each situation should be carefully adjusted according to the objectives of the scan and the patient's characteristics (Muhogora et al., 2010; Smith-Bindman et al., 2019; Ataç & İnal, 2020). In the literature, there are not many experimental studies on the organ doses that pediatric patients are exposed to during CT scans with different imaging protocols and examinations. The difficulties of working with pediatric patients and the requirement for special permissions are among the reasons for this.

The aim of this study is to calculate the doses received by organs by varying parameters such as pitch factor, kVp, and mAs during head, chest, and pelvis scans using the Virtual Dose (NIBIB, USA) program. Additionally, the Volume Computed Tomography Dose Index (CTDI$_{vol}$), Dose Length Product (DLP), and effective patient doses (ED) were calculated and compared with results from the literature.

2. MATERIAL AND METHOD

Using the Virtual Dose program (Albany, New York, USA), the organ dose, CTDI$_{vol}$, DLP, and ED values for pediatric patients in four different age groups (0 years, 1 year, 5 years, and 10 years) were calculated. Funded by a grant from the National Institute of Biomedical Imaging and Bioengineering (NIBIB), Virtual Dose is designed to improve existing software packages by incorporating validated CT scanner models, scanner-specific correction factors, and the latest ICRP recommendations. It is a program that includes a series of voxel phantoms and 25 anatomically accurate patient phantoms (Ding et al., 2015). VirtualDose™CT is advanced radiation dose simulation software designed for radiologists, radiologic technologists, medical physicists, regulators, manufacturers, and researchers. By utilizing a well-tested anatomically accurate phantom family, revolutionary GPU-based Monte Carlo simulation, and innovative SaaS programming techniques, it enables radiation health professionals to achieve highly accurate images with significantly enhanced patient safety. VirtualDoseCT allows users to assess organ doses in addition to the CTDI$_{vol}$ and DLP data provided by the CT scanner. It can differentiate for individuals outside the "average" population body habitus. It is compatible with the latest CT scanners and adheres to the latest effective dose recommendations from ICRP-60 and ICRP-103. In this study, measurements were taken using a Toshiba Aquilion 16 CT scanner. The Toshiba Aquilion 16 CT scanner has a 16-slice detector with 896 channels, a slice width of 0.5mm, and can reconstruct images at 12 frames per second. It has a large aperture, slip-ring gantry, and extra-wide patient couch. The scanner provides high resolution imaging and has advanced capabilities such as ECG gating and cardiac function analysis. The relationship between CTDI$_{vol}$, DLP, and ED parameters used in dose calculation in CT systems is given below.

$$\text{CTDI}_{vol} = \left(\frac{1}{3} \cdot \text{CTDI}_{Center} + \frac{2}{3} \cdot \text{CTDI}_{Periphery} \right) \Big/ \text{pitch}$$

$$\text{DLP} = \text{CTDI}_{vol} \times \text{lenght of scan (cm)}$$

(1)

$$\text{ED} = \text{DLP} \times k$$

$$\text{CTDI}_{vol} = \text{CTDI}_w / pitch$$

(2)

$$H_E = \sum w_T \, H_T$$

$$H_{T=} Q \, D_T$$

(3)

where, k is a conversion factor (mSv mGy^{-1} cm^{-1}). Pitch is the ratio of the table speed during a 360-degree rotation of the gantry to the thickness of the X-ray beam (collimation). Following the k-factors for adult patients, k-factors for pediatric patients, including newborns and those aged 1, 5, 10, and 15 years, have also been introduced for head and body CT examinations. The k-factors for extended scan regions have been published in the updated EC report, as adopted in the American Association of Physicists in Medicine (AAPM) Report (Shrimpton & Wall, 2000; EC, 2000; McCollough, 2012). w_T is the weighting coefficient for each tissue (T) or organ and H_T is the tissue equivalent dose. Q represents the quality factor of the radiation type, while D_T refers to the absorbed dose at a specific point within a given tissue (ICRP, 1977). Table 1 shows the CT scan parameters. Figure 1 displays the calculation screen in the virtual dose program.

Table 1. Irradiation conditions of CT scan protocols

	Head scan	Chest scan	Pelvis scan
Tube voltage (kVp)	80/100/120	80/100/120	80/100/120
Tube current (mAs)	80/90/100	80/90/100	80/90/100
Pitch factor	0.75/1/1.5	0.75/1/1.5	0.75/1/1.25
CT Manufacturer	Toshiba Aquilion 16	Toshiba Aquilion 16	Toshiba Aquilion 16
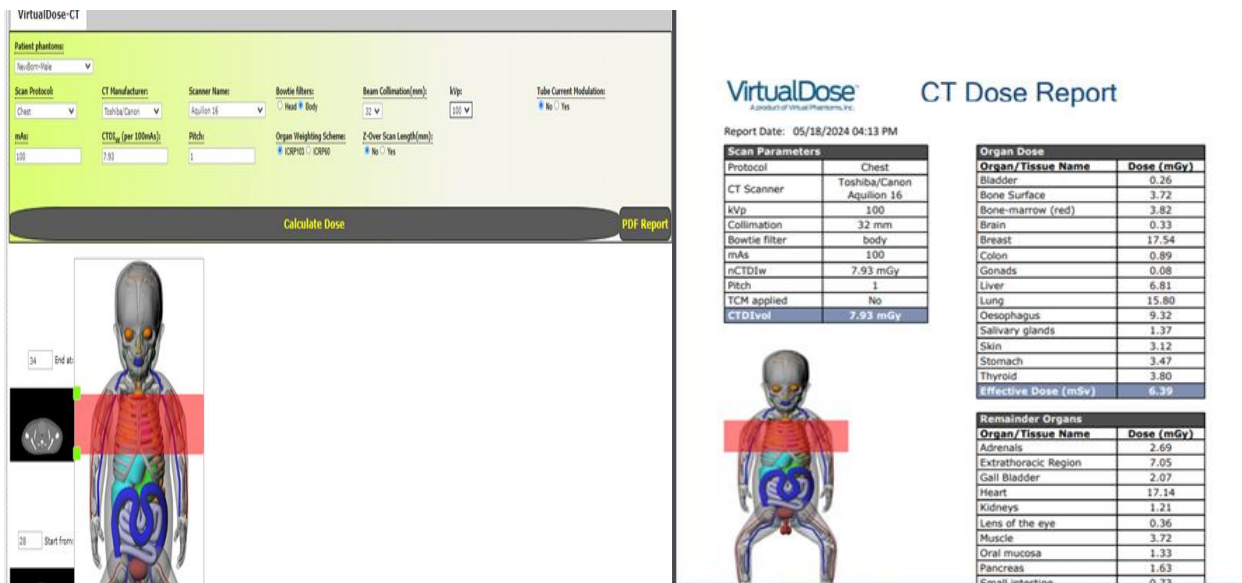
Figure 1. The calculation screen in the virtual dose program.

3. RESULTS AND DISCUSSION

The changes in CTDI$_{vol}$, DLP, and ED values for the head, chest, and pelvis phantoms in the 0-year-old, 1-year-old, 5-year-old, and 10-year-old groups are shown in Tables 2, 3, and 4. In Table 2, in the head_a section, when the mAs and pitch values are kept constant, the ED value obtained at 80 kVp for the 0-year-old is calculated as 1.05 mSv, while at 120 kVp, this value is calculated as 3.05 mSv. An increase of 190.48% is found in the ED value when increased from 80 kVp to 120 kVp. For the 1-year-old, 5-year-old, and 10-year-old groups, when increased from 80 kVp to 120 kVp, the increase in the ED value is found to be 205.31%, 201.01%, and 222.08%, respectively. In Table 2, in the head_b section, when the kVp and pitch values are kept constant, the ED value obtained at 90 mAs for the 0-year-old is found to be 0.75 mSv, while at 110 mAs, this value is found to be 0.92 mSv. An increase of 22.67% is found in the ED value when increased from 90 mAs to 110 mAs. For the 1-year-old, 5-year-old, and 10-year-old groups, when increased from 90 mAs to 110

mAs, the increase in the ED value is found to be 22.22%, 22.35%, and 21.92%, respectively. In Table 2, in the head_c section, a decrease in CTDI$_{vol}$, DLP, and ED values is observed when the pitch value is increased and the kVp and mAs values are kept constant. In Table 1, in the head_c section, when the kVp and mAs values are kept constant, the ED value obtained at a pitch factor of 0.75 for the 0-year-old is found to be 0.52 mSv, while at a pitch of 1.5, this value is found to be 0.26 mSv. When the pitch factor is increased from 0.75 to 1.5, a 50.00% decrease in the ED value is observed. For the 1-year-old, 5-year-old, and 10-year-old groups, when the pitch value is increased from 0.75 to 1.5, the decrease in the ED value is found to be 51.02%, 50.88%, and 48.94%, respectively. There is a linear inverse relationship between the pitch factor and radiation dose. As the pitch factor increases, the dose decreases, and as it decreases, the dose increases.

In Table 2, in the Head_a section, the DLP value has shown an increase with the change in kVp. When increased from 80 kVp to 120 kVp, the DLP value has increased by 174.82%, 174.05%, 174.06%, and 174.06% for the 0-year-old, 1-year-old, 5-year-old, and 10-year-old groups, respectively. In Table 2, in the Head_b section, the DLP value has increased with the change in tube current. When increased from 90 mAs to 110 mAs, the DLP value has increased by 22.23%, 22.24%, 22.21%, and 22.24% for the 0-year-old, 1-year-old, 5-year-old, and 10-year-old groups, respectively. In Table 1, in the Head_c section, the DLP value has decreased as the pitch factor decreased. When the pitch factor increased from 0.75 to 1.5, the DLP value has decreased by 39.17%, 50.00%, 50.00%, and 50.00% for the 0-year-old, 1-year-old, 5-year-old, and 10-year-old groups, respectively.

Table 2. *Comparison of CTDI$_{vol}$ (mGy), DLP (mGy cm), and ED (mSv) values at different kVp, mAs, and pitch values in head scans*

		80 kVp-80mAs-1 pitch			100 kVp-80 mAs-1 pitch			120 kVp-80 mAs-1 pitch		
	Age	CTDI$_{vol}$	DLP	ED	CTDI$_{vol}$	DLP	ED	CTDI$_{vol}$	DLP	ED
Head_a	0	6.40	46.72	1.05	11.35	82.85	1.93	17.54	128.04	3.05
	1		71.68	1.13		127.12	2.14		196.44	3.45
	5		81.92	0.99		145.28	1.85		224.51	2.98
	10		85.76	0.77		152.09	1.51		235.03	2.48
		100 kVp-90mAs-1 pitch			**100 kVp-100 mAs-1 pitch**			**100 kVp-110 mAs-1 pitch**		
	Age	CTDI$_{vol}$	DLP	ED	CTDI$_{vol}$	DLP	ED	CTDI$_{vol}$	DLP	ED
Head_b	0	12.77	93.22	0.75	14.19	103.58	0.84	15.61	113.95	0.92
	1		143.02	0.72		158.92	0.80		174.83	0.88
	5		163.45	0.85		181.63	0.94		199.80	1.04
	10		171.11	0.73		190.14	0.81		209.17	0.89
		80 kVp-90mAs-0.75 pitch			**80 kVp-90 mAs-1 pitch**			**80 kVp-90 mAs-1.50 pitch**		
	Age	CTDI$_{vol}$	DLP	ED	CTDI$_{vol}$	DLP	ED	CTDI$_{vol}$	DLP	ED
Head_c	0	9.60	57.60	0.52	7.20	52.56	0.39	4.80	35.04	0.26
	1		107.52	0.49		80.64	0.36		53.76	0.24
	5		122.88	0.57		92.16	0.43		61.44	0.28
	10		128.64	0.47		114.48	0.36		64.32	0.24

In Table 3, in the chest_a section, when the mAs and pitch values are kept constant, the ED value obtained at 80 kVp for the 0-year-old is calculated as 2.53 mSv, while at 120 kVp, this value is calculated as 7.19 mSv. An increase of 184.19% is found in the ED value when increased from 80 kVp to 120 kVp. For the 1-year-old, 5-year-old, and 10-year-old groups, when increased from 80 kVp to 120 kVp, the increase in the ED value is found to be 197.85%, 202.65%, and 211.11%, respectively.

In Table 3, in the chest_b section, when the kVp and pitch values are kept constant, the ED value obtained at 90 mAs for the 0-year-old is found to be 5.15 mSv, while at 110 mAs, this value is found to be 6.29 mSv. An increase of 22.14% is found in the ED value when increased from 90 mAs to 110 mAs. For the 1-year-old, 5-year-old, and 10-year-old groups, when increased from 90 mAs to 110 mAs, the increase in the ED value is found to be 22.13%, 22.18%, and 21.22%, respectively.

In Table 3, in the chest_c section, when the kVp and mAs values are kept constant, the ED value obtained at a pitch factor of 0.75 for the 0-year-old is found to be 3.80 mSv, while at a pitch of 1.5, this value is found to be 1.90 mSv. A decrease of 50.00% in the ED value is observed when the pitch factor is increased from 0.75 to 1.5. For the 1-year-old, 5-year-old, and 10-year-old groups, when the pitch value is increased from 0.75 to 1.5, the decrease in the ED value is found to be 50.00%, 50.15%, and 50.00%, respectively. In Table 3, in the chest_a section, when increased from 80 kVp to 120 kVp, the DLP value has increased by 174.06%, 174.05%, 174.06%, and 174.06% for the 0-year-old, 1-year-old, 5-year-old, and 10-year-old groups, respectively. In the chest_b section, the DLP value has increased as the tube current increased. When increased from 90 mAs to 110 mAs, the DLP value has increased by 22.24% for the 0-year-old, 1-year-old, 5-year-old, and 10-year-old groups. In the chest_c section, the DLP value has decreased as the pitch factor decreased. When the pitch factor increased from 0.75 to 1.5, the DLP value has decreased by 50.00% for the 0-year-old, 1-year-old, 5-year-old, and 10-year-old groups.

Table 3. *Comparison of CTDI$_{vol}$ (mGy), DLP (mGy cm), and ED (mSv) values at different kVp, mAs, and pitch values in chest scans*

		80 kVp-80mAs-1 pitch			100 kVp-80 mAs-1 pitch			120 kVp-80 mAs-1 pitch		
	Age	CTDI$_{vol}$	DLP	ED	CTDI$_{vol}$	DLP	ED	CTDI$_{vol}$	DLP	ED
Chest_a	0	6.40	38.40	2.53	11.35	68.10	4.58	17.54	105.24	7.19
	1		63.36	2.33		112.36	4.34		173.64	6.94
	5		83.20	2.26		147.55	4.25		228.02	6.84
	10		101.76	1.80		180.46	3.44		278.88	5.60
		100 kVp-90mAs-1 pitch			100 kVp-100 mAs-1 pitch			100 kVp-110 mAs-1 pitch		
	Age	CTDI$_{vol}$	DLP	ED	CTDI$_{vol}$	DLP	ED	CTDI$_{vol}$	DLP	ED
Chest_b	0	12.77	76.62	5.15	14.19	85.14	5.72	15.61	93.66	6.29
	1		126.42	4.88		140.48	5.42		154.53	5.96
	5		166.01	4.78		184.47	5.31		202.93	5.84
	10		203.04	3.87		225.62	4.30		248.19	4.73
		80 kVp-90mAs-0.75 pitch			80 kVp-90 mAs-1 pitch			80 kVp-90 mAs-1.50 pitch		
	Age	CTDI$_{vol}$	DLP	ED	CTDI$_{vol}$	DLP	ED	CTDI$_{vol}$	DLP	ED
Chest_c	0	9.60	57.6	3.80	7.20	43.2	2.85	4.80	28.8	1.90
	1		95.04	3.50		71.28	2.62		47.52	1.75
	5		124.80	3.39		93.6	2.54		62.4	1.69
	10		152.64	2.70		114.48	2.02		76.32	1.35

In Table 4, in the pelvis_a section, when the mAs and pitch values are kept constant, the ED value obtained at 80 kVp for the 0-year-old is calculated as 1.07 mSv, while at 120 kVp, this value is calculated as 3.08 mSv. An increase of 187.85% is found in the ED value when increased from 80 kVp to 120 kVp. For the 1-year-old, 5-year-old, and 10-year-old groups, when increased from 80 kVp to 120 kVp, the increase in the ED value is found to be 203.48%, 207.14%, and 218.99%, respectively.

In Table 4, in the pelvis_b section, when the kVp and pitch values were kept constant, the ED obtained at 90 mAs was found to be 2.17 mSv at the age of 0, while at 110 mAs, this value was found to be 2.65 mSv. When the mAs was increased from 90 to 110, an increase of 22.12% was observed in the ED value. For the age groups of 1, 5, and 10 years, when the mAs was increased from 90 to 110, the increase in the ED value was found to be 22.41%, 22.01%, and 21.76%, respectively.

In Table 4, in the pelvis_c section, when the pitch value was increased and the kVp and mAs values were kept constant, a decrease was observed in the CDTI$_{vol}$, DLP, and ED values. In Table 1, in the pelvis_c section, when the kVp and mAs values were kept constant, the ED value obtained at a pitch factor of 0.75 was found to be 1.58 mSv at the age of 0, while at a pitch of 1.5, this value was found to be 0.79 mSv. When the pitch factor was increased from 0.75 to 1.5, the decrease in the ED value was found to be 50.00% for each age group.

In Table 4, in the pelvis_a section, according to the variation in kVp, the DLP value increased as the kVp increased. When it increased from 80 kVp to 120 kVp, the DLP value showed an increase of 174.05%,

174.06%, 174.06%, and 174.06% in the age groups of 0, 1, 5, and 10 years, respectively. In Table 4, in the pelvis_b section, according to the variation in tube current, the DLP value increased as the current increased. When it increased from 90 mAs to 110 mAs, the DLP value showed an increase of 22.23%, 22.24%, 22.24%, and 22.24% in the age groups of 0, 1, 5, and 10 years, respectively. In Table 4, in the pelvis_c section, according to the variation in pitch factor, the DLP value showed a decrease as the pitch factor decreased. When the pitch factor was increased from 0.75 to 1.5, the decrease in the DLP value was found to be 50.00% for each age group.

In Tables 2, 3, and 4, the $CTDI_{vol}$ value increased as the kVp increased. When it increased from 80 kVp to 120 kVp, the $CTDI_{vol}$ value showed an increase of 174.06%. According to the variation in tube current, the $CTDI_{vol}$ value increased as the current increased. When it increased from 90 mAs to 110 mAs, the $CTDI_{vol}$ value showed an increase of 22.24%. Regarding the variation in pitch factor, the $CTDI_{vol}$ value showed a decrease as the pitch factor increased. When the pitch factor increased from 0.75 to 1.5, it was calculated that the $CTDI_{vol}$ value decreased by 50.00%.

In the study conducted by Ataç et al. (2015), for head scans, the $CTDI_{vol}$ values were found to be 31 mGy, 33.4 mGy, and 40.3 mGy for <1 year, 1-5 years, and 5-10 years age groups, respectively. For chest scans, the values were 13.6 mGy, 13.5 mGy, and 13.5 mGy, and for pelvis scans, they were 11.1 mGy, 12 mGy, and 13.3 mGy, respectively.

Table 4. *Comparison of $CTDI_{vol}$ (mGy), DLP (mGy cm), and ED (mSv) values at different kVp, mAs, and pitch values in pelvis scans*

		80 kVp-80mAs-1 pitch			100 kVp-80 mAs-1 pitch			120 kVp-80 mAs-1 pitch		
	Age	$CTDI_{vol}$	DLP	ED	$CTDI_{vol}$	DLP	ED	$CTDI_{vol}$	DLP	ED
Pelvis_a	0		35.84	1.07		63.56	1.93		98.22	3.08
	1		57.60	1.15		102.15	2.14		157.86	3.49
	5	6.40	67.84	0.98	11.35	120.31	1.85	17.54	185.92	3.01
	10		99.20	0.79		175.92	1.51		271.87	2.52
		100 kVp-90mAs-1 pitch			100 kVp-100 mAs-1 pitch			100 kVp-110 mAs-1 pitch		
	Age	$CTDI_{vol}$	DLP	ED	$CTDI_{vol}$	DLP	ED	$CTDI_{vol}$	DLP	ED
Pelvis_b	0		71.51	2.17		79.46	2.41		87.41	2.65
	1		114.93	2.41		127.71	2.68		140.49	2.95
	5	12.77	135.36	2.09	14.19	150.41	2.32	15.61	165.46	2.55
	10		197.93	1.70		219.94	1.88		241.95	2.07
		80 kVp-90mAs-0.75 pitch			80 kVp-90 mAs-1 pitch			80 kVp-90 mAs-1.50 pitch		
	Age	$CTDI_{vol}$	DLP	ED	$CTDI_{vol}$	DLP	ED	$CTDI_{vol}$	DLP	ED
Pelvis_c	0		53.76	1.58		40.32	1.58		26.88	0.79
	1		86.40	1.70		64.80	1.27		43.20	0.85
	5	9.60	101.76	1.48	7.20	76.32	1.11	4.80	50.88	0.74
	10		148.80	1.16		111.6	0.87		74.40	0.58

The organ dose values obtained from head CT examinations for each age group are summarized in Table 5. In head CT scans, the highest organ dose is associated with the brain (18.30 mGy). Following the brain, salivary glands (8.58 mGy), bone surface (5.80 mGy), and bone marrow (4.89 mGy) had the highest organ doses among all major and other organs. The results indicated that as the kVp and mAs values increased, the doses received by the organs also increased. When the pitch value was increased from 0.75 to 1.5, approximately a 50.00% decrease in organ doses was observed. Among the radiosensitive organs in childhood, the dose absorbed by the red bone marrow, which includes the highest dose, was found to be highest in the 10-year-old group (4.83 mGy). In the 0, 1, and 5-year-old groups, it was found to be 4.13 mGy, 4.33 mGy, and 4.70 mGy, respectively. The absorbed doses in the red bone marrow increased with age in pediatric patients.

Table 5. *The organ doses (mGy) obtained at different kVp, mAs, and pitch values in head scans*

	80/100/120 kVp				90/100/110 mAs				0.75/1/1.5 pitch			
	0	1	5	10	0	1	5	10	0	1	5	10
Bladder	0.01	0.00	0.00	0.00	0.02	0.01	0.00	0.00	0.01	0.00	0.00	0.00
	0.02	0.01	0.01	0.00	0.02	0.01	0.00	0.00	0.01	0.00	0.00	0.00
	0.03	0.01	0.01	0.01	0.03	0.01	0.01	0.01	0.01	0.00	0.00	0.00
Bone surface	1.73	1.76	0.93	0.96	3.76	3.91	2.12	2.18	2.60	2.64	1.40	1.65
	3.35	3.47	1.88	1.94	4.18	4.34	2.36	2.42	1.95	1.98	1.05	1.08
	5.50	5.80	3.19	3.29	4.60	4.78	2.59	2.66	1.30	1.32	1.70	0.72
Red bone marrow	1.30	1.31	1.37	1.43	2.83	2.92	3.12	3.24	1.95	1.97	2.06	2.10
	2.51	2.59	2.78	2.88	3.14	3.24	3.47	3.61	1.46	1.47	1.55	1.60
	4.13	4.33	4.70	4.89	3.45	3.56	3.89	3.97	0.97	0.98	1.03	1.07
Brain	6.45	5.45	4.34	4.56	13.52	11.58	9.47	10.01	9.68	8.18	6.51	6.85
	11.67	10.31	8.42	8.90	14.58	12.88	10.52	11.12	7.26	6.13	4.88	5.13
	18.30	16.60	13.76	14.60	16.04	14.17	11.57	12.23	4.84	4.09	3.26	3.42
Breast	0.08	0.06	0.05	0.02	0.18	0.14	0.13	0.05	0.12	0.09	0.08	0.04
	0.16	0.12	0.12	0.05	0.20	0.15	0.15	0.06	0.09	0.06	0.06	0.03
	0.25	0.22	0.21	0.09	0.22	0.17	0.16	0.07	0.06	0.04	0.04	0.02
Colon	0.02	0.01	0.00	0.00	0.04	0.02	0.01	0.00	0.03	0.01	0.01	0.01
	0.04	0.02	0.01	0.00	0.04	0.02	0.01	0.00	0.02	0.01	0.00	0.00
	0.07	0.03	0.02	0.01	0.05	0.02	0.01	0.01	0.01	0.00	0.00	0.00
Gonads	0.00	0.01	0.00	0.00	0.01	0.00	0.00	0.00	0.01	0.00	0.00	0.00
	0.01	0.00	0.01	0.00	0.01	0.00	0.00	0.00	0.01	0.00	0.00	0.00
	0.02	0.02	0.01	0.01	0.02	0.00	0.01	0.01	0.00	0.00	0.00	0.00
Liver	0.05	0.03	0.02	0.01	0.13	0.07	0.06	0.03	0.08	0.04	0.04	0.03
	0.11	0.06	0.06	0.02	0.14	0.08	0.07	0.03	0.06	0.03	0.03	0.01
	0.19	0.11	0.10	0.04	0.15	0.09	0.08	0.04	0.04	0.02	0.02	0.01
Lung	0.14	0.11	0.15	0.06	0.32	0.25	0.34	0.14	0.22	0.16	0.22	0.15
	0.29	0.22	0.30	0.13	0.36	0.28	0.38	0.16	0.16	0.12	0.17	0.07
	0.47	0.38	0.51	0.22	0.39	0.31	0.42	0.17	0.11	0.08	0.11	0.04
Oesophagus	0.20	0.24	0.23	0.11	0.45	0.57	0.55	0.26	0.30	0.36	0.35	0.18
	0.40	0.51	0.49	0.23	0.50	0.63	0.61	0.29	0.23	0.27	0.26	0.12
	0.65	0.85	0.83	0.41	0.55	0.70	0.67	0.32	0.15	0.18	0.17	0.08
Salivary glands	1.26	1.00	4.32	2.48	2.65	2.23	9.05	5.29	1.90	1.50	6.47	3.54
	2.35	1.98	8.04	4.71	2.94	2.48	10.06	5.88	1.42	1.12	4.85	2.79
	3.74	3.27	7.33	8.58	3.24	2.73	11.06	6.47	0.95	0.75	3.24	1.86
Skin	1.24	1.07	0.80	0.55	2.44	2.15	1.62	1.12	1.86	1.61	1.21	0.84
	2.17	1.91	1.44	0.99	2.71	2.39	1.81	1.24	1.39	1.21	0.90	0.62
	3.35	3.27	2.27	1.56	2.98	2.63	1.99	1.37	0.93	0.80	0.60	0.41
Stomach	0.04	0.03	0.02	0.01	0.09	0.07	0.05	0.02	0.06	0.04	0.03	0.02
	0.08	0.06	0.05	0.02	0.10	0.08	0.06	0.02	0.04	0.03	0.02	0.01
	0.13	0.10	0.09	0.03	0.11	0.09	0.07	0.03	0.03	0.02	0.02	0.01
Thyroid	0.57	0.35	0.49	0.30	1.26	0.83	1.10	0.72	0.86	0.53	0.74	0.69
	1.12	0.74	1.01	0.64	1.41	0.93	1.26	0.80	0.63	0.40	0.55	0.34
	1.82	1.25	1.70	1.39	1.55	1.03	1.38	0.88	0.44	0.27	0.37	0.22

Table 6 displays the doses received by organs at different kVp, mAs, and pitch values in chest scans. In chest CT scans, the highest organ dose is received by the breast (20.00 mGy). Following the breast, the doses received by the lungs (18.01 mGy), oesophagus (11.68 mGy), and stomach (6.62 mGy) are observed. In chest scans, the dose values received by the gonads at 80 kVp are 0.03 mGy, 0.02 mGy, 0.01 mGy, and 0.01 mGy for the age groups of 0, 1, 5, and 10 years, respectively. When the kVp value is increased to 120, these values are found to be 0.09 mGy, 0.06 mGy, 0.03 mGy, and 0.02 mGy, respectively.

***Table 6.** The organ doses (mGy) obtained at different kVp, mAs, and pitch values in chest scans*

	80/100/120 kVp				90/100/110 mAs				0.75/1/1.5 pitch			
	0	**1**	**5**	**10**	**0**	**1**	**5**	**10**	**0**	**1**	**5**	**10**
Bladder	0.08	0.04	0.02	0.01	0.19	0.10	0.06	0.02	0.13	0.06	0.03	0.01
	0.17	0.09	0.05	0.02	0.21	0.11	0.07	0.02	0.10	0.04	0.02	0.01
	0.28	0.16	0.10	0.03	0.23	0.12	0.07	0.02	0.06	0.03	0.02	0.00
Bone Surface	1.34	1.36	1.26	0.98	2.89	3.01	2.82	2.23	2.01	2.04	1.89	1.47
	2.57	2.67	2.50	1.98	3.21	3.34	3.13	2.48	1.50	1.53	1.42	1.10
	4.21	4.44	4.19	3.35	3.53	3.68	3.44	2.73	1.00	1.02	0.94	0.74
Bone-marrow	1.38	1.42	1.23	0.97	2.97	3.12	2.76	2.21	2.06	2.12	1.84	1.45
	2.64	2.78	2.45	1.96	3.33	3.47	3.07	2.45	1.55	1.59	1.38	1.09
	4.62	4.61	4.11	3.32	3.63	3.82	3.37	2.70	1.03	1.06	0.92	0.72
Brain	0.11	0.08	0.06	0.05	0.25	0.20	0.14	0.12	0.17	0.12	0.08	0.07
	0.22	0.18	0.13	0.11	0.28	0.22	0.16	0.13	0.19	0.09	0.06	0.05
	0.37	0.30	0.22	0.19	0.31	0.24	0.17	0.15	0.08	0.06	0.04	0.04
Breast	7.33	5.35	5.56	4.43	14.48	11.00	11.52	9.23	10.99	8.03	8.34	6.64
	12.87	9.77	10.24	8.20	16.09	12.22	12.80	10.25	8.25	6.02	6.25	4.98
	20.00	15.58	16.41	13.18	17.70	13.44	14.08	11.28	5.50	4.01	4.17	3.32
Colon	0.32	0.17	0.14	0.10	0.69	0.40	0.33	0.26	0.48	0.25	0.20	0.15
	0.61	0.35	0.29	0.23	0.76	0.44	0.36	0.29	0.36	0.19	0.15	0.12
	0.98	0.60	0.50	0.41	0.84	0.49	0.40	0.32	0.24	0.13	0.10	0.08
Gonads	0.03	0.02	0.01	0.01	0.06	0.04	0.02	0.01	0.04	0.02	0.02	0.00
	0.06	0.03	0.02	0.01	0.07	0.04	0.02	0.01	0.03	0.01	0.01	0.00
	0.09	0.06	0.03	0.02	0.08	0.05	0.02	0.01	0.02	0.01	0.01	0.00
Liver	2.65	1.74	2.71	2.12	5.42	3.71	5.82	4.64	3.97	2.61	4.07	3.18
	4.82	3.30	5.17	4.13	6.03	4.13	6.47	5.16	2.98	1.96	3.05	2.38
	7.56	5.30	8.36	6.76	6.43	4.54	7.11	5.68	1.99	1.31	2.03	1.59
Lung	6.25	6.22	5.41	4.85	12.70	12.81	11.28	10.30	9.38	9.33	8.11	7.28
	11.29	11.39	10.03	9.15	14.11	14.23	12.53	11.44	7.03	7.00	6.08	5.46
	17.71	18.01	15.97	14.74	15.52	15.66	13.79	12.59	4.69	4.66	4.06	3.59
Oesophagus	3.50	3.78	3.22	2.79	7.38	8.08	7.12	6.32	5.25	5.67	4.83	4.19
	6.53	7.19	6.33	5.61	8.17	8.99	7.91	7.02	3.94	4.26	3.62	3.14
	10.44	11.68	10.35	9.35	8.98	9.89	8.70	7.72	2.63	2.84	2.41	2.09
Salivary glands	0.50	0.51	0.26	0.21	1.06	1.12	0.60	0.49	0.76	0.76	0.39	0.31
	0.94	0.99	0.54	0.43	1.18	1.24	0.67	0.54	0.57	0.55	0.30	0.23
	1.51	1.63	0.90	0.74	1.29	1.37	0.74	0.59	0.38	0.35	0.29	0.15
Skin	1.31	1.17	1.00	0.86	2.58	2.34	2.02	1.75	1.96	1.75	1.50	1.29
	2.29	2.08	1.81	1.55	2.86	2.59	2.25	1.94	1.47	1.31	1.13	0.97
	3.53	3.23	2.80	2.44	3.15	2.85	2.47	2.13	0.98	0.88	0.75	0.65
Stomach	1.31	1.67	2.13	1.18	2.73	3.58	4.60	2.67	1.92	2.50	3.20	1.78
	2.42	3.18	4.09	3.37	3.03	3.98	5.11	2.37	1.45	1.88	2.40	1.33
	3.83	5.13	6.61	3.94	3.33	4.58	6.62	3.26	0.94	1.25	1.60	0.89
Thyroid	1.45	2.00	0.81	0.73	2.99	4.24	1.79	1.68	2.17	2.99	1.21	1.10
	2.65	3.77	1.59	1.49	3.32	4.71	1.99	1.86	1.63	2.25	0.91	0.82
	4.17	6.04	2.61	2.48	3.65	5.19	2.19	2.05	1.08	1.50	0.61	0.55

Table 7 presents the doses received by organs at different kVp, mAs, and pitch values in pelvis scans. In pelvic CT scans, the highest organ dose is received by the bladder (18.77 mGy). Following the bladder, the doses received by the gonads (14.29 mGy), colon (8.23 mGy), and skin (3.27 mGy) are observed. In pelvic scans, the dose values received by the gonads at 80 kVp are 1.18 mGy, 2.36 mGy, 5.09 mGy, and 3.39 mGy for the age groups of 0, 1, 5, and 10 years, respectively. When the kVp value is increased to 120, these values are found to be 3.33 mGy, 6.61 mGy, 14.29 mGy, and 9.68 mGy, respectively.

Table 7. *The organ doses (mGy) obtained at different kVp, mAs, and pitch values in pelvis scans*

	80/100/120 kVp				90/100/110 mAs				0.75/1/1.5 pitch			
	0	**1**	**5**	**10**	**0**	**1**	**5**	**10**	**0**	**1**	**5**	**10**
Bladder	6.70 12.03 18.77	5.57 10.49 16.83	5.84 10.84 17.26	4.69 9.17 15.03	13.53 15.03 16.54	11.80 13.11 14.42	12.20 13.55 14.91	10.31 11.46 12.61	10.05 7.54 5.02	8.36 6.27 4.18	8.76 6.57 4.38	7.04 5.28 3.52
Bone Surface	0.53 1.04 1.73	0.47 0.69 1.62	0.69 1.42 2.42	0.75 1.57 2.70	1.17 1.33 1.43	1.08 1.20 1.32	1.60 1.77 1.95	1.76 1.96 2.15	0.80 0.60 0.40	0.70 0.53 0.35	1.04 0.78 0.52	1.13 0.84 0.56
Bone-marrow	0.06 1.17 1.93	0.52 1.02 1.80	0.51 1.17 2.00	0.61 1.27 2.18	1.31 1.46 1.60	1.19 1.33 1.46	1.32 1.47 1.62	1.42 1.58 1.74	0.89 0.67 0.47	0.78 0.59 0.39	0.86 0.65 0.43	0.91 0.68 0.46
Brain	0.01 0.02 0.03	0.01 0.01 0.01	0.01 0.00 0.01	0.01 0.00 0.00	0.02 0.02 0.03	0.01 0.01 0.01	0.01 0.01 0.01	0.01 0.00 0.01	0.01 0.01 0.01	0.01 0.00 0.00	0.01 0.00 0.00	0.01 0.00 0.00
Breast	0.05 0.11 0.18	0.02 0.04 0.08	0.01 0.02 0.03	0.00 0.01 0.02	0.12 0.13 0.15	0.05 0.06 0.07	0.02 0.02 0.02	0.01 0.01 0.02	0.08 0.06 0.04	0.03 0.02 0.01	0.01 0.01 0.00	0.01 0.00 0.00
Colon	1.73 3.10 4.83	2.74 5.13 8.23	1.37 2.59 4.16	0.82 1.63 2.70	3.48 3.87 4.27	5.77 6.41 7.06	2.92 3.23 3.56	1.84 2.04 2.25	2.59 1.89 1.30	4.11 3.08 2.05	2.06 1.55 1.03	1.23 0.92 0.61
Gonads	1.18 2.15 3.33	2.36 4.25 6.61	5.09 9.13 14.29	3.39 6.16 9.68	2.41 2.68 2.95	4.78 5.31 5.84	10.48 11.42 12.56	6.93 7.71 8.48	1.77 1.33 0.89	3.54 2.65 1.77	7.64 5.73 3.82	5.09 3.82 2.54
Liver	0.32 0.60 0.96	0.26 0.53 0.89	0.06 0.14 0.25	0.04 0.10 0.18	0.67 0.75 0.82	0.59 0.66 0.73	0.16 0.18 0.21	0.11 0.12 0.13	0.47 0.35 0.24	0.38 0.29 0.19	0.09 0.07 0.05	0.06 0.05 0.03
Lung	0.09 0.18 0.30	0.06 0.14 0.29	0.02 0.04 0.06	0.01 0.03 0.05	0.20 0.23 0.25	0.16 0.17 0.19	0.03 0.04 0.05	0.02 0.02 0.04	0.14 0.10 0.07	0.10 0.07 0.05	0.02 0.02 0.01	0.02 0.01 0.01
Oesophagus	0.07 0.19 0.32	0.04 0.08 0.14	0.01 0.03 0.05	0.01 0.04 0.05	0.21 0.24 0.26	0.09 0.11 0.13	0.03 0.04 0.05	0.02 0.03 0.04	0.13 0.09 0.06	0.05 0.04 0.03	0.02 0.01 0.01	0.01 0.01 0.00
Salivary glands	0.02 0.04 0.06	0.01 0.02 0.03	0.00 0.01 0.01	0.00 0.00 0.01	0.04 0.04 0.05	0.02 0.02 0.03	0.01 0.01 0.01	0.01 0.01 0.02	0.03 0.02 0.01	0.02 0.01 0.01	0.01 0.01 0.00	0.01 0.01 0.00
Skin	1.22 2.12 3.27	1.09 1.94 3.02	0.83 1.48 2.31	0.82 1.47 2.31	2.35 2.39 2.45	2.19 2.43 2.67	1.66 1.85 2.03	1.66 1.84 2.03	1.82 1.37 0.91	1.64 1.23 0.82	1.24 0.93 0.62	1.23 0.92 0.61
Stomach	0.38 0.73 1.17	0.32 0.65 1.09	0.07 0.16 0.28	0.05 0.13 0.24	0.82 0.95 1.00	0.73 0.82 0.90	0.18 0.20 0.22	0.15 0.17 0.19	0.57 0.43 0.28	0.47 0.35 0.24	0.11 0.08 0.05	0.08 0.06 0.04
Thyroid	0.03 0.06 0.11	0.02 0.04 0.07	0.01 0.01 0.02	0.00 0.00 0.01	0.07 0.08 0.09	0.05 0.06 0.07	0.01 0.01 0.01	0.01 0.01 0.02	0.04 0.03 0.02	0.03 0.02 0.01	0.01 0.00 0.00	0.01 0.00 0.00

In many studies, reducing the kVp value has a greater impact on the dose received by organs than reducing the mAs value. To reduce patient dose, it is necessary to reduce the kVp value (Szucs-Farkas et al., 2009; Lee S. M. et al., 2013; Li et al., 2013; Sarpün et al., 2019). In these studies, contrast-enhanced scans recommend lower kVp values for children and thin patients, while higher kVp values are recommended for obese patients (Schimmöller et al., 2014). In our study, as well, the changes in organ doses due to variations in kVp values in head, chest, and pelvic scans are higher compared to changes in mAs values. Similarly to adults, pediatric CT scans have been reported to use kVp values between 120 and 140 in recent years, whereas these values have

decreased to between 80 kVp and 120 kVp (Frush et al., 2003). In their study, Shah et al. (2005) stated that there was no significant change in image quality as a result of reducing the mAs value in pediatric patients. Kamel et al. (1994) mentioned in their study that there was no significant difference in image quality or diagnostic accuracy in imaging protocols ranging from 80 mAs to 240 mAs. In our study as well, an increase in organ doses was observed with an increase in the mAs value.

4. CONCLUSION

CT is an important tool for pediatric diagnosis. However, minimizing the radiation dose given to children and preventing unnecessary scans are even more crucial. Physicians and technicians can significantly reduce exposure to children by using special imaging protocols. The brain received the highest organ dose in head CT scans, the breast received the highest organ dose in chest scans and the bladder received the highest organ dose in pelvis scans. As kVp and mAs values increased, $CTDI_{vol}$, ED and DLP values also increased. In addition, $CTDI_{vol}$ and DLP values decreased linearly as the pitch value increased. All clinicians requesting pediatric CT scans should continually assess the benefits and risks of the requested examination. Many studies have shown that high kVp or mAs values are not necessary for a good CT scan. Children, pregnant women, and patients undergoing repeated scans are particularly at risk. Exposure to high radiation doses can lead to serious health problems such as cancer. There are several strategies for reducing organ doses. Firstly, screening protocols should be reviewed, and low-dose protocols should be preferred. Secondly, devices that provide lower dose scanning due to technological advancements should be used. Additionally, regular calibration and adjustments are important for reducing radiation doses.

CONFLICT OF INTEREST

The author declares no conflict of interest.

REFERENCES

AAPM. (2010). *Comprehensive Methodology for the Evaluation of Radiation Dose in X-Ray Computed Tomography*. Report of the American Association of Physicists in Medicine Task Group 111. Report No. 111. https://doi.org/10.37206/109

Al Mahrooqi, K. M. S., Ng, C. K. C., & Sun, Z. (2015). Pediatric Computed Tomography Dose Optimization Strategies: A Literature Review. *Journal of Medical Imaging and Radiation Sciences*, *46*(2), 241-249. https://doi.org/10.1016/j.jmir.2015.03.003

Ataç, G. K., & İnal, T. (2020). BT İncelemelerde Görüntü Kalitesi ve Artefaktlar. *Türk Radyoloji Seminerleri*, *8*(1), 110-128. https://doi.org/10.5152/trs.2020.842

Ataç, G. K., Parmaksız, A., İnal, T., Bulur, E., Bulgurlu, F., Öncü, T., & Gündoğdu, S. (2015). Patient doses from CT examinations in Turkey. *Diagnostic and Interventional Radiology*, *21*(5), 428-434. https://doi.org/10.5152/dir.2015.14306

Çakmak, E. D., Tuncel, N., & Sindir, B. (2015). Assessment of organ dose by direct and indirect measurements for a wide bore X-ray computed tomography unit that used in radiotherapy. *International Journal of Medical Physics, Clinical Engineering and Radiation Oncology*, *4*(2), 132-142. https://doi.org/10.4236/ijmpcero.2015.42017

Ding, A., Gao, Y., Liu, H., Caracappa, P. F., Long, D. J., Bolch, W. E., Liu, B., & Xu, X. G. (2015). VirtualDose: a software for reporting organ doses from CT for adult and pediatric patients. *Physics in Medicine & Biology*, *60*(14), 5601. https://doi.org/10.1088/0031-9155/60/14/5601

EC. (2000). *European Guidelines on Quality Criteria for Computed Tomography*. European Commission Report No: EUR 16262.

Frush, D. P., Donnelly, L. F., & Rosen, N. S. (2003). Computed tomography and radiation risks: what pediatric health care providers should know. *Pediatrics*, *112*(4), 951-957. https://doi.org/10.1542/peds.112.4.951

Gul, O. V., Sengul, A., & Demir, H. (2024). Effects of radiation at different dose rates on hematologic parameters in rats. *Journal of Radiation Research and Applied Sciences*, *17*(2), 100873. https://doi.org/10.1016/j.jrras.2024.100873

Gul, O. V., Basaran, H., & Inan, G. (2022). Evaluation of incidental testicular dose with thermoluminescence dosimetry during prostate radiotherapy. *Medical Dosimetry*, *47*(3), 203-206. https://doi.org/10.1016/j.meddos.2022.02.007

Habib Geryes, B. H., Hornbeck, A., Jarrige, V., Pierrat, N., Ducou Le Pointe, H., & Dreuil, S. (2019). Patient dose evaluation in computed tomography: a French national study based on clinical indications. *Physica Medica*, *61*, 18-27. https://doi.org/10.1016/j.ejmp.2019.04.004

Huang, W.-Y., Muo, C.-H., Lin, C.-Y., Jen, Y.-M., Yang, M.-H., Lin, J.-C., Sung, F-C., & Kao, C.-H. (2014). Paediatric head CT scan and subsequent risk of malignancy and benign brain tumour: a nation-wide population-based cohort study. *British Journal of Cancer*, *110*(9), 2354-2360. https://doi.org/10.1038/bjc.2014.103

ICRP. (1977). *Recommendations of the International Commission on Radiological Protection*. International Commission on Radiological Protection Publication 26.

Journy, N. M. Y., Lee, C., Harbron, R. W., McHugh, K., Pearce, M. S., & Berrington de González, A. (2017). Projected cancer risks potentially related to past, current, and future practices in paediatric CT in the United Kingdom, 1990–2020. *British Journal of Cancer*, *116*(1), 109-116. https://doi.org/10.1038/bjc.2016.351

Kamdem, F. E., Ngano, S. O., Alla Takam, C., Fotue, A. J., Abogo, S., & Fai, C. L. (2021). Optimization of pediatric CT scans in a developing country. *BMC Pediatrics*, *21*, 44. https://doi.org/10.1186/s12887-021-02498-2

Kamel, I. R., Hernandez, R. J., Martin, J. E., Schlesinger, A. E., Niklason, L. T., & Guire, K. E. (1994). Radiation dose reduction in CT of the pediatric pelvis. *Radiology*, *190*(3), 683-687. https://doi.org/10.1148/radiology.190.3.8115611

Kost, S. D., Fraser, N. D., Carver, D. E., Pickens, D. R., Price, R. R., Hernanz-Schulman, M., & Stabin, M. G. (2015). Patient-specific dose calculations for pediatric CT of the chest, abdomen and pelvis. *Pediatric Radiology*, *45*(12), 1771-1780. https://doi.org/10.1007/s00247-015-3400-2

Lee, C., Pearce, M. S., Salotti, J. A., Harbron, R. W., Little, M. P., McHugh, K., Chapple, C.-L., & Berrington de Gonzalez, A. (2016). Reduction in radiation doses from paediatric CT scans in Great Britain. *The British Journal of Radiology*, *89*(1060), 20150305. https://doi.org/10.1259/bjr.20150305

Lee, S. M., Lee, W., Chung, J. W., Park, E.-A., & Park, J. H. (2013). Effect of kVp on image quality and accuracy in coronary CT angiography according to patient body size: a phantom study. *The international Journal of Cardiovascular Imaging*, *29*(S2), 83-91. https://doi.org/10.1007/s10554-013-0298-3

Li, Q., Yu, H., Zhang, L., Fan, L., & Liu, S.-y. (2013). Combining low tube voltage and iterative reconstruction for contrast-enhanced CT imaging of the chest initial clinical experience. *Clinical Radiology*, *68*(5), e249-e253. https://doi.org/10.1016/j.crad.2012.12.009

Malchair, F., & Maccia, C. (2020). Practical advices for optimal CT scanner dose in children. *Radioprotection*, *55*(2), 117-122. https://doi.org/10.1051/radiopro/2020046

Mathews, J. D., Forsythe, A. V., Brady, Z., Butler, M. W., Goergen, S. K., Byrnes, G. B., Giles, G. G., Wallace, A. B., Anderson, P. R., Guiver, T. A., McGale, P., Cain, T. M., Dowty, J. G., Bickerstaffe, A. C., & Darby, S. C. (2013). Cancer risk in 680 000 people exposed to computed tomography scans in childhood or adolescence: data linkage study of 11 million Australians. *BMJ*, *346*, f2360. https://doi.org/10.1136/bmj.f2360

McCollough, C. H., Chen, G. H., Kalender, W., Leng, S., Samei, E., Taguchi, K., Wang, G., Yu, L., & Pettigrew, R. I. (2012). Achieving routine submillisievert CT scanning: report from the summit on management of radiation dose in CT. *Radiology*, *264*(2), 567-580. https://doi.org/10.1148/radiol.12112265

Meulepas, J. M., Ronckers, C. M., Smets, A. M. J. B., Nievelstein, R. A. J., Gradowska, P., Lee, C., Jahnen, A., van Straten, M., de Wit, M.-C. Y., Zonnenberg, B., Klein, W. M., Merks, J. H., Visser, O., van Leeuwen, F. E., & Hauptmann, M. (2019). Radiation exposure from pediatric CT scans and subsequent cancer risk in the

Netherlands. *JNCI: Journal of the National Cancer Institute*, *111*(3), 256-263. https://doi.org/10.1093/jnci/djy104

Muhogora, W. E., Ahmed, N. A., AlSuwaidi, J. S., Beganovic, A., Ciraj-Bjelac, O., Gershan, V., Gershkevitsh, E., Grupetta, E., Kharita, M. H., Manatrakul, N., Maroufi, B., Milakovic, M., Ohno, K., Ben Omrane, L., Ptacek, J., Schandorf, C., Shaaban, M. S., Toutaoui, N., Sakkas, D., … Rehani, M. M. (2010). Paediatric CT examinations in 19 developing countries: frequency and radiation dose. *Radiation Protection Dosimetry*, *140*(1), 49-58. https://doi.org/10.1093/rpd/ncq015

NCRP. (2009). *Ionizing Radiation Exposure of the Population of the United States*. National Council on Radiation Protection and Measurements Report No.160. Bethesda.

Olgar, T., & Şahmaran, T. (2017). Establishment of radiation doses for pediatric x-ray examinations in a large pediatric hospital in Turkey. *Radiation Protection Dosimetry*, *176*(3), 302-308. https://doi.org/10.1093/rpd/ncx010

Pace, E., & Borg, M. (2018). Optimisation of a paediatric CT brain protocol: a figure-of-merit approach. *Radiation Protection Dosimetry*, *182*(3), 394-404. https://doi.org/10.1093/rpd/ncy078

Pearce, M. S., Salotti, J. A., Little, M. P., McHugh, K., Lee, C., Kim, K. P., Howe, N. L., Ronckers, C. M., Rajaraman, P., Craft, A. W., Parker, L., & Berrington de González, A. (2012). Radiation exposure from CT scans in childhood and subsequent risk of leukaemia and brain tumours: a retrospective cohort study. *The Lancet*, *380*(9840), 499-505. https://doi.org/10.1016/S0140-6736(12)60815-0

Power, S. P., Moloney, F., Twomey, M., James, K., O'Connor, O. J., & Maher, M. M. (2016). Computed tomography and patient risk: Facts, perceptions and uncertainties. *World Journal of Radiology*, *8*(12), 902-915. https://doi.org/10.4329/wjr.v8.i12.902

Priyanka, Kadavigere, R., & Sukumar, S. (2024). Low Dose Pediatric CT Head Protocol using Iterative Reconstruction Techniques: A Comparison with Standard Dose Protocol. *Clinical Neuroradiology*, *34*(1), 229-239. https://doi.org/10.1007/s00062-023-01361-4

Sarpün, İ. H., İnal, A., & Çeçen, B. (2019). Voltaj ve Akım Değerlerinin Hasta Dozu Üzerindeki Etkilerinin CTDI Fantomu ile Araştırılması. *Süleyman Demirel University Faculty of Arts and Science Journal of Science*, *14*(2), 327-334. https://doi.org/10.29233/sdufeffd.605430

Schimmöller, L., Lanzman, R. S., Dietrich, S., Boos, J., Heusch, P., Miese, F., Antoch, G., & Kröpil, P. (2014). Evaluation of automated attenuation-based tube potential selection in combination with organ-specific dose reduction for contrast-enhanced chest CT examinations. *Clinical Radiology*, *69*(7), 721-726. https://doi.org/10.1016/j.crad.2014.02.008

Shah, R., Gupta, A. K., Rehani, M. M., Pandey, A. K., & Mukhopadhyay, S. (2005). Effect of reduction in tube current on reader confidence in paediatric computed tomography. *Clinical Radiology*, *60*(2), 224-231. https://doi.org/10.1016/j.crad.2004.08.011

Shrimpton, P. C., & Wall, B. F. (2000). Reference doses for paediatric computed tomography. *Radiation Protection Dosimetry*, *90*(1-2), 249-252. https://doi.org/10.1093/oxfordjournals.rpd.a033130

Smith-Bindman, R., Wang, Y., Chu, P., Chung, R., Einstein, A. J., Balcombe, J., Cocker, M., Das, M., Delman, B. N., Flynn, M., Gould, R., Lee, R. K., Nelson, T. R., Schindera, S., Seibert, A., Starkey, J., Suntharalingam, S., Wetter, A., Wildberger, J. E., & Miglioretti, D. L. (2019). International variation in radiation dose for computed tomography examinations: prospective cohort study. *BMJ*, *364*, k4931. https://doi.org/10.1136/bmj.k4931

Strauss, K. J., Somasundaram, E., Sengupta, D., Marin, J. R., & Brady, S. L. (2019). Radiation dose for pediatric CT: comparison of pediatric versus adult imaging facilities. *Radiology*, *291*(1), 158-167. https://doi.org/10.1148/radiol.2019181753

Szucs-Farkas, Z., Schaller, C., Bensler, S., Patak, M. A., Vock, P., & Schindera, S. T. (2009). Detection of pulmonary emboli with CT angiography at reduced radiation exposure and contrast material volume: comparison of 80 kVp and 120 kVp protocols in a matched cohort. *Investigative Radiology*, *44*(12), 793-799. https://doi.org/10.1097/RLI.0b013e3181bfe230

Tahmasebzadeh, A., Maziyar, A., Reiazi, R., Kermanshahi, M. S., Anijdan, S. H. M., & Paydar, R. (2022). Pediatric effective dose assessment for routine computed tomography examinations in Tehran, Iran. *Journal of Medical Signals & Sensors*, *12*(3), 227-232. https://doi.org/10.4103/jmss.jmss_115_21

UNSCEAR. (2013). Sources, effects and risks of ionizing radiation. New York: United Nations Scientific Committee on the Effects of Atomic Radiation Report.

Zhang, Y., Li, X., Paul Segars, W., & Samei, E. (2012). Organ doses, effective doses, and risk indices in adult CT: comparison of four types of reference phantoms across different examination protocols. *Medical Physics*, *39*(6Part1), 3404-3423. https://doi.org/10.1118/1.4718710

Arduino Based Flight Control Card Design and Quadcopter Integration

Emirhan GUNES[1*]   iD   Hidir DUZKAYA[1] iD

[1] Gazi University, Faculty of Engineering, Ankara, Türkiye

Keywords	Abstract
UAV (Unmanned Aerial Vehicle) Quadcopter Arduino PID Control	Unmanned aerial vehicles are used quite widely today, especially quadcopters, which we often encounter in areas such as the defense industry, agriculture, and civil aviation. Dec Jul Flight control cards are the products with the highest cost among these products, especially for someone who has a hobby in civilian life or who is curious about electronics and aviation, so it is pretty expensive to supply or produce these vehicles. We are designing and making a cost-effective, easily accessible, and affordable flight control card by using Arduino and Gyroscope sensors in the works we are planning. At the same time, a design is considered one in which the user can code as open-source hardware. The project has two working areas: hardware and software. The work in the hardware field involves designing the flight control board through the drawing program, producing printed circuits for the designed board, and integrating Arduino Mega and other components into this board. On the software side, it is the control algorithm and flight software coding via Arduino IDE. Due to the fact that it has a large number of libraries, it is accessible and understandable to most people, so the Arduino IDE program has been used.

1. INTRODUCTION

Quadcopters are aircraft often encountered in areas such as the defense industry, agriculture, and civil aviation. Especially for people who have hobby purposes in civilian life or are interested in electronics and aviation, the supply of these vehicles is quite costly. When the prices of some flight control cards, which are mostly widely used in competitions, hobbies, and agricultural fields, are approximately examined, it is seen that the "Emlid Navio2" flight control card is 235$, and the "Pixhawk" control card is 230$. The price of the "Flight Control Card with KK2 Display", which is a much less advanced flight control card compared to these flight control cards, is also seen to be around 60$. This project aims to design and manufacture a more cost-effective, easily accessible, and affordable flight control board for quadcopters using Arduino and IMU (Inertial Measurement Unit).

Papa and Del Core (2014) consider the design and installation of a low-cost mini–Unmanned Aerial Vehicle (UAV) quadcopter system in their study. The main goal is to create a lower-cost structure than more expensive alternatives. This quadcopter is designed to be used as a test platform for applying new numerical techniques for air navigation. GPS module is used in the navigation system of the quadcopter. The system consists of customized avionics and a Bluetooth-connected ground control station. The avionics system includes an Arduino ATMEGA2560 controller, GPS antenna, DHT11 heat sensor, BMP180 Pressure sensor, SD card module, and MPU6050 inertial measurement unit. A WIFI/Bluetooth communication method provides wireless communication between the UAV and the ground station. The article details the UAV quadcopter's design, installation, and avionics system. It is also stated that they are working on automatic landing systems

and will study automatic modes in the future. This work includes designing and installing a low-cost UAV system suitable for scientific applications.

Aziz et al. (2020) discuss the design and application of an inexpensive GPS-controlled quadcopter device in their research. The article describes in detail how the quadcopter is designed, how it is assembled, and how it is managed with a modern GPS-based control system. Information is also provided on how the PID control controller increases the system's stability. The GPS-based system determines the flight range of the quadcopter as 500 meters. When the quadcopter goes out of this range with the control, it returns it safely. The project's avionics system uses a NEO 6M GPS sensor, MPU6050 gyro sensor, and Arduino Uno as a microprocessor. The study mentions the products and the control algorithm used in a GPS-controlled quadcopter system. It also provides explanations about the issues necessary for safe flight.

In their article, Vishwakarma et al. (2023) describe the basic steps of designing and building a quadcopter using an Arduino Uno microcontroller. In the study conducted in this article, MPU6050 is used as the acceleration sensor, and Arduino Uno is used as the processor.

Kishor and Singh (2017) discuss designing and developing an Arduino Uno-based quadcopter device. This article started with the increase in technology due to traffic congestion, noise pollution, and air pollution. It emphasized the need to control some air and land traffic to reach one place more quickly. This article proposes a design and development to make the quadcopter economical and efficient using the Arduino Uno board. This design has many applications where the quadcopter equipped with a camera and GPS tracker can be used for surveillance of large areas, such as forest and coast guard applications. In the study, Arduino Uno is used as the processor and L3GD20H is used as the gyro sensor. The article includes designing and developing an Arduino Uno-based quadcopter, describing the hardware components and software applications. It is stated that Arduino Uno is used as the central controller of the quadcopter, and explanations are given about how the device works. In addition, details such as flight calibration of the quadcopter, connection and working principles of hardware components, Arduino code and motor drive tests are included, as well as touching on the potential areas of use of the quadcopter for different applications and future developments.

In their study, Ji and Turkoglu (2015) describe the integration process of an autonomous quadcopter platform and the design of a new Arduino-based software architecture that enables the implementation of advanced control laws on a low-cost ready-made product-based framework. Here, quadcopter dynamics are studied through non-classical equations of motion. The quadcopter is designed, built, and assembled using low-cost, off-the-shelf products to carry a camera payload. This camera payload is planned to be used specifically for surveillance tasks. Arduino Mega is used as the flight control card, Geeetech 10DOF as the gyro sensor, GlobalSat EM 406a as the GPS sensor, SD card module to record flight data and Xbee telemetry to provide data communication by connecting with the ground control station. These components used in the system are given in Ji & Turkoglu (2015). The purpose of the study in this article is to perform surveillance tasks by connecting a camera to it.

Mandal et al. (2016) introduce a design that offers collision detection, avoidance, and control features integrated with Arduino and controlled by Bluetooth. This design offers unique capabilities that provide flight stability, hover control, and landing features. The design is equipped with ultrasonic sensors with integrated accelerometers, which control the speed of the quadcopter and prevent collisions with detected obstacles during flight. HC-05 Bluetooth sensor is used to receive data from the quadcopter; ultrasonic distance sensor is used to avoid collision and to stay in the hover state; Arduino Nano as a processor, MPU6050 as a gyro sensor, and PID control algorithm is used for quadcopter control.

Tagay et al. (2021) focus on deriving a mathematical model of a quadcopter to solve the problem of automatic balancing in their research. The research determines the mathematical model of industrial vehicles and then integrates the characteristic values of the created model into the overall model. The obtained equation is used to determine the control parameters of the quadcopter. This research focuses on developing a cost-effective, self-balancing, and robust control system. Arduino Uno as the microprocessor and MPU6050 as the gyro sensor are used in the study. The main purpose of this study is to design a control system that is maximally

stable for quadcopters using the PID control algorithm. A specially designed balance device is used at the experimental stage.

Akay et al. (2021) conducted an extensive literature review on autopilot systems and solutions. In this literature review, other studies in the literature are evaluated in terms of feature systems and simulation systems used in autopilot systems. Various ideas about autopilots are obtained from this study.

When the literature studies mentioned are examined, it is possible to design and manufacture control cards in an easily accessible and cost-effective way with the developing technology. In this study, an easily accessible, cost-effective, and original design is being made by using the literature and developing technology. With our open-source study, the end user will be able to program the flight control card according to their own wishes. The flight control card consists of two parts, Arduino Mega and shield. The shield design was originally made. Thanks to these two parts, the required part will be replaced with a new one in case of any malfunction, avoiding excessive costs. These features emphasize the originality of our study.

2. MATERIAL AND METHOD

2.1. Receiving Data From MPU6050 Acceleration Sensor

When the literature is researched and the gyroscope sensors used are examined, it is seen that the MPU6050 sensor is most used. The reasons for this are that the sensor is cheap, easy to use and accessible. It was decided to use this sensor to make the project cost effective and accessible. To basically explain the working principle of the MPU6050 sensor, the sensor is a system that can detect angular velocity. In other words, the direction and speed of rotation of a stationary object are determined by comparing the angular rates in three vertical axes. It processes the detected data through the processor and converts it into an electrical signal. This signal is then transmitted to the main processor and processed there according to its purpose. When choosing a microprocessor, the criteria of being easy to use, accessible and cheap were taken into consideration, as in the gyroscope sensor. As a result of these criteria and project requirements, it was decided to use Arduino Mega. After these two products were selected, research was conducted on the use of the MPU6050 sensor as the first stage of the experiments. Then, the connections of the experimental circuit were shown through the block diagram. Circuit connections are made to communicate with the MPU6050 sensor and Arduino Mega I2C protocol. The block diagram is shown in Figure 1. After the necessary connections are made and the controls are provided, the circuit is established in the real environment. After installation, a basic test code was written and tested to see if the sensor was working. The "CONNECTION SUCCESSFUL" statement is made to test whether the IMU sensor is broken or its connections are correct. In Figure 2a, if the connections are correct and the sensor is intact, the "CONNECTION SUCCESSFUL" message and real data will appear. However, in Figure 2b, if the sensor is broken or the connections are incorrect, fixed values and the message "CONNECTION FAILED" appear. The baud rate used in the tests performed is 9600 bps. Communication with microcontrollers and sensors may be more stable at lower speeds. 9600 bps is a common and reliable speed for serial communications, ensuring data transmission is smooth and error rate is low. Communication at higher speeds causes more energy consumption. For this reason, this speed was chosen for low power consumption.
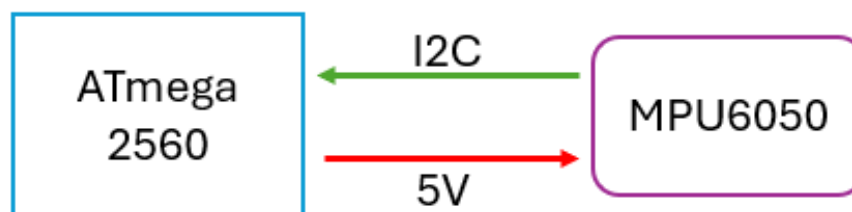

Figure 1. *Connection notation*

```
MPU6050 WORKING EXPERIMENT        MPU6050 WORKING EXPERIMENT
CONNECTION SUCCESSFUL             CONNECTION FAILED
89                                90
98                                90
121                               90
57                                90
74                                90
74                                90
131                               90
105                               90
6                                 90
18                                90
122                               90
167                               90
77                                90
31                                90
61                                90
108                               90
15                                90
91                                90
35                                90
```

(a)   (b)

Figure 2. a) Test successful, b) Test failed

2.2. Motor Testing and Control with Arduino

This step of our work is motor control with microcontroller. A test assembly has been prepared for ESC – motor tests and motor control with microcontroller. Figure 3a shows the shape of the test assembly drawn in the design program, and Figure 3b shows the application. In the test assembly, a potentiometer was used for motor control, a microcontroller, a brushless motor, and an electronic speed controller were used to drive the motor as a processor. The test code was written via Arduino IDE to test the electronic assembly made. A PWM signal drives the electronic speed controller. Basically, PWM is a technique for obtaining the analog electrical value or signal desired to be generated at the output by controlling the widths of the pulse signals to be generated. This technique allows the rotation speeds of brushless motors to be adjusted by giving the desired values to the electronic speed controller.
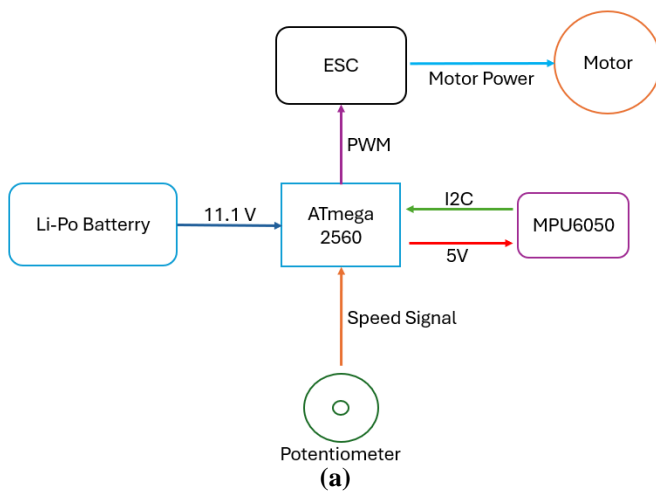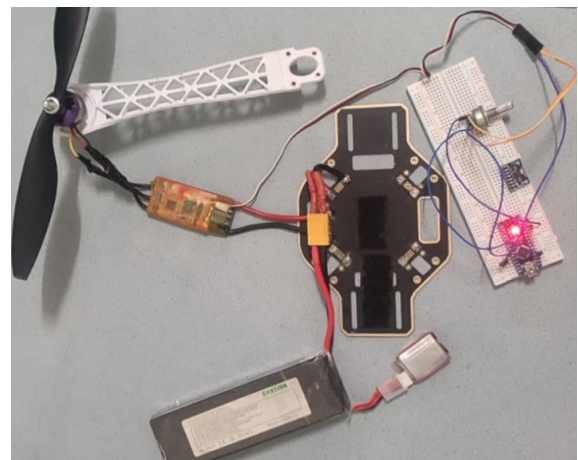
(a)   (b)

Figure 3. a) Block diagram design, b) Applied design

2.3. Ensuring Communication with SBUS Protocol

Research has been conducted on the communication protocol to be used in the project. As a result of this research, four different protocols have been determined: PPM, PWM, I-BUS, and S-BUS. A comparison of these four basic communication protocols used in quadcopters and RC vehicles in various aspects is given in Table 1.

Table 1. Comparison of four protocols

Protocol	Advantages	Disadvantages	Speed	Error Rate
PWM	Simple, compatible	Cable clutter, slow update rate	50 Hz	Low (but noise-sensitive)
PPM	Less cabling, simple	Timing sensitivity, noise-sensitive	50-100 Hz	Slightly higher than PWM
I-BUS	High speed, low latency	Less common, complex	115200 baudrate	Low
S-BUS	High-speed	Complex, compatibility issues	100-300 Hz	Low

Among these protocols, the communication protocol to be used in the project has been selected as SBUS. The reason for choosing this protocol is that communication is provided over a single channel, avoiding over-cabling, and because it is a newly developed protocol, it performs a more stable data flow than other protocols. However, when using this protocol, the data is sent from the controller in a reversed manner. In order to read this inverted data properly, an inverting circuit was used, as shown in Figure 4. Thanks to this circuit, the data received as reversed is reversed again, and its real values are seen. After the circuit installation was provided, the code that prints the data to the serial screen was written on the Arduino IDE thanks to the "FUTABA_SBUS" library, which allows us to use the SBUS protocol more easily. In Figure 5a and Figure 5b, the visuals of the serial display are given. When the images are examined, it is seen that the first value is error, the second value is "roll", the third value is "pitch", the fourth value is "throttle" and the fifth value is "yaw". The error value, which is the first value, tells that there is an error in the system by sending the value "1" in case of possible control or receiver failure. a value of "0" indicates that there are no errors in the system and that it is working correctly.
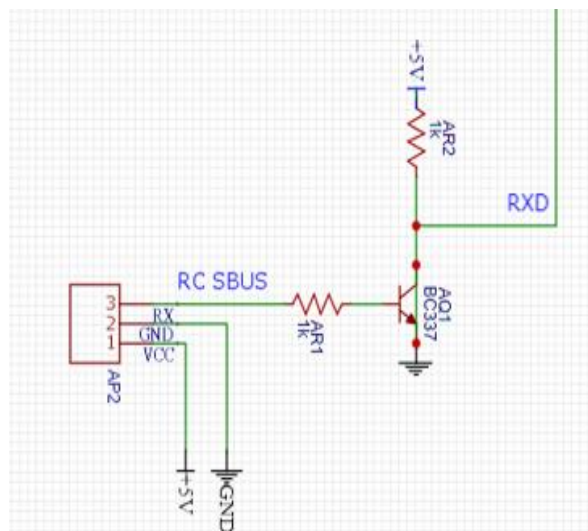

Figure 4. SBUS ınverting schematic circuit

After the installed circuit is successful in the test, the engine driving process is started with the incoming control data. The added ESC and motor are seen in the drawing shown in Figure 6. While making this drawing, a connection is made to pin number 4, one of the pins that generates the PWM signal to start the engine. Figure 7 shows an image of this connection working in a real environment.

```
1,0,0,0,0          0,-20,-13,150,20
1,0,0,0,0          0,-20,-13,150,20
1,0,0,0,0          0,-20,-13,150,20
1,0,0,0,0          0,-20,-13,150,20
1,0,0,0,0          0,-20,-13,150,20
1,0,0,0,0          0,-20,-13,150,20
1,0,0,0,0          0,-20,-13,150,20
1,0,0,0,0          0,-20,-13,150,20
1,0,0,0,0          0,-20,-13,150,20
1,0,0,0,0          0,-20,-13,150,20
1,0,0,0,0          0,-20,-13,150,20
1,0,0,0,0          0,-20,-13,150,20
1,0,0,0,0          0,-20,-13,150,20
1,0,0,0,0          0,-20,-13,150,20
1,0,0,0,0          0,-20,-13,150,20
1,0,0,0,0          0,-20,-13,150,20
1,0,0,0,0          0,-20,-13,150,20
1,0,0,0,0          0,-20,-13,150,20
1,0,0,0,0          0,-20,-13,150,20
```

(a)   **(b)**

***Figure 5. a)** The error value is "1", **b)** The error value is "0"*
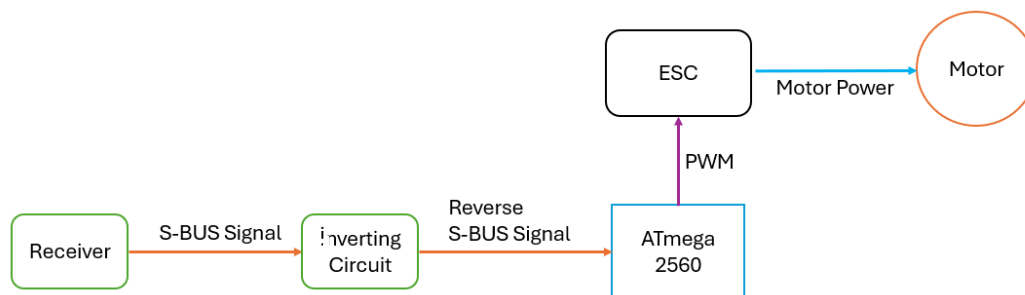
***Figure 6.** Motor driving circuit with S-BUS*
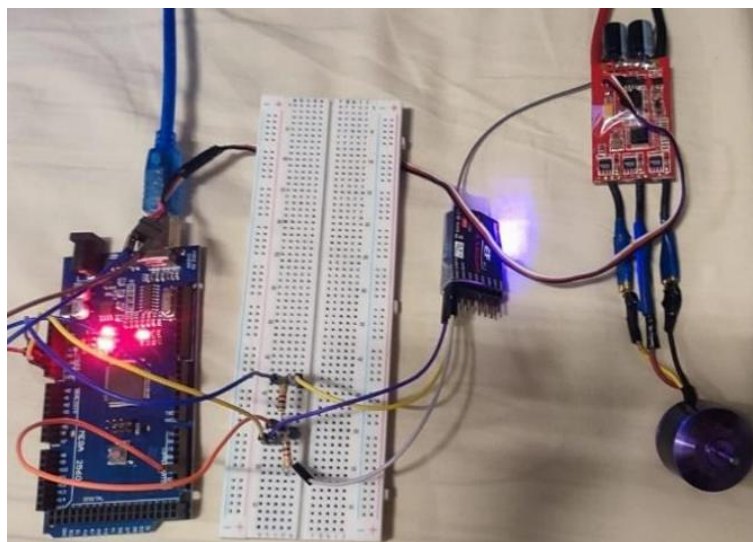
***Figure 7.** The motor circuit in operation*

2.4. Reading "Yaw", "Pitch" and "Roll" Values from MPU6050 Sensor

In order for the PID control algorithm to be used, "Yaw", "Pitch" and "Roll" values must be read from the MPU6050 sensor. The control of the UAV will be carried out using the values here. For this reason, the circuit in Figure 1, which was previously installed, and a new test code were used to check whether these values were entered correctly or not via the serial display. When there is no problem with the connection, the "error" value is 0. If there is any disconnection in the connection, the "error" value is 1. In Figure 8a, it is seen that the

connection is smooth and the angular values "yaw", "pitch" and "roll" come in a smooth format, respectively. Figure 8b shows the images on the serial screen in case of disconnection. It can be seen that all the angular values of the faulty connection are 0.
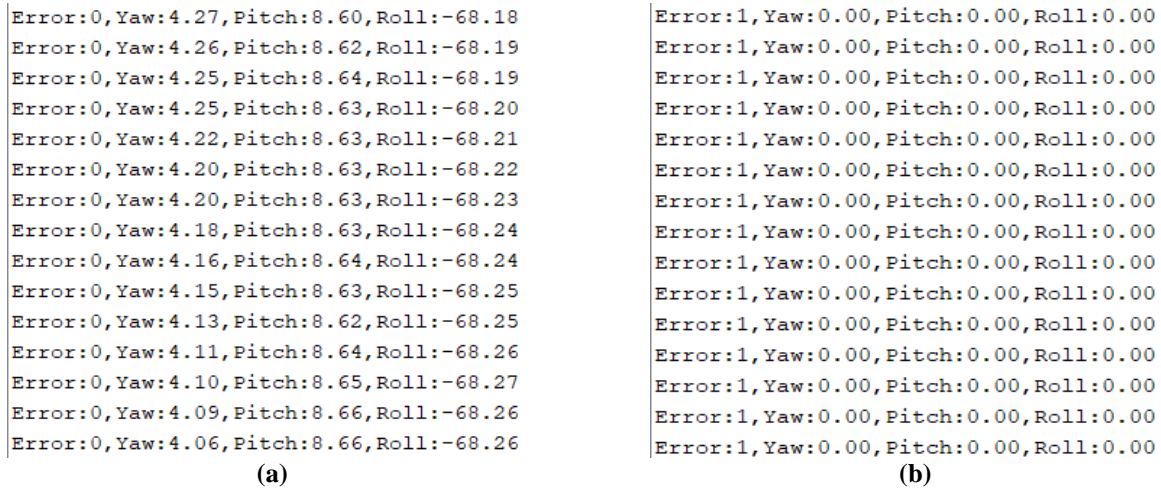
```
Error:0,Yaw:4.27,Pitch:8.60,Roll:-68.18
Error:0,Yaw:4.26,Pitch:8.62,Roll:-68.19
Error:0,Yaw:4.25,Pitch:8.64,Roll:-68.19
Error:0,Yaw:4.25,Pitch:8.63,Roll:-68.20
Error:0,Yaw:4.22,Pitch:8.63,Roll:-68.21
Error:0,Yaw:4.20,Pitch:8.63,Roll:-68.22
Error:0,Yaw:4.20,Pitch:8.63,Roll:-68.23
Error:0,Yaw:4.18,Pitch:8.63,Roll:-68.24
Error:0,Yaw:4.16,Pitch:8.64,Roll:-68.24
Error:0,Yaw:4.15,Pitch:8.63,Roll:-68.25
Error:0,Yaw:4.13,Pitch:8.62,Roll:-68.25
Error:0,Yaw:4.11,Pitch:8.64,Roll:-68.26
Error:0,Yaw:4.10,Pitch:8.65,Roll:-68.27
Error:0,Yaw:4.09,Pitch:8.66,Roll:-68.26
Error:0,Yaw:4.06,Pitch:8.66,Roll:-68.26
```
(a)

```
Error:1,Yaw:0.00,Pitch:0.00,Roll:0.00
Error:1,Yaw:0.00,Pitch:0.00,Roll:0.00
Error:1,Yaw:0.00,Pitch:0.00,Roll:0.00
Error:1,Yaw:0.00,Pitch:0.00,Roll:0.00
Error:1,Yaw:0.00,Pitch:0.00,Roll:0.00
Error:1,Yaw:0.00,Pitch:0.00,Roll:0.00
Error:1,Yaw:0.00,Pitch:0.00,Roll:0.00
Error:1,Yaw:0.00,Pitch:0.00,Roll:0.00
Error:1,Yaw:0.00,Pitch:0.00,Roll:0.00
Error:1,Yaw:0.00,Pitch:0.00,Roll:0.00
Error:1,Yaw:0.00,Pitch:0.00,Roll:0.00
Error:1,Yaw:0.00,Pitch:0.00,Roll:0.00
Error:1,Yaw:0.00,Pitch:0.00,Roll:0.00
Error:1,Yaw:0.00,Pitch:0.00,Roll:0.00
Error:1,Yaw:0.00,Pitch:0.00,Roll:0.00
```
(b)

Figure 8. a) Right connection, b) Faulty connection

2.5. Setting Up the Mechanism for PID and Performing the Test

The fifth step is to set up the mechanism for the PID algorithm and perform the test using the angular data read from the MPU6050 sensor. After reading the "Yaw", "Pitch" and "Roll" values from the MPU6050 sensor, a literature research was conducted on the PID algorithm to be used to control the UAV. In the research, simulation outputs of control systems such as PID, LQR and Adaptive were examined (Altinors & Kuzu, 2021). As a result of the review, it was decided to use the PID control algorithm so that there are many resources about it and users can easily access it. To talk about the PID control algorithm at a basic level, it is a feedback mechanism used in a control system. This algorithm produces a control signal using the error in the system (the difference between the desired value and the actual value). This control signal attempts to reset the error with the closed-loop PID algorithm. PID consists of three main control terms. In the UAV system, optimum values of peak time, settling time, rise time, and overshoot are tried to be achieved by using P, I, and D controls (Kose, 2021; Oktay & Ozen, 2021). Figure 9 shows the general formula of the PID control algorithm. In this formula, u(t) is the control signal, e(t) is the instantaneous error and Kp, Ki and Kd are the coefficients of the terms P, I and D, respectively (Kose, 2021).
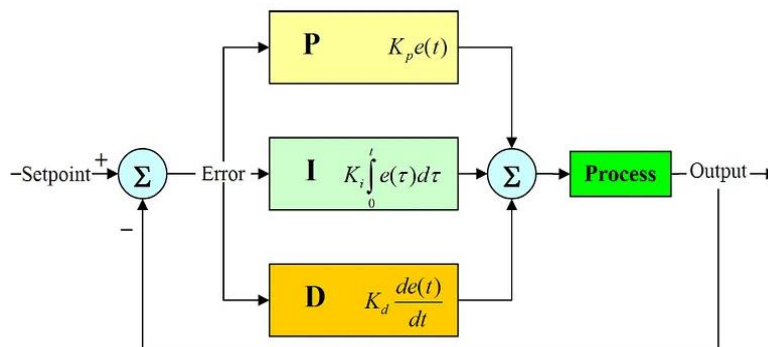

Figure 9. General Representation of PID

A special balance mechanism has been installed so that the algorithm can operate at maximum efficiency and stability (Pehlivan & Akuner, 2020). The "Roll" value was tested in the balance mechanism and the optimum values were tried to be found. There is a motor at both ends of the balance assembly and an MPU6050 sensor at the exact center point. Changes in the arrangement can be measured more stable by having the sensor in the

exact center (Kucuksezer & Sancaktar, 2021). Arduino Mega 2560, which will also be used in the UAV, was used as the microcontroller in the assembly. At the same time, the test device is controlled by signals from the control by using it on the receiver. The device is connected with an elastic rope in such a way that it does not affect the system despite the bad results that may occur in undesirable situations such as sudden gas or sudden operation. Figure 10a shows the oblique, working and balanced stabilizer from the front, while Figure 10b shows the system's appearance that is in operation and remains centrally balanced. When the system is started, the mechanism starts horizontally and stable as shown in Figure 10b, and then it can adjust its position according to the commands from the user. An example of this is the position in Figure 10a. In both images in Figure 10, noise was added to the balanced mechanism by external manual intervention. Despite this noise, their positions in both images were successfully preserved thanks to the PID algorithm used. It can maintain its current position stably without experiencing any saturation in the process of reaching equilibrium. These noises, which emerged from external human intervention, were made separately according to their positions in both images and were successful. It has been found through experiment and observation that the parameters of the PID algorithm here work in optimum condition.

(a)   (b)

Figure 10. a) Oblique and balanced view, b) Central and balanced view

2.6. System Integration

At this stage, the actual status of the product and flight control card will be examined and the necessary configuration settings can be made easily. The design of the system to be used is shown in Figure 11. After the system design is completed, the implementation phase of this system with real products began. At this stage, the necessary products are selected according to calculations, needs and cost (Kazan & Solak, 2023). The criteria for selecting important products are as follows:

Microcontroller: As in every field of study, criteria such as being easily accessible to the user and having many resources available are taken into consideration when choosing a processor. In addition, the number of output pins is quite high compared to other processors, which is very important for future developments. In this way, the user can install external equipment such as GPS and telemetry on the UAV system. Considering these criteria, it is deemed appropriate to use the Arduino Mega 2560 model. Compared to other frequently used Arduino models, it has more Flash Memory (256 KB), SRAM (8 KB), EEPROM (4 KB) memory, UART (4) and GPIO pins. Thanks to these features, it provides easier use for other users. In this way, savings can be made in areas such as time and cost in the later development stages of the study.

Brushless Motor: When selecting the engine, the weight of the UAV and the attainable and high efficiency level of the engine are taken into account. According to these criteria, the user will be able to easily access the engine in case of any problem. As a result of these criteria, it is decided to use the EMAX 980kV brushless motor. When market research is done, it is one of the engines with high thrust and efficiency at low battery voltages. In addition, high efficiency ensures long flight time. The reason for choosing low voltage is to try to keep the weight of the UAV low, because the weight of low voltage batteries is less than others. The reason for using a brushless motor is that it provides high thrust at low voltage values when using a Li-Po battery. Thanks to this feature, brushless motors are the most frequently used motor type in unmanned aerial vehicles.

When the datasheet is examined, the highest thrust can be obtained with 3s Li-Po Battery and 1047 propeller. These values are 880 grams of thrust at 15 ampere current.

ESC (Electronic Speed Controller): In the selection of ESC, the choice is made taking into account the motor and the cost. A cost-effective ESC has been selected to be easily accessible to the user. When determining the values of the ESC, the current drawn by the motor at maximum power is taken into account, and more than 50% is selected as the safety margin. The motor draws about 20 amps at maximum load in the designed system. The 10-ampere safety margin is determined and selected as ESC 30A.

IMU: The ideal and cost-effective sensor for the system has been selected as the acceleration sensor. Designs can be made with different sensors. However, in this study, the most suitable sensor for the user has been selected.

Li-Po Battery: The most efficient operating voltage of the selected motor is indicated in the datasheet as 3S. Based on this information, the cell of the battery has been designated as 3S. If we need to talk about a 3S Battery cell, it means connecting 3 cells in series. The rated voltage of each cell is 3.7 V, and in the case of full charge it is 4.2 V. Li-Po can have very dangerous consequences when used incorrectly. For this reason, proper use is very important. The product selection is made taking into account these criteria.

Later, the electronic and mechanical assemblies of the quadcopter are completed. The image of the completed quadcopter (excluding the flight control card) is shown in Figure 12.
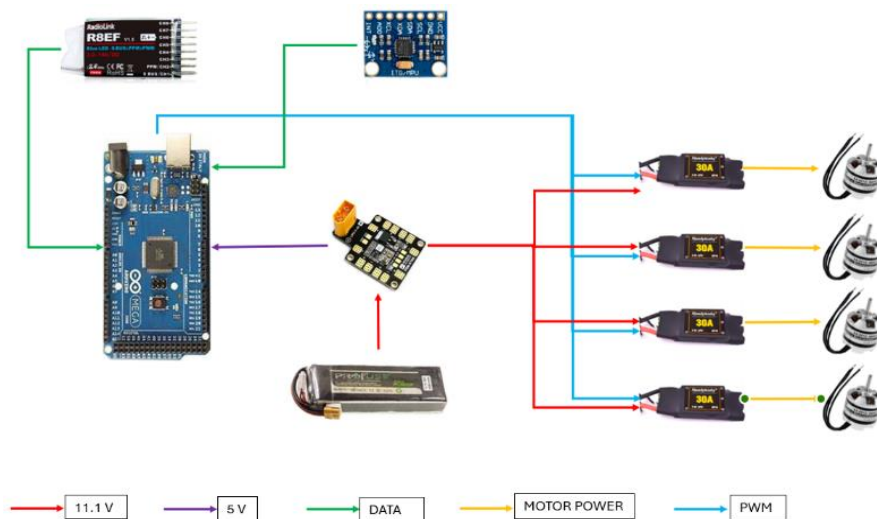

Figure 11. System design

Figure 12. Mounted quadcopter

2.7. Arduino Mega "Shield" Design

This step is the shield design for Arduino Mega used in the Flight Control Board. It is requested to perform some tests of the flight control card on the installed quadcopter. These tests are carried out over the circuit installed on the breadboard. However, stable data could not be obtained due to the large number of cables and the lack of contact on the breadboard. For this reason, it is envisaged that a 'shield' design that will be used both in tests and in the final product will be simpler and more reliable. For this reason, the card design has been started, and the circuits used in previous studies have been drawn on the card. The PCB layout, which is the completed version of the drawing and design, is given in Figure 13a. When this PCB layout is examined, the MPU6050 acceleration and gyro sensor, led and buzzer for warning, output pins for driving motors, SBUS_IN pin for connecting the receiver, UART pins for later development, ON-OFF switch for switching power on and off are used to determine the orientations. The PCB design consists of two layers and is designed to fit completely on top of the microcontroller. There are 5V energy input pins on the PCB to supply the flight control card externally. While the PCB is being designed to be easy to use, the placement of the components and pins have been carefully selected. The 3D image of the designed PCB is shown in Figure 13b.
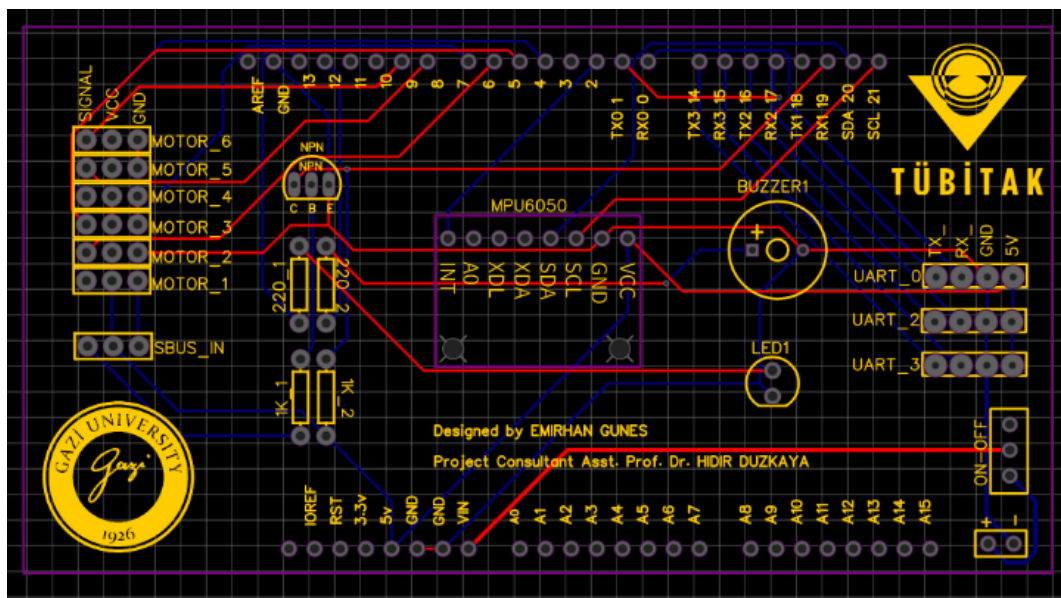
(a)
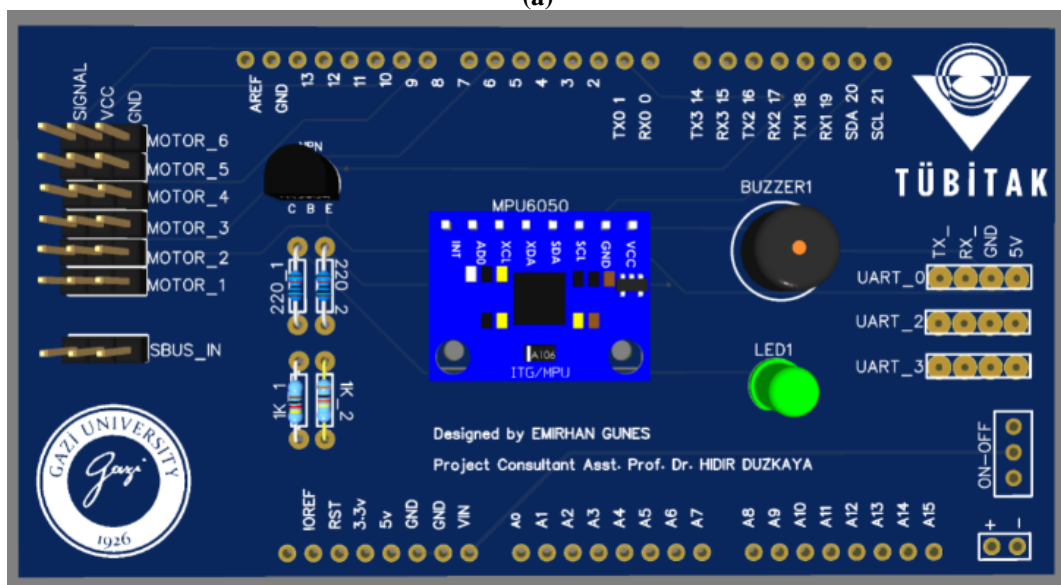
(b)

Figure 13. a) PCB layout, b) 3D view

2.8. Final Product

The final step is the stage of finalizing the product. At this stage, the necessary components are soldered onto the PCB, which has been designed and manufactured. Then, it is integrated into the microcontroller. The Flight Control Card has been finalized by integrating the prototype software prepared during the study process into the processor. The final version of the Flight Control Card is given in Figure 14. This card is integrated into the pre-installed system by making the necessary connections. The final state of the system is given in Figure 15. Additionally, the features of the system are stated in Table 2.
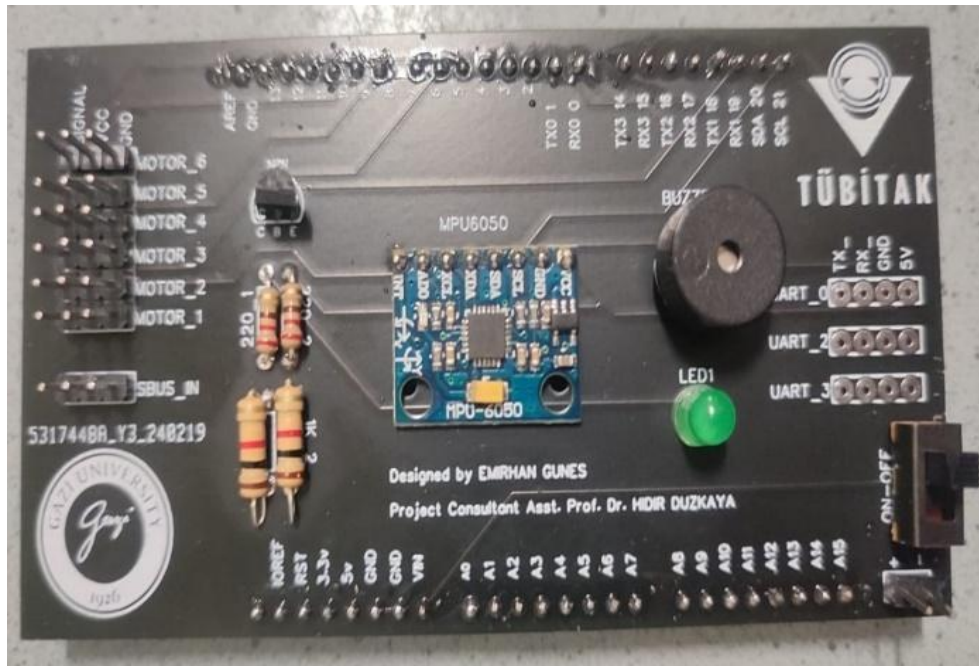
Figure 14. Designed PCB
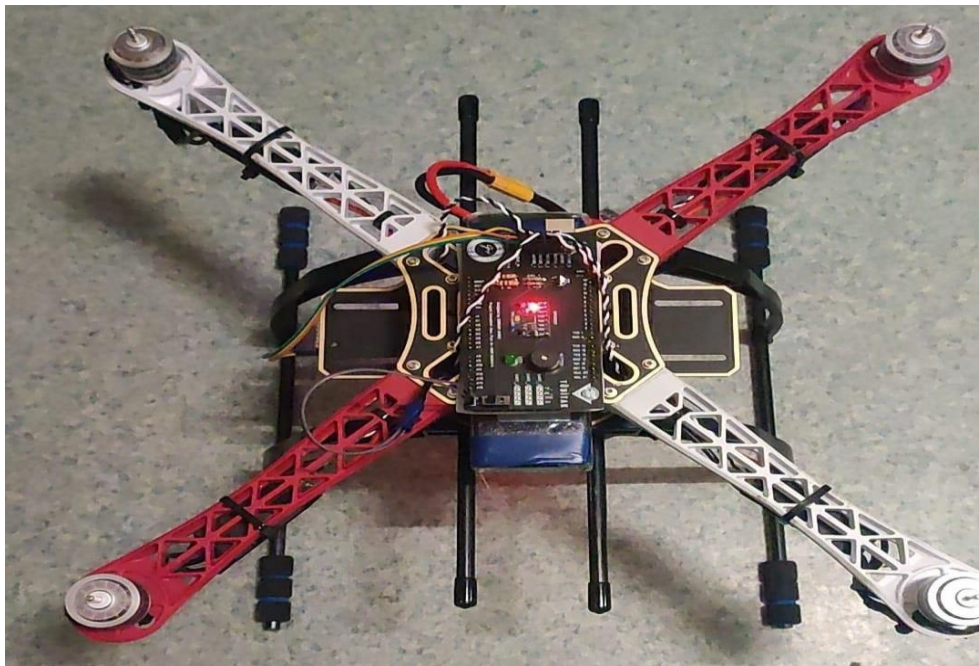
Figure 15. The final product

Table 2. *Product Specifications*

Battery		Total Drive	
Load	13.14 C	Drive Weight	704 g
Voltage	10.47 V	Thrust Weight	2.8 : 1
Rated Voltage	11.1 V	Current Hover	10.77 A
Energy	46.62 Wh	P(in) Hover	119.6 W
Total Capacity	4200 mAh	P(out) Hover	88.8 W
Used Capacity	3360 mAh	Efficiency Hover	% 74.3
Min. Flight Time	3.7 min	Current Max.	54.19 A
Mixed Flight Time	11.0 min	P(in) Max.	601.5 W
Hover Flight Time	17.1 min	P(out) Max.	433.7 W
Weight	324 g	Efficiency Max.	% 72.1
Multicopter		**Motor-Optimum Efficiency**	
All-Up Weight	1000 g	Current	8.14 A
Add. Payload	1420 g	Voltage	10.66 V
Max. Tilt	20°	Revolutions	9359 rpm
Max. Speed	23 km/h	Electric Power	86.8 W
Est. Range	2319 m	Mech. Power	69.5 W
Est. Rate of Climb	8.6 m/s	Efficiency	% 80.1
Total Disc Area	20.27 dm^2		

3. RESULTS AND DISCUSSION

"eCalc" calculation site is used to determine the flight time, maximum speed, efficiency, tilt angle, battery capacity and power consumption values of the final product with the components used in the system. eCalc is a web-based program developed to simulate, calculate, evaluate and design drivers of UAVs and helicopters (Elmas & Alkan, 2023). The results of the calculations made in practice are given in Table 1. When the table is examined, it is seen that the flight time is 17.1 minutes, the current drawn is 10.77 amperes, the maximum speed is 23 km/hour, and the maximum speed is 23 km/hour. is the slope. angle is 20°, battery capacity used is 80%, and the thrust-to-weight ratio is 2.8:1. It is seen that a battery with a larger weight is used for a longer flight time, and, considering the thrust-to-weight ratio, the engines will not be affected by this situation. The features of the components used in the system are given below. Table 3. When the table is examined and the necessary comparisons are made, it can be seen that every user can easily purchase the products.

Table 3. *Specifications of the Components Used*

Product	Brand / Model	Voltage	Weight	Dimension	Price
Acceleration Sensor	MPU6050	3-5V	6 g	22x17 mm	2.41$
Processor	Arduino Mega	7-12V	36 g	101.6x53.4 mm	16.55$
ESC	Readtosky 30A	7.4–22.2V	25 g	45x24x11 mm	6.06$
Motor	EMAX XA2212 980KV	7.4–11.1V	49 g	3 x 11.7 mm	16.65$
Battery	Profuse 3S 4200 mAh	11.1V	325 g	138x43x24 mm	58.10$

Papa and Del Core (2014) used the Arduino Mega model, which is powered by the Atmega2560 processor. Aziz et al. (2020) used the Arduino Uno model, powered by the Atmega328 processor, as a microcontroller. When our work is examined, it can be seen that we used Arduino Mega, which is powered by the Atmega2560

processor, as a microcontroller in our project. The differences between our study and the referenced studies are compared on a microcontroller basis: Our study aimed to design the flight control card in an open source way and can be coded by anyone. For this reason, Arduino Mega is chosen over other Arduino models. The reason for choosing this model is that it has more than one UART pin. The advantage of having more than one UART pin is that it allows the user to code more easily. For example, the Arduino Uno model has only one UART port connected to both pins and the USB interface. The UART port with USB connection is used to upload the code to the microcontroller. Additionally, communication with the RF receiver takes place via UART. However, since Arduino Uno has a single UART port and it is busy, the microcontroller can only perform one task. In order to load the code written by the user, the UART pins of the RF receiver must be disconnected. This requires extra effort from the user and makes usage difficult. In contrast, the Arduino Mega model has 4 UART pins. When any of these pins are used, there will be no problems during code loading since the other pins are not used. Additionally, the design is open source, allowing users to connect various sensors to the UART pins and increase functionality.

Another aspect to consider is the communication protocols between the transmitter and receiver. In their research, Tagay et al. (2021) utilized a receiver that operates using PPM-PWM modulation techniques. Upon examining their study, it's evident they utilized four channels of the receiver. These channels control the "throttle," "yaw," "pitch," and "roll" movements of the drone, with each movement requiring a separate channel for control. The transmission of each signal is facilitated using PPM or PWM protocols. In our study, however, we opted for a newer technology: the SBUS protocol. SBUS and PWM/PPM protocols have been compared based on some significant features. PWM/PPM uses one channel for each signal, necessitating multiple connection points and cable connections. In contrast, SBUS serially transmits a series of data over a single cable to convey multiple channels, allowing multiple channels to be controlled using just one cable. This aspect is crucial for user-friendliness. While PWM/PPM generally offers good precision, it provides less data transmission than SBUS. SBUS typically provides higher precision and greater data transmission, resulting in faster and more accurate control. Despite the circuit complexity of SBUS compared to PWM/PPM, its advantages include reduced cable complexity, increased precision, faster data transmission, and ease of use. Although SBUS signals may arrive inverted from the transmitter, requiring an inverting circuit on the flight control board, the benefits outweigh this inconvenience, making SBUS the preferred choice for its modern applications.

Upon further examination of the research by Tagay et al. (2021), it is found that they referenced the specialized balance control system, like the one utilized in my own studies, for the control algorithm. This system aims to determine optimal values for flight through experimentation and integrate them into the system. Acceptable results are obtained from the experiments. There is potential for further exploration in the control aspect of our study. To explain further, the system's transfer function is determined alongside this method, and a PID control algorithm is modeled using MATLAB/Simulink. Optimal values for parameters such as Peak time, Settling time, Rise Time, Overshoot, and Percent Overshoot can be found either through trial and error or automatically using PID tuning. These results obtained from the simulation are then integrated into the experimental setup to compare the real-world response with the simulated results.

4. CONCLUSION

This study emphasizes the importance of UAV systems in present and future contexts. Furthermore, it focuses on designing this technology to be accessible and applicable to everyone. The study is completed through comprehensive literature research and systematic experimentation to contribute to the existing literature. The paper details the essential procedures required for the stable operation of a quadcopter UAV. These functions include establishing communication with the ground control station, implementing control using a PID algorithm, reading and evaluating data from the IMU sensor, and designing the flight control card for easy usability. Throughout the study, these four fundamental functions are elaborated on sequentially. In addition to constructing the UAV system, the study also highlights important considerations to be taken into account during these processes. Contemporary practices are integrated into the project. For instance, the relatively new S-BUS protocol is utilized for communication between the transmitter and receiver. Moreover, current web computation platforms are employed to verify test results and determine system characteristics. As a result of the research, a basic-level flight control board for a quadcopter UAV is designed, integrated, and tested. The

steps of this study are described in detail. Information obtained from research and literature surveys on various subjects and areas contributes to this study, allowing for a comprehensive perspective. The study enables theoretical concepts to be observed in a physical environment, facilitating further development by other users and researchers due to its open-source nature. This, in turn, can lead to greater contributions to the literature in this field. The applications conducted during the study can be further investigated and developed, and more precise experiments can be conducted in simulation environments. Additionally, different approaches can be applied to these applications. For example, various control algorithms, such as LQR and MPC, can be utilized and tested. In conclusion, this study addresses the fundamental aspects required for a quadcopter and translates them into design and implementation.

AUTHOR CONTRIBUTIONS

Conceptualization, E.G. and H.D.; methodology, E.G. and H.D.; fieldwork, E.G. and H.D.; software, E.G.; title, E.G. and H.D.; validation, E.G. and H.D.; laboratory work, E.G.; formal analysis, E.G.; research, E.G. and H.D.; sources, E.G.; data curation, E.G.; manuscript-original draft, E.G.; manuscript-review and editing, H.D.; visualization, E.G.; supervision, H.D.; project management, E.G.; funding, E.G. and H.D.

ACKNOWLEDGEMENT

CONFLICT OF INTEREST

The authors declare no conflict of interest.

REFERENCES

Akay, A., Kuris, U., & Senan, S. (2021). Unmanned air vehicles and autopilots. *Journal of Aviation Research*, *3*(2), 128-149. https://doi.org/10.51785/jar.894721

Altinors, A., & Kuzu, F. (2021). Dynamic analysis of a quadcopter using PID, adaptive and LQR control methods. International *Journal of Innovative Engineering Applications*, *5*(2), 65-74. https://doi.org/10.46460/ijiea.929552

Aziz, D. A., Algburi, S. S., Alani, S., & Mahmood, S. N. (2020, June 28-30). *Design and implementation of GPS-based quadcopter control system*. In: Proceedings of the 1st International Multi-Disciplinary Conference Theme: Sustainable Development and Smart Planning (IMDC-SDSP 2020), (pp. 1-14), Cyperspace. https://doi.org/10.4108/eai.28-6-2020.2297931

Elmas, E. E., & Alkan, M. (2023). Design, simulation and implementation of an unmanned aerial vehicle system. *Journal of Polytechnic*, *26*(2), 929-940. https://doi.org/10.2339/politeknik.1037319

Ji, A., & Turkoglu K. (2015). Development of a low-cost experimental quadcopter tested using an arduino controller and software. *arXiv Preprint*, 1508-04886. https://doi.org/10.48550/arXiv.1508.04886

Kazan, F. A., & Solak, H. (2023). Improvement of ultrasonic sensor-based obstacle avoidance system in drones. *International Journal of Aeronautics and Astronautics*, *4*(1), 9-35. https://doi.org/10.55212/ijaa.1261912

Kishor, V., & Singh, S. (2017). Design and development of arduino uno based quadcopter. *International Journal of Engineering and Manufacturing Science*, *7*(1), 14-19.

Kose, O. (2021). *İnovatif Yöntemlerle Kuadkopter Modellenmesi, Kontrolü ve Gerçek Zamanlı Uygulamaları*, PhD Thesis, Erciyes Üniversitesi.

Kucuksezer, H. C., & Sancaktar, I. (2021). Drone flight test system design with microcontroller. *BSEU Journal of Science*, *8*(2), 778-787. https://doi.org/10.35193/bseufbd.942380

Mandal, S., Saw, S. K., Shaw, K., Thakur, A. K., Seth, V., & Singh, P. (2016). Low-cost bluetooth-arduino hover control design of a quad copter. *IOSR Journal of Electronics and Communication Engineering (IOSR-JECE)*, *11*(4), 81-90. https://doi.org/10.9790/2834-1104048190

Oktay, T., & Ozen, E. (2021). System design and control of rotary wing unmanned aerial vehicle. *European Journal of Science and Technology*, *27*, 318-324. https://doi.org/10.31590/ejosat.957056

Papa, U., & Del Core, G. (2014). *Design and assembling of a low-cost mini UAV quadcopter system*. DRAFT: Department of Science and Technology, University of Naples Parthenope.

Pehlivan, K., & Akuner, M. C. (2020). Designing PID controller for quadrotor test bench and implementation. *International Periodical of Recent Technologies in Applied Engineering*, *2*(1), 15-24. http://doi.org/10.35333/porta.2020.209

Tagay, A., Omar, A., & Ali, Md. H. (2021). Development of control algorithm for a quadcopter. *Procedia Computer Science*, *179*, 242-251. https://doi.org/10.1016/j.procs.2021.01.003

Vishwakarma, R., Kumar, A., Verma A. K., Maurya, D., Gupta, U. D., & Jaiswal, P. (2023). Quadcopter drone using arduino uno. *International Journal for Research Trends and Innovation*, *8*(4), 276-279.

Effect of ZrO₂ on Radiation Permeability Properties of Polypropylene

Zübeyde ÖZKAN[1,2*] Berkay ÇAKIR[3] Seda Gürgen AVŞAR[3] Emir OLÇAY[3] Uğur GÖKMEN[3]

[1] Gazi University, Institute of Science and Technology, Ankara, Türkiye
[2] Gazi University, Institute of Science and Technology, Department of Advanced Technologies, Ankara, Türkiye
[3] Gazi University, Institute of Science and Technology, Department of Metallurgical and Materials Engineering, Ankara, Türkiye

Keywords	Abstract
Polypropylene (PP) ZrO2 Gamma Shielding Neutron Composite	The study investigates the radiation permeability properties including mass attenuation coefficient (MAC), linear attenuation coefficient (LAC), tenth value layer (TVL), half value layer (HVL), fast neutron cross section (FNRC), and mean free path (MFP) of polypropylene (PP) polymer, as well as the produced polymer matrix composites (PP+5% ZrO2, PP+10% ZrO2, PP+15% ZrO2). The studied materials were examined by considering their effect on radiation permeability against gamma and neutron radiation. Additionally, powder size, Archimedes principle (density), XRD, DSC, ATR, and DTA-TG analyses were performed. According to the radiation permeability results of the studied four materials, PP + 15% ZrO2 was found to have the highest LAC values, while PP was found to have the lowest LAC values. The FNRC values of the PP, PP+5% ZrO2, PP+10% ZrO2, and PP+15% ZrO2 materials were found to be 10.038 cm-1, 12.651 cm-1, 15.002 cm-1, and 17.091 cm-1, respectively. The most suitable material for gamma and neutron shielding was found to be 15% ZrO2 reinforced material.

Author ID (ORCID Number)		Article Process	
0000-0003-2901-7749	Zübeyde ÖZKAN	**Submission Date**	29.04.2024
0009-0001-5500-9438	Berkay ÇAKIR	**Revision Date**	22.05.2024
0009-0008-9991-7236	Seda Gürgen AVŞAR	**Accepted Date**	05.06.2024
0009-0009-5257-6929	Emir OLÇAY	**Published Date**	28.06.2024
0000-0002-6903-0297	Uğur GÖKMEN		

1. INTRODUCTION

With the development of technology, energy demand has been rising with each passing day because of the increase in consumption. Thanks to nuclear power plants, it is possible to generate power in any quantity and at any time in line with demand. Therefore, the number of nuclear power plants has been increasing rapidly across the world. Nuclear power plants, like everything else, have several advantages, as well as some disadvantages. Any leak or explosion causes irreversible damage that will affect nature and human health for many years. As a result of radiation spreading to the environment, it affects not only the immediate surroundings of the nuclear power plant but also areas kilometers away from the power plant. As a result of the Chernobyl disaster that occurred on April 26, 1986, Bulgaria, Türkiye, Romania, etc. they were affected by radioactive substances spread throughout the countries. Therefore, radiation shielding is crucial for nuclear power plants (Akman et al., 2022; Szondy et al., 2024). Having a short wavelength, gamma rays emit high-frequency electromagnetic radiation. Since they are uncharged, neutron particles are not affected by Coulomb forces and do not interact with the nucleus. As a result of this, they have a higher penetration depth. Any leak in a nuclear power plant might pose severe health risks for living beings. It might result in hair loss, cataracts, gene damage, cancer, and even mortality in living beings (Tyagi et al., 2021; Ardiansyah et al., 2023; Aldawood et al., 2024). As a result, radiation shielding material is very important for human health and nature. Recently, Alzahrani et al. (2022), Malidarre et al. (2021), Kamislioglu (2021), and several

other researchers have carried out many studies on materials to offer an alternative radiation shielding material that can eliminate the negative aspects of the shielding material currently used.

In this study, recyclable polypropylene (PP) material was used among polymer materials used for different purposes. In this way, as a result of the recycling of materials that have completed their intended use, their usability as gamma and fast neutron shielding material, which is a new field, has been investigated. Polymer matrix composite materials designed by adding ZrO_2 ceramic material at varying rates of 5-10-15% into the PP polymer matrix; the linear attenuation coefficient (LAC), mass attenuation coefficient (MAC), half value thickness (HVL), tenth value thickness (TVL), mean free distance (MFP) and fast neutron cross section (FNRC) parameters were examined and the radiation transmittance results against gamma and neutron radiations were analyzed. In addition, density, XRD, ATR, DSC and DTA-TG analyses of the PP material and SEM-EDS analyses of the ZrO_2 ceramic material, which provide information on powder grain size analysis and microstructural properties, were carried out.

2. MATERIALS AND METHOD

The powder size of the ZrO_2 ceramic powder used was dimensional utilizing Malvern Mastersizer 3000, which is a laser diffraction particle size analyzer. In addition, the microstructure of the material was examined under the SEM microscope to understand the powder grain shape, which is important in determining the production parameters. Then the XRD analyses of the PP were performed. Table 1 shows the chemical composition of the studied materials in the radiation permeability analysis. The melting point and vaporization temperature are crucial parameters in terms of radiation shielding. This is because the degradation of the radiation shielding material's chemical structure is very important for its resistance against radiation. Therefore, ATR, DSC, and DTA-TG analyses were performed on the studied PP polymer materials.

Table 1. Chemical composition of the materials

Name of the sample	Composition
S0	PP
S5	PP+5% ZrO_2
S10	PP+10% ZrO_2
S15	PP+15% ZrO_2

The gamma and neutron permeability analyses of polymer composites were performed by employing Phy-x/PSD (Şakar et al., 2020). The LAC and MAC which provide significant details about the material's shielding feature against radiation, are very prominent in the selection of shielding material. LAC (μ), which is the fraction of attenuated radiation in an energy beam per unit thickness of material, is obtained by utilising the Beer-Lambert law (Equation 1). MAC, on the other hand, is obtained by taking into account the density of the material in absorbing the incoming radiation. It is a measure of the possible interaction between photon and matter. The MAC value is given by divide the LAC value by the material intensity, as shown in Equation 2, where I_o, I, and x are the intensity of the radiation on the material, the intensity of the radiation passing through the material and the thickness of the material (cm), respectively

$$I = I_o e^{-\mu x} \tag{1}$$

$$\mu_m = \frac{\mu}{\rho} \tag{2}$$

HVL, MFP and TVL are very important parameters as they are utilizing to specify the thick of the radiation shielding material to be used. HVL indicates the thickness at which the shielding material decreases the incident radiation by half the intensity, while TVL indicates the thickness at which it reduces the incident radiation by 90% in centimeters. The mean distance traveled between two successive collisions by an incoming photon is specified by MFP. These parameters are calculated using Equations 3-4-5. FNRC is significant in terms of the absorption of fast neutrons. FNRC is calculated in centimeters by employing Eq. 6 (Kılıçoğlu & Tekin, 2020; Kavun et al., 2022).

$$HVL = \frac{\ln(2)}{\mu} \tag{3}$$

$$TVL = \frac{\ln(10)}{\mu} \tag{4}$$

$$MFP = \frac{1}{\mu} \tag{5}$$

$$\sum_R = \sum_i \rho_i \left(\sum R/\rho\right)_i \tag{6}$$

3. RESULTS AND DISCUSSION

The average density of the studied PP, which was measured by Archimedes' principle, was found to be approximately 0.77 g/cm^3. Figure 1 shows the powder grain size distribution of the ZrO_2 ceramic powder used in the study. Dv (90), Dv (50), and Dv (10) values of the ZrO_2 ceramic powder were found to be 38.6 μm, 18.0 μm, and 3.46 μm, respectively. In Figure 2, it can be seen that the ZrO_2 ceramic powder has an angular shape at x1000 magnification. When the SEM image is examined, Dv (90), Dv (50) and Dv (10) differences in the powder grain size distribution are seen.
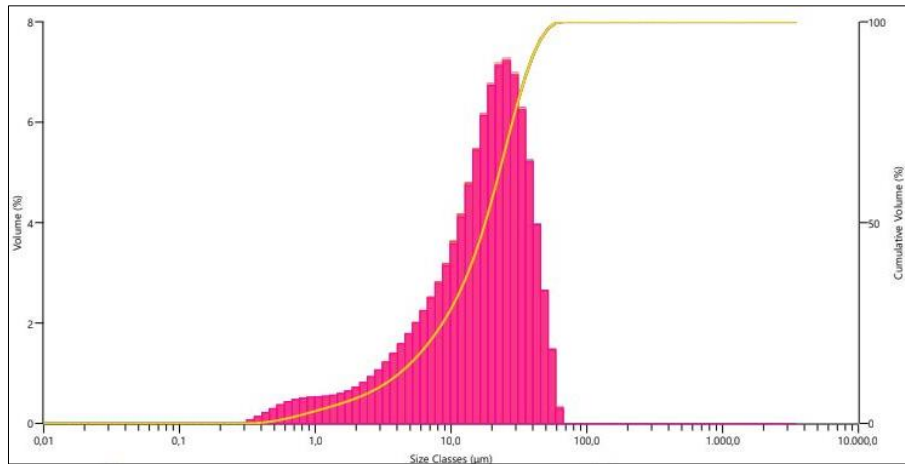
Figure 1. *Grain size distribution of the ZrO₂ ceramic powder*
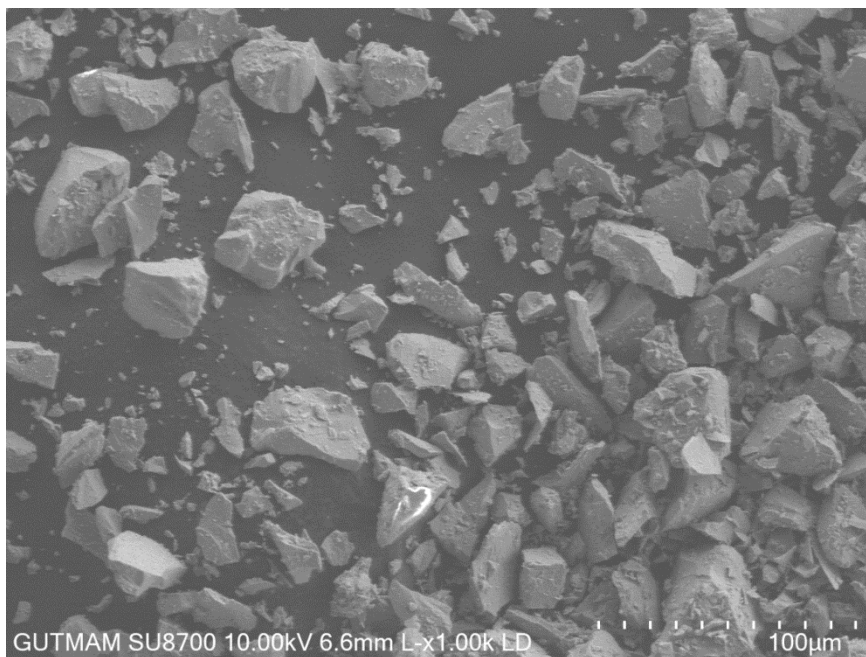
Figure 2. *SEM of the ZrO₂ ceramic powder*

Figure 3 presents the XRD analysis of PP, as well as the characteristic peaks with (hkl) Miller indices of the material. XRD analyzes of PP material were analyzed at 2θ° between 10°-90°. At 2θ°, the PP material gives peaks of (011), (040), (130), (111), and (060) to the crystal planes at about 14.3°, 17.2°, 18.7°, 21.3°, and 25.5°, respectively. The peaks of the XRD spectrum curve are also consistent with those of PP reported in the literature (Akinci et al., 2007; Mingliang et al., 2007). In addition, the crystallinity rate of the studied material was found by measuring the ratio of the entire area under the curve (Figure 3) to the crystal peak areas, using the equation given in Equation 7, and was calculated as 82.24%.

$$\%Crystallinity = \frac{A_{crystal}}{A_{curve}} \ x \ 100 \tag{7}$$
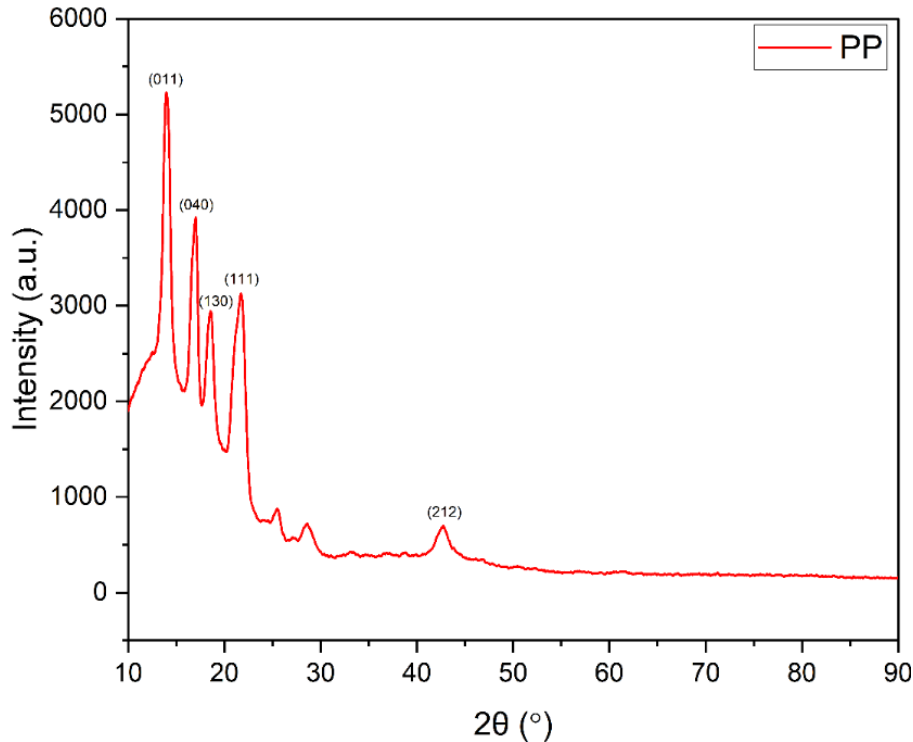
Figure 3. XRD spectrum of the polypropylene

Isotactic PP, a widely used commercial polymer, may have a simple chemical composition, but its self-assembly behavior and crystal structures are surprisingly complex. The type of polymer significantly affects semi-crystalline polymers' properties, including crystal thicknesses and crystallinity levels. The morphology of crystals is also greatly affected by thermo-mechanical processes (Labour et al., 2001; Akinci et al., 2007). In polymeric materials, the crystallization rate and amorphous regions change the materiel's thermal, physical, and mechanical characteristics (Akinci et al., 2007). Pure PP can usually be obtained in the following crystal shapes; α (monoclinic)γ (orthorhombic), and β (trigonal) as well as smectic mesophase, an intermediate state between amorphous and ordered phases. As it is the most stable state in terms of thermodynamic conditions, α state is the most commonly used form of PP in industry. Also, the melting point of isotactic polypropylene (iPP) is around 160–165 °C, which is relatively higher than other variations (Papageorgiou et al., 2012).

In Figure 4, the DSC spectrum of polypropylene was analyzed between 25°C - 250°C with increasing temperature at 10°C per minute. Multiple endothermic peaks occur at 136°C and 168°C, depending on the process involved in various fusion transitions. The main peak is observed at 168°C. Recrystallization or rearrangement of some crystallized fractions are the primary reasons for these multiple endothermic reactions (Cho et al., 1999). According to the TGA and DSC analysis results, it is observed that the melting point varies between 168°C and 172°C. In Figure 5, the DTA spectrum of polypropylene was analyzed between 25°C - 600°C with increasing temperature at 10°C per five minutes. Additionally, thermal decomposition of PP material begins around 453°C.
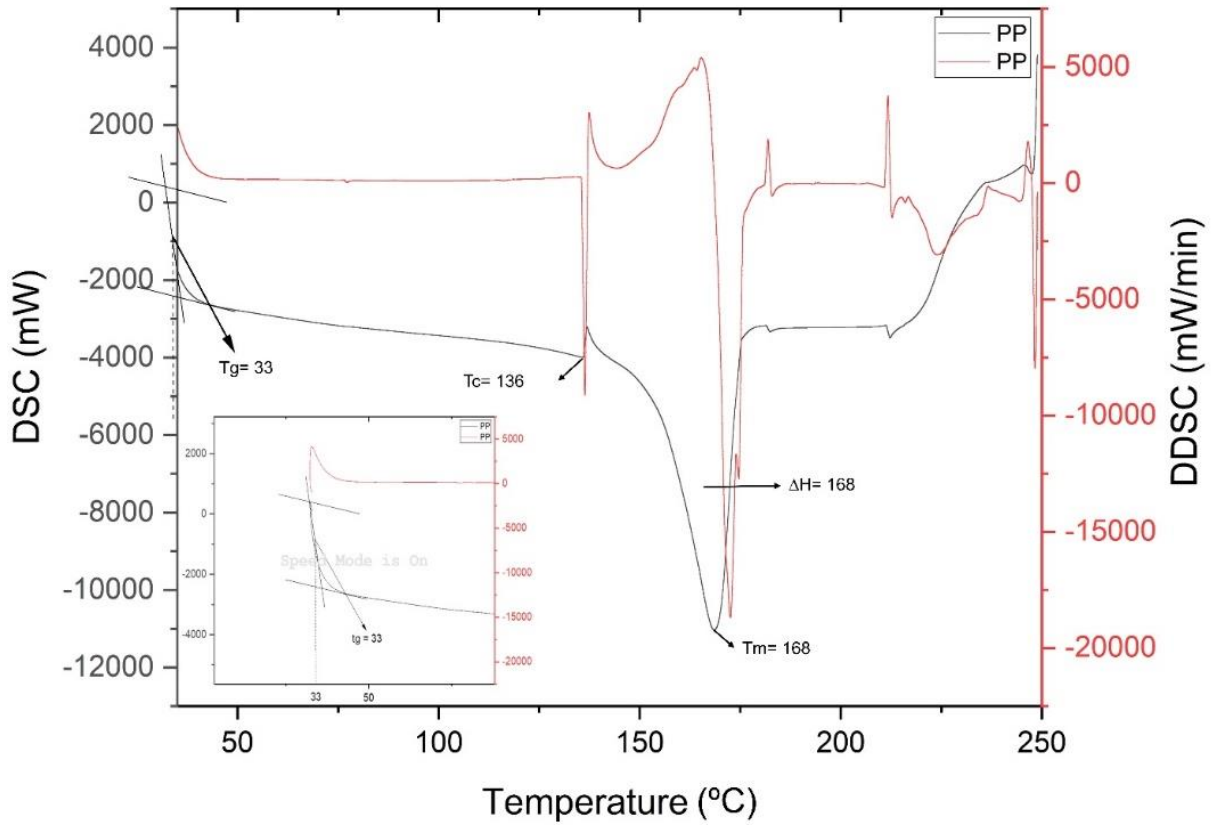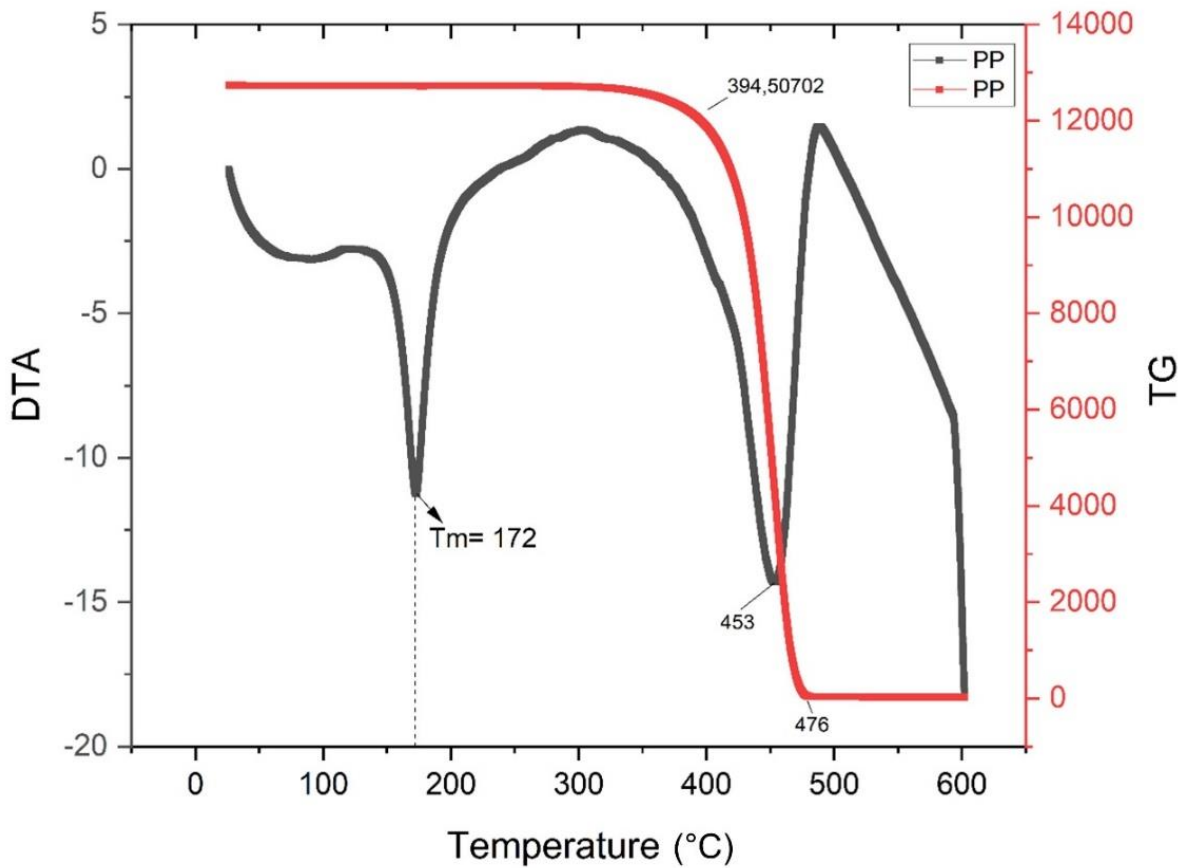
Figure 4. DSC analysis of polypropylene

Figure 5. DTA-TGA analysis of polypropylene

ATR analysis PP material was analyzed at wavelengths of 550 cm^{-1} -4000 cm^{-1}. Figure 6 shows the spectrum of the PP material and the absorption peaks, which are consistent with those reported by the previous studies. In the isotactic polypropylene spectrum, the methylene group arises between the range from 1445 cm^{-1} to 1485 cm^{-1} while the methyl group originates between 430 cm^{-1} and 1470 cm^{-1} or between 1365 cm^{-1} and 1395 cm^{-1}. In spectrum, such peaks show 1451 cm^{-1} and 1377 cm^{-1}, respectively. The peak around 2915 cm^{-1} was linked to CH band vibration. The pure PP spectrum also contains characteristic peaks at 840, 1000, and 1170 cm^{-1}. These characteristic curves are observed at 1170, 997, and 840 cm^{-1}; however, they are not clearly detachable owing to the smoothing process (Krylova & Dukštienė, 2013).
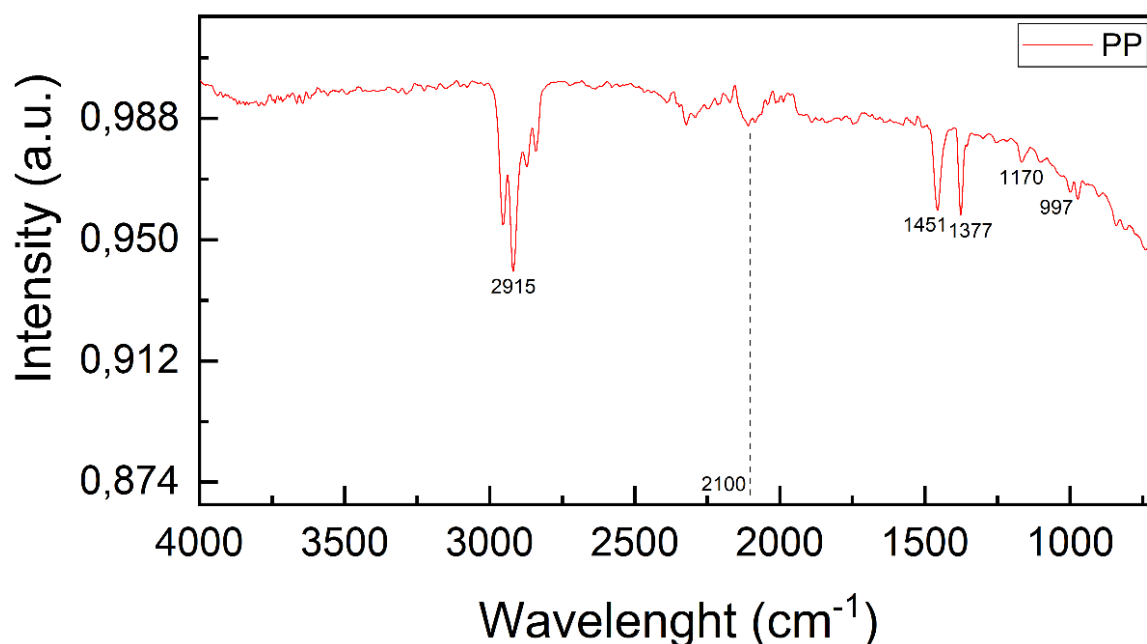
Figure 6. ATR spectrum of polypropylene

According to the LAC values (Figure 7), all studied samples have lower LAC figures with the increase in energy. It is observed that the radiation absorption abilities of materials are higher in the low energy range. The addition of 5% ZrO_2 in PP leads to a two-fold rise in the LAC worth of the PP polymer material. This is mainly because the ZrO_2 material is a high-density ceramic and contains elements with much higher atomic numbers compared to PP. The sample's LAC value increases depending on the increase in the proportion of the ZrO_2 addition. The photoelectric effect (PE) occurs dominantly in the of 0.005888 MeV<E<0.511 MeV. In this energy region, the PP, PP+5% ZrO_2, PP+10% ZrO_2, and PP+15% ZrO_2 materials exhibit the following ranges of the LAC values: 777.564 cm^{-1}–7.764 cm^{-1}, 2179.104 cm^{-1}–10.025 cm^{-1}, 4134.525 cm^{-1}– 12.344 cm^{-1}, and 6643.827 cm^{-1}–14.633 cm^{-1}, respectively. At the energy of 0.662 MeV (^{137}Cs), where Compton scattering (CS) is predominant, PP, PP+5% ZrO_2, PP+10% ZrO_2, and PP+15% ZrO_2 materials get LAC values of 6.859 cm^{-1}, 8.947 cm^{-1}, 11.001 cm^{-1}, and 13.021 cm^{-1}, respectively. The studied polymer composites' LAC values are observed to get higher figures with the increase in the proportion of the ZrO_2 addition.

Figure 8 reveals that the MAC and LAC curves of the materials exhibit similar behaviors. While the variation in the studied materials' MAC values is more evident in the low photon energy regions, the variation in the samples' MAC values is closer to each other in the high photon energy region. This is because the materials have more interaction with photons and, accordingly, the absorption amount is higher at lower photon energies. In other words, it is due to the weaker ability of materials to absorb photons at high photon energies. For the energy level of 0.723 MeV (^{131}I), where CS is dominant, PP, PP+5% ZrO_2, PP+10% ZrO_2 and PP+15% ZrO_2 materials have the MAC values of 8.464 cm^2/g, 8.395 cm^2/g, 8.326 cm^2/g, and 8.256 cm^2/g, respectively. MAC values of the materials show well stability in the energy region after 2 MeV, where pair production predominantly occurs. At a photon energy of 2 MeV, the MAC values of PP, PP+5% ZrO_2, PP+10% ZrO_2, and PP+15% ZrO_2 materials are 5.064 cm^2/g, 5.023 cm^2/g, 4.981 cm^2/g, and 4.939 cm^2/g, respectively.
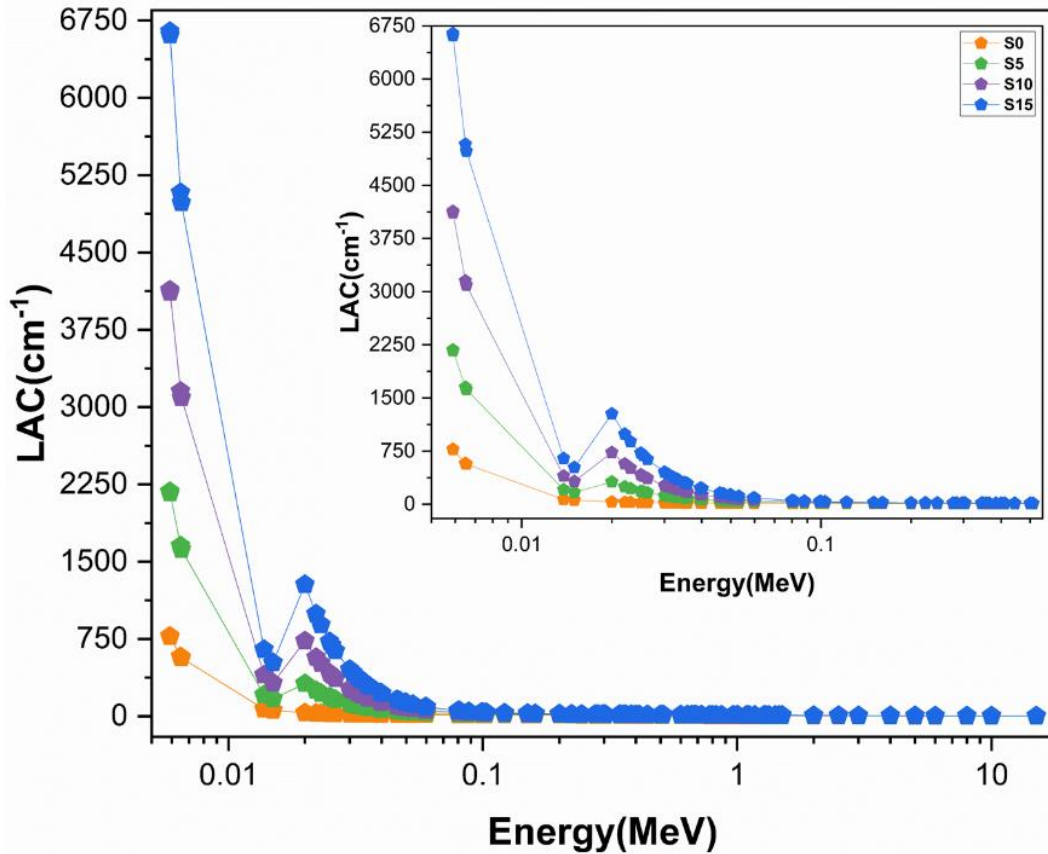
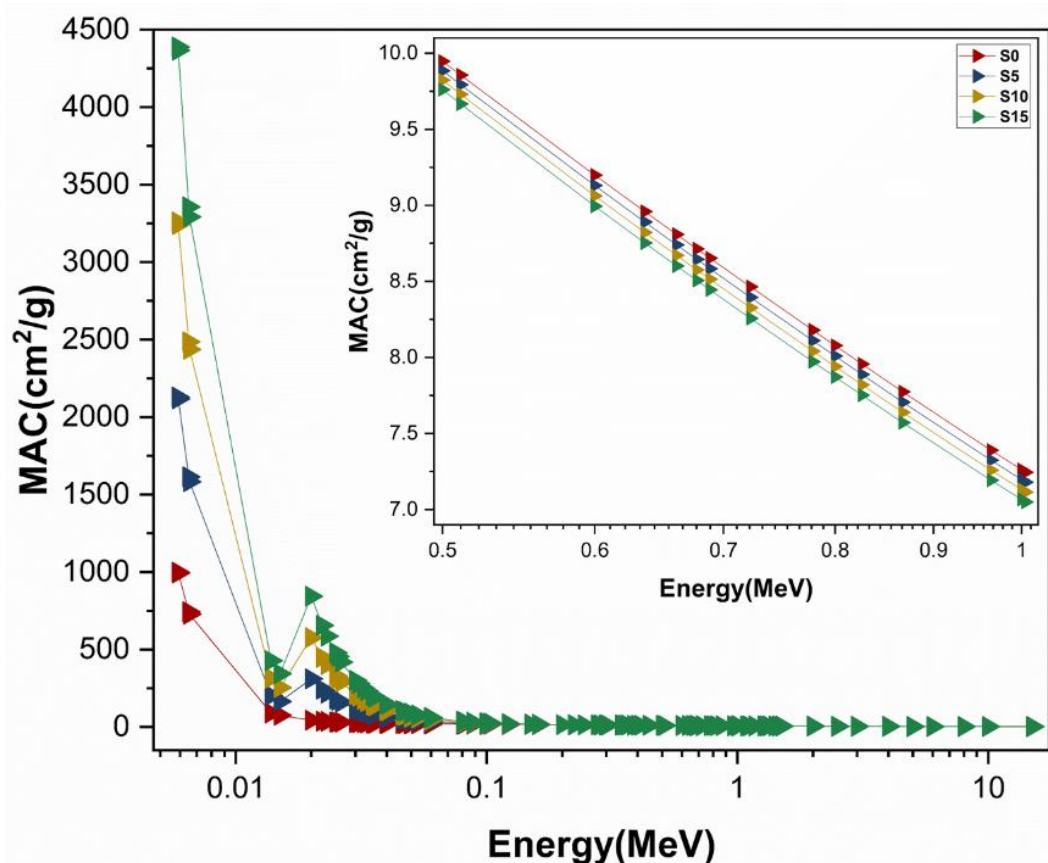*Figure 7. LAC values of the samples*

Figure 8. MAC values of the samples

Considering the HVL plot of the studied materials, the HVL values get lower figures due to the higher absorption of the materials at low energies (Figure 9). The HVL values of the PP, PP+5% ZrO_2, PP+10% ZrO_2, and PP+15% ZrO_2 samples range from 0.0001 cm to 0.09 cm in the energy range of 0.005888-0.511 MeV, where the PE occurs predominantly. On the other hand, Compton scattering occurs predominantly between the energy levels 0.511-1.02 MeV, where HVL gets a value between 0.047 cm and 0.123 cm. Finally, pair production occurs predominantly in the high energy zone, where HVL values range from 0.123 cm to 0.489 cm. The relationship between the material thickness required to halve the incoming photon power and the incoming photon energy is clearly seen from these HVL values. Figure 8 shows that the material thickness required by the S15 sample, which is produced by adding 15% ZrO_2 ceramic material into the PP, to absorb the same photon energy is reduced to approximately half, even in the high energy region.
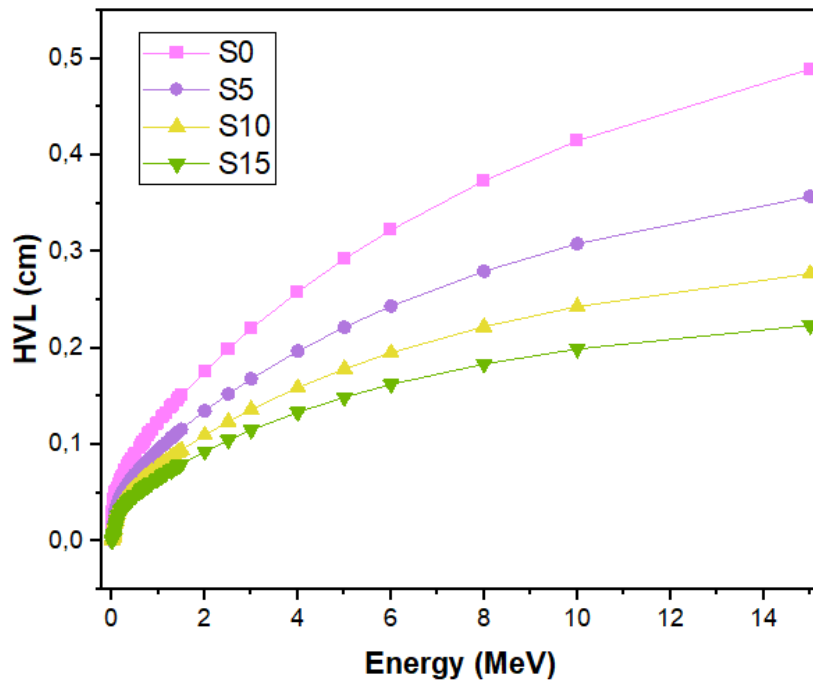

Figure 9. *HVL value of the samples*

Figure 10 shows the TVL plot, which indicates the material thick necessary to reduce the incoming radiation intensity by 90%. In this figure, it is plainly observed that the thickness values of the studied materials should be higher than their HVL values. The ^{60}Co source, which is widely used in industry, is a radioactive gamma radiation source. This gamma radiation source has various photopeaks in the energy regions where Compton scattering, PE, and pair production are predominant. When the energy level is 0.3471 MeV, the PE is dominant, and the PP, PP+5% ZrO_2, PP+10% ZrO_2, and PP+15% ZrO_2 samples have TVL values of 0.257 cm, 0.196 cm, 0.158 cm, and 0.133 cm, respectively. When the energy level is 0.8261 MeV, the Compton scattering is dominant, and the studied samples get values of 0.372 cm, 0.285 cm, 0.232 cm, and 0.196 cm, respectively. On the other hand, pair production is dominant at the energy level of 1.173 MeV, and these values are observed to be 0.441 cm, 0.338 cm, 0.276 cm, and 0.233 cm, respectively. This analysis results reveal the addition's effect on the radiation shielding material's thickness with the increase in the photon energy emitted from a radioactive source, even if the gamma sources are the same.

Figure 11 shows that the material thick required for successful two-photon interaction increases with the increase in photon energy. It is evident that the increase in ZrO_2 ceramic addition in the studied materials results in decreases in their MFP values. It is because the atomic number and density of the ZrO_2 ceramic are higher than those of the PP material. Therefore, the increase in the ZrO_2 addition results in a large number of electrons' interactions with photons. After 2 MeV, the MFP values of all the studied samples increase rapidly. This is because the LAC values of these materials become more stable after 2 MeV, and the absorption of high-energy photons decreases considerably. At the energy range 2-15 MeV, the materials PP, PP+5% ZrO_2, PP+10% ZrO_2 and PP+15% ZrO_2 have MFP ranges of 0.254 cm- 0.706 cm; 0.194 cm- 0.515 cm; 0.158 cm- 0.4 cm and 0.134 cm- 0.323 cm respectively.

FNRC is a significant in terms of indicating the shielding performance of a designed material against fast neutrons. The FNRC values of the PP, PP+5% ZrO_2, PP+10% ZrO_2, and PP+15% ZrO_2 materials are 10.038 cm^{-1}, 12.651 cm^{-1}, 15.002 cm^{-1}, and 17.091 cm^{-1}, respectively. Among the four samples, the PP material has the lowest FNRC value, while the PP+15% ZrO_2 polymer matrix has the highest value (Figure 12). The density value of the PP+15% ZrO_2 polymer composite is about 95% higher than that of the PP material. Also, the FNRC value of the PP+15% ZrO_2 polymer matrix is about 70% higher than that of the PP material. The increase in the ZrO_2 ceramics addition to the PP material leads to more neutron interaction of nuclei; as a result, the FNRC values get higher figures.
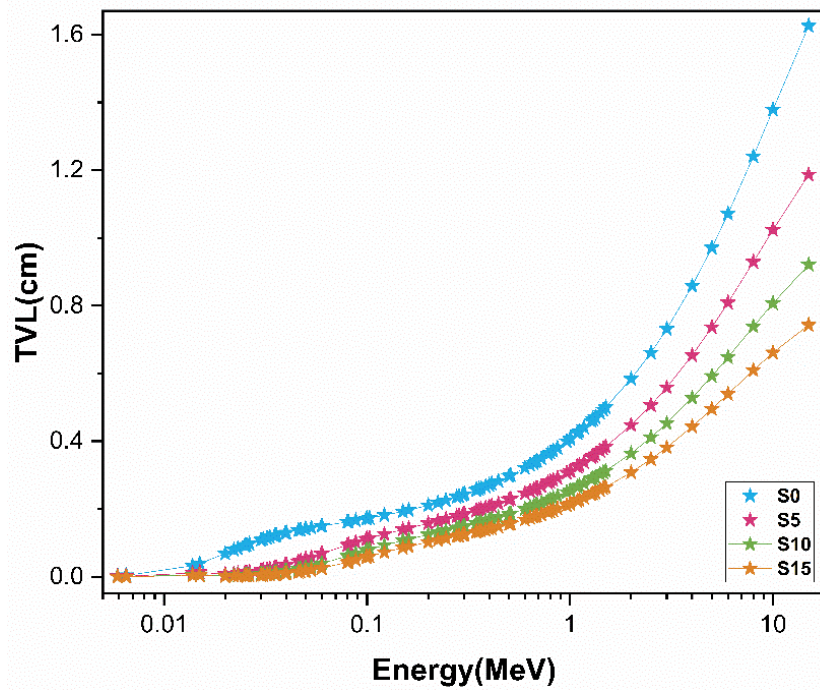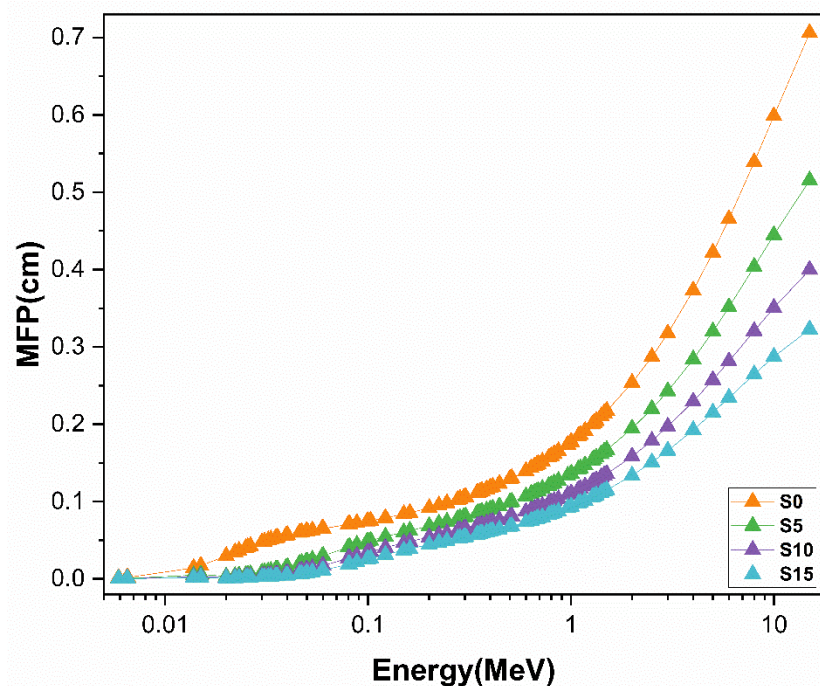

Figure 10. TVL value of the samples

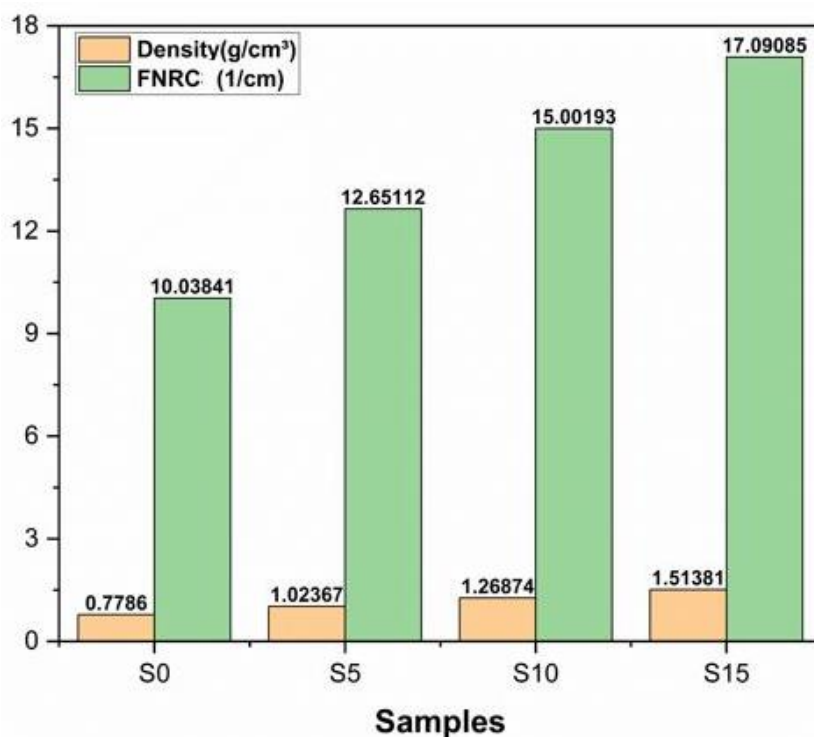*Figure 11. MFP value of the samples*

Figure 12. *FNRC and density values of the samples*

4. CONCLUSION

This study examined the radiation shielding performance of polypropylene and polymer matrix composites produced by adding ZrO_2 ceramic powder in varying proportions (5%, 10%, and 15%) to the PP material. The LAC, MAC, HVL, TVL, MFP, and FNRC, which provide significant information about gamma and neutron radiations, were analysed by utilizing the Phy-x/PSD software. Grain size and microstructures of ZrO_2 ceramic material were analyzed by SEM. Moreover, the XRD, ATR, DSC, and DTA-TG analyses were performed to obtain information about the density and characteristic properties of the PP material. Among the studied PP, PP+5% ZrO_2, PP+10% ZrO_2 and PP+15% ZrO_2 samples, PP+10% ZrO_2 had the highest LAC value while PP had the lowest LAC value. The samples with higher LAC values had lower HVL values. Therefore, the material with the highest HVL value is PP while the material with the lowest HVL value is PP+15% ZrO_2. As for the FNRC values, PP material has the lowest value (10.038 cm^{-1}) while the PP+15%ZrO_2 polymer matrix composite has the highest FNCR value (17.091 cm^{-1}). To conclude, the neutron and gamma radiation shielding features of the PP material were improved by increasing the ZrO_2 ceramic addition.

ACKNOWLEDGEMENT

AUTHOR CONTRIBUTIONS

Conceptualization, U.G. and Z.Ö; methodology, U.G; fieldwork, Z.Ö, S.G.A., B.Ç and E.O.; software, Z.Ö, B.Ç and E.O; title, U.G, and Z.Ö; validation, U.G., Z.Ö. and S.G.A.; laboratory work, Z.Ö, S.G.A., B.Ç and E.O.; formal analysis, U.G.; research, Z.Ö, S.G.A. and B.Ç; sources, Z.Ö and B.Ç.; data curation, Z.Ö and B.Ç.; manuscript-original draft, U.G. and Z.Ö.; manuscript-review and editing, U.G and Z.Ö; visualization, S.G.A, B.Ç and Z.Ö.; supervision, U.G; project management, U.G; funding, Gazi BAP. All authors have read and legally accepted the final version of the article published in the journal.

CONFLICT OF INTEREST

The authors declare no conflict of interest.

REFERENCES

Akinci, A. & Akbulut, H. & Yilmaz, F. (2007). The Effect of the Red Mud on Polymer Crystallization and the Interaction between the Polymer-Filler. *Polymer-Plastics Technology and Engineering*, *46*(1), 31-36. https://doi.org/10.1080/03602550600916258

Akman, F., Ogul, H., Ozkan, I., Kaçal, M. R., Agar, O., Polat, H., & Dilsiz, K. (2022). Study on gamma radiation attenuation and non-ionizing shielding effectiveness of niobium-reinforced novel polymer composite. *Nuclear Engineering and Technology*, *54*(1), 283-292. https://doi.org/10.1016/j.net.2021.07.006

Aldawood, S., Asemi, N. N., Kassim, H., Aziz, A. A., Saeed, W. S., Al-Odayni, A.-B. (2024). Gamma radiation shielding by titanium alloy reinforced by polymeric composite materials. *Journal of Radiation Research and Applied Sciences*, *17*(1), 100793. https://doi.org/10.1016/j.jrras.2023.100793

Alzahrani, J. S., Lebedev, A. V., Avanesov, S. A., Hammoud, A., Alrowaili, Z. A., Mahmoud, Z. M. M., Olarinoye, I. O., & Al-Buriahi, M. S. (2022). Synthesis and properties of tellurite based glasses containing Na_2O, BaO, and TiO_2: Raman, UV and neutron/charged particle shielding assessments. *Ceramics International*, *48*(13), 18330-18337. https://doi.org/10.1016/j.ceramint.2022.03.092

Ardiansyah, A., Heryanto, H., Armynah, B., Salah, H., Sulieman, A., Bradley, D. A., & Tahir, D. (2023). Physical, mechanical, optical, and gamma radiation shielding properties of the BaO-based glass system prepared by the melt-quench technique: A review. *Radiation Physics and Chemistry*, *210*, 111059. https://doi.org/10.1016/j.radphyschem.2023.111059

Cho, K., Li, F., & Choi, J. (1999) Crystallization and melting behavior of polypropylene and maleated polypropylene blends. *Polymer*, *40*(7), 1719-1729. https://doi.org/10.1016/S0032-3861(98)00404-2

Kamislioglu, M. (2021). Research on the effects of bismuth borate glass system on nuclear radiation shielding parameters. *Results in Physics*, *22*, 103844. https://doi.org/10.1016/j.rinp.2021.103844

Kavun, Y., Kerli, S., Eskalen, H., & Kavgacı, M. (2022). Characterization and nuclear shielding performance of Sm doped In_2O_3 thin films. *Radiation Physics and Chemistry*, 194, 110014. https://doi.org/10.1016/j.radphyschem.2022.110014

Kılıçoğlu, O., & Tekin, H. O. (2020). Bioactive glasses with TiO_2 additive: Behavior characterization against nuclear radiation and determination of buildup factors. *Ceramics International*, *46*(8-Part A), 10779-10787. https://doi.org/10.1016/j.ceramint.2020.01.088

Krylova, V. & Dukštienė, N. (2013). Synthesis and Characterization of Ag_2S Layers Formed on Polypropylene. *Journal of Chemistry*, *2013*(1), 987879. https://doi.org/10.1155/2013/987879

Labour, T., Gauthier, C., Séguéla, R., Vigier, G., Bomal, Y., & Orange, G. (2001) Influence of the β crystalline phase on the mechanical properties of unfilled and $CaCO_3$-filled polypropylene. I. Structural and mechanical characterization. *Polymer*, *42*(16), 7127-7135. https://doi.org/10.1016/S0032-3861(01)00089-1

Malidarre, R. B., Akkurt, İ., & Kavas, T. (2021). Monte Carlo simulation on shielding properties of neutron-gamma from 252Cf source for Alumino-Boro-Silicate glasses. *Radiation Physics and Chemistry*, *186*, 109540. https://doi.org/10.1016/j.radphyschem.2021.109540

Mingliang, G., Demin, J., & Weibing, X. (2007). Study on the Crystallization Properties of Polypropylene/Montmorillonite Composites. *Polymer-Plastics Technology and Engineering*, 46(10), 985-990. https://doi.org/10.1080/03602550701519449

Papageorgiou, D. G., Bikiaris, D. N., & Chrissafis, K. (2012). Effect of crystalline structure of polypropylene random copolymers on mechanical properties and thermal degradation kinetics. *Thermochimica Acta*, *543*, 288-294. https://doi.org/10.1016/j.tca.2012.06.007

Szondy, B., Bodnár, B., Grossetête, A., Gain, T., & Aszódi, A. (2024). Review of solutions developed for improving maneuvering flexibility in German, French and Russian PWRs targeting to explore future

possibilities for the new VVER-1200 nuclear power plant units in Hungary. *Nuclear Engineering and Design*, *419*, 112965. https://doi.org/10.1016/j.nucengdes.2024.112965

Şakar, E., Özpolat, Ö. F., Alım, B., Sayyed, M. I., & Kurudirek, M. (2020). Phy- X / PSD: Development of a user friendly online software for calculation of parameters relevant to radiation shielding and dosimetry. *Radiation Physics and Chemistry*, *166*, 108496. https://doi.org/10.1016/j.radphyschem.2019.108496

Tyagi, G., Singhal, A., Routroy, S., Bhunia, D., & Lahoti, M. (2021). Radiation Shielding Concrete with alternate constituents: An approach to address multiple hazards. *Journal of Hazardous Materials*, *404*(Part B), 124201. https://doi.org/10.1016/j.jhazmat.2020.124201

JOURNAL OF SCIENCE

PART A: ENGINEERING AND INNOVATION

GAZİ UNIVERSITY
Gazi
1926